University of Southampton

Faculty of Medicine

Clinical and Experimental Sciences

Toxicity of nanoparticles on lung cells and pulmonary immune defences

by

Artur Kirjakulov

Thesis for the degree of Doctor of Philosophy

June 2020

University of Southampton

Abstract

Faculty of Medicine

Clinical and Experimental Sciences

Thesis for the degree of Doctor of Philosophy

TOXICITY OF NANOPARTICLES ON LUNG CELLS AND PULMONARY IMMUNE DEFENCES

by Artur Kirjakulov

Background: Nanoparticles (NPs) are a large area of research due to their unique properties. On the one hand, NPs are actively developed as drug delivery systems and diagnostic tools. On the other hand, their excessive use in modern products and inappropriate utilisation can increase existing air pollution. The most common route of NP exposure is via the pulmonary system. Once the particles reach the alveoli, they encounter pulmonary surfactant, rapidly adsorbing biomolecules. Surfactant proteins A (SP-A) and D (SP-D) are innate immunity proteins and are essential in the resolution and clearance of allergens and microorganisms. They are also thought to play an essential role in opsonisation and clearance of engineered NPs and particulate matter. This research aimed to explore the role of SP-A and SP-D in the uptake, clearance, and translocation of 20 nm gold NPs (AuNPs) and to understand potential hazards that can be encountered in individuals deficient in these proteins.

Methods: The research employed a combination of *in vitro* and *in vivo* methods. Advanced multimodal microscopy was used for the semi-quantitative three-dimensional imaging of AuNPs and analysis within the cells and tissue. AuNPs were used to study their behaviour in physiological-like buffers and bio-nano interactions with SP-A and SP-D, applying spectrophotometric and protein analysis methods. The cell culture model, RAW264.7 cells, were exposed to AuNPs, and the impact of SP-A and SP-D on the viability was measured. Genetic knockout mice for SP-A and SP-D, respectively, and wild-type mice were nose-only exposed to 20 nm AuNPs aerosol, followed by the quantitative analysis of the clearance and translocation of AuNPs to secondary organs. Finally, environmental particles were collected from Southampton's harbour and analysed for their elemental composition, morphology, and nanotoxicity on RAW264.7 cells.

Results: Label-free multimodal microscopy was optimised for AuNPs imaging within single cells, but not tissue. This technique allowed semi-quantitative AuNPs analysis. The presence of proteins in physiological-like buffers was essential to prevent aggregation. The results showed tentative

evidence of selective SP-A and SP-D adsorption to AuNPs; no opsonisation could be detected. SP-A and SP-D had no or little impact on the viability of the cells in the presence of AuNPs, but suppressed uptake of AuNPs. The *in vivo* results were inconclusive. The SP-D knockout mice showed altered clearance of AuNPs from the lungs compared to the SP-A knockout and wild-type mice. Both SP-A and SP-D knockout mice macrophages showed suppressed AuNPs uptake. Environmental particles were highly heterogeneous in composition and morphology, and potentially more toxic than AuNPs. No alteration on cell viability was found in the presence of SP-A or SP-D.

Conclusion: Multimodal microscopy was shown to be a powerful tool for semi-quantitative analysis; more research is required to shift into the fully quantitative analysis. *In vitro* experiments partially supported the hypothesis, as proteins semi-selectively adsorbed to AuNPs and suppressed the phagocytosis. However, additional verification techniques are required to overcome the intrinsic limitations of AuNPs. It can be speculated that SP-D is essential for clearance of AuNPs, although it remains unclear whether this is a phenotype induced effect or if it is protein-mediated.

Table of Contents

Table of Tables

Table of Figures

List of Accompanying Materials

Supplementary data can be accessed using the link: https://doi.org/10.5258/SOTON/D1522

- Figure_3_2.mp4 – video file which represents a montage of 40 individual images as a uniform rebuilt particle corresponding to **Figure 3.2. A montage of 40 µm polystyrene particles stack imaged with CARS in a Z-stack mode with 1 µm step.**
- Figure_3_9.pptx – PowerPoint file with animated Z-stack images corresponding to **Figure 3.9. Multimodal images of RAW264.7 cells exposed to 20 nm AuNPs.**
- Figure_3_10.pptx – PowerPoint file with animated Z-stack images corresponding to **Figure 3.10. Composite images of RAW264.7 containing 20 nm AuNPs acquired with the multimodal imaging system.**
- Figure_3_11.zip – additional set of collected TEM images corresponding to **Figure 3.11. Transmission electron microscopy image of RAW264.7 cell incubated with 20 nm AuNPs.**
- Figure_3_12.pptx – PowerPoint file with animated Z-stack images corresponding to **Figure 3.12. 3View images of RAW264.7 cells incubated with 20 nm AuNPs**.
- Figure_5_20.pptx – PowerPoint animation which provides visual explanation of the concept corresponding to **Figure 5.20. Illustration of AuNPs mass and total number distribution in WT/AKO and DKO mice.**
- Figure_5_2_and_5_3.pptx - additional set of collected TEM and SEM images corresponding to **Figure 5.3. Representative TEM images of collected aerosolised 20 nm AuNPs.** and **Figure 5.4. Representative SEM images of collected aerosolised 20 nm AuNPs.**
- Figure_6_2_SEM.zip – additional set of collected SEM images corresponding to **Figure 6.2. Selected electron microscopy micrographs of environmental particles.**
- Figure_6_2_TEM.zip – additional set of collected TEM images corresponding to **Figure 6.2. Selected electron microscopy micrographs of environmental particles.**
- Readme.txt – a file with a list of accompanying materials, identical to the list above.

Research Thesis: Declaration of Authorship

Print name: Artur Kirjakulov

Title of thesis: Toxicity of nanoparticles on lung cells and pulmonary immune defences.

I declare that this thesis and the work presented in it are my own and has been generated by me as the result of my own original research.

I confirm that:

1. This work was done wholly or mainly while in candidature for a research degree at this University;
2. Where any part of this thesis has previously been submitted for a degree or any other qualification at this University or any other institution, this has been clearly stated;
3. Where I have consulted the published work of others, this is always clearly attributed;
4. Where I have quoted from the work of others, the source is always given. With the exception of such quotations, this thesis is entirely my own work;
5. I have acknowledged all main sources of help;
6. Where the thesis is based on work done by myself jointly with others, I have made clear exactly what was done by others and what I have contributed myself;
7. None of this work has been published before submission.

Signature: .....

Date: .....

Acknowledgements

This PhD project would not be possible without the support of a large number of individuals. Firstly, I would like to express my sincere gratitude to my supervisors, Dr Jens Madsen, Professor Sumeet Mahajan, Professor Howard Clark and Dr Maurits de Planque, for their continuous support, guidance and immense knowledge. I would like to particularly thank Dr Jens Madsen, who was always there for me and guided me throughout this journey, and became both a mentor and a friend.

I would also like to thank all my fellow ex-labmates, especially Peter Johnson, Niall Hanrahan, Adam Lister and Kostas Bourdakos, for teaching and assisting me with complicated physics, microscopy and image analysis.

I would also like to thank collaborators from Public Health England, Dr Rachel Smith, Dr Adam Laycock, Dr Matthew Wright and Dr Chang Guo. Their expertise and support were invaluable for this project. Additionally, I would like to thank our collaborator Dr Michaela Kendall who was very supportive.

I would like to thank the entire Biomedical Imaging Unit, particularly Dr Anton Page, Ms Patricia Goggin and Ms Regan Doherty, for assisting with aspects of biomedical imaging, as well as Mr Jon Ward from the histochemistry unit for the training and his expertise.

Thank you to Ms Bethany Mulliner for proofreading this work. Without your help some really embarrassing typos could have been missed.

Last but not least, I would like to thank my family: my parents for investing so much effort; my little sister, who did not do much, but still was there for me; and my wife Viktorija, who experienced all the beauty of PhD student life together with me.

I want to additionally thank the Faculty of Medicine and Institute for Life Sciences for funding this project. Also, I would like to thank the Royal Society of Chemistry for awarding me with the Research Mobility Grant, which was extremely helpful in performing the studies with our collaborators.

Definitions and Abbreviations

µCT – X-ray microtomography

3View – serial block face scanning electron microscopy

aa – amino acid

AgNPs – silver nanoparticles

AKO – SP-A knockout mice

ATI – alveolar type I cell

ATII – alveolar type II cell

AuNP – gold nanoparticles

BALF – bronchoalveolar lavage fluid

BCA – bicinchinoninic acid

BSA – bovine serum albumin

C57BL/6 – wild-type mice

CARS – coherent anti-Stokes Raman scattering

COPD – chronic obstructive pulmonary disease

CRD – carbohydrate recognition domain

CV – column volume

DKO – SP-D knockout mice

DLS – dynamic light scattering

DNA – deoxyribonucleic acid

DPPC – dipalmitoyl-phosphatidylcholine

EDTA – ethylenediaminetetraacetic acid

EDX – energy dispersive X-ray spectroscopy

Definitions and Abbreviations

EU – endotoxin units

FAD - flavin adenine dinucleotide

HI FCS – heat inactivated foetal calf serum

ICP-MS - inductively coupled plasma mass spectrometry

LA-ICP-MS – laser ablation inductively coupled plasma mass spectrometry

LAL – limulus amebocyte lysate

LD50 –a concentration required to kills 50% of the population

LDH – lactate dehydrogenase

LPS – lipopolysaccharide

ManNAc – N-Acetyl-D-mannosamine

MTT – 3-[4,5-dimethylthiazol-2-yl]-2,5 diphenyl tetrazolium bromide

MWCO – molecular weight cut off

NAD(P)H – nicotinamide adenine dinucleotide(phosphate)

NADH – nicotinamide adenine dinucleotide

NMs – nanomaterials

NPs – nanoparticles

OGP – octyl β-D-glucopyranoside

PAP – pulmonary alveolar proteinosis

PBS – phosphate buffered saline

PCR – polymerase chain reaction

PM – particulate matter

PM – particulate matter

$PM_{0.1}$ – particulate matter, less than 0.1 µm

PM_{10} – particulate matter, less than 10 µm

$PM_{2.5}$ – particulate matter, less than 2.5 µm

PMA – phorbol 12-myristate 13-acetate

PSNPs – polystyrene nanoparticles

PVDF – polyvinylidene difluoride

QCM – quartz crystal microbalance

ROS – reactive oxygen species

SDS-PAGE – sodium dodecyl sulphate polyacrylamide gel electrophoresis

SEM – scanning electron microscopy

SF – serum-free

SHG – second harmonic generation

SLS – static light scattering

SP-A – surfactant protein A

SP-B – surfactant protein A

SP-C – surfactant protein A

SP-D – surfactant protein D

SP-ICP-MS – single particle inductively coupled plasma mass spectrometry

SPR – surface plasmon resonance

TBS – Tris-buffered saline

TBS^{Ca} – Tris-buffered saline supplemented with 5 mM calcium chloride

TBS^{EDTA} – Tris-buffered saline supplemented with 5 mM EDTA

TEM – transmission electron microscopy

TPF – two photon induced autofluorescence

Tris – tris(hydroxymethyl)aminomethane

VSSA – volume specific surface area

WT – wild type mice

Chapter 1 Introduction

Many aspects of modern biomedical research require a collaborative approach across various research fields. As a result, current scientific problems are increasingly addressed using knowledge, methods, and techniques from a variety of disciplines. Such an approach is known as interdisciplinary research. While such research predominantly evolves from neighbouring fields, distant disciplines are catching up rapidly.[1,2] Some of these approaches advance into independent fields, such as nanotoxicology.

Nanotoxicology, as a sub-discipline at the interface of toxicology and nanomaterial sciences, has emerged in 2004 specifically to address the potential adverse effects of engineered nanomaterials on living organisms and ecosystems, as well as to develop methods and guidelines for the testing of nanomaterials.[3] The need for such a discipline was dictated by an exponential rise in the synthesis and application of nanomaterials.[4] As of January 2020, there were almost 8700 nanotechnology products registered on Nanotechnology Products Database (**Table 1.1**).[5]

Table 1.1. Number of registered biotechnology products by fields. Top 3 fields are highlighted in bold. Adapted from Nanotechnology Products Database (January 2020).[5]

Field	Products	Field	Products	Field	Products
Agriculture	225	Automotive	566	Construction	668
Cosmetics	**814**	**Electronics**	**2051**	Environment	531
Food	331	Home Appliance	286	**Medicine**	**999**
Petroleum	303	Printing	139	Renewable Energies	468
Sports and Fitness	150	Textile	725	Other	437

Why is advancing nanotoxicology so important? The rapid development of nanotechnology products creates particles with perplexing and unexpected properties. These properties often cannot be extrapolated from studies of their bulk materials, thus it is hard to predict how these particles will interact with biological systems at the molecular, cellular, organismal, and ecosystem level. At the same time, the abundance of nanotechnology products increases intentional (cosmetics, medicines) and unintentional (environmental, occupational) exposure to nanoparticles. Based on physicochemical characteristics of nanoparticles and routes of exposure, there is a possibility of adverse health effects, varying from an acute response to long-term chronic complications. Evaluating the toxicity of nanoparticles is not a straightforward process, and there is an unmet demand for fast, reliable and reproducible ways of toxicity testing. The need for such methods is especially vital since nanomedicine and nanotoxicology are two sides of the same coin.[6]

For the best possible pathological assessment, classical biochemical assays and pathological examinations should be combined with imaging techniques for the visualisation of nanoparticles within a single cell, tissue, organ, or entire organism. However, the choice of imaging techniques to study bio-nano-interactions is minimal. A light microscope is unable to resolve particles smaller than 200-500 nm at the highest magnification due to the Abbe diffraction limit, thus only larger particles or aggregates can be detected. On the other hand, more powerful imaging techniques require laborious sample preparation, such as sectioning and staining, resulting in a complete and irreversible sample loss.[7]

The centre of this research are Surfactant Proteins A and D (SP-A and SP-D), two proteins predominantly found in the lungs and well known for the binding and clearance of bacteria, viruses and other natural pollutants such as pollen, thus keeping the lungs free from pathogens and other potentially noxious particles. While their role in clearing pathogens is well described, the hypothesis that the same proteins play an essential role in removing inhaled nanoparticles is currently neither confirmed nor denied. This research aims to explore the role of SP-A and SP-D in the uptake and clearance of nanoparticles and to understand what consequences can be encountered by individuals deficient in these proteins. A combination of *in vitro* and *in vivo* experiments were used. Studying this hypothesis, for the first time SP-A and SP-D knockout mice were used, as they are the closest and the most realistic models currently available for studying the importance of these proteins in nanoparticle clearance. Additionally, non-linear multi-modal microscopy, a promising technique for the rapid and semi-quantitative imaging, was used. It requires little to no sample preparation, is label-free and is non-destructive.

There is no single nanoparticle model which represents the properties and biological effects of an "average" particle, as explained later in **Chapter 1**. Dr Madsen's and Prof Clark's research group has previously published papers on the interaction of SP-A and SP-D with surface modified polystyrene NPs using *in vitro* models[8–11]. For the *in vivo* models used in this thesis, performed in collaboration with Public Health England (PHE), it was not possible to use previously established models, as it would not be possible to detect them using available methods. The original plan, at the beginning of the project, was to use radioactive iridium particles, as PHE is experienced in their use. These particles were planned to be produced by a generator located at Imperial College London. Unfortunately, this was not possible due to the closure of the facilities. Furthermore, it proved impossible to obtain these particles from another source. Instead, it was decided to use 20 nm spherical AuNPs, as there is evidence in literature of using these particles for *in vivo* inhalation studies, and they are also easily detectable by mass spectrometry and multimodal microscopy.

1.1 Nanoparticles

Nanoparticles (NPs) have gained prominence due to their unique and sometimes unpredictable characteristics that are not found in their bulk counterparts. These unprecedented properties bear a great potential for technological advancements, from medicine and electronics, to various consumer products as textiles and cosmetics. At the same time, they might pose a great challenge due to their unexpected behaviour and unwanted effects. Nevertheless, NPs have become an integral part of our lives. The aim of this chapter is to cover the basics of NPs without reviewing their influence on biological systems, give their definition and classification, explain what makes nanoparticles different from bulk materials, and explore the most common sources and size ranges.

1.1.1 Definition and classification of nanoparticles

According to governing bodies[12–14], nano-objects are defined as materials that have at least one external dimension in the nanoscale range (1-100 nm). These can be further classified into three major groups: nanoparticles, nanofibers or nanotubes, and nanoplates (**Figure 1.1**) that have three, two and one nanoscale dimensions, respectively. However, there is still no single internationally agreed definition for NPs and in biopharmaceutics, for instance, particles in the range of 1-1000 nm are often referred as *"nano".*[15,16] Sometimes volume-specific surface area (VSSA) is used as a complementary definition, where particles with equal to or greater than 60 m^2/cm^3 VSSA can be considered as NPs. This definition allows clarification where classification based only on diameter/length is not applicable, such as in the case of agglomerates which can give primary particles under certain conditions.[17]

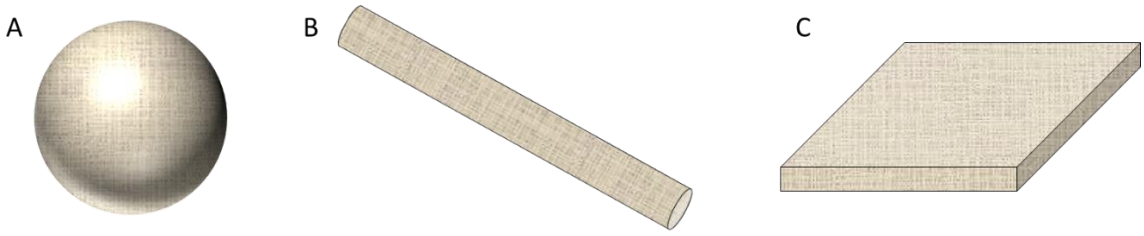

Figure 1.1. Schematic representation of three the most abundant nano-objects' shapes.
A – nanoparticle (nanospheres), **B** – nanofiber or nanotube, **C** – nanoplate.

1.1.2 Reactivity and size

Whilst "*nano"* particles are defined as being particles less than 100 nm in diameter, it is argued that novel non-bulk properties appear only for NPs that are less than 20–30 nm.[18] This is explained by the relationship between the particle size and the number of atoms located at the

particle's surface (**Figure 1.2A**). The smaller the particle is, the greater number of atoms lie on the surface, and the lower their coordination numbers. Those atoms have an excess of energy and are therefore less thermodynamically stable. There is a synergistic effect due to the greater accessibility of surface atoms and enhanced reactivity due to the low coordination number. Hence, as the particle size decreases, the reactivity of NPs increases.[19] For example, the bulk tin melting point is 232 °C and can be reduced by 70 °C by reducing the particle size to 10 nm. After 15 nm, the melting temperature drops exponentially.[20]

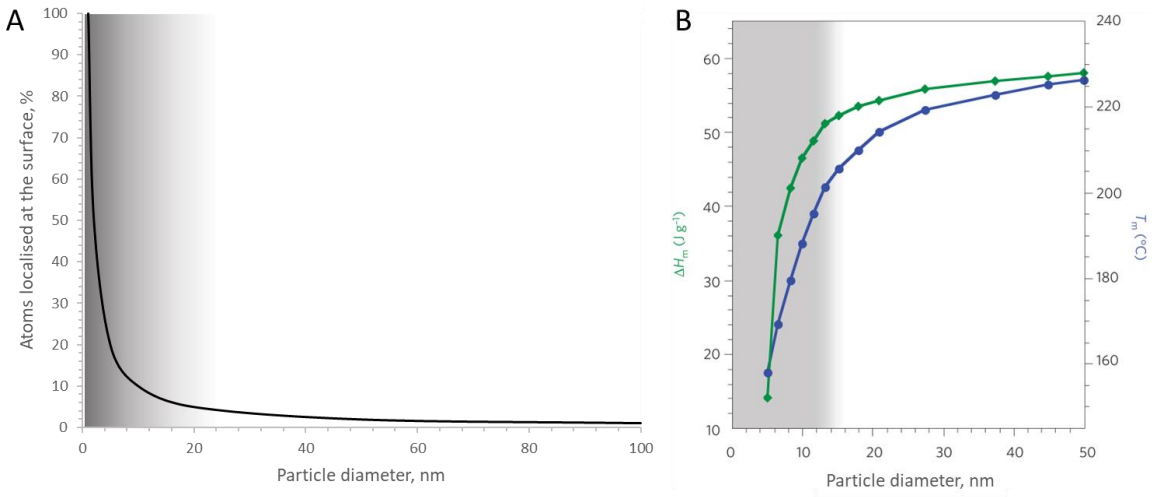

Figure 1.2. Size dependence of various physicochemical parameters of NPs. A – Schematic illustration of the percentage of atoms localised at the surface of a nanoparticle as a function of size. **B** - The melting temperature (T_m; green line) and heat of fusion (ΔH_m; blue line) of tin particles as a function of size. Grey areas mark the particle size at which properties start to change significantly. Adapted from Auffan et al[18].

As well as the size of the particles, the shape also plays a major role in reactivity. For the same total number of atoms, the amount of surface-exposed atoms will be different in stars, cubes, rods, disks, or other differently shaped particles. In the case of 10 nm spherical gold NPs (AuNPs), about 9% of all atoms are on the surface, while for the cube, rod and disk these numbers are ~11%, ~14% and ~30%, respectively.[21]

1.1.3 Sources of nanoparticles

1.1.3.1 Natural sources

Nature itself is the largest source of nanoparticles, as most objects and materials undergo a nano-phase transformation during their life cycle, either as a part of their formation or break-down process. Multiple organisms synthesise and incorporate NPs into their structure, like magnetotactic bacteria[22], while some are small enough (viruses and some bacteria) to be

considered nano-organisms (but not actual NPs). A clear distinction between nano-organisms or organelles and actual "nanoparticles" (non-self-replicating particles that require no energy supply to exist/remain stable)[23] should be made to avoid confusion. About 90% of all airborne particles have a natural origin while the remaining 10% are a result of human activity. The primary natural sources of NPs are forests, deserts, oceans, and atmospheric formations. Episodic events, such as forest fires, dust storms and volcanic eruptions, produce a significant number of particles, but they are short-lived and contribute in a lesser way over an extended period.[24]

It is estimated that about 50% of all NPs in the atmosphere are sourced from the deserts and their boundaries, further being transmitted over large distances.[25] For example, particles from a dust storm in the Gobi Desert of April 1998 crossed the Pacific Ocean and reached North America in less than a week.[26] Dust storms produce characteristic nanoscale minerals comprised of aluminosilicates and metal oxides (high to low %: Si, O, Al, Ca, K, Fe, Mg, Na, S, Ti), with a size range from tens nm to several micron.[25]

A volcanic eruption can release up to 3×10^7 tons of NPs in the form of ash[24], ranging from several nanometres to micrometres in diameter. It has been shown that the concentration of Zn, Cu, Pb, Tl, Bi, Sn, As and Sb in <200 nm particles can be two orders of magnitude higher compared to the particles derived from other anthropogenic sources.[23,27] Forest fires also emit a notable amount of particles into the atmosphere, that are mostly carbon-based with a median size range of 100-500 nm, depending on the fuel type and burning conditions (temperature, oxygen concentration).[28]

1.1.3.2 Anthropogenic sources

Vehicle exhaust fumes are the primary source of anthropogenic NPs in urban areas. Road transport contributes to a total of 60% of all particulate matter (PM), followed by non-road transport (19%) and domestic combustion (13%).[29] These numbers vary significantly based on the country and location where the measurements were taken, as well as the weather, season and other conditions.[30] About 99% (by number) of combustion PM is smaller than 300 nm. Because of complex formation mechanisms, combustion derived PM is heterogeneous in composition, size and shape. The particles consist of a solid carbon core (soot) and adsorbed by-products of organic fuel combustion, such as sulphur dioxide, nitrogen dioxide, sulphuric acid and unburnt hydrocarbons (**Figure 1.3**). It is estimated that 90% of all carbon NPs present in the atmosphere are diesel-generated.[31] Metal particles are also found since they can be used as fuel additives (e.g. cerium, aluminium) [32,33]; they will be adsorbed to carbon NPs core or covered with other by-products. The majority of PM is spherical, but tends to form larger irregular shape aggregates; nanotubes have also been found.[34] The most common metals found in exhaust fumes are: Al, Ca, Cu, Fe, Mg, Mn, Ni, V, Zn, Sr and Ce.[35]

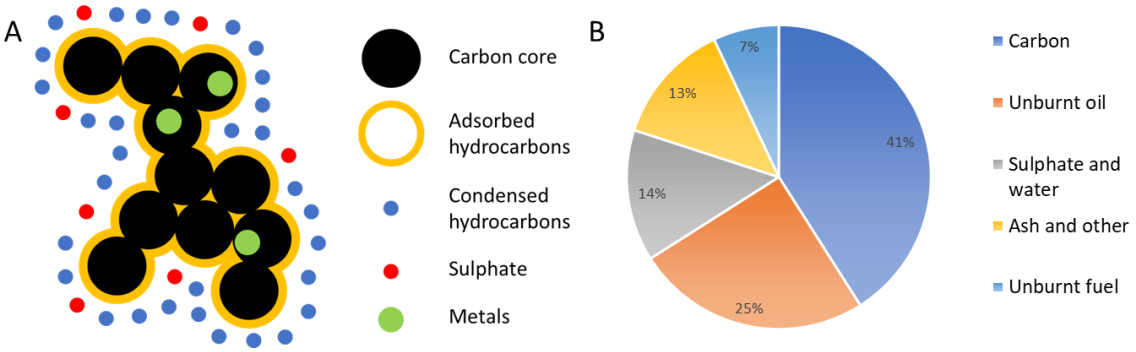

Figure 1.3. Schematic representation of combustion derived particulate matter. A – Structure and composition of engine exhaust particles. **B** – Typical composition of diesel engine derived particles. Adapted from Kittelson et al[36].

Another category of particulate matter are non-exhaust traffic sources that often generate more metal-based particles, rather than carbon. These include PM derived from friction, abrasive and volatilisation of metals due to temperature processes.[37] Up to 44% of particles emitted from brakes are less than 100 nm. The quantity and size vary significantly depending on the temperatures during braking. Cold surfaces generate a negligible amount of particles, while the number gradually goes up with an increase in temperature.[38] Tyre wear is mostly linked to coarse particles, however, most particles are not associated with the tyres themselves, but rather with abraded asphalt and paint, or the resuspension of sedimented particles.[39,40] The most common metals found in non-exhaust and industrial sources are: Fe, Cu, Sn, Zn, Cd, Co, Cr, Mn, Pb, Al, K, Na, V, Sb and Ce.[35]

Nanoparticles created under controlled environment with well-known parameters (composition, shape, size, etc) are often referred to as engineered nanomaterials (ENM). Compared to combustion-derived nanoparticles they are mostly homogenous in their size and composition. Additionally, they are not intentionally released into the environment, which makes their contribution to total airborne particulate matter negligible.[35] However, there are currently no specific regulations on how to utilise ENM and products containing them, which can lead to their accumulation in the environment over time. Aluminium oxide NPs, used in fuel cells, polymers, paints, coatings, textiles and biomaterials contribute 20% to all ENM. Copper oxide is utilised in semiconductors, antimicrobial reagents, heat transfer fluids. Silver is mostly used as an antibacterial agent in wound dressings and coatings. Zinc oxide is used in paints, various detectors and filters, and in personal care products (such as in sunscreens or to treat skin irritation).[41] There has been an increase in the research of gold particles, as gold NPs are promising agents for drug delivery and theranostics, as they allow simple surface modification.[42] One of the most successful applications of gold NPs is photothermal therapy for cancer treatment.[43] In addition to metallic NPs, there are countless types of organic NPs which are used in different fields.[44–46]

1.2 Respiratory system

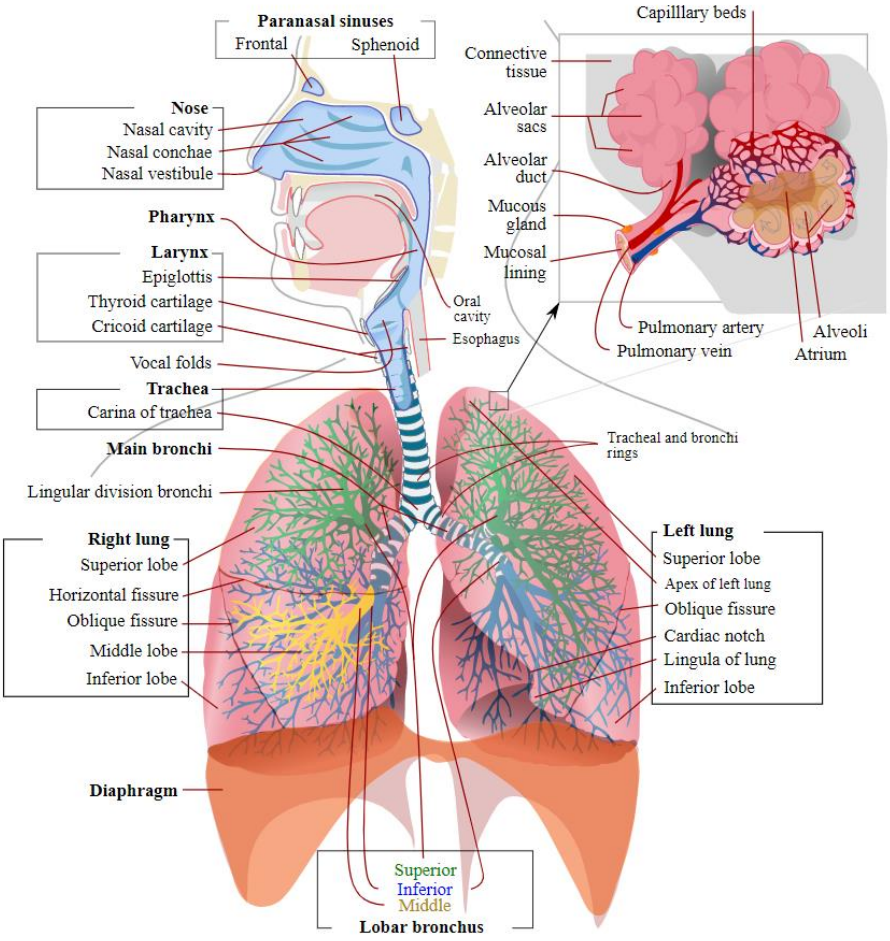

Figure 1.4. A schematic view of the human respiratory system. Image by Mariana Ruiz Villarreal distributed under CC BY 4.0 license.

The main function of the respiratory system is gas exchange – the intake of oxygen and the removal of carbon dioxide. Breathing starts with the nose, where inhaled air is warmed and humidified (upper airways). In the lower airways the air continues to warm and humidify as it travels through the trachea, which branches into right and left bronchus, with a further 23 (on average) generations of successive tubes that branch into bronchi, bronchioles and terminate with alveoli where gas exchange occurs.

1.2.1 Alveoli

Alveoli (**Figure 1.5**) are the endpoint units of the respiratory system where the gas exchange occurs. The alveolar epithelium is a mosaic of alveolar type I (ATI) and type II (ATII) epithelial cells, which have distinct specialisation and thus structural differentiation. The numerical ratio of ATI to ATII is about 1:2, whilst ATI cover around 95% of the total alveolar surface.[47] In addition to pneumocytes, alveoli are constantly monitored by alveolar macrophages.

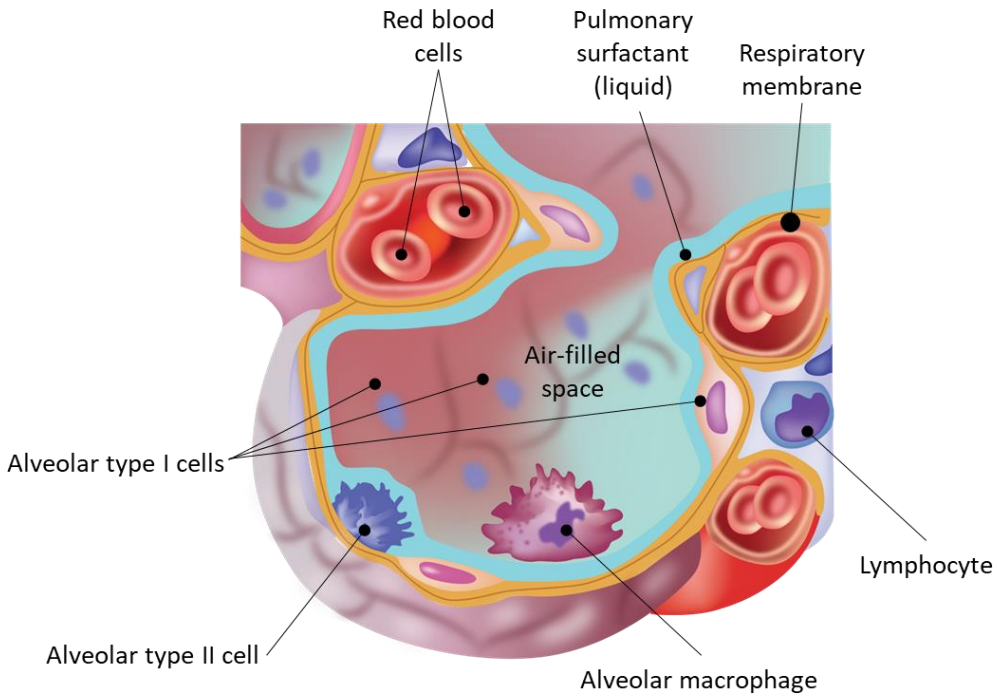

Figure 1.5. Schematic structure of an alveolus. Drawn by Viktorija Kirjakulova.

Alveolar type I cells are flat and extremely thin (<100 nm) and the cytoplasm contains few organelles that are grouped around the nucleus, which makes them ideally suited for gas exchange. Type I cells are terminally differentiated and unable to proliferate, though it is debated that ATI cells may have more functions than is generally believed, such as metabolic, development and lung repair after injury[48,49]. In case of damage, ATII cells proliferate and differentiate to replace ATI cells. Alveolar type II cells are cuboidal and are mostly found in a group of several cells. The opposite of generally passive ATI cells, ATII are highly metabolic. They are best known for their ability to synthesise, secrete, and recycle components of pulmonary surfactant. Type II cells are also important in water and ion transport, the release of cytokines in response to pathogens and damage, and the secretion of xenobiotic-metabolising enzymes.[50,51]

There are two different macrophage populations: alveolar macrophages, residing on the ATI and ATII cells of alveoli[52], and interstitial macrophages, residing in the parenchyma between the microvascular endothelium and alveolar epithelium[53]. They are long-lived self-renewing cells with a turnover rate of about 40% a year.[52,54] Alveolar macrophages are the best known for the immunomodulation and clearance of cellular debris, potential pathogens and particulate matter, but are also responsible for maintenance of pulmonary homoeostasis e.g. recycling pulmonary surfactant. Impaired functions of alveolar macrophages are often associated with pulmonary surfactant accumulation and the development of pulmonary alveolar proteinosis.[52,55]

1.2.2 Pulmonary surfactant

Pulmonary surfactant is a surface-active complex of lipids and proteins secreted into alveolar space by alveolar type II (ATII) cells. The presence of a surfactant layer is essential for reducing surface tension at the air-liquid interface thereby preventing alveolar collapse on exhalation, and as a part of innate immunity to control inflammation and to prevent microbial infections.[56,57] Dysfunction of the surfactant system has been linked to severe respiratory disorders such as acute respiratory distress syndrome or neonatal respiratory distress syndrome.[57]

The composition of pulmonary surfactant varies from person to person. On average 92% of pulmonary surfactant is composed of lipids and phospholipids, with saturated dipalmitoyl phosphatidylcholine (DPPC) being the major component, followed by unsaturated phosphatidylcholine (PC), anionic phosphatidylglycerol (PG) and phosphatidylinositol, as well as neutral lipids of which cholesterol is most abundant (Chol). The coexistence of saturated and unsaturated lipids is vital for controlling the melting point (i.e. fluidity), as lipids are essential for forming surface-active films at the respiratory air-liquid interface and provide the scaffold or matrix on which different surfactant structures are assembled. On average 8-10% of pulmonary surfactant are neutral lipids, mostly cholesterol, which are essential elements modulating the structure of surfactant membranes. The remaining 8-10% are four surfactant proteins (SP) – SP-A, SP-B, SP-C and SP-D (**Figure 1.6**). These proteins can be further divided into two groups. Small and hydrophobic SP-B and SP-C, soluble only in lipid matrices, such as, phospholipid bilayers or detergent micelles, or in organic solvents. Large and hydrophilic SP-A and SP-D, which are water soluble.[58–60]

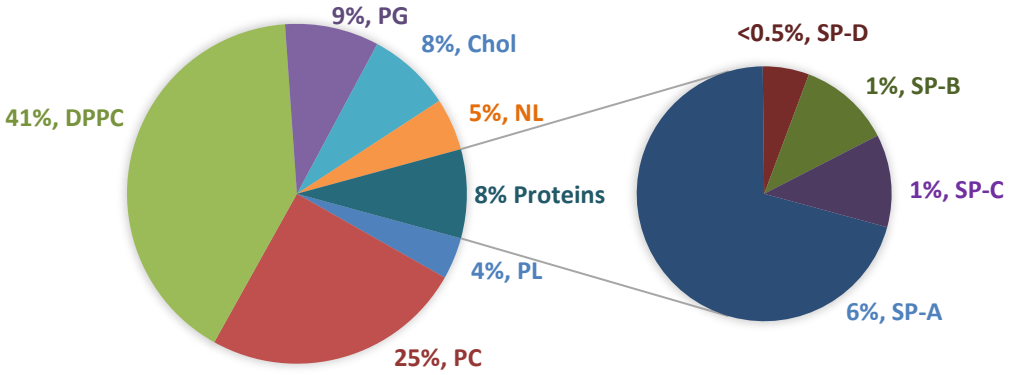

Figure 1.6. The composition of pulmonary surfactant. DPPC – dipalmitoyl phosphatidylcholine; **PC** – unsaturated phosphatidylcholine; **PG** – phosphatidylglycerol; **PL** – phospholipids; **Chol** – cholesterol; **NL** – neutral lipids; **SP-A/B/C/D** – surfactant protein A/B/C/D. Percentages are represented with respect to total mass. Adapted from [58].

Originally pulmonary surfactant was described for its essential role in surface tension reduction at the air–liquid interface, and only later the proteins were characterised and named in the order of their discovery. Unlike the names suggest, the proteins are not *de facto* surfactant molecules. However, SP-B and SP-C directly interact with pulmonary surfactant, promoting the lipid arrangement and surface tension reduction, while SP-A and SP-D are involved in innate immunity. The proteins are named in their order of discovery, and because of their association with pulmonary surfactant they are referred as "Surfactant-Associated Proteins" in literature.[61,62]

1.2.3 Surfactant proteins B and C (SP-B and SP-C)

Surfactant protein B is a small covalently linked homodimer (79 amino acids, 8.7 kDa in the reduced state). The protein expressed in the lungs only, however, some studies confirm small quantities in the Eustachian tube.[63] Surfactant protein B directly interacts with negatively charged lipids and facilitates their adsorption and spreading to a monolayer along with the air-liquid interface, reducing surface tension within lung air spaces. The importance of SP-B in lung function was defined by the study of a lethal neonatal respiratory disease – new-born respiratory distress syndrome.[64] Experiments with transgenic SP-B knockout mice showed that despite the presence of normal amounts of phospholipids, SP-B deficient mice failed in maintaining the lungs open, resulting in death.[65] SP-B deficiency is also associated with abnormal ATII cell ultrastructure, including absent lamellar bodies and abnormal SP-C processing.[66]

Surfactant protein C is short (35 amino acids, 4.2 kDa) and one of the most lipophilic naturally occurring polypeptides.[67] SP-C is expressed only in the lung and is a highly specific marker for identifying ATII cells.[58] It enhances spreading and arrangement of the surfactant, reducing surface tension and maintaining the lipid monolayer throughout the respiration cycle. In contrast to SP-B deficiency, disease severity associated with SP-C deficiency is highly variable and symptoms may develop as soon as within the first hours of life or late at adulthood. Clinical presentations vary from asymptomatic to severe respiratory distress and deteriorating lung function that is exacerbated by recurring viral and bacterial lung infections.[68] Animals with the SP-C mutation are viable, but with lung development diseases and increased susceptibility to infection.[69]

1.2.4 Surfactant proteins A and D (SP-A and SP-D)

1.2.4.1 Structural organisation

Surfactant proteins A and D are components of innate immune defence and expressed in pulmonary ATII and Clara cells, as well as non-pulmonary epithelia. They large hydrophilic glycoproteins that belong to mammalian lectins, the family of collagenous Ca^{2+} dependent

(C-type) lectins called collectins. C-type lectins contain a collagen-like region linked to a carbohydrate recognition domain (CRD), known as the carbohydrate-binding C-type lectin domain, which enables binding to specific carbohydrates found in oligosaccharide (or lipid) structures expressed on the surface of an array of microorganisms. The collagen-like region acts as a signalling molecule via its interaction with the cell's surface receptors.[70]

Their primary structure comprises of four regions: 1) a cysteine-containing *N*-terminus; 2) a triple-helical collagen-like region composed of repeating Gly-X-Y (where X and Y represent any amino acid) amino acid triplets; 3) an α-helical coiled-coil neck region; and 4) a globular structure at C-terminus comprising of a carbohydrate recognition domain (CRD), involved in binding to oligosaccharide (or lipid) structures expressed on the surface of microorganisms. All known collectins assemble into trimeric structural units, which often further assemble into higher-order structures (**Figure 1.7**).[71,72]

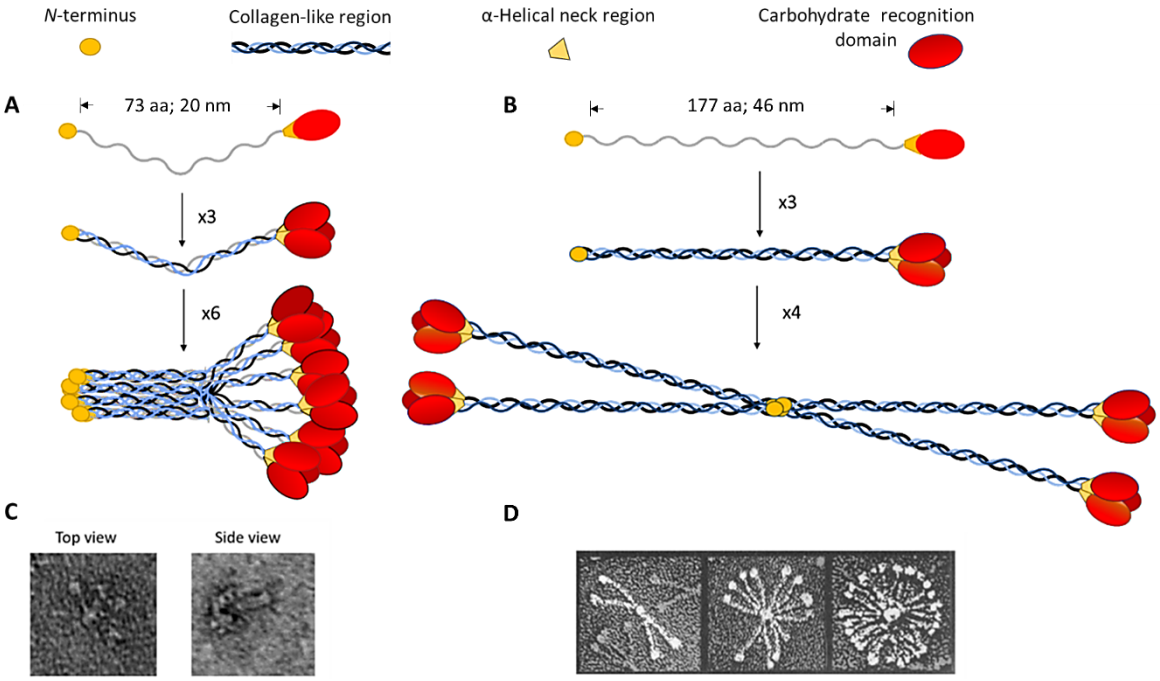

Figure 1.7. Structure of surfactant proteins A and D. A – schematic structure of SP-A octadecamer. **B** – schematic structure of SP-D dodecamer. **C** – TEM micrograph of human SP-A.[73] **D** – TEM micrograph of rat SP-D.[74] Micrographs reprinted with permission from Elsevier.

Surfactant protein A is octadecamer about 20 nm in diameter, where six 105 kDa trimers assemble into a bouquet-like structure of 630 kDa.[73] Each trimer is composed of three 35 kDa polypeptide chains that are held together by disulphide bonds located in the *N*-terminus. The SP-A CRD region contains an asparagine-linked oligosaccharide.[73] Human SP-A can exist in homomeric (made of either SP-A1 or SP-A2 monomers) and heteromeric (made of both SP-A1 and

SP-A2) forms, however, the actual *in vivo* ratio is not known.[70,75] There is a difference of 10 amino acids between SP-A1 and SP-A2 that results in altered oligomerisation properties, sugar-binding capacity, structural stability, aggregation, and ability to form phospholipid monolayers and tubular myelin has also been observed.[70,76] *In vitro* studies with recombinant proteins showed SP-A2 being more biologically active than SP-A1 in carbohydrate-binding characteristics[77], *P. aeruginosa* phagocytosis enchancement[78], cytokine levels induction[79], lipopolysaccharides (LPS) and phospholipid aggregation[80]. Thorenoor et all[81] showed that the survival rate of mice infected with *Klebsiella pneumoniae* is genotype-dependent in the following order: SP-A2 > SP-A1 > knock outs.

Surfactant protein D is a dodecamer about 100 nm in diameter[74], where four 130 kDa trimers assemble into the cruciform structure of 520 kDa. Each trimer is composed of three identical 43 kDa polypeptide chains that are held together by disulphide bonds, as well as an oligosaccharide structure located in the collagenous region.[82] The dodecamer is a dominant form[83], however up to 8 of the 520 kDa units can undergo further oligomerisation and yield “astral bodies”, which are cross-linked by disulphide and non-disulphide bonds (**Figure 1.7**).[74]

1.2.4.2 Extrapulmonary expression of SP-A and SP-D

Extrapulmonary expression, where the maintenance of a sterile milieu is critical, supports the role of SP-A and SP-D roles as important proteins of the innate immune system even outside the lungs. The majority of locations in which they are expressed are at interfaces with the external milieu, particularly in mucosal tissue, or with plasma, urine, tears, cerebrospinal fluid, and amniotic fluid.[84]

Surfactant protein A has been detected in small and large intestines, mesentery, colon, prostate, thymus, amniotic fluid and epithelium, and salivary glands. It has also been detected in the entire lacrimal apparatus. Both SP-A and SP-D have been detected in the foetal membranes and the choriodecidual layer of the late pregnant uterus; skin as well as skin-derived cell lines.[85–88]

Surfactant protein D has been detected in human trachea, brain, testis, salivary gland, heart, prostate, kidneys, small intestine, pancreas, and placenta. Lower levels have also been detected in spleen, adrenal gland, uterus, mammary glands, epithelial cells of large and small ducts of the parotid gland, sweat and lacrimal glands, epithelial cells of gall bladder and intra-hepatic bile ducts, exocrine pancreatic ducts, epidermal cells, oesophagus and small intestine, and in the urinary tract, including the collecting ducts of the kidney.[87,89–91]

1.2.4.3 Interaction of SP-A and SP-D with microorganisms

Pulmonary surfactant proteins A and D can directly interact with microorganisms including bacteria, fungi, viruses, and yeasts, resulting in their agglutination, enhanced phagocytosis, or direct killing by increasing membrane permeability (**Figure 1.8**). The binding occurs through the various ligands on the surface of microbes such as lipopolysaccharides on Gram-negative bacteria, lipoteichoic acid on Gram-positive bacteria, glycoproteins on fungi and viruses, phospholipids on mycoplasma and lipoarabinomannan on mycobacteria.[92,93] Among these ligands, LPS is a well-established ligand for SP-A and SP-D, though they interact in a different manner. Both proteins interact with rough LPS serotype only, SP-A predominantly binds to lipid A or LPS missing O-antigen, while SP-D interacts with core oligosaccharides.[93,94] Surfactant proteins can inhibit bacterial growth by indirect killing, via the formation of a physical barrier on the surface of bacteria and thus significantly reduce nutrient uptake.[95,96]

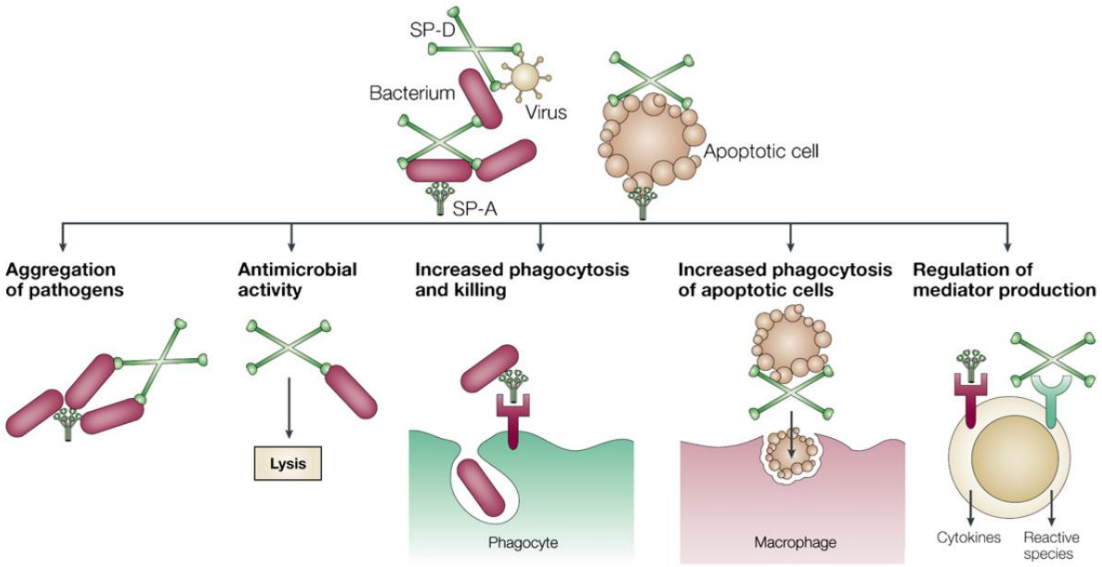

Figure 1.8. Functions of SP-A and SP-D. Surfactant proteins A and D bind to and opsonise viruses, bacteria, allergens, and apoptotic cells. They also enhance microbial phagocytosis by aggregating bacteria and viruses, possess direct bactericidal effects, and potentially bind to a variety of receptors to modulate immune cell cytokine and inflammatory mediator expression. Reprinted from Pastva et al[92], with permission of the American Thoracic Society. Copyright © 2020 American Thoracic Society.

A study by Wu at al[97] examined the effect of SP-A and SP-D on the growth and viability of Gram-negative bacteria. It has been shown that the pulmonary clearance of *E. coli* was reduced in SP-A deficient mice and increased in SP-D overexpressing mice. Purified proteins inhibited *in vitro* bacteria proliferation for some strains of *E. coli, K. pneumoniae,* and *E. aerogenes.* The proteins also induced bacteria agglutination in a calcium dependent manner, though bacteria growth

inhibition was independent of bacteria aggregation. The findings suggested that antibacterial properties of SP-A and SP-D had a direct effect on growth inhibition by increasing the permeability of Gram-negative bacteria cell membrane. A study by Bufler et al[98] showed that both SP-A and SP-D bind to *P. aeruginosa,* but only SP-D lead to increased phagocytosis by macrophages and only for opsonised bacteria, while SP-A did not have any effect. Contrary, a study by Giannoni et al[99] demonstrated that SP-A and SP-D enhanced pulmonary clearance of *P. aeruginosa* by stimulating phagocytosis by alveolar macrophages and by modulating the inflammatory response. The authors infected SP-$A^{-/-}$, SP-$D^{-/-}$ and double knockout mice with *P. aeruginosa* via intratracheal instillation and measured bacterial counts after 6 and 48 hours. After 6 and 48 hours knockout mice had 7-10 times and 2-10 times more, respectively, bacteria than wild type, while double knockouts had about 2 times more bacteria than SP-$A^{-/-}$ or SP-$D^{-/-}$ only. Another study investigated the role of the proteins on *M. tuberculosis* infection following aerosol challenge of SP-$A^{-/-}$, SP-$D^{-/-}$ and SP-$AD^{-/-}$ mice identified no gross defects in uptake or immune control of *M. tuberculosis.* The findings indicated that the proteins had no immunologic function on *M. tuberculosis.*[100]

The role of SP-A and SP-D is also well observed within the clinical environment. Respiratory distress syndrome (RDS) – a significant cause of morbidity and mortality in preterm babies, caused by a deficiency, dysfunction, or inactivation of pulmonary surfactant. Surfactant replacement therapy is an established method for the treatment of RDS, exogenous surfactants lack SP-A and SP-D.[101] Preterm neonates with RDS and low level of SP-A and SP-D show higher risk of infection and development of bronchopulmonary dysplasia. While studies indicate that SP-A and SP-D enriched formulations of exogenous surfactant potentially enhance the function of immune system and lungs in neonates.[102] *In vivo* studied performed in mice in a non-sterile environment have similar observations, where SP-A and SP-D knockout mice pups had significant mortality associated with bacterial infection, compared to wild-type mice.[103] The role of the proteins is also documented in patients with cystic fibrosis (CF), where SP-A and SP-D deficiency occurs early in CF airways and is inversely related to inflammation in CF airways. The protein concentrations in CF patients were inversely related to inflammation, bacterial colony-forming units per millilitre, and age.[104] Additionally, SP-D not only play a role in fighting the infection, it as anti-inflammatory functions and inhibits production of proinflammatory cytokines and chemokines in the lung. A study performed on preterm lambs indicated that treatment with recombinant SP-D containing exogenous surfactant inhibited lung inflammation and enhanced the resistance of surfactant to inhibition.[105] Hence, recombinant SP-D fragment is being actively explored for therapeutic applications for the treatment of lung infection and inflammation.[106]

1.2.4.4 Interaction of SP-A and SP-D with nanoparticles

Nanoparticles are similar in size (though generally smaller) to viruses and bacteria, and it is known that SP-A and SP-D bind to microorganisms. Hence, NPs may act as simplified versions of microorganisms and encounter similar immunological response. Surfactant proteins A and D are also known to facilitate aggregation and stimulate the uptake of some nanoparticles by macrophages with subsequent clearance. Salvador-Morales et al[107] demonstrated the selective binding of SP-A and SP-D to carbon nanotubes. SDS-PAGE, Western blot and mass spectrometry results showed that in the presence of calcium-chelator, almost no proteins bind to particles, however, in the presence of 0.15 mM $CaCl_2$ there were 6-8 proteins detected, including SP-A and SP-D. Electron microscopy images confirmed selective binding. Schulze et al[108] were the first who tried to link SP-A binding with physicochemical properties of metal oxide NPs ($BaSO_4$, AlOOH, TiO_2 and CeO_2). They employed bicinchoninic acid (BCA) protein quantification assay and SDS-PAGE with Western blotting to characterise and quantify NP binding with SP-A. However, these methods were not successful, and there was no correlation in the SP-A adsorption patterns, as the results were inconsistent and varied significantly even for NPs made of the same material but with different sizes and shapes. In the study by Ruge et al[109] it was shown that the uptake of 110-180 nm magnetite NPs coated with different polymers (starch, carboxymethyl dextran, chitosan, polymaleic-oleic acid, phosphatidylcholine) by rat alveolar macrophages increased for NPs treated with SP-A, whilst bovine serum albumin (BSA) led to a significant decrease showing that this increased uptake was specific to the SP-A protein. In their subsequent study, they used mannosylated poly(lactic acid)−poly(ethylene glycol) (PLA−PEG) copolymer to produce 140 nm particles with a polyester core and PEG shell decorated with mannose residues. Dynamic light scattering (DLS) and transmission electron microscopy (TEM) showed SP-A binding to the particles, confirming the earlier findings. The association with SP-A increased NP uptake by THP-1 cells *in vitro*.[109] Slightly different results were observed by McKenzie et al[8], where the author used 100 nm amine-modified (A-PS) and unmodified polystyrene (U-PS) NPs. SP-A associated with both types of NPs in a Ca^{2+} dependent manner and induced strong aggregation of U-PS, but inhibited self-aggregation of A-PS. Additionally, SP-A inhibited the uptake of A-PS by rat macrophages, while increased the uptake of U-PS particles. Since A-PS had the same core material as U-PS, polystyrene, but different surface modification (positively charged -NH_2 groups), it is evident that surface modifications such as electrical charge, may alter the bio-nano interactions.

Kendall et al[9] used the same particles (U-PS and A-PS) with SP-D. DLS and SEM showed that SP-D adsorbed onto the particle surfaces, causing their aggregation. Additionally, SP-D enhanced the uptake of the particles into the human lung epithelium ATII-like A549 cell line. The uptake of NPs by primary alveolar macrophages (AMs) and lung dendritic cells (LDCs) from C57BL/6 mice was

compared with SP-D knock-out mice. A decrease in NPs uptake by AMs and LDCs was observed in knock-out mice, compared to wild-type C57Bl/C mice. Schleh et al[110] used *in vivo* wild type C57BL/6 mice model to investigate the role of SP-D in the clearance of 20 nm radioactively labelled AuNP at a very early (2 hours) time point after inhalation, where one group of mice received 10 µg of solubilised SP-D by intratracheal instillation prior to the AuNP exposure. However, SP-D had only a minor effect on AuNP clearance and translocation at such an early time point.

1.2.5 SP-A and SP-D gene knock-out mice phenotypes

The experiments carried out using mice models made deficient for SP-A (SP-$A^{-/-}$), SP-D (SP-$D^{-/-}$) or both (SP-$AD^{-/-}$) revealed the importance of these proteins in pulmonary immune response and surfactant homeostasis. Under baseline conditions, SP-$A^{-/-}$ mice exhibit normal pulmonary phenotype[111], SP-B, SP-C and SP-D levels, phospholipid composition, secretion and clearance, and the incorporation of phospholipid precursors, except that tubular myelin is absent and the typical lattice-like structure is not formed.[112] The surface activity appears relatively unaffected, suggesting that SP-A may not play a major role in surfactant homeostasis.[113,114] Although they can survive and breed with no apparent pathology in a sterile environment, their pulmonary immune response is insufficient during an immune challenge. SP-$A^{-/-}$ mice are susceptible to bacterial (group B streptococci, *Haemophilus influenza, and Pseudomonas aeruginosa*) and viral (respiratory syncytial virus, adenovirus, and influenza A virus) pathogens. SP-A deficiency was associated with enhanced inflammation and the production of proinflammatory cytokines. Intranasal delivery of SP-A lead to normalisation of the immunological response.[70,115]

SP-$D^{-/-}$ mice have normal survival rates in perinatal and postnatal periods but develop marked disturbances of surfactant homeostasis and alveolar cell morphology. Progressive accumulation of surfactant lipids and apoproteins is observed in the alveolar space, leading to an alveolar lipoproteinosis and an increase of the intracellular surfactant pool, indicating that SP-D has a role in surfactant homeostasis.[116–118] Mice exhibit hypertrophy and hyperplasia of ATII cells with a massive increase in the number of intracellular lamellar bodies, and the accumulation of foamy alveolar macrophages secreting 10-fold higher levels of hydrogen peroxide. These mice spontaneously develop an emphysema-like phenotype and pulmonary fibrosis.[116,119] An intranasal delivery of SP-D is sufficient to correct emphysema and surfactant disturbances.[120]

SP-$A^{-/-}$ and SP-$D^{-/-}$ double knock-out (SP-$AD^{-/-}$) mice feature an emphysema phenotype that is characterised by a progressive and excessive increase in bronchoalveolar phospholipid, protein, and macrophage content. Alveolar macrophages are foamy with up-regulation of Matrix

Metallopeptidase 12 (MMP-12). Compared to wild type mice, double knock-out mice have fewer and larger alveoli, ATII cells increased in number and size, and macrophages were found to be larger in size and greater in number.[121] Overall the phenotype of double knock-outs is similar to SP-D$^{-/-}$ mice.

1.3 Pulmonary nanotoxicology

As the number of consumer products containing nanomaterials (NMs) is rapidly increasing, so is the public awareness surrounding them. Consumers are able to freely purchase nano silver-containing deodorants or titanium dioxide sunscreens, intentionally or unintentionally exposing themselves to NMs, in addition to those already present in the environment naturally or due to human activity. The toxicity of NMs depends on a combination of physical and chemical properties rather than a single parameter, thus there is a knowledge gap in methods evaluating and predicting potential adverse effects. Nanomaterials can enter the host system via skin pores, damaged tissues, injection, respiratory and intestinal tracts. This work will focus on airborne particles and their main entry route – the respiratory system.

1.3.1 Deposition

After inhalation, NPs can travel through the respiratory system where they are sequentially filtered in a size-dependent manner by general physical laws, followed by a potential deposition throughout the entire respiratory tract.[23] The deposition rate depends on the breathing pattern (oral inhalation leads to higher deposition than nasal), where 5-40% of all inhaled particles are exhaled. There are five deposition mechanisms described, based on aerodynamic diameter: 1) inertial impaction; 2) sedimentation; 3) diffusion; 4) interception; 5) electrostatic precipitation (driven by particle charge). Inertial impaction deposition occurs when airborne particles possess enough momentum to keep their trajectory regardless of changes in the direction of the air stream, resulting in a collision with the walls of the respiratory tract in the first 10 bronchial generations[122] (extrathoracic and upper tracheobronchial airways), where the air speed is high, and the flow is turbulent. Gravitational sedimentation is a time-dependent process where particles settle due to the influence of gravity and govern deposition in the last five bronchial generations[122] (tracheobronchial tract and alveoli), where the air speed is slow and the residence time is longer. Brownian diffusive deposition is a process where sufficiently small particles undergo a random motion due to molecular bombardment. The distance a particle travels by diffusional transport increases with decreasing respiratory rate and is inversely related to the size of a particle. The interception deposition of particles depends on the particle's shape. For instance, elongated particles like fibres are subjected to interception due to their length.[123–125]

Particles larger than 1 µm undergo both inertial impaction and gravitational sedimentation, while those smaller than 1 µm are simultaneously affected by gravitational sedimentation and diffusion. However, diffusional deposition decreases with an increase in the particle size up to 1 µm and becomes negligible. Hence, particles less than 0.1 µm in diameter are deposited solely due to Brownian diffusion (**Figure 1.9**).[126]

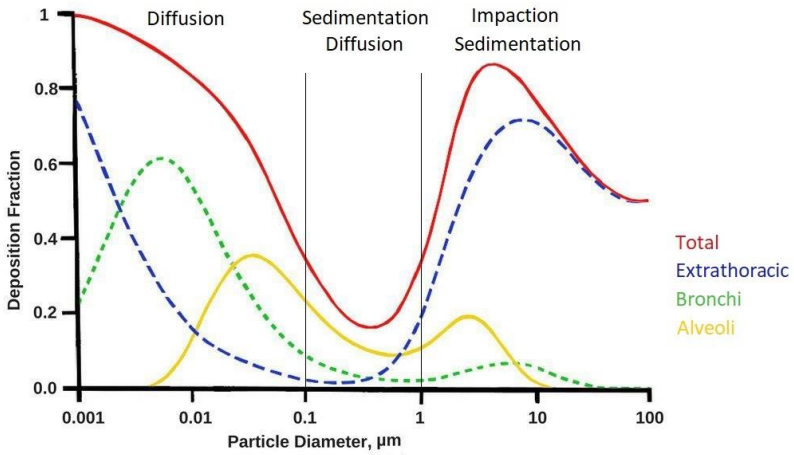

Figure 1.9. Size-dependent deposition mechanism of airborne particles in the human respiratory tract. Adapted from [125].

The research performed by Sturm[127] utilised a computer-aided visualisation of spatial deposition for 1 nm, 10 nm and 100 nm particles. According to the computational model, the highest concentration of 1 nm NPs accumulated at the uppermost airways (trachea, main bronchi, and lobar bronchi), decreasing towards the central and distal airways. The opposite was observed for 10 nm and 100 nm which distributed over the whole tracheobronchial tree with some deposition maxima in the deeper lungs, but with different deposition efficiency (**Figure 1.10**). According to the model developed by the International Commission on Radiological Protection, NPs of approximately 20 nm have the highest probability of reaching alveoli.[128] Additionally, Garcia et al[129] showed, that the smallest NPs can deposit in the olfactory region. The highest rate was for 1-2 nm NPs with about 1% of inhaled particles depositing, while this number decreased to about 0.01% as the particle size reached 100 nm.

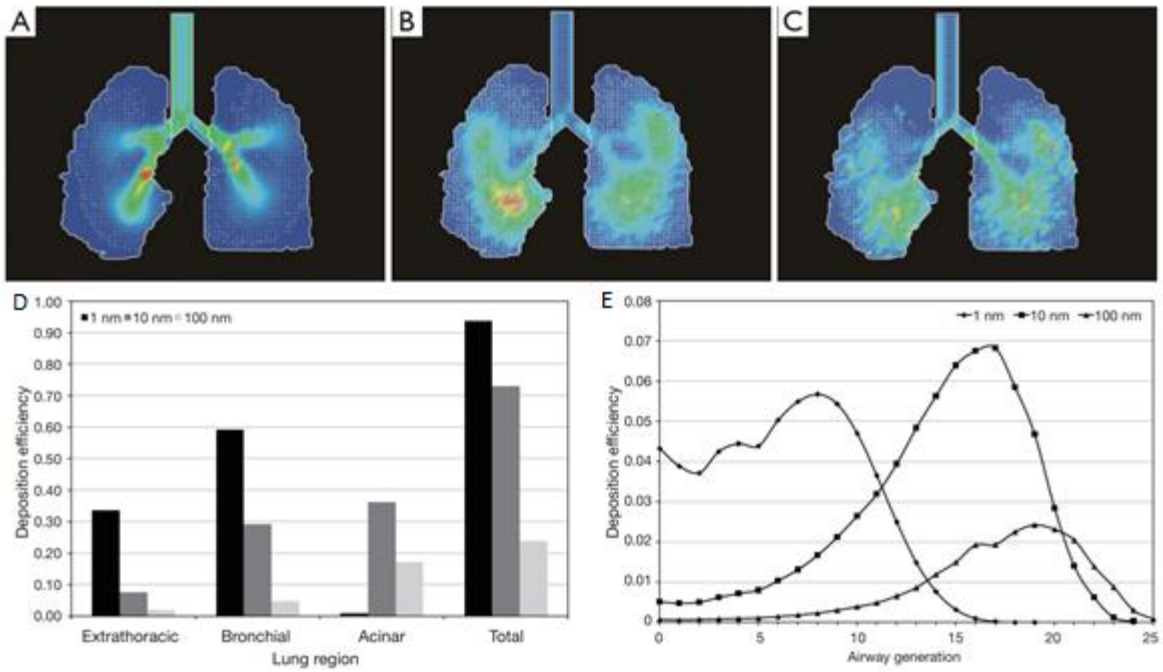

Figure 1.10. Deposition patterns of three different size nanoparticles. Deposition patterns for **A**) 1 nm, **B**) 10 nm, and **C**) 100 nm NPs. **D**) The total and regional deposition efficiency of three different NPs sizes. **E**) Airway generation-specific deposition efficiency graphs for three different NPs sizes. Reprinted with permission of Nancy International Ltd Subsidiary AME Publishing Company, from Robert Sturm[127]; permission conveyed through Copyright Clearance Center, Inc.

1.3.2 Clearance

Particles can be removed from the respiratory system via several mechanisms (**Figure 1.11**), such as the mucociliary escalator, coughing and sneezing, translocation from the airways to secondary organs, lymph nodes, phagocytosis by macrophages and physicochemical processes.[130] Clearance from the upper airways is dominated by the mucociliary escalator, while the alveoli are cleared by macrophage phagocytosis and the movement of surfactant from the alveoli and up to the upper airways. However, the quantitative relationship of these pathways is not established. The mucociliary escalator operates in the ciliated airways (from generation 0 to 16 in humans) and transports the particles carried in mucus from tracheobronchial and nasopharyngeal airways up to the pharynx, where they are then swallowed to the gastrointestinal tract or excreted through the mouth.[131] The average transport speed by the mucociliary escalator in human trachea has been estimated at 3–10 mm/min and transports 10-100 ml of mucus per day.[132] The efficiency of mucociliary escalator depends on the size of the particle and deposition area. Particles larger than 6 µm are removed within 24 hours, while smaller particles are retained for significantly longer periods, showing an inverse relationship between the 24-h airway retention and the geometric

particle size.[132] It is hypothesised that delayed particle clearance and its dependency on size is because the airway surface is not evenly covered with ciliated cells and mucus, resulting in discontinuous transport. As a result, particles can deposit on non-ciliated cells or penetrate between cilia, where they are adsorbed to the cell membrane and then uptaken.[133]

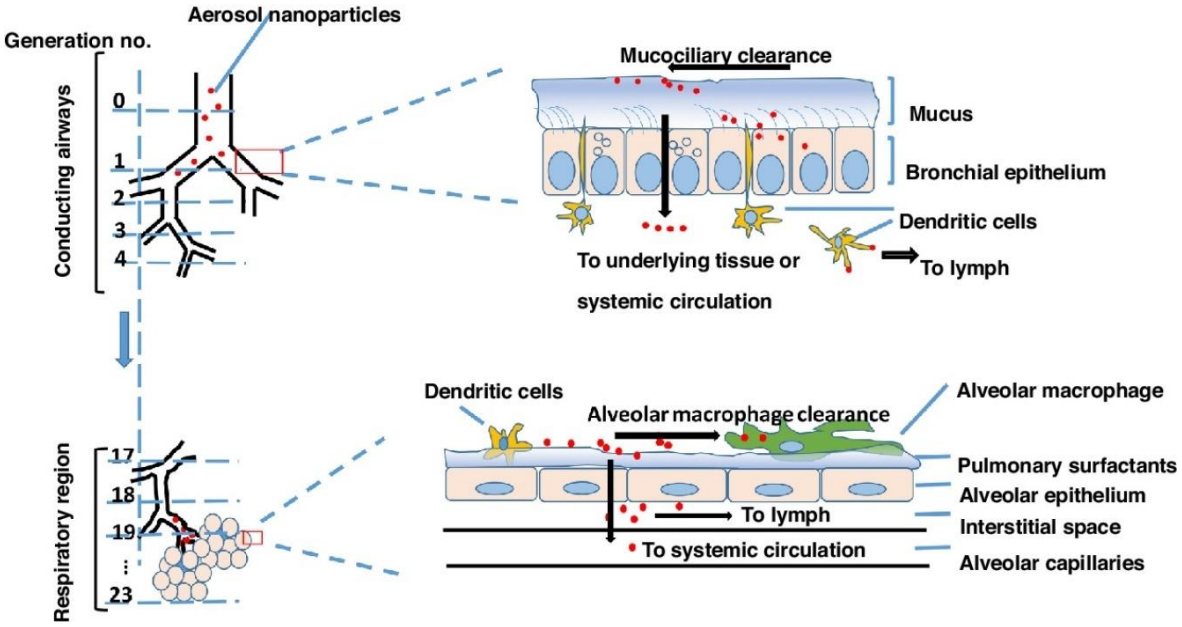

Figure 1.11. Differences in the clearance of nanoparticles based on deposition area within the lungs. The first 16 branching generations are the conducting airway, where the main clearance mechanism is mucociliary clearance. Macrophage clearance dominates in respiratory regions at generations 17-23. Nanoparticles that cross epithelial cells to the interstitial space can translocate into the circulatory system or lymph. Dendritic cells can capture nanoparticles and translocate into lymph nodes. Reprinted from Liu et al[134], copyright (2020), with permission from Elsevier.

In the alveolar region, where the mucociliary escalator is absent, particles are cleared via three major pathways: 1) particle-carrying macrophages migrating to the ciliated airways where the mucociliary escalator removes them; 2) particle transport towards lung-associated lymph nodes; 3) translocation into the circulatory system for subsequent accumulation/clearance in secondary organs.[135] It is estimated that one macrophage is present for every three alveoli.[136] Usually, particles undergo phagocytosis by alveolar macrophages within 6-12 hours.[137] However, this is also a size-dependent process. 1-3 µm particles are taken up better than those of 6 µm, while particles smaller than 100 nm can evade phagocytosis.[135] Geiser et al[138] conducted inhalation studies using 20 nm titanium oxide particles in a rat model. After inhalation, the lungs were lavaged and macrophages analysed for the presence of NPs via TEM. The data revealed that only 0.06-0.12% of particles were internalised by macrophages after 24 hours, while ultrastructural analysis showed the uptake was sporadic and unspecific. A possible explanation for such evasion

is a reduced recognition due to scattered and diluted chemotactic signals because of higher NPs number concentration (compared with the same mass/volume microparticles) and fewer opsonin molecules available per particle.[139,140] While more than 70% of alveoli surface is covered with blood vessels, it might look as a considerable amount of particles potentially could be translocated via the bloodstream. However, studies have shown that less than 1% of NPs will translocate this way.[141–143]

1.3.3 Toxicity

The severity of side effects of inhaled nanoparticles varies from long-term chronic complications to immediate and acute responses, from single tissue level to systemic diseases. The toxicity of NPs is influenced by a combination of physicochemical characteristics such as size, surface charge and modifications, chemistry, shape, solubility, exposure concentrations and duration, as well as an individual's health condition.[132] Mechanisms of toxicity can be either physical or chemical. Physical mechanisms are influenced by the size and shape, causing membrane penetration, changes in protein conformation, or physical hindrance of active sites. Chemical toxicity is predominantly linked to the generation of reactive oxygen species (ROS) causing lipid peroxidation, protein and DNA damage, and the dissolution and release of toxic ions.[144]

The size of NPs is one of the most important parameters correlating with toxicity, as it has a significant role in the particle's ability to penetrate the cell's membranes and interact with subcellular compartments. The amount of uptake (by number) decreases with the increase in particle size.[145–147] A study by Sakai et al[146] employed the PC12 cell line derived from rat pheochromocytoma and exposed it to 22 nm, 100 nm and 1000 nm particles for 3 hours. The results showed that the number of 22 nm particles taken up by cells was 53 times higher compared to 100 nm particles. However, by weight, there were more 100 nm particles. Particle penetration can induce membrane damage, affecting membrane integrity and stability through the formation of nano-sized holes, which can disrupt normal cell functioning. Once inside the cell, the particle can translocate into the organelles affecting their functions. Hence, particles can diffuse into the nucleus through the nuclear pores, where they potentially can bind to DNA and prevent its replication.[148,149] Lebedova et al[150] studied size-dependent genotoxicity of 5 and 50 nm silver, gold and platinum. The results showed gold and platinum NPs cause DNA damage in the size-dependent manner, where 5 nm caused more DNA damage than 50 nm. Silver particles caused damage irrespectively of their size (likely due to dissolution). Nanoparticles of the same size as protein molecules can interfere with signalling processes or interaction with proteins, causing aggregation and fibrillation.[151,152] Protein misfolding and fibrillation can potentially lead to amyloid-like structures, which are associated with neurodegenerative diseases.[153]

Lysosomes can be affected by nanoparticles resulting in lysosomal dysfunction, including enzyme inhibiting and biopersistence. Lysosomal membrane permeabilisation (LMP), a process where the lysosomal content is released into the cytosol, is not unique to nanoparticles but leads to a much greater potency for induction compared to microparticles. This is especially relevant to positively charged particles.[154] Xia et al[155] linked this effect with the proton pump theory, where polyamine groups with high proton binding affinity can lead to buffering and exaggerated proton pump activity, leading to osmotic swelling (as a mechanism to maintain neutral charge) and rupture. Lysosomal membrane permeabilisation releases lysosomal hydrolases, resulting in ROS generation, cytosolic acidification and necrosis.[156–158]

Biopersistency also correlates with histopathological changes, inflammatory response, and other biomarkers after NPs exposure.[159] Particle solubility and shape are key parameters when evaluating biopersistency. Therefore, for particles with rapid dissolution, biopersistency is unlikely, but they may trigger an acute toxicological response. Insoluble particles, on the other hand, may reside for a prolonged period. This may lead to bioaccumulation and cause a diverse range of chronic effects, including carcinogenicity.[159,160] Moreover, the uptake process itself can cause a response, for example, “frustrated phagocytosis”, where a cell tries to completely engulf a particle but fails due to its size or shape, which can often be observed with multi-wall carbon nanotubes[161] or asbestos[162]. Also, the shape may directly influence uptake into cells in the following order: rods/spheres > cylinders > cubes.[163,164]

Among the most important mechanisms of nanotoxicity is the generation of reactive oxygen species, leading to membrane, protein and DNA damage, unregulated cell signalling, changes in cell motility, cancer initiation and promotion, cytotoxicity, and apoptosis. The ROS formation depends on the particle physicochemical properties, cell type and concentration. Thus, cells exposed to relatively low NPs concentrations are capable of overcoming oxidative stress and recovering redox balance with the help of antioxidants. However, antioxidants are no longer effective at high NP concentrations, leading to adverse effects.[165] Zhu et al[166] used three different NP metal oxides, CuO, TiO_2 and CdO, to determine the differences in cytotoxicity and DNA damage. Results showed that CuO was the most toxic and leading to DNA damage via formation of 8-hydroxy-20 deoxyguanosine (8-OHdG), while TiO_2 appeared to be less toxic and did not induce a significant level of 8-OHdG. Wang et al[167] compared the cytotoxicity of four particles ZnO, TiO_2, CuO and Co_3O_4, using an *in vitro* model of primary culture of channel catfish hepatocytes and human HepG2 cells. In both cell types, the particles induced cytotoxicity in the following order: CuO > ZnO > Co_3O_4 > TiO_2. The toxicity was due to ROS and mitochondrial damage. Moreover, Choudhury et al[168] showed that 90 nm ZnO NPs induced toxicity at the epigenetic level particularly in conjunction with DNA methylation. The particles induced rapture

of the cell membrane, disturbed structural dynamics of the cytoskeleton, caused mitochondrial dysfunctions, and impaired cellular oxidative stress management machinery.

1.3.4 Nanoparticles and protein corona

Nanoparticles may enter the body by different routes, such as inhalation, ingestion, skin contact, or injections. Regardless of the method of entry, NPs will encounter body fluids and immediately adsorb biomolecules forming a e.g. protein corona.[169,170] Its composition and stability depend on size, shape, composition, surface charges, and functional groups of the NPs; the nature of the surrounding environment such as blood, pulmonary surfactant, interstitial fluid, or cell cytoplasm; and parameters as the duration of the exposure and temperature. The composition of corona can change over time in response to the surrounding environment.[171,172]

The composition of protein corona is a dynamic and competitive process. Protein coronas are divided into “soft” and “hard” (**Figure 1.12**.) The soft corona is made of loosely bound proteins that are exchanged with the surrounding environment over time. The exchange process is rapid and takes seconds to minutes.[173] The soft corona may be bound directly to the NPs surface, or to the hard corona via weak protein-protein interactions. The hard corona consists of tightly bound proteins to the NPs surface with high affinity and forms a stable shell. Once physiological fluid surrounds the particle, the soft corona is formed from the most abundant proteins.[169] Later, these proteins are exchanged with less abundant but with higher affinity proteins, resulting in the hard corona. The speed of hard corona formation varies from seconds to hours, based on protein type and affinity. It has been shown, that after 30 seconds of incubation in human plasma the protein corona is formed of almost 300 different proteins, while increased incubation reduces the quantity.[173] Gorshkov et al[174] characterised the corona formed on 60 nm silver NPs incubated in blood plasma at varying pH and temperatures. Out of >350 proteins, 38% bound at all temperatures (4-47 °C), 47% at all pH (4.9-8.9) and about 60% of these proteins did not change in abundance within the corona. Protein binding is promoted by a larger number of β-sheets, higher hydrophobicity, and a smaller number of α-helices. The corona is important in evaluating the toxicity of NPs, as it alters the size, stability, and surface chemistry of a nanomaterial. Regardless of whether it is hard or soft, the corona is what the cell “sees” and interacts with in the first place. As a result, differences in uptake and biological effects can be observed compared with ‘naked’ particles.[171,172,175,176]

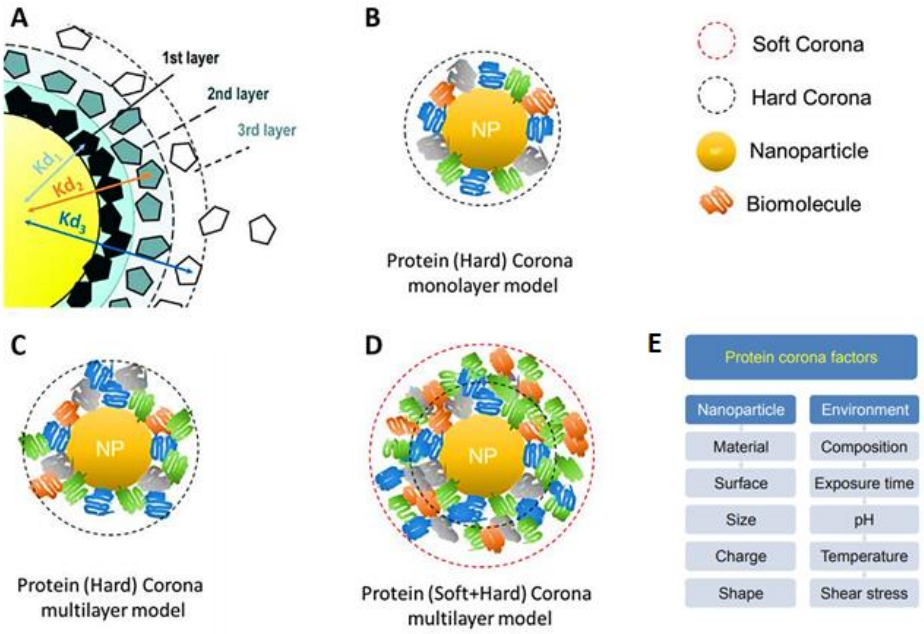

Figure 1.12. Schematic illustration of the hard and soft protein corona. A – Multi-layered organisation of protein corona. The binding of the different proteins to the NP surface is characterised by specific dissociation constants (K_d)**. B-D** – illustration of different models of corona formation. The hard corona is made of tightly bound proteins, while soft corona is made of loosely bound proteins. **E** – factors affecting corona composition. Reprinted with permission of Future Medicine Ltd, from Maiolo et al[169]; permission conveyed through Copyright Clearance Center, Inc.

Protein corona formation is an important variable to account for the planning of assay or experiments, and toxicity studies, as once proteins adsorb to NPs, the surrounding environment becomes depleted for the same proteins.[177] In a simple experiment Sohaebuddin et al[178] showed that after the addition of TiO_2, SiO_2 NPs and carbon nanotubes into serum containing cell culture media, about 30% of all proteins adsorb to NPs within 30 min, with further desorption in the next 2 hours to 5-25%. McKenzie et al[10] hypothesised that the ability of SP-A and SP-D to combat infection can be affected due to their sequestration by NPs and thereby an individual could potentially become functionally deficient in these proteins and more susceptible to infections or inflammatory diseases. In a series of *in vitro* experiments, cell cultures were infected with influenza A virus in the presence of SP-A/SP-D and NPs. The results showed that presence of nanoparticles affect the infection rate in a concentration dependent manner.

As has been discussed, nanoparticles can cause a wide range of adverse effects. However, protein corona can alter uptake and toxicity. In experiments by Smith et al[179], the role of serum has been investigated in the association of NPs with cells. HeLa and MDCK cell lines were exposed to 20 nm fluorescent carboxylate-modified polystyrene particles. The results showed that the presence of

serum reduces the cellular association by up to 20-fold, compared to cells incubated in a serum-free medium. Hence the internalisation of the particles was also reduced. It was concluded that cellular entry is reduced in the presence of serum primarily through inhibition of cell surface binding.[179] Another research by Garcia-Alvarez et al[180] investigated corona formation using an *in vivo* mice model exposed to 40 nm and 70 nm gold nanostars and nanorods. The results showed, that 70 nm nanostars had higher protein concentration than 70 nm nanorods, which was ascribed to the larger surface area of nanostars. When using either the *in vivo* mice model[180] or the *in vitro* human blood[173], the most abundant protein found was serum albumin.

While most of the research is focused on investigating corona formation in whole blood or serum, there exists little data about corona formation in a lung context. Pulmonary surfactant in the alveoli is the first physiological barrier NPs encounter once inhaled. Whitwell et al[11] incubated polystyrene nanoparticle with different surface modifications (aminated, carboxylated and unmodified) and TiO_2 in human BALF from patients with pulmonary alveolar proteinosis (PAP) to determine the composition of the protein corona. It has been shown that protein binding properties are independent of particle functionalisation, as the surfaces become averaged upon inhalation regardless of intrinsic properties. SP-A was detected among the most abundant proteins on the surface, suggesting it might have an important role in NPs clearance or mediating immune response. SP-B was also detected, indicating that pulmonary surfactant lipids might bind to the surface and further alter the properties of NPs.

Hu et al[181] employed a coarse-grained molecular dynamics simulation to study the interaction between nanoparticles and a pulmonary surfactant system. It was found that regardless of physicochemical properties, both silver and polystyrene particles formed a corona of both lipids and proteins. The structure of the protein corona was dependent on the hydrophilicity of NPs. Hence, more hydrophobic NPs formed a single layer lipid corona, and AgNPs formed a bilayer. Hydrophilic SP-A partially associated with the surface of AgNPs, whilst it oriented parallel with the lipid monolayer on polystyrene NPs. However, in both cases, SP-A binds to bare NPs via hydrophilic carbohydrate recognition domain (CRD), compete with hydrophobic lipid heads (**Figure 1.13**).

1.3.5 Dose-metrics for nanoparticles assessment

In the standard toxicity studies with conventional chemical substances the concentration is expressed as the total administered mass of the substance, because the mass of a substance is unique to the number of molecules of that substance. The mass concentration can be easily

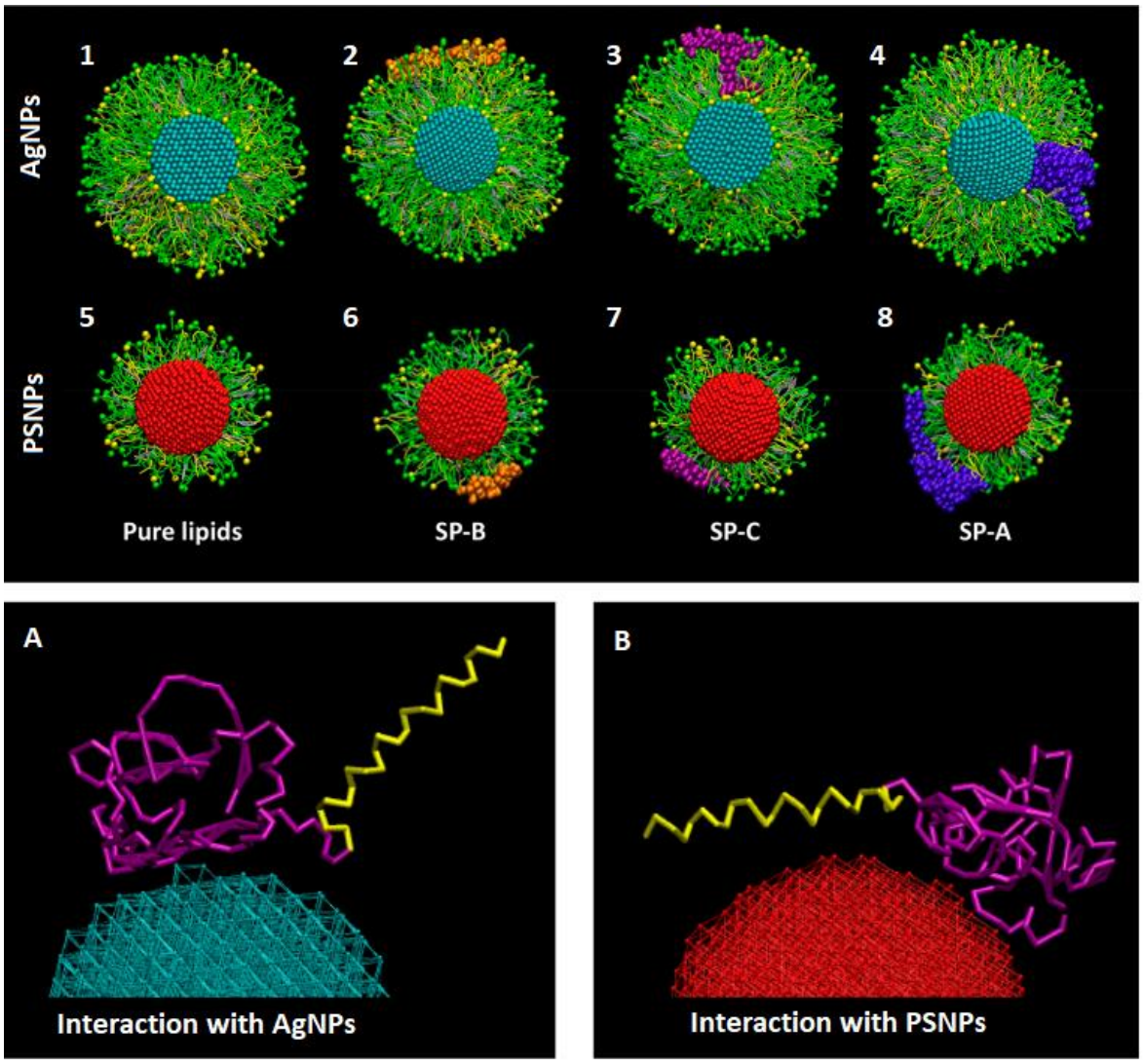

Figure 1.13. Coarse-grained molecular dynamics simulated pulmonary surfactant composition and SP-A interaction with a silver (AgNPs) and polystyrene (PSNPs) particles. Corona composition on (**1-4**) AgNPs and (**5-8**) PSNPs surface. AgNPs and PSNPs are shown in cyan and red, respectively. DPPC molecules - green, POPG - yellow, cholesterol – silver, SP-B - orange, SP-C - purple, and SP-A - violet. **A, B** - Molecular conformation of the SP-A fragment bound to AgNPs and PSNPs, respectively. Yellow – collagen region, purple – CRD. Reprinted with permission from Hu et al[181]; Copyright (2017) American Chemical Society.

converted into moles or other relevant metrics, if required, and used interchangeably. Hence, the mass alone is sufficient to describe the safety or toxicity.[182]

For NPs, the mass is not uniquely related to the number of NPs. This, in turn, does not allow direct comparison of the toxicity even for the NPs with the exact same composition. In general, at equal mass concentrations NPs of the same composition have higher cytotoxicity profile, while the

cellular uptake is greater for larger particles.[182,183] While there is no universal metric, the most common dose metrics are expressed as particle number, mass, volume and surface area.[184,185]

It is generally agreed that surface area is the most important parameter assessing and comparing toxicity.[186–189] According to Delmaar et al, if administered surface area is an adequate dose metric, a large number of small spheres will give the same response as a smaller number of larger spheres with the same total surface area.[187] Yet, surface area cannot be used alone comparing the effect induced by the particles at the same concentration but with different physicochemical properties, thus multiple parameters (i.e. chemistry, diameter, shape, charge) have to be reported.[189]

Largely, the selection of the metric depends on the aims and objectives of a study, as well as the particles themselves. For example, if NPs are heterogenous in size and shape (i.e. environmental particles) it is not always possible to determine their number, surface area and even mean diameter, hence mass concentration is often used. Engineered NPs are usually homogenous and well characterised, hence their dose metrics can be expressed in different formats and recalculated if needed (i.e. from number concentration to surface area, volume, or mass).

1.4 Label-free microscopy

Microscopy is among the most important and widespread tools in scientific research, especially in life sciences. Because of imaging, it is possible to *see* the complexity of biological systems, rather than rely on indirect methods. However, in light microscopy the image contrast is produced by the difference in the refractive index and overall optical density, limiting the amount of useful information that can be generated. To overcome such specific limitations, the biological systems of interest often require the introduction of additional chemicals (i.e. fluorescent dyes) or alterations in their structural integrity. Such changes can disrupt the native structure or homeostasis and lead to data misinterpretation. Hence, researchers strive to find ways that allow studying these systems without any interference from the outside and increase information output, employing intrinsic properties of the molecules.

The chemical bonds between atoms are not rigid, they can stretch and bend. These oscillations are named molecular vibrations and each chemical bond type has its unique pattern. Vibrational spectroscopy is a technique that utilises these vibrational motions of molecules and can be used for chemical and structural characterisation in qualitative and quantitative analyses. It is a label-free, non-invasive, and non-destructive method that allows acquiring chemical-specific information without affecting the natural state of biological systems. While spectroscopy yields data in a form of graphs and peaks, a combination of optical spectroscopy and microscopy provides a direct and non-invasive approach to the visualisation of cellular structures and

molecules of interest in the form of an image. Microscopy techniques based on vibrational spectroscopy offer intrinsic chemical selectivity and avoid perturbation of the cell's functions induced by fluorophore labelling, while infrared or near-infrared femtosecond pulse lasers allow deeper tissue penetration, 3D spatial resolution, none or reduced phototoxicity.

This section will give a brief overview of Coherent anti-Stokes Raman scattering (CARS), Second Harmonic Generation (SHG) and Two-Photon Fluorescence (TPF), as these imaging methods we used the most during the research.

1.4.1 Coherent anti-Stokes Raman scattering microscopy (CARS)

Coherent anti-Stokes Raman scattering is a four-wave mixing non-linear process, where molecules are irradiated using two lasers, a temporally and spatially overlapped pump (higher frequency) and Stokes (lower frequency) pulses. These beams simultaneously interact with the sample and when their frequency difference matches with the frequency of the target bond of the molecule – blue-shifted anti-Stokes frequency is generated (**Figure 1.14**). Blue-shifted signal is one of the CARS advantages, as the signal can be easily detected in the presence of one-photon fluorescence background. CARS is a multiphoton process with no net deposition of energy within the molecule, allowing label-free, non-invasive imaging with no adverse effect on cell growth and behaviour.[190]

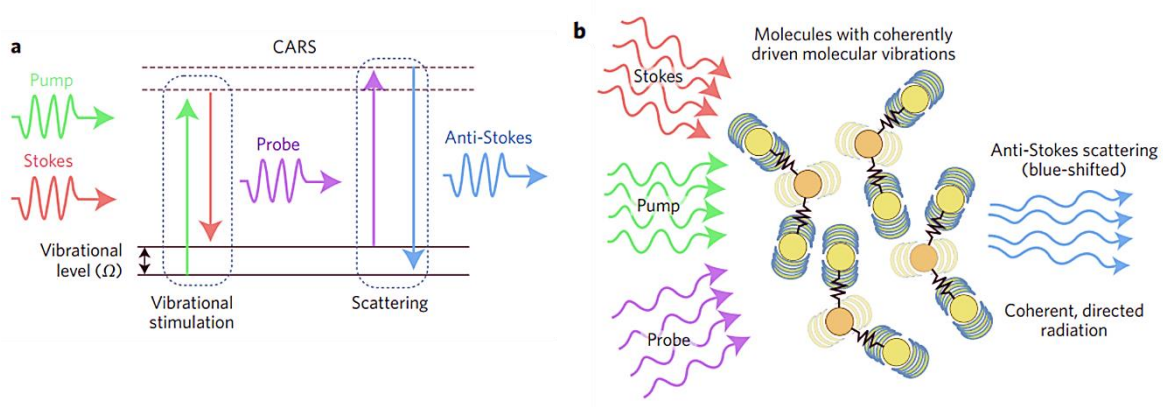

Figure 1.14. Schematic illustration of CARS mechanisms. A - Pump and Stokes photons stimulate a vibration, resulting in a probe photon inelastic scattering. When the probe photon interacts with the target molecule, the CARS signal is generated. **B** - CARS occurs through the inelastic scattering of probe photons of coherently driven vibrationally excited molecules. The incident light consists of a pump, Stokes, and probe sources. Reprinted from Camp Jr et al[191], by permission from the Springer Nature; Copyright 2015.

The intensity of the CARS signal is determined by the local concentration of the molecular species, thus CARS is highly sensitive for the imaging of lipids because of their abundance within the cell

(e.g. cell membrane) and a large number of CH_2 bonds in a lipid molecule.[192] Because of the above advances, CARS microscopy is becoming a powerful technique for the vibrational imaging of biological samples where chemical-specific information is needed and staining is not an option. CARS also allows for video-rate microscopy to track the processes in live biological systems in real-time. Thus, CARS is often used to study lipids[193,194], nucleic acids[195] and proteins[196].

With the development of nanomedicine, there is a need for techniques enabling the visualisation of bio-nano interactions. Polystyrene particles can be imaged relatively easily because of the abundance of CH_2 bonds.[8,197,198] Rago et al[199] studied 1.18 μm iron oxide particles and showed that they can be visualised and distinguished from cellular components by overlaying on-resonant and off-resonant CARS images. Several studies applied CARS imaging with 3D reconstruction to study the uptake of CeO_2, TiO_2 and Au in cells. While they successfully visualised the localisation of nanoparticles, they were not able to determine the size of aggregates within the cells.[200,201]. In some studies, particles as small as 10 nm[162] could be seen on the image, however, it is impossible to differentiate whether it is a single particle or an aggregate of particles, as the resolution of CARS microscopy is ~250-300 nm. It is known that optical properties of metal nanoparticles depend on their chemistry, size and shape; aggregates of nanoparticles also result in signal enhancement, which might make quantification more complicated, not only for different particles but even for the same size and chemistry.[202,203]

1.4.2 Second harmonic generation microscopy (SHG)

Second harmonic generation is a coherent non-linear process where two incident lower frequency photons interact with non-centrosymmetric structures and are directly converted into a single photon of the same energy with exactly twice the incident frequency, without absorption or reemission of photons.[204] Similar to CARS, SHG offers label-free non-destructive imaging with deep tissue penetration (up to 300 μm)[205] due to the use of infra-red lasers, high spatial resolution and optical sectioning, and significantly reduced phototoxicity.[206] Collagen is the most abundant protein in mammals (up to 25% of all proteins), and due to its abundance and optical properties, the SHG signal can be effectively collected from different tissues.[207] SHG is also used to study myosin[208], tubulin[209], starch[210] and cellulose[211], as well as biological membranes labelled with SHG-active dyes[212].

The application of SHG in the imaging of NPs in biological systems is a relatively new methodology and hence there is a limited amount of research on this topic. Breunig et al[213] applied SHG to study the penetration of ZnO NPs from sunscreens into human skin. The study demonstrated that ZnO particles can be visualised with SHG, showing strong ZnO related signals on top of the skin,

where the sunscreen was applied. At 15–20 µm, no particles were detected, and at the boundary of the epidermis/dermis (25-40 µm) the collagen SHG signal became visible. Several studies used *in vivo* models to detect $BaTiO_3$ particles. The results showed SHG signal can be recovered as deep as 100 µm under the tissue, while even at high powers (above those necessary for imaging) no bleaching or photodamage was observed.[214,215]

1.4.3 Two-photon fluorescence (TPF)

Two-photon fluorescence microscopy is a non-linear process that involves the absorption of two photons whose joint energy is sufficient to induce a molecular transition to an excited state followed by a release of a shorter wavelength (higher energy) photon. In conventional one-photon fluorescence (i.e. confocal microscopy) fluorophores are excited with shorter wavelength (higher energy) UV-Vis light. Two-photon fluorescence employs longer near infra-red photons (less energetic). Since pulsed near-infra-red light excitation is used, TPF is less phototoxic compared to single-photon fluorescence microscopy.[212] Unlike SHG, there is energy lost during this process, so the emitted photon has an energy that is lower than the sum of the energy of the two incident photons.[216] The TPF relies on major endogenous fluorophores: nicotinamide adenine dinucleotide(phosphate) (NAD(P)H) and flavin adenine dinucleotide (FAD), which are two major cofactors of redox reactions in the cell and central regulators of energy production and metabolism.[217]

Two-photon fluorescence is widely used in nanoparticle-assisted photodynamic therapy research, where particles (photosensitisers) are irradiated with near infra-red light followed by the emission of high-energy visible light. This emitted light can sensitize oxygen to produce cytotoxic ROS to kill e.g. cancer cells.[218–220] Morales-Dalmau et al[221] administered mice with 11 nm × 44 nm gold nanorods via a tail injection, followed by tissue harvesting and TPF imaging. Researchers successfully localised and quantified the concentration of particles in the different tissues. Moreover, the two-photon luminescence, originating from the absorption of two photons by gold NPs, was significantly stronger than background autofluorescence and thus particles were easily differentiated from the tissue's background signal.

1.5 Study hypothesis, aims and objectives

The research hypothesis of this study is that lung Surfactant Proteins A (SP-A) and D (SP-D) bind to and agglomerate inhaled engineered and environmental nanoparticles *in vivo*, reducing translocation to the blood and secondary organs.

The aims, supported by the objectives, of this study are:

1. Develop multimodal imaging methods, based on CARS, SHG and TPF for label-free imaging of gold nanoparticles (AuNPs) inside the cells.

1.1. Optimise the system for the imaging of single cells and tissue slices.

1.2. Apply the optimised system to detected 20 nm AuNPs within biological samples.

2. Characterise the interaction of AuNPs with SP-A and SP-D

2.1. Determine the behaviours of gold nanoparticles in physiological-like fluids.

2.2. Characterise and quantify the interaction of AuNPs with SP-A and SP-D, applying dynamic light scattering, static light scattering, transmission electron microscopy (TEM), serial block-face three-dimensional electron microscopy, sodium dodecyl sulphate polyacrylamide gel electrophoresis (SDS-PAGE) and Bradford assay.

3. Characterise the possible *in vitro* nanotoxicity of gold NPs on cell culture models in the presence of SP-A and SP-D.

3.1. Determine the role of SP-A and SP-D in the potential toxicity of NPs by 3-(4,5-dimethylthiazol-2-yl)-2,5 diphenyl tetrazolium bromide (MTT) and lactate dehydrogenase (LDH) assays.

3.2. Detect and quantify the number of internalised AuNPs by multimodal microscopy (established in aim **1**) and confirm these finding by electron microscopy.

3.3. Establish the link between AuNPs uptake by the cells and the presence of SP-A and SP-D.

4. Characterise the potential *in vivo* translocation and toxic effects of NPs using mice deficient for SP-A, deficient for SP-D and wild-type mice.

4.1. Expose deficient and wild-type mice to 20 nm AuNP in the established inhalation model.

4.2. Quantify the concentration of AuNPs in the lungs, liver, spleen, and kidneys via multimodal imaging, inductively coupled plasma mass spectrometry (ICP-MS), single particle ICP-MS, laser ablation ICP-MS and TEM.

5. Characterise environmental nanoparticles collected from Southampton's harbour and investigate their toxicity.

5.1. Determine elemental composition, size, and morphology of environmental nanoparticles.

5.2. Expose the cell line to environmental particles and determine their toxicity via MTT assay.

Chapter 2 Materials and methods

All reagents and consumables were purchased from Fisher Scientific (United Kingdom) unless otherwise stated. The list of reagents and kits, as well as their catalogue numbers, can be found in **Appendix A**.

The methods are grouped into the sections specific for each block of the experiments (i.e. *in vitro, in vivo,* imaging), rather than in chronological order, to allow easier navigation based on the experiment type.

2.1 Reagents and buffers

Tris-buffered saline (TBS). General-purpose Tris-buffered saline was prepared from commercially available 20x concentrate, diluting the stock solution to 1x concentration (20 mM Tris, 150 mM NaCl) with distilled water. General-purpose TBS was used for non-aseptic and non-LPS sensitive assays. For more sensitive assays, such as protein purification, dialysis and characterisation of protein-nanoparticle interaction, TBS was prepared by dissolving 150 mM NaCl and 25 mM Tris in Milli-Q water, adjusting the pH to 7.4 with HCl. Furthermore, this TBS was supplemented with 5 mM $CaCl_2$ (referred as TBS^{Ca}) or with 10 mM EDTA (further referred as TBS^{EDTA}). Supplemented buffers were further vacuum filtered through a 0.2 µm nylon membrane to remove undissolved impurities.

Phosphate-buffered saline (PBS). General-purpose PBS was prepared by dissolving a commercially available 5 g Gibco PBS tablet in 500 ml of distilled water (final concentration 137 mM NaCl, 2.7 mM KCl, 8 mM Na_2HPO_4, and 2 mM KH_2PO_4). General-purpose TBS was used for non-aseptic and non-LPS sensitive assays. Commercially available sterile PBS was used for cell culture experiments.

Phosphate buffer (PB). Na_2HPO_4 and NaH_2PO_4 1 M stock solutions were prepared in Milli-Q water, resulting in buffer A and B, respectively. Then, buffer A and buffer B were mixed in a 4:1 ratio yielding 1 M PB. The buffer pH was adjusted to 7.4 and vacuum filtered through a 0.2 µm nylon membrane. A working 1x solution was prepared by diluting the stock solution with Milli-Q water.

Tris-acetate-EDTA buffer (TAE). The TAE buffer 50x stock solution was prepared by dissolving 50 mM EDTA, 2 M Tris and 1 M glacial acetic acid in distilled water. The pH was adjusted to 8.0. A

working TAE buffer solution of 1x concentration was prepared by diluting the stock with distilled water.

Red blood cell (RBC) lysis buffer. RBC lysis buffer was prepared and used at 10x concentration. 1.55 M NH_4Cl, 100 mM $KHCO_3$ and 1 mM EDTA were dissolved in Milli-Q water, adjusted to pH 7.4 and sterile filtered through a 0.22 µm syringe filter.

Paraformaldehyde (PFA) fixative. To prepare 4% PFA in PB fixative, 4 g of PFA powder was mixed with 40 ml Milli-Q water and heated on a magnetic stirrer hot plate (**in a fume cupboard, as fumes are toxic!**) at approximately 60 °C. Three drops of 0.1 M NaOH were added and left stirring until fully dissolved. Then, the volume was adjusted to 50 ml with Milli-Q water, yielding 8% PFA in water. This solution was further diluted with 0.2 M PB, adjusted to pH 7.4 and filtered through a 0.22 µm syringe filter, yielding a working 4% PFA solution in PB. The fixative was aliquoted and stored at -20 °C.

Mowiol. To prepare the mowiol mounting medium 4.8 g of Mowiol 4-88 and 12 g of glycerol were added into 100 ml beaker and placed on a magnetic stirrer for 30 min. Then, 12 ml of Milli-Q water and 24 ml 0.2 M Tris HCl (pH 8.5) were added and left stirring overnight at 50 °C. Once dissolved, the solution was centrifuged at 4000 × g for 10 min to precipitate undissolved reagents. The supernatant was removed, aliquoted and stored at -20 °C. Mowiol cures (transitions from the liquid into the solid/hard state) overnight at room temperature.

2.2 Purification of surfactant proteins A and D

2.2.1 Preparation of bronchoalveolar lavage fluid

The BALF was collected from patients at the Royal Brompton Hospital with informed consent and necessary ethical permission (the Royal Brompton and Harefield Research Ethics Committee NRES 10/H0504/9). A Material Transfer Agreement has been signed between the Royal Brompton and Harefield NHS Foundation Trust and University of Southampton (UK) covering the usage of the bronchoalveolar lavage fluid (BALF) for the purification of native human SP-A and SP-D for research purposes.

Frozen at -80 °C, BALF was thawed and supplemented with Tris (20 mM final concentration) and EDTA (10 mM final concentration) and adjusted to pH 7.4 with concentrated HCl or 10 M NaOH and left under constant stirring for 1 h at room temperature. The BALF was then centrifuged at 10,000 × g for 45 min at 4 °C. The pellets and supernatant were stored separately at -20 °C.

2.2.2 SP-A purification by butanol extraction

Surfactant protein A (SP-A) was purified from the bronchoalveolar pellets using an adapted version of a butanol extraction method.[222] 1.5 ml of thawed SP-A containing pellets (prepared as in **Section 2.2.1**) were added dropwise into 75 ml of 1-butanol left at room temperature for 3 h under constant stirring, with subsequent centrifugation at 10,000 × g for 30 min at 4 °C. After discarding the supernatant, the pellets were resuspended in 1-butanol and centrifugation was repeated. The resulting pellets were dried under a steady flow of nitrogen at 37 °C and resuspended thoroughly in 5 ml of 20 mM Octyl β-D-glucopyranoside (OGP), 150 mM NaCl and 5 mM Tris-buffered water (TBW) at pH 7.4 (OGP/NaCl/TBW). The suspension was centrifuged at 4,200 × g for 45 min at 4 °C. After resuspension of pellets in OGP/NaCl/TBW, centrifugation was repeated. The pellets were then resuspended in 5 ml of TBW adjusted to 100 mM OGP and rotated at room temperature for 30 min.

To remove endotoxin, 0.42 ml of prewashed Polymyxin B beads were added to the mixture. The solution was then dialysed against TBW using SnakeSkin dialysing tubing (30,000 Da molecular weight cut off (MWCO)) according to the manufacturer's instructions. To remove Polymyxin B beads, the mixture was centrifuged at 3,000 × g for 10 min at 4 °C. The supernatant was then collected and centrifuged at 130,000 × g for 60 min at 4 °C. The SP-A containing supernatant was sterile filtered using a 0.22 µm syringe filter and stored as 1 ml aliquots at -20 °C. The purity of the SP-A protein was evaluated using SDS-PAGE and Western blot analyses. The endotoxin concentration was assessed by Limulus Amebocyte Lysate test, as described in **Section 2.2.4.**

2.2.3 SP-D purification by affinity chromatography

Surfactant protein D (SP-D) was purified from the BALF supernatant using an adapted version of the previously reported method.[223] N-Acetyl-D-mannosamine (ManNAc) coupled sepharose affinity resin was washed with TBS and 50 mM EDTA at pH 7.4. Following the wash step, the resin was re-equilibrated with TBS^{Ca}. The SP-D containing supernatant (prepared and described in **Section 2.2.1**) was adjusted to 50 mM $CaCl_2$. The pH was adjusted to 7.4 with 10 M NaOH. The equilibrated ManNAc resin was added to the mixture and left overnight under constant stirring at 4 °C. The BALF was filtered through a grade 1 sintered funnel under vacuum, and the resin with bound SP-D was collected, packed into an affinity column, and connected to the Akta 900 system (Amersham BioSciences). The column was then washed with a high salt buffer (1 M NaCl) TBS^{Ca} before the column was re-equilibrated with TBS^{Ca}. The SP-D was eluted with TBS with 100 mM $MnCl_2$ (pH 7.4). The eluant was pooled and buffer exchanged into TBS^{EDTA} and then

concentrated to approximately 1 mg/mL with an Amicon Ultra 30 kDa MWCO centrifugal filter at 4000 × g and 4 °C. The column was then washed with a 3-column volume (CV) of TBS^{EDTA} and 3 CV of 20% (v/v) ethanol solution. To remove endotoxin, SP-D was mixed with Polymyxin B beads at 1:4 ratio and rotated at room temperature for 30 min. Endotoxin bound beads were removed by centrifugation at 4,000 × g at 4 °C for 5 min. SP-D containing supernatant was then collected and sterile filtered through 0,45 µm filter and aliquots were stored at -20 °C. SP-D in the preparation was confirmed using SDS-PAGE and Western blot analysis. The endotoxin concentration was assessed by the Limulus Amoebocyte Lysate test, as described in **Section 2.2.4.**

2.2.4 Endotoxin detection assay

The Limulus Amoebocyte Lysate (LAL) chromogenic quantitation kit was used to measure levels of bacterial endotoxins in purified proteins. The LAL assay was performed according to the manufacturer's recommendations. All samples were analysed in duplicates. In brief, 50 µL of each known standard or unknown sample were diluted in endotoxin-free water and added into an appropriate microplate well, covered with a lid and incubated for 5 min at 37 °C. 50 µL of LAL was added to each well and incubated for 10 min at 37 °C. Then, 100 µL of substrate solution was added to each well and incubated again for 6 min at 37 °C. The reaction was stopped by the addition of 50 µL of 25% (v/v) acetic acid to each well. The SpectraMax 340PC microplate reader was used to measure absorbance at 405 nm. A blank-corrected two-fold serial diluted standard curve (1 endotoxin unit/ml (EU/ml) to 0.125 EU/ml; $r^2 \geq 0.98$) was prepared to determine the endotoxin concentration of each sample.

2.2.5 Sodium dodecyl sulphate polyacrylamide gel electrophoresis

The SDS-PAGE analysis was conducted using 4-12% NuPAGE Bis-Tris mini gels (1 mm thick) with a NuPAGE MES SDS running buffer. Reduced protein samples were prepared according to the manufacturer's instructions. In brief, 5 µg of protein samples were mixed with 2.5 µl of NuPAGE LDS Sample Buffer (4X) and 1 µl of NuPAGE Reducing Agent (10X), adjusted to 10 µl with Milli-Q water and heated at 70 °C for 10 minutes. Protein marker (**Table 2.1**) was analysed alongside protein samples to determine the molecular weight. Gel electrophoresis was performed at 200 volts for 35 minutes and stained using SimplyBlue or silver or transferred onto western blot membranes.

Table 2.1. List of protein markers used in the analyses.

Analysis type	Marker name	Volume
Western Blot	SeeBlue Plus2	7 µl
SimplyBlue staining	Mark12	5 µl
Silver staining	Mark12	5 µl, 1:20 dilution

2.2.5.1 SimplyBlue staining

The SimplyBlue staining was conducted by applying the microwave protocol as recommended by the manufacturer to achieve maximum sensitivity. After the electrophoresis, the gels were removed from their casing and rinsed twice with distilled water. Then, the gels were placed in 100 ml of distilled water, microwaved on high (900 watts) for 45 sec or until they almost boiled and placed on a rocker for 1 min at 30 oscillations per minute. This wash step was repeated 3 times with clean distilled water after each step. SimplyBlue SafeStain was then added to the gels and microwaved on high for 30 sec or until they almost boiled and placed on a rocker for 5 min. Gels were then de-stained using distilled water (2 washes of 15 min each) and 20% NaCl (w/v) (2 washes of 10 min each) on a rocker. The image of the gel was captured using the ChemGenius imaging system.

2.2.5.2 Silver staining

The silver staining was conducted as recommended by the manufacturer. Immediately after electrophoresis, the gels were incubated in a fixative solution containing 90 ml Milli-Q water, 100 ml methanol and 20 ml acetic acid for 10 minutes. The fixative was then removed, and the gels were incubated in 100 ml of sensitising solution 2 × 30 min and rinsed 3 × 10 min in Milli-Q water. The gels were then incubated in 100 ml of silver staining solution for 7-15 min and washed 3 × 5 min in Milli-Q water. Finally, the gels were incubated in 100 ml of developing solution for 2-10 min following the addition of 5 ml of stop reagent. The gels were washed, and images were captured using the ChemGenius imaging system.

2.2.5.3 Western Blot

Proteins were transferred to a polyvinylidene difluoride (PVDF) membrane using the iBlot Dry Blotting System with iBlot PVDF Transfer Stacks, as recommended by the manufacturer. All incubations of the membrane were conducted with rocking at room temperature. Primary and secondary antibodies used for Western blot analysis are given in **Table 2.2**. Membranes were

blocked in TBS with 5% (w/v) skimmed milk powder (Sainsbury's, UK) and 0.05% (v/v) Tween 20 (block buffer) for 1 h. The membrane was incubated for 1 h with the primary antibody diluted 1:1000 in 10 ml of block buffer, following three washes in block buffer for 5 min. Then, the membrane was incubated for 1 h with the secondary antibody diluted 1:1000 in 10 ml of block buffer and washed three times in TBS with 0.05% Tween 20 for 5 min.

The SuperSignal West Pico Chemiluminescent Substrate was used to visualise the protein bands. The reagents were mixed in a 1:1 ratio before use, and 1 ml of the mixture was applied to the top of the membrane. The chemiluminescence was recorded using the ChemGenius imaging system (Syngene, Cambridge, UK) with a 2 min exposure time. For protein mixture analysis on the same membrane, antibodies were stripped away by incubating the membrane with 15 ml of Restore Stripping Solution for 15 minutes and rinsed with TBS for 2 min three times. Then, the membrane was blocked again and probed with new antibodies.

Protein molecular weights were determined by creating a composite image of light and dark images. Monochromatic composite images were created using the native ChemGenius software (GeneSnap). Polychromatic composite images were created using Fiji software.

Table 2.2. List of antibodies used for Western blot analysis.

Antibody	SP-A	SP-D	BSA
Primary	Mouse α-nhSP-A monoclonal antibody HYB 238-04 (1 mg/ml) (kindly provided by Prof Uffe Holmskov, University of Southern Denmark, Denmark)	Rabbit α-rfhSP-D polyclonal antibody (1.6 mg/ml)	Bovine Serum Albumin Polyclonal Antibody
Secondary	HRP-conjugated Goat α-Mouse IgG (H+L) antibody	HRP-conjugated Goat α-Rabbit IgG (H+L) antibody	HRP-conjugated Goat α-Rabbit IgG (H+L) antibody

2.2.6 Protein concentration quantification

2.2.6.1 UV absorbance assay

The protein concentration was measured with a UV spectroscopy at 280 nm and calculated based on protein molar extinction coefficients from the amino acid sequence.[224]

$$c = \frac{Abs}{\epsilon \times l} \times dilution\ factor$$

Where c is protein concentration, Abs is the absorbance at 280 nm, ϵ is molar extinction coefficient, l is cuvette length.

The molar extinction coefficient is related to its tryptophan (W), tyrosine (Y) and cysteine (C) amino acid composition and calculated using the following equation:

$$\epsilon = (nW \times 5500) + (nY \times 1490) + (nC \times 125)$$

Where n is the number of each residue. The ϵ for SP-A and SP-D are 27310 $M^{-1}cm^{-1}$ and 17780 $M^{-1}cm^{-1}$ respectively.

2.2.6.2 Bradford assay

The Bradford assay was conducted using Pierce Coomassie Plus (Bradford) Assay Reagent, following the protocol for a 1-25 µl/ml working range and 96-well microplates as recommended by the manufacturer. 150 µl of standard (BSA) or unknown sample and 150 µl of Bradford reagent were pipetted into the appropriate microplate wells and mixed with plate shaker for 30 sec, following 10 min incubation at room temperature. The absorbance was measured at 595 nm on a plate reader (Molecular Devices SpectraMax 340pc). Blank-corrected two-fold serial diluted standard curves were prepared individually for each protein to determine the concentration of each unknown sample.

2.3 Nanoparticles and nanoparticle-protein interaction characterisation

Due to the nature of the proteins and intrinsic characteristics of nanoparticles used in this study, all experiments were performed in Eppendorf Protein LoBind tubes to minimise the adsorbance to the tube walls.

2.3.1 Collection of environmental particles

The particulate matter (PM) was collected at the harbour of National Institute of Oceanography by Dr Matthew Loxham (University of Southampton). The PM was collected using a high-volume cascade impactor operating at a flow rate of 0.9 m^3/min with 50% cut points (d50) at 10 µm, 2.5 µm, and 0.1 µm, to collect PM_{10} (coarse), $PM_{2.5}$ (fine) and $PM_{0.1}$ (ultrafine). Particles larger than 10 µm were excluded by a silicon grease impaction stage. PM_{10} and $PM_{2.5}$ were collected on

polyurethane foam impaction substrates. Polyurethane foam collection substrates were pre-cleaned by two sonications in methanol, followed by drying in an oven at 50 °C overnight. $PM_{0.1}$ were collected using a terminal polytetrafluoroethylene (Teflon) filter with pore size 5 µm. All filters were conditioned overnight in a class 100 cleanroom before weighing.

After the collection, filters were equilibrated overnight at the room's ambient atmosphere before being weighed to determine the collected PM mass. The PM was prepared by sonication of the respective filters into methanol and drying in a centrifugal evaporator at 30 °C. The PM was then resuspended in 3 ml of methanol by 30 sec sonication and transferred to a pre-weighed vial and dried under nitrogen stream on a 30 °C hotplate. The PM was then conditioned overnight and weighed to determine the extracted PM mass. The PM was resuspended in ultrapure water at a concentration of 5 mg/ml.

2.3.2 Energy dispersive x-ray spectroscopy of environmental nanoparticles

Samples were prepared by drying 50 µl of coarse, fine and ultrafine particles (5 mg/ml) on carbon tape stuck to aluminium stubs. An FEI Quanta 200 SEM equipped with an X-ray energy-dispersive spectrometer (EDXS) was employed to qualitatively determine the elemental composition of environmental particles.

2.3.3 Raman spectroscopy of environmental nanoparticles

Raman spectroscopy was performed by Adam Lister (University of Southampton). The spectra were obtained using a Renishaw inVia Raman microscope with a 633 nm laser in streamline mode and a Leica 50x water immersion objective. Data was collected in WiRE 3.4 software. The spectra were recorded with an exposure time of 10 sec, 5 averages and 1 mW laser power at the sample. Cosmic ray artefacts were removed using WiRE 3.4. At least 5 different areas were scanned within each sample. Raman spectroscopy was used to confirm the presence of carbon.

2.3.4 ICP-MS of environmental nanoparticles

Particle analysis was performed by Dr Matthew Loxham, University of Southampton. All analysis steps were performed in a clean laboratory (class 100) environment to minimize possible contamination. PM suspensions were vortexed and water bath sonicated for 30 s each. A 100 µl aliquot of the suspension was reserved for future anion analysis, and the remaining volume was recorded and transferred to a Teflon pot. The suspensions dried at 130 °C. Three overnight

digestion steps were performed: respectively, 900 µl of concentrated nitric acid (15 M, Primar Plus grade; Fisher Scientific, Loughborough, UK) with 100 µl of concentrated hydrofluoric acid (27 M, UpA grade; Romil, Cambridge, UK) pressurised at 180 °C, 1 mL of 6 M hydrochloric acid (12 M, Primar Plus grade; Fisher) at 130 °C, and 1 mL of 2% (v/v) nitric acid spiked with Be, In, and Re to monitor instrument drift. Evaporation at 130 °C was performed after each of the first two steps. Hydrochloric and nitric acids were sub-boiled prior to use. Immediately before analysis, an additional 2% nitric acid was added to adjust a final mass to about 3 g per digest. Standards were prepared using a variety of commercially available standard solutions to assess a range of metals. Blanks were prepared by performing acid digests in the absence of the PM suspension, to monitor the contribution of any contamination during the digestion process. Samples, standards, and blanks were analysed by inductively coupled plasma mass spectrometry (ICP-MS) using a ThermoFisher XSeries2 inductively coupled plasma mass spectrometer (ThermoFisher Scientific, Bremen, Germany) located in the Isotope Geochemistry Instrument Suite at NOCS, Southampton.

2.3.5 Nanoparticle stability in a physiological-like environment

To test the stability of 20 nm AuNP under physiological-like conditions 7×10^{10} particles/ml were mixed with Milli-Q water, TBS^{Ca}, TBS^{EDTA} and RPMI 1640 with and without 1-10% HI FCS. Changes were analysed by colourimetric assessment, dynamic light scattering, zeta potential, static light scattering and transmission electron microscopy.

2.3.5.1 Static light scattering

Static light scattering (SLS) measurements were performed at 25 °C with an in-house system. The spectra were recorded at a 90° scattering angle using the halogen lamp light source. In all measurements, 100 µl of AuNP were mixed with 900 µl of the relevant solvent. A complete data point was an average of 5 measurements at 2 sec acquisition.

2.3.5.2 Dynamic light scattering

The hydrodynamic diameter of 20 nm AuNP was determined using Zetasizer Nano ZS (Malvern, UK). All measurements were performed at a concentration of 7×10^{10} particles/ml in a polystyrene semi-micro cuvette. Samples were equilibrated for 90 sec at 37 °C and illuminated with a 633 nm laser. The intensity of the scattered light was then measured at a 173° angle. All samples were measured in at least triplicate, with each data point recorded as an average of 12 measurements for 10 sec each. All solvents were filtered through a 20 nm syringe filter before use. Colourless RPMI 1640 (no phenol red) was used to avoid interference.

Table 2.3. A table of solvents and additives used for AuNP DLS analysis. "Mod + number" indicates an additive used for analysis. SP-A, SP-D and BSA were used at concentrations of 1, 5 and 10 µg per ml. All solvents were measured with nanoparticles as well as on their own.

Base solvent	*Mod 1*	*Mod 2*	*Mod 3*	*Mod 4*	*Mod 5*
Milli-Q water	+ No additives				
TBS^{Ca}	+ No additives	+ SP-A	+ SP-D	+ BSA	
TBS^{EDTA}	+ No additives	+ SP-A	+ SP-D	+ BSA	
RPMI 1640	+ No additives	+ SP-A	+ SP-D	+ BSA	1% HI FCS

2.3.5.3 Zeta potential

The zeta potential of 20 nm AuNP was determined using Zetasizer Nano ZS (Malvern, UK). All measurements were performed at an approximate concentration of 7×10^{10} particles/ml in the folded capillary cell. Prior to the measurement, AuNPs were preincubated in RPMI 1640 medium supplemented with 10% HI FCS. Then, particles were washed by centrifugation at 4000 × g, replacing the supernatant with 0.1x PBS (10 times diluted PBS solution) twice. After the last wash, the particles were centrifuged one more time and resuspended with 0.1x PBS, resulting in a ready-to-measure sample. Samples were equilibrated for 90 sec at 37 °C and then three measurements for each sample were taken at automatic settings. All solvents were filtered through a 20 nm syringe filter before use. Colour free RPMI 1640 (no phenol red) was used.

2.3.6 Quartz crystal microbalance

A quartz crystal microbalance (QCM; Attana AB, Stockholm, Sweden) was employed to test whether SP-A and SP-D can bind to the gold surface. A gold sensor chip was purchased from Attana AB. The running buffers were TBS^{Ca} and TBS^{EDTA}. The chip was fitted to the machine and allowed to stabilise for 1 h at 37 °C at a flow rate of 10 µl/min. The measurements were initiated when the resonant frequency was relatively stable (baseline drift <0.5 Hz/min). The protein (SP-A, SP-D and BSA) samples prepared in running buffers (10 µg/ml) were injected into Channel A of the instrument. The results were recorded and quantified as frequency variation (ΔHz) over time.

2.3.7 SP-A and SP-D adsorption to AuNPs

Gold nanoparticles at a concentration of 7×10^{10} particles/ml were washed once with Milli-Q water by centrifuging at 6,000 × g replacing the supernatant with TBS^{Ca} or TBS^{EDTA}, containing 20 µg/ml

of SP-A, SP-D or BSA. The mixtures were vortexed vigorously, placed into an ultrasonic bath for 5 minutes and mixed on the end-over-end mixer for 30 min at 37 °C. Then, mixtures were centrifuged at 4,000 × g for 30 min at 37 °C; supernatants were collected for further analysis. The pellets were washed in a relevant buffer, sonicated for 5 minutes and centrifuged again at 4,000 × g for 30 min at 37 °C; the wash step was repeated three times. Two negative controls, one without particles and another without proteins, were run in parallel. Supernatants were used to determine protein concentration using a Bradford assay; particles were analysed using SDS-PAGE. The workflow is schematically represented in **Figure 2.1.**

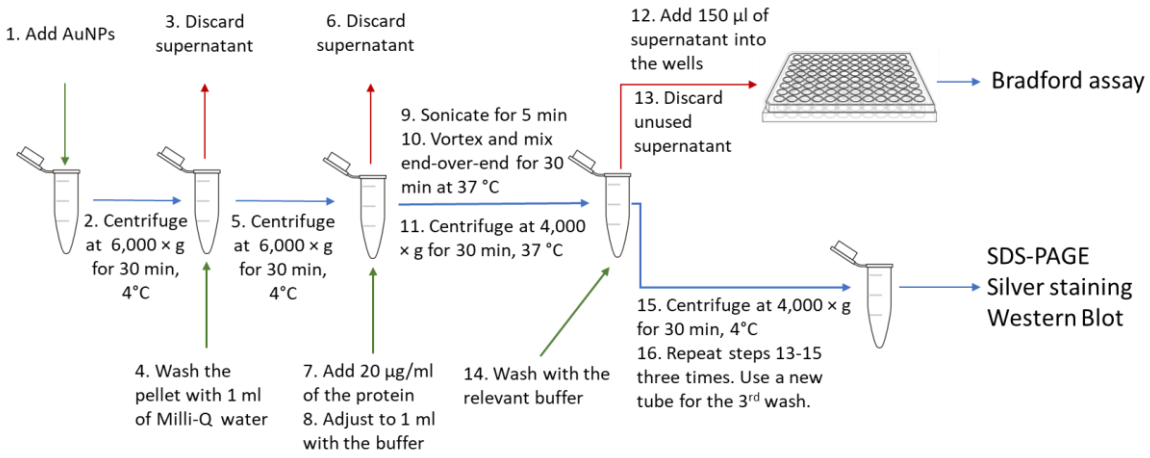

Figure 2.1. A summary of protein adsorption to AuNPs analysis. The particles underwent a series of washes to ensure only protein-particle complexes are in the solution. A Bradford assay was utilised to analyse supernatant and record the difference in concentration after incubation with particles. The SDS-PAGE assays were performed directly on the particles to confirm that proteins had bound to the particles.

2.3.8 Transmission electron microscopy

The morphology and size of both environmental and gold nanoparticles was analysed using transmission electron microscopy (TEM). 5 µl of PM_{10}, $PM_{2.5}$, $PM_{0.1}$ (5 mg/ml) and AuNP (7×10^{11}) were placed on formvar-carbon coated copper grids and left for 30 sec. The excess liquid was blotted with a torn filter paper. Samples were analysed using a Hitachi HT7700 transmission electron microscope (TEM).

2.3.9 Scanning electron microscopy

For the imaging of environmental nanoparticles, 13 mm round glass coverslips were stuck onto aluminium stubs using carbon tape. The surface of the coverslips was covered with a 7 nm

platinum layer using a sputter coater. Then, 50 µl of PM_{10}, $PM_{2.5}$, $PM_{0.1}$ were placed separately on coated glass coverslips and left to dry in the air for 30 min. The specimens were coated with a 5 nm platinum layer to improve conductivity. The analysis was performed using an FEI Quanta 250 scanning electron microscope (SEM) under high vacuum.

2.4 Cell culture model experiments

In all cell culture experiments that employed 96-well plates and required longer than 4 h incubation, the wells around the perimeter were not used for the experiments. Those wells were filled with PBS to avoid edge evaporation effect and to reduce the variability of results across the plate.

2.4.1 RAW264.7 cell line

The mouse leukemic monocyte-macrophage cell line[225] (RAW264.7) was routinely cultured in RPMI-1640 medium supplemented with 10% (v/v) heat-inactivated foetal bovine serum (HI FBS) and 1% (v/v) penicillin/streptomycin and incubated in a humidified atmosphere with 5% CO_2 at 37 °C. Cells were subcultured every 2-3 days, when the density of the cells reached 75-85% confluence, by scraping the cells and replacing with fresh medium in a ratio of 1:4.

2.4.2 Nanotoxicity tests

RAW264.7 cells were plated at a density of 1×10^4 cells per well in a 96-well tissue culture plate and incubated for 6 h in 200 µl growth medium at 37 °C with 5% CO_2 in a humidified atmosphere. After the cells adhered to the surface, the growth medium was replaced with reduced serum RPMI 1640 medium supplemented with 0.5% (v/v) HI FCS and incubated overnight. The nanotoxicity tests were performed by replacing the medium with a mixture of 20 nm AuNP or environmental particles at various concentrations in RPMI 1640 medium supplemented with 1% (v/v) HI FCS and the proteins of interest, SP-A and SP-D, at 1, 5 or 10 µg/ml, and incubated for 4 and 18 h. Bovine serum albumin (BSA) was used at the same concentrations as a reference protein. The medium with AuNP only, with the proteins of interest only, and the medium without particles and proteins were used as controls.

2.4.2.1 3-(4,5-dimethylthiazol-2-yl)-2,5-diphenyltetrazolium bromide (MTT) assay

The MTT assay was based on a previously reported method[226] and used with slight modifications. The MTT stock solution was prepared by dissolving the tetrazolium salt in serum-free RPMI 1640

medium to a concentration of 5 mg/ml, sterile filtering the solution through a 0.22 µm syringe filter, aliquoting into 1 ml sterile tubes and storing at -20 °C. The stock solution was further diluted with serum-free RPMI 1640 medium to a working concentration of 0.5 mg/ml.

After the incubation with nanoparticles (as explained in **Section 2.4.2**), the cells were washed with serum-free RPMI 1640 medium twice. Then, 100 µl of MTT solution was added and the cells were incubated for 2 h at 37 °C with 5% CO_2 in a humidified atmosphere. Following the incubation, The MMT solution was removed and replaced with 200 µl of DMSO, to dissolve formazan crystals, and incubated for 10 minutes or put into an orbital shaker at 400 rpm. Then, the whole plate was centrifuged at 4,000 × g and supernatants were transferred into a new 96-well plate. The absorbance was read at 540 nm using a Molecular Devices SpectraMax 340pc plate reader. All samples were run in triplicate.

2.4.2.2 LDH assay

A lactate dehydrogenase (LDH) cytotoxicity assay was performed on RAW264.7 cell and 20 nm AuNPs at 7×10^{10} particles/ml using a Pierce LDH Cytotoxicity Assay Kit. The assay was performed according to the manufacturer's recommendations. In brief, the cells were treated as described in **Section 2.4.2.** The cells were subdivided into three groups: spontaneous LDH activity controls (addition of 10 µL of Milli-Q water to one set of triplicates); maximum LDH activity controls (no additives); and chemical compound (the medium with AuNP and proteins of interest). The plate was incubated for 24 h at 37 °C with 5% CO_2 in a humidified atmosphere. After the incubation, 10 µL of Lysis Buffer (10X) were added to maximum LDH activity controls, mixed by gentle tapping and incubated for 45 min at 37 °C with 5% CO_2 in a humidified atmosphere. Then, 50 µl of each sample was transferred into a new plate and mixed with 50 µl of the reaction mixture and was protected from light, following the 30 min incubation at room temperature. After 30 min the reaction was stopped by the addition of 50 µl of stop reagent. The absorbance was measured at 490 nm and 680 nm. To determine LDH activity, the 680 nm absorbance value was subtracted from the 490nm absorbance before the calculation of cytotoxicity.

2.4.2.3 Reactive oxygen species (ROS)

The production of reactive oxygen species (ROS) was examined using the CellROX Deep Red reagent. The assay was performed according to the manufacturer's recommendations. In brief, the cells were treated as described in **Section 2.4.2.** After 4 h incubation with AuNP and proteins, CellROX Reagent was added to the cells at a final concentration of 5 µM and incubated for 30 minutes at 37 °C. After the incubation, the cells were washed with PBS three times and the

fluorescence was measured at $\lambda_{ex/em}$ 644/665 nm using a fluorescence microplate reader (FLUOstar OPTIMA, BMG Labtech).

2.4.2.4 Whole-cell protein immunoblotting

Whole-Cell protein analysis was performed to analyse the uptake of SP-A, SP-D and BSA by RAW264.7 cell line adsorbed to the surface of AuNPs. The cells were subcultured in a T25 tissue culture flask, as described in **Section 2.4.1**. When the confluence reached 70%, the cells were incubated overnight in reduced serum RPMI 1640 supplemented with 0.5% (v/v) HI FCS. Then, 7 ml of RPMI 1640 medium supplemented with 1% (v/v) FCS, containing:

1. 7×10^{10} AuNP/ml + 10 µg/ml SP-A
2. 7×10^{10} particles/ml + 10 µg/ml SP-D
3. 7×10^{10} particles/ml + 10 µg/ml BSA
4. 10 µg/ml SP-A
5. 10 µg/ml SP-D
6. 10 µl/ml BSA
7. Control with no additives

were added into corresponding T25 flasks with cells and incubated for 4 h in a humidified atmosphere with 5% CO_2 at 37 °C. Prior to the addition, all mixtures were vortexed and sonicated in a water bath for 5 min to avoid aggregates. After 4 h, the cells were washed five times with PBS, scraped and transferred into 1 ml tube.

A whole-cell SDS-PAGE was performed using the same methods as used during regular SDS-PAGE analysis, described in **Section 2.2.5**. Approximately 2×10^6 cells were used in each sample. Each sample was split into two equal parts and run on the gel in parallel. One gel was used for SimplyBlue staining and another for further western blot analysis. Western blot was performed as described in **Section 2.2.5.3**, where the same membrane was probed multiple times against SP-D, SP-A and BSA in the listed order (the order was chosen to avoid possible interference because of the same secondary antibodies used to probe SP-D and BSA).

2.4.3 Gold nanoparticle uptake

RAW264.7 cells were seeded onto pre-cleaned 13 mm circular glass coverslips in 24-well plates at a concentration of 5×10^4 cell/well and incubated in a humidified atmosphere with 5% CO_2 at 37 °C, to allow the cells to adhere to the surface of the plate. Prior to the experiments, the cells were incubated overnight in reduced serum RPMI 1640 supplemented with 0.5% (v/v) HI FCS. Then, 500 µl of RPMI 1640 medium supplemented with 1% (v/v) FCS, containing:

1. 7×10^9 AuNP/ml + 10 µg/ml SP-A
2. 7×10^9 particles/ml + 10 µg/ml SP-D
3. 7×10^9 particles/ml + 10 µg/ml BSA
4. 10 µg/ml SP-A
5. 10 µg/ml SP-D
6. 10 µl/ml BSA
7. Control with no additives

were added into corresponding wells with cells and incubated for 4 h in a humidified atmosphere with 5% CO_2 at 37 °C. Prior to the addition, all mixtures were vortexed and water bath sonicated for 5 min to avoid aggregates. After 4 h incubation, the cells were washed with PBS three times to aid removal of extracellular particles, fixed in 4% PFA for 10 min, washed with distilled water to remove any salts and mounted on a glass slide with mowiol. After the mowiol was set hard cured, the samples were analysed and semi-quantified with Coherent anti-Stokes Raman Scattering microscopy.

Another complementary experiment was run in parallel. RAW264.7 cells were subcultured in a T25 tissue culture flask, as described in **Section 2.4.1**. When the confluence reached 70%, the cells were incubated overnight in reduced serum RPMI 1640 supplemented with 0.5% (v/v) HI FCS. Then, 7 ml of RPMI 1640 medium supplemented with 1% (v/v) FCS and 7×10^{10} particles/ml were added to a flask and incubated for 18 h in a humidified atmosphere with 5% CO_2 at 37 °C. Prior to the addition, the suspension was vortexed and water bath sonicated for 5 min to avoid aggregates. Then the cells were washed with PBS three times to aid the removal of extracellular particles before being collected by trypsinisation. The cell suspension was centrifuged to replace trypsin with PBS and transferred to 1 ml tube, where the cells were fixed in 3% glutaraldehyde

and 4% PFA in 0.1 PIPES buffer at pH 7.2 overnight at 4 °C. The sample was then prepared for TEM and serial block-face scanning electron microscopy (3View), as described in **Sections 2.4.4** and **2.4.5**.

2.4.4 Transmission electron microscopy

Firstly, the cells were embedded into alginate to form an intact pellet.[227] To do so, the cells were vortexed and a drop of 5% (w/v) sodium alginate was added to the bottom of the tube using a Pasteur pipette and the suspension was centrifuged at 1250 × g for 5 min. The fixative (supernatant) was discarded and replaced with an equal volume of 0.1 M $CaCl_2$ and left for 15 min to form a gel. Then, the cells embedded into alginate were processed according to general TEM staining protocol (described **below**) or high contrast staining for 3View imaging (described in **Section 2.4.5**).

General TEM staining was performed using the standard protocol established within the Biomedical Imaging Unit at the University of Southampton. In brief, the sample was rinsed 2 × 10 min with 0.1 M PIPES buffer and incubated in post-fixative 1% (w/v) osmium tetroxide for 1 h, followed by 2 × 10 min washes in PIPES buffer and one brief rinse in Milli-Q water. Next, the sample was stained with 2% (w/v) uranyl acetate for 20 min. After staining, the sample was dehydrated in a graded ethanol series (30%, 50%, 70%, 95%, and 2 × 100%) for 10 min during each step. The pellet was infiltrated with acetonitrile for 20 min and 1:1 acetonitrile:Spurr resin mixture overnight. Finally, the sample was infiltrated with pure Spurr resin for 6 h and then polymerised in fresh resin for 16 h at 60 °C. All wash steps were performed at room temperature and with constant stirring on a rotator.

For TEM imaging, the resin was cut into ultrathin sections (<100 nm) with a Reich Om-U3 ultramicrotome. The thickness was determined by comparing the colour of a section with the ultramicrotome section colour reference chart. Cut sections were placed on TEM grids and imaged as normal with a Hitachi HT7700 TEM.

2.4.5 Serial block-face scanning electron microscopy

Similar to TEM processing, the cells were embedded into alginate first (as described in **Sections 2.4.4)**. High contrast staining was performed using the standard protocol established within the Biomedical Imaging Unit at the University Hospital Southampton. The samples were rinsed 2 × 5 min in cold 0.15 M sodium cacodylate and incubated in 0.15 M sodium cacodylate solution

containing 2% (w/v) osmium tetroxide, 1.5% (w/v) potassium ferrocyanide and 2 mM calcium chloride for 1 h at 4 °C. The samples were rinsed 3 × 5 min with Milli-Q water, incubated for 20 min in 1% (w/v) thiocarbohydrazide in water, rinsed 3 × 5 min again with Milli-Q water, and incubated in 2% (w/v) osmium tetroxide for 30 min. Then, rinsed 3 × 5 min with Milli-Q water and incubated overnight at 4 °C in 1% uranyl acetate, rinsed 3 × 5 min with Milli-Q water, incubated in 1% Walton's lead aspartate at 60 °C for 30 min, and rinsed 3 × 5 min with Milli-Q water. After staining, the sample was dehydrated in a graded ethanol series (30%, 50%, 70%, 95%, 100%, 100%) for 10 min during each step. The pellet was infiltrated with acetonitrile for 20 min and 1:1 acetonitrile:Spurr resin mixture overnight. Finally, the sample was infiltrated with pure Spurr resin for 6 h and then polymerised in fresh resin for 16 h at 60 °C.

Further steps were kindly performed by Ms Patricia Goggin (Biomedical imaging Unit, University of Southampton). The sample block was trimmed and mounted on an aluminium pin with conductive epoxy glue. 3View imaging was performed with a FEI Quanta 250 SEM in a high vacuum at 3700 times magnification and 50 nm section thickness step (50 nm of the top layer were cut after each image acquisition). A total of 500 images were acquired.

2.5 Mice model experiments

2.5.1 Animals

All procedures involving animals were approved by the UK Home Office and the local University of Southampton Animal Committee and conducted in accordance with the approved guidelines and the Personal License. Wild type C57BL/6 (WT), SP-D knockout (DKO)[116] and SP-A knockout (AKO)[228] mice were maintained in a specific pathogen-free environment, 12 h light/dark cycle, food and water *ad libitum* at the University of Southampton Biomedical Research Facility, before being transferred to Public Health England (PHE; Didcot, UK) and acclimatised for at least one week. The mice were aged between 22 and 26 weeks at the time of exposure. Both males and females were used.

2.5.1.1 Genotyping by the polymerase chain reaction

To confirm that mice with a correct genotype were used in the study, genotyping was performed prior to breeding and experiments. Genotyping was performed using a Phire Animal Tissue Direct PCR Kit according to the manufacturer's instructions. In brief, a 2 mm punch of mouse ear was placed in 20 µl of dilution buffer containing 0.5 µl of DNA Release Additive. The samples were

incubated at 65 °C for 5 min and then at 98 °C for 2 min, followed by cooling at 20 °C. The samples were spun down, and 1 µl of supernatant was used as a template in a 20 µl PCR reaction mix. The remaining supernatant was frozen at -20 °C.

Polymerase chain reaction (PCR) was performed using the PCR reaction mix with appropriate DNA templates and primers specific to AKO and DKO mice genotyping (**Table 2.4**). Positive controls of purified WT, AKO and DKO DNA were analysed in parallel. The PCR was undertaken with an initial incubation at 94 °C for 5 min, followed by 35 PCR amplification cycles:

1. Denaturation at 94 °C for 5 sec
2. Annealing at 63 °C (AKO) or 57 °C (DKO) for 5 sec
3. Extension at 72 °C for 30 sec

A final extension step at 72 °C for 1 min was undertaken after the amplification cycles.

Table 2.4. Primers used for PCR-based mice genotyping.

Genotype	Name	Sequence
AKO	3 sense neo	GTGGGGTGGGATTAGATAAATGC
	murine A sense 3	GCATTAGACGACAGAACTCCAGCC
	murine A antisense 2	TACTGAGAGATGTGTGCTTGGTGAG
DKO	SP-D share sense	TGGTTTCTGAGATGGAGTCGTG
	SP-D WT antisense	TGGGGCAGTGGATGGAGTGTGC
	SP-D neo KOantisense	GTGGATGTGGAATGTGTGCGAG

PCR products were analysed using agarose gel electrophoresis. The gel was prepared by dissolving 2% (w/v) agarose powder in 1x TAE buffer and pre-stained with SYBR Safe DNA Gel Stain. PCR products were mixed with 6x DNA gel loading buffer and separated by electrophoresis at 150 volts for 30 min using TAE buffer. To determine DNA sizes, a 1 kb Plus DNA Ladder was used.

A homozygous AKO genotype appeared as a single 400 bp band, WT genotype as a single 220 bp band and heterozygous genotype as two bands at 400 and 220 bp. A homozygous DKO genotype appeared as a single 220 bp band, WT genotype as a single 400 bp band and heterozygous genotype as two bands at 220 and 400 bp.

2.5.2 Inhalation of gold nanoparticles

The inhalation experiments were performed together with Dr Rachel Smith, Dr Matthew Wright and Dr Chang Guo (Public Health England, Didcot). The exposure system (inExpose, SCIREQ, Montreal, Canada) allowed 12 mice to be exposed nose-only to the aerosol generated via the Constant Output Atomiser (COA, Model 3076, TSI Incorporated, Shoreview, MN, USA) and was contained within a glovebox, held at a slight negative pressure (7.5 mbar) relative to the laboratory for safety purposes. Mice were restrained in individual mesh tubes and exposed to aerosolised AuNP (nominal size 20 nm) for 3 hours. The total aerosol flow generated from the COA was approximately 4 LPM, with the flow rate across the exposure system set to 2 LPM. The excess was directed to aerosol measurement instrumentation (Scanning Mobility Particle Sizer, SMPS, Model 3936, TSI Incorporated, Shoreview, MN, USA) at 0.3 LPM to allow online measurement of the aerosol mobility size distribution in the diameter range 15 – 660 nm during the exposures, and through a 37 mm polycarbonate filter (flow balance) via a vacuum pump, which collected a known volume of particulate matter for subsequent gravimetric mass and Au concentration analysis (via ICP-MS). Separate sampling onto TEM grid for subsequent analysis was undertaken using a Mini Particle Sampler (MPS, Ecomesure, Saclay, France).

2.5.3 Tissue collection

The mice were euthanised within 4 h and 1, 7, 28 days post-exposure via intraperitoneal injection of a lethal dose of sodium pentobarbital (200 µl). After the breathing had ceased and to confirm lethal anesthetisation, the rear paw of the mouse was pinched with forceps to check the foot reflex. If no reflexes where observed, the abdomen was cut opened and the renal artery of the left kidney was cut to allow exsanguination. Dissection and organ collection were then performed together with Dr Chang Guo and Dr Martin Leonard (Public Health England, Didcot). Liver, spleen, kidney and lungs were collected into pre-weighed 5 ml tubes and frozen at -20 °C. Lung lobes were used for: BALF collection (left lobe), multimodal and TEM imaging (cranial lobe), inductively coupled plasma mass spectrometry (ICP-MS) (middle, caudal, and accessory lobes) and thus were collected in a specific order described above and **Figure 2.2**.

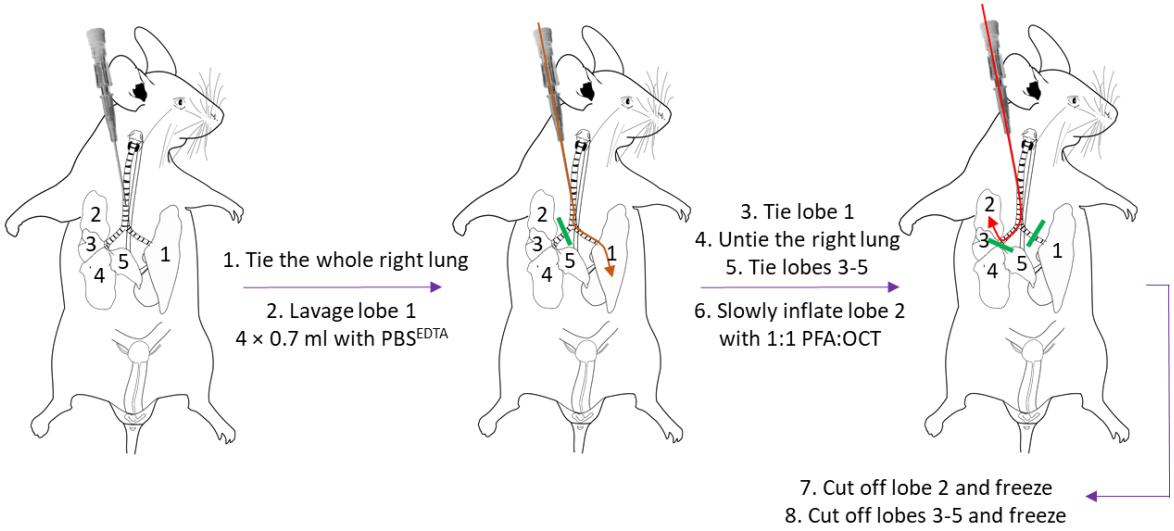

Figure 2.2. A schematic illustration of single lobe lavage and single lobe inflation. After the BALF collection, the right lobe was not used for further studies. Lobe 2 was collected for TEM and multimodal microscopy imaging. Lobes 3-5 collected for ICP-MS. Numbers on the image: **1** – left lobe; **2** – right cranial lobe; **3** – right middle lobe; **4** – right caudal lobe; **5** – accessory lobe. The orange arrow represents the flow direction of PBS^{EDTA}; red – 1:1 mixture of 8% PFA in OCT. The image was adapted from Portal et al[229] distributed under CC BY 4.0 license.

The dissection process was performed following a standard protocol established within Dr Jens Madsen's group with modifications developed specifically for this study. After the mouse was confirmed dead, it was placed on its back on a dissection board, fixed by pinning down the limbs and sprayed with 70% ethanol. The abdominopelvic cavity was exposed by midline incision through the skin and connective tissue, making two lateral cuts and a cut up to the neck, exposing the trachea. The renal artery was cut to ensure termination of the mouse but also to drain the blood, followed by kidney, spleen and liver collection. The diaphragm was punctured to collapse the lungs first, and the ribcage was then removed, fully exposing the thoracic cavity. The trachea was carefully punctured between two cartilage rings with an 18 G cannula, and the catheter was inserted halfway down. The right bronchus was tied with a surgical thread with a single knot. The left lobe was lavaged with 4 × 0.7 ml with PBS supplemented with 0.1 mM EDTA (PBS^{EDTA}) and collected BALF was temporarily stored (less than 5 h) on ice. Then, the left bronchus was tied and right untied, while the bronchi leading to the middle, caudal, and accessory lobes were tied. A 1:1 mixture of 8% PFA:OCT was slowly injected into the cranial lobe, inflating the lung. The lobe was cut off, placed into a mould with pure OCT, frozen on an aluminium block on dry ice and then

transferred into -80 °C freezer. Remaining lobes were collected into pre-weighed 5 ml tubes and frozen at -20 °C.

Collected BALF was mixed with 10x RBC lysis buffer resulting in 10% (v/v) mixture, incubated for 5 min on ice, diluted 5 times with PBS^{EDTA} and centrifuged at 200 × g for 5 min. All but ~20 µl of the supernatant was removed. The cells were resuspended in the remaining fluid and cytospun onto #1.5 20 mm circular coverslips, fixed in 4% PFA for 10 min, washed in distilled water and mounted on a glass slide with mowiol. Once the mowiol had cured, the cells were analysed with multimodal microscopy within three months.

2.5.4 Tissue analysis

2.5.4.1 Inductively coupled plasma mass spectrometry

The clearance and biodistribution of 20 nm AuNPs in lung, kidney, liver, and spleen were analysed by inductively coupled plasma mass spectrometry (ICP-MS) in both standard solution and time-resolved single particle mode (spICP-MS) and single-particle (SP)-ICP-MS. All mass spectrometry analyses were performed by Dr Adam Laycock. Tissues were collected straight in pre-weighed tubes. The tissue mass was determined by subtracting the mass of pre-weighed tubes from the tubes with the tissue. All samples were homogenised (IKA T-10 basic ULTRA-TURRAX disperser) in 50 mM ammonium bicarbonate buffer.

For total metal ICP-MS analysis, half of the homogenised samples were added to 10 ml polytetrafluoroethylene microwave digestion vessels and acidified to 10% HNO_3. All samples were digested by microwave-assisted high-pressure acid digestion system (UltraWave, Milestone Srl, Italy). Digested samples were diluted to 5% HNO_3 using Milli-Q water prior to analysis. At the start of each measurement session a series of gold standard solutions were prepared in 5% HNO_3 for analysis by ICP-MS (iCAP Q ICP-MS, Thermo Scientific). The resulting calibration curve was used to determine the mass of gold in each sample.

For spICP-MS lung tissue samples were enzyme-digested using a protocol adapted from Loeschner et al[230]. The Proteinase K solution was prepared by dissolving the enzyme to a concentration of 6 mg/ml in 50 mM ammonium bicarbonate buffer (pH 7.4) with 1 mg/ml SDS. The second aliquot of the homogenised tissue was doubled in volume from the addition of the Proteinase K solution. The mixtures were incubated at 37 °C overnight in a water bath until no tissue fibres left. As a blank sample, unexposed mouse tissue was used at treated using the same procedure. Samples were analysed by spICP-MS in time resolved mode. For each sample, ^{197}Au signal intensity was

monitored and data was acquired for 60 sec using dwell time of 0.4 ms. A threshold value of 20 counts per dwell time was used to distinguish baseline noise from particle events, this equated to a minimum size of detection of about 19.5 nm.

2.5.4.2 Laser ablation inductively coupled plasma mass spectrometry

Laser ablation inductively coupled plasma mass spectrometry (LA-ICP-MS) analyses of lung sections mounted on microscope slides were undertaken using a New Wave Research NWR213 laser ablation system (Electro Scientific Industries, Portland, Oregon, USA) coupled to an iCAP Q ICP-MS (Thermo Fisher Scientific, Hemel Hempstead, UK). For laser ablation the following conditions were used: 50 µm diameter laser spot size, fluence 2 J/cm^2, scan speed 178 µm/s and repetition rate of 20 Hz. Helium was used as the cell gas which was run as a flow rate of 0.8 ml/min. The ICP-MS was used in KED mode with helium as the collision gas. The isotopes monitored were ^{13}C, ^{56}Fe, ^{65}Cu, ^{66}Zn and ^{197}Au. The dwell time used for each isotope was 0.07 s.

2.5.4.3 Tissue imaging

For the lungs TEM imaging, the samples were stained, cut and analysed using the same method as described in **Section 2.4.4**, without alginate embedding only.

For multimodal non-linear microscopy, frozen lung lobes embedded into OCT were cut into 14 µm sections on a cryostat at -30 °C. The sections were collected onto square 22 x 22 mm #1.5 coverslips, fixed in 4% PFA for 20 min, washed in distilled water to remove excess salts with OCT and mounted onto a glass slide with mowiol. Once the mowiol had cured, lung sections were analysed with multimodal microscopy (described in **Section 2.6**) within 3 weeks.

2.6 Multimodal imaging: CARS, SHG, TPF

The multimodal non-linear microscopy system was built in-house by researchers in the BioNanoPhotonics group in the Institute of Life Sciences (B85, Highfield Campus, University of Southampton) and allowed simultaneous image acquisition with Coherent anti-Stokes Raman Scattering (CARS), Second Harmonic Generation (SHG) and Two-Photon Fluorescence (TPF). The imaging system was equipped with a fibre laser (1031 nm, 2 picoseconds, 80 MHz, Emerald Engine, APE) which used as a Stokes beam, and the output of an optical parametric oscillator (OPO) (APE, Levante Emerald, 650–950 nm) which is synchronously pumped by the second harmonic (516 nm) of the fibre laser, is used as a pump beam. The two beams are made collinear and then coupled through a galvanometric scanner into an inverted microscope (Nikon Ti-U),

where it is focussed onto the sample by an objective. The scattered radiation is collected in epi-mode, it passes through a set of filters that are selected to transmit CARS (643 ± 20 nm), SHG (400 ± 10 nm) and TPF (520 ± 20 nm) signals and detected by a corresponding photomultiplier tube. Cells and tissue samples were imaged at a C-H (found in the long tails of fatty acids) stretching frequency of 2845 cm^{-1} with the OPO adjusted to 797.7 nm. SHG and TPF signals were collected in parallel using the same settings. Samples were imaged with a 40x/1.2 NA Nikon water immersion objective, with an additional 6x (for cells) or 3x (for lung tissue) optical zoom using galvanometric scanning. The images were taken at 512×512 pixel resolution, 32 µs pixel dwell time and 3 averages with a total incident power on the sample of approximately 60 mW (40 mW pump, 20 mW Stokes) for cells and 90 mW (60 mW pump, 30 mW Stokes) for tissue unless otherwise stated.

2.6.1 Image analyses

All image processing and analysis were performed using Fiji software.[231] All scripts used to assist image analysis are provided in **Appendix B**. Brightness and contrast was automatically adjusted for all images. For single images, it was done applying automatic balance. The brightness and contrast of images in the stack was adjusted according to a reference image, a manually chosen image with the highest contrast (determined by eye). Then all images were balanced with automatic settings using the reference image.

Image quality was assessed by measuring the signal to noise ratio of a region of interest to the background. A single 3 pixels wide straight line was drawn across an area of interest, such as the cells and background (**Figure 2.3**). Then, “plot profile” was used to produce a pixel intensity graph. The signal to noise ratio was assessed by analysing the pixel intensity difference between the image features (cells) and background.

Before the quantitative analysis of AuNP inside cells and tissue, all multichannel images (images with CARS+SHG or CARS+SHG+TPF channels) were split into single-channel images. The process was semi-automated with a script. For AuNP quantification, only the SHG channel was used, as particles were visible there, while other channels were used to distinguish the outline of a cell. First, images were thresholded, applying the intermodes method with automatic settings. Then, images were despeckled to remove background noise. Finally, using the “freehand selection” tool, a region of interest (the cell outline) was selected, and the number of pixels was measured inside it. The quantification process was semi-automated with a script for image stacks. The data was exported as a sum of pixels within the area of interest of all slices.

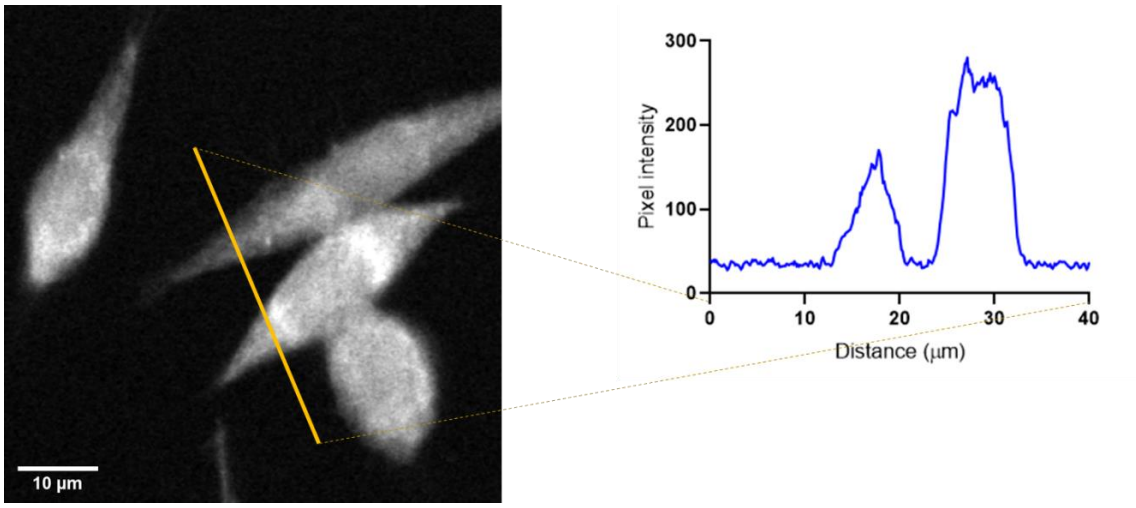

Figure 2.3. RAW264.7 TPF signal to noise ratio measurement. The straight yellow line defines the region of pixel intensity measurement. The chart shows the ratio between the background noise and signal from the cells.

To measure the diameter of 20 nm AuNP on TEM micrographs, a built-in "analyse particles" tool was used. Images were automatically thresholded using the intermodes method first. Watershed was applied to separate particles with merged edges. If particles were separated incorrectly or the overlap resulted in a significant size alteration, they were manually excluded from quantification by masking them on the image. To exclude imaging artefacts, only particles with the circularity of 0.5-1 and ≥10 nm diameter were analysed.

The 3View image was reconstructed using Trainable Weka Segmentation to visualise the distribution of nanoparticles within the cells. The software was trained on three randomly selected slices to distinguish nanoparticles from other elements on the image. An equal number of particles and background elements were randomly selected in each image with a line tool. The model was trained based on these features: gaussian blur, maximum, minimum, entropy and variance. Because of the large number of images and their weight, the analysis was performed using Galileo cloud computing software (Hypernet labs, California, USA).

2.7 Statistical analysis

GraphPad Prism 8 (San Diego, CA, USA) was used to create graphs and perform statistical analyses. Data distributions were tested for normality using the D'Agostino-Pearson test and statistical significance was tested using one-way analysis of variance (ANOVA) for samples following a normal distribution, or the Kruskal-Wallis for samples not following normal

distribution (unless otherwise stated). Differences were considered statistically significant at $p \leq 0.05$. Only statistically significant differences are indicated in the figures where appropriate.

2.8 Augmented reality and QR codes

All augmented reality (AR) features were added using Zapworks (Zappar Ltd) software. Only images which have a QR code in their caption have AR features. The QR codes were generated automatically by the software and are unique for each figure or page. In order to reveal the AR features the reader should follow the steps:

1. Download the QR code scanner (use “QR scanner” keywords on any app store) on any mobile device, such as phone or tablet. NB: Modern phones have in-built scanner in standard camera app.
2. Scan the code. The code will reveal the link. Tap on the link.
3. Once you open the link, a browser page will load. Hit “launch” and point on the page.
4. Once you scan the page, the AR elements should reveal.

Chapter 3 Application and optimisation of multimodal label-free microscopy for imaging of gold nanoparticles

3.1 Introduction

Multimodal imaging is a combination of different techniques used to acquire complex and information-rich images from a biological tissue or any other samples. Such an approach is used to overcome the limitations of independent techniques. The multimodal images may be acquired asynchronously, and then merged manually through image processing techniques, or synchronously, where images from multiple techniques are recorded and merged automatically. Asynchronous imaging allows the application of a greater number of imaging techniques on the same sample, but post-processing (i.e. aligning and merging) presents a range of constrictions. The synchronous acquisition is limited in the selection of tools, however, it is quicker and requires fewer manipulations during the image analysis.

Multimodal imaging systems that utilise intrinsic sources of contrast, rather than exogenous labels, allow for the non-destructive and non-invasive characterisation of biological samples in their native state, and the features of synchronous acquisition and analysis are of great interest both in fundamental research and clinical diagnostics.[232,233] The majority of chemically selective techniques (i.e. fluorescence spectroscopy and imaging, near-infrared spectroscopy, Raman spectroscopy)[234–236] lack tissue penetration, contrast or imaging speed. Non-linear microscopy is emerging as an alternative and popular non-invasive, label-free imaging tool. The three major types are coherent anti-Stokes Raman scattering (CARS), second-harmonic generation (SHG), and two-photon fluorescence (TPF) microscopies, which can operate as a synchronous multimodal system.[237] In some applications CARS/SHG/TPF multimodal imaging proved to be an alternative to haematoxylin and eosin staining for pathological screening[238], and was even explored as neural network-aided automated breast cancer detection tool[239].

The imaging of nanoparticles is not a straightforward process, even on their own and not within biological samples, as they are too small to be visualised with light microscopy techniques. The "gold standard" imaging method for nanoparticles is electron microscopy, as it provides the best resolution and details. However, it requires time-consuming sample preparation and staining with hazardous heavy metals. Additionally, it cannot be performed *in vivo*, as it is an invasive and destructive method. While CARS, SHG or TPF are being applied for NPs imaging (see **Section 1.4**),

there is still little research on applying multimodal setups for the visualisation, tracking and quantification of NPs.

In this chapter, the application and optimisation of CARS, SHG and TPF as a single synchronous imaging system for the visualisation of cells and tissue is shown. Additionally, semi-selective imaging of the 20 nm AuNPs within the biological samples using a multimodal imaging system is explored. The current work establishes the utility of label-free, non-invasive, and non-destructive imaging for the detection of AuNPs in biological samples.

3.2 Aims and objectives

This chapter addresses the aims and objectives summarised in clause 1 of **Section 1.5**, which are:

1. Develop multimodal imaging methods, based on CARS, SHG and TPF for the label-free imaging of gold nanoparticles (AuNPs) inside the cells.

1.1. Optimise the system for the imaging of single cells and tissue slices.

1.2. Apply the optimised system to detected 20 nm AuNPs within biological samples.

3.3 Methods

All methods used in this chapter are detailed in **Chapter 2**.

3.4 Results

3.4.1 Optimisation of imaging parameters

Initial imaging optimisation was performed using CARS with only 40 µm polystyrene beads. Polystyrene is not SHG and TPF active, thus there was no corresponding signal collected and the corresponding data are not shown. The images were acquired at pump and Stokes lasers set at equal powers – 30 mW, with a total power of 60 mW on the sample, 40x objective magnification and additional 6x digital zoom (**Figure 3.1**). To produce a 3D image, the beads were scanned from top to bottom with 1 µm step between slices (**Figure 3.2**). The very top and very bottom out of focus images were excluded. The stack was reconstructed into a 3D image (**Figure 3.2**, scan the QR code). The ability to reconstruct a 3D image was essential for future cell imaging and the quantification of particles inside the cells.

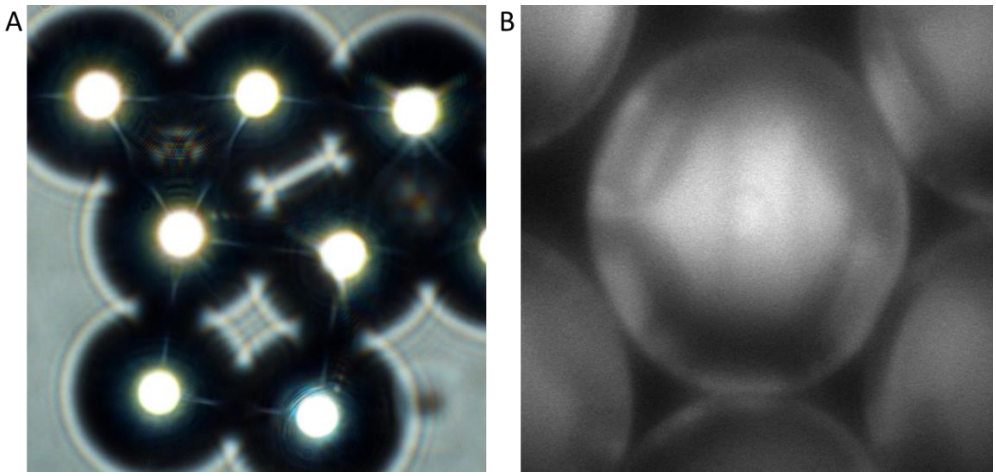

Figure 3.1. An image of 40 µm polystyrene beads. A – a bright-field image; **B** – a CARS image.

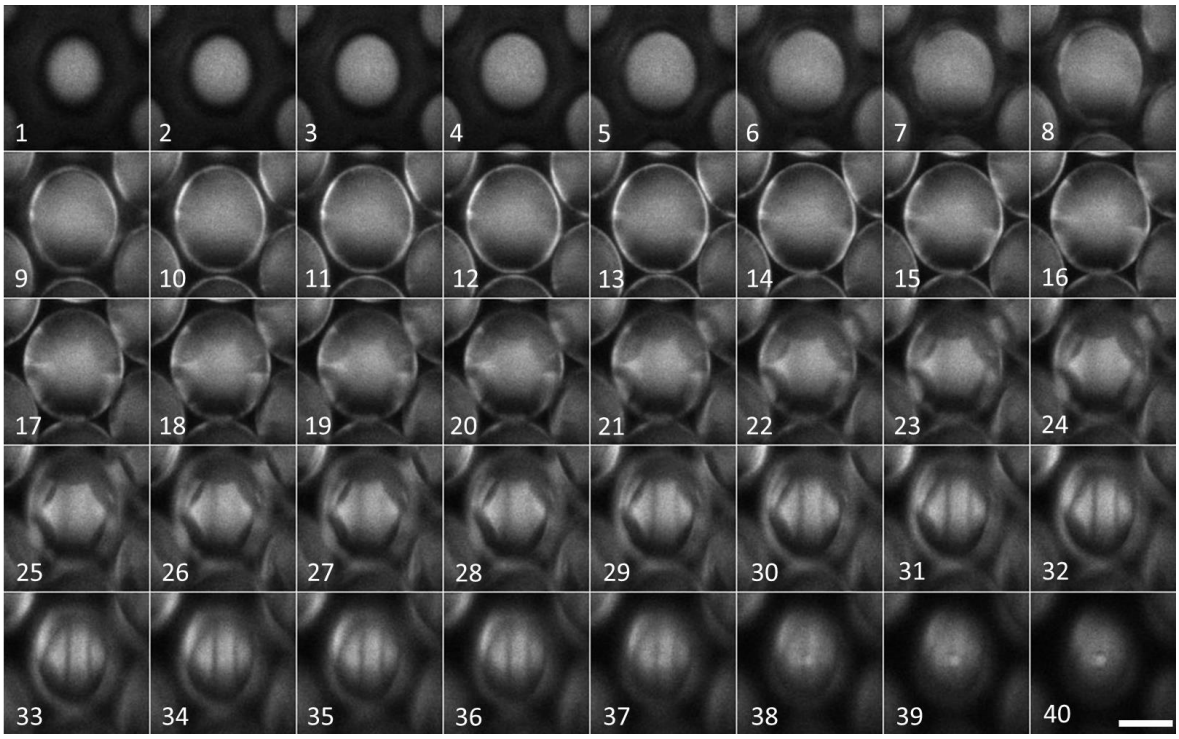

Figure 3.2. A montage of 40 µm polystyrene particles stack imaged with CARS in a Z-stack mode with 1 µm step. The image was acquired at 400x magnification, 6x digital zoom and 60 mW total laser power (1:1 pump:Stokes). Scale bar – 20 µm. Reconstructed and animated version available via supplementary data.

The next step was to optimise the imaging of single cells by adjusting the power ratios between the pump and Stokes laser beams. The imaging was performed for CARS and TPF channels. The data for the SHG channel was not shown, as RAW264.7 cells do not contain enough SHG active molecules that can be detected by the system. The total laser power was constantly kept at about 60 mW and only pump:Stokes power ratios were varied from 0:60 mW to 60:0 mW, respectively

(**Figure 3.3**). When one of the lasers was shut down (0 mW), no images were acquired in the CARS channel. In the TPF channel, the cells were seen, however with a significantly reduced contrast compared to when both lasers were on. Based on the visual assessment, it is required to have the pump laser at higher power than the Stokes to achieve better CARS quality, while in TPF this parameter had less influence.

After the initial visual assessment, a straight line was drawn at a random location and pixel intensity values were measured. The heat-map presented in **Figure 3.4** displays normalised grey values (1 highest pixel intensity, 0 no signal) supports the visual assessment of the imaging quality. In both CARS and TPF, the sampling profiles with one of the lasers off are very different compared to the profiles with both lasers switched on. In CARS, the images were absent if a laser was off. The quality improved significantly when the pump laser's power was equal or greater than Stokes', which can be observed by a more homogenous signal on the heat-map and an improved signal-to-noise ratio within the cell areas. In TPF, the images had reduced contrast when a laser was switched off, while in other cases, irrespective of laser power ratios, the quality was equally good. Pump:Stokes power ratios from 1:1 to 5:1 were equally suitable. It was decided to use 2:1 for all further imaging.

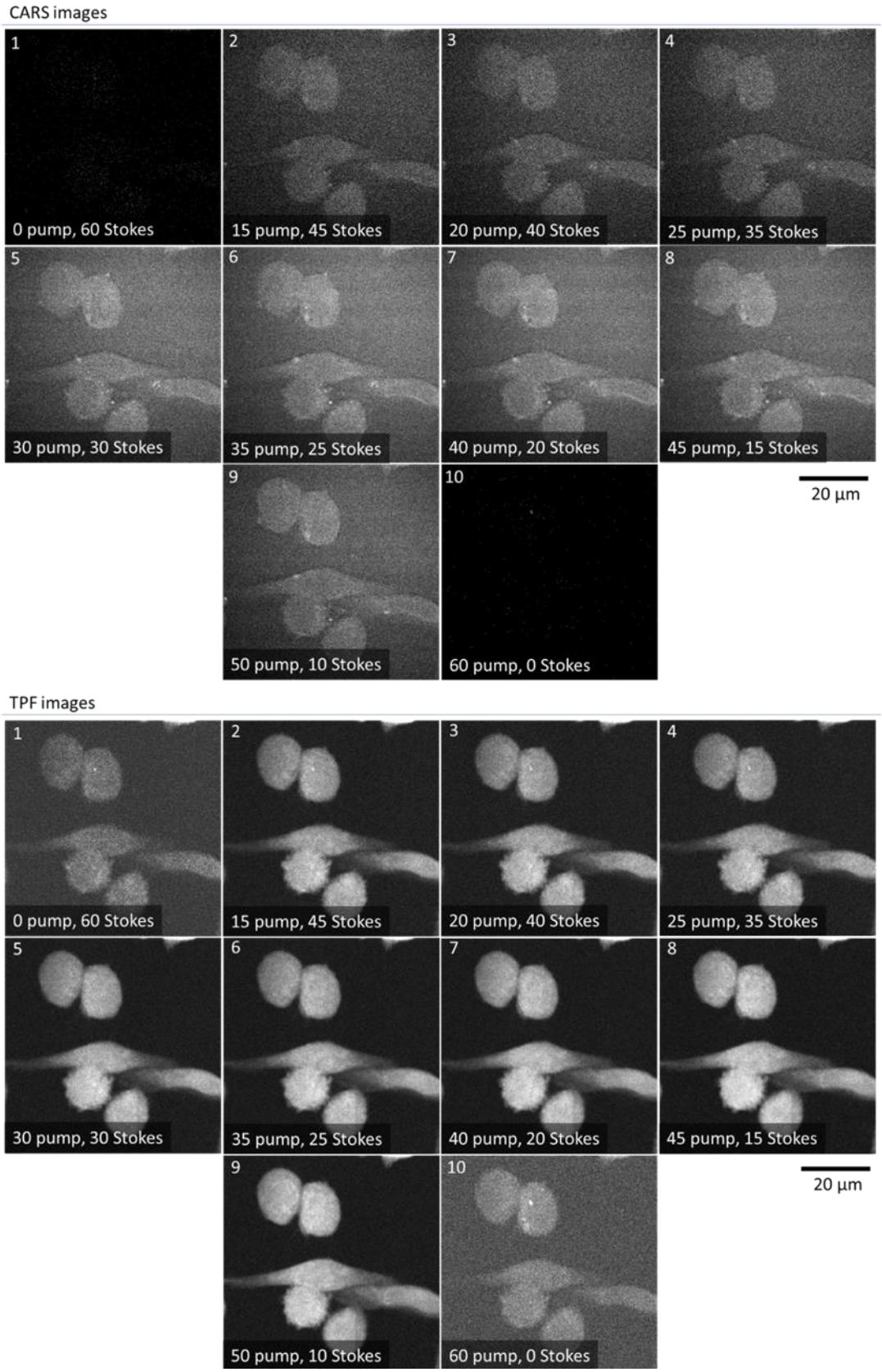

Figure 3.3. Dependence of RAW264.7 cell line image quality based on the varying pump:Stokes power ratios. The upper 10 images correspond to CARS channel, the lower 10 to TPF channel.

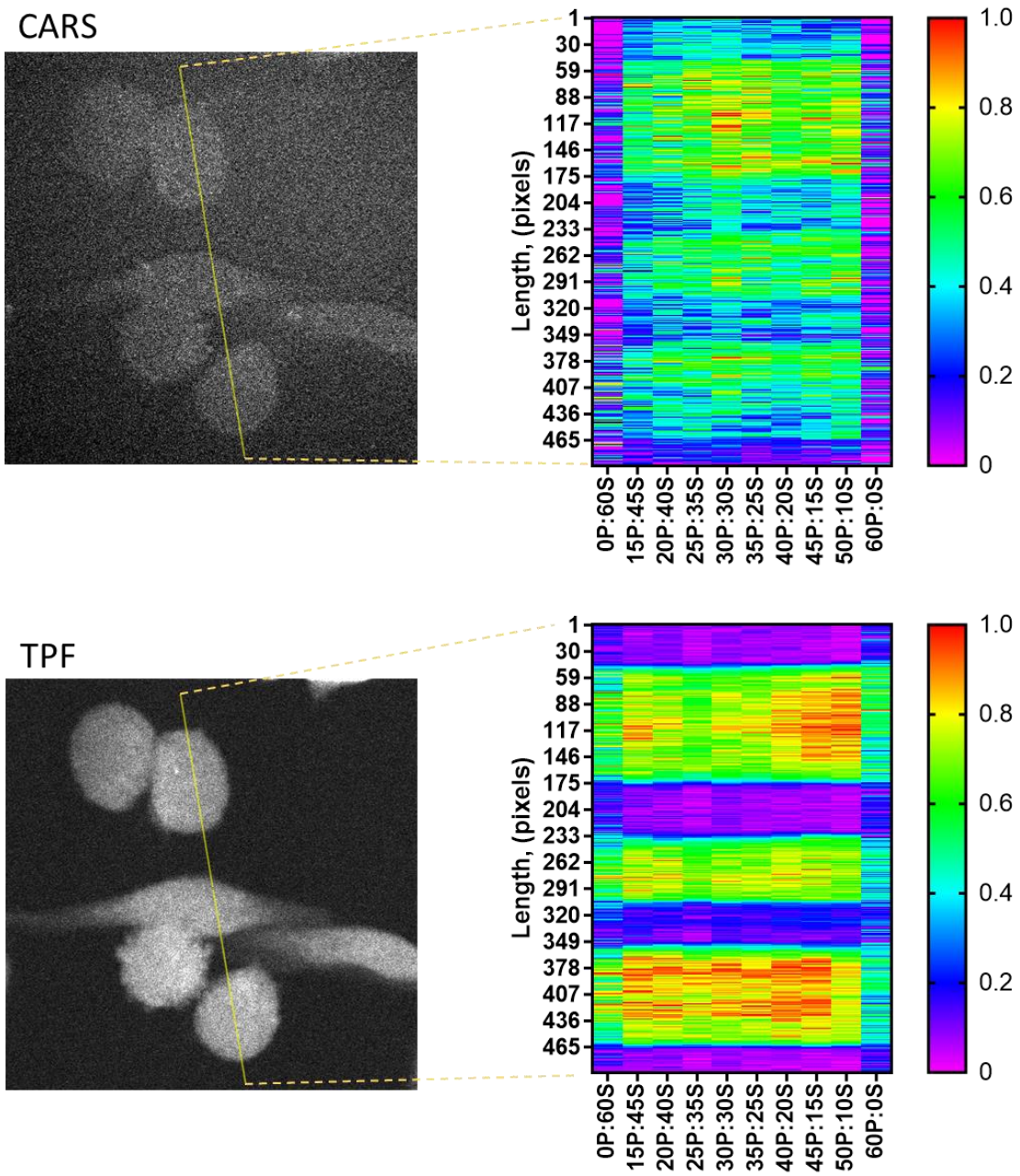

Figure 3.4. Evaluation of RAW264.7 cell line images acquired at the varying pump:Stokes power ratios. The yellow line displays the sampling area and is the same for all CARS and TPF images. Heat-map displays normalised pixel intensity across the sampling area.

The pixel dwell time (PDT; the time the focused laser beam illuminates a single pixel) was then optimised to reduce the photodamage. The images were acquired at 8, 16, 32, 64 and 128 µs PDT and 512×512 resolution (**Figure 3.5**). With an increase of PDT, the image quality significantly improved for CARS and slightly for TPF. At 64 and 128 µs, PDT imaging artefacts started to appear (horizontals lines in CARS and diagonal in TPF). It was decided to use 32 µs PDT for all further imaging.

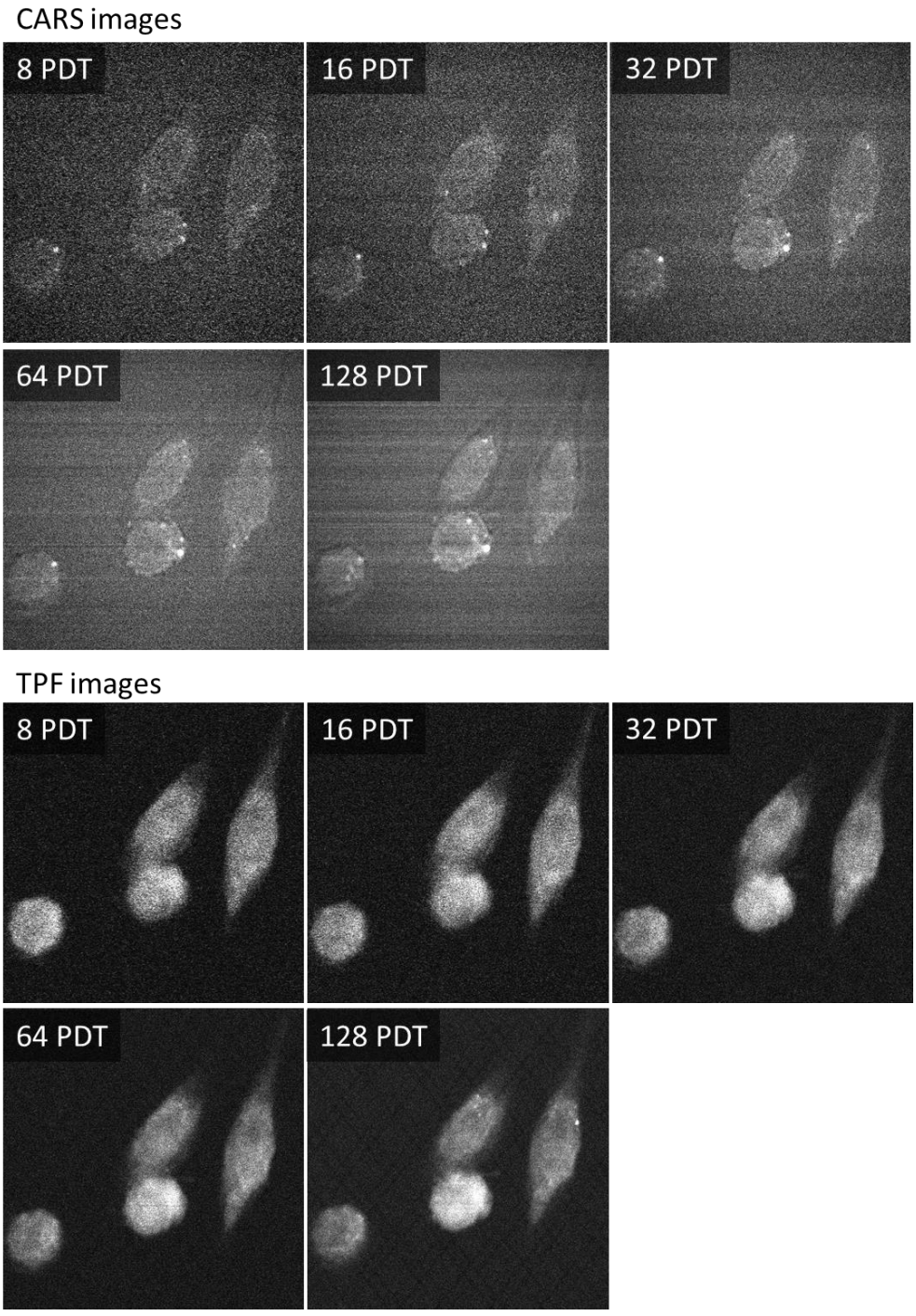

Figure 3.5. Dependence of image quality based on pixel dwell time. The upper 5 images correspond to CARS channel, the lower 5 to TPF channel. PDT corresponds to pixel dwell time in microseconds (μs).

Finally, the optimal image averaging value (the number of images taken of the same area followed by their averaging into a single image) was explored to reduce random noise (**Figure 3.6**). With an increase in the number of averages the quality also improved. According to the visual evaluation, the CARS images had an acceptable quality with at least 4 averages, which can also be seen on the

heat-map where distinct warm colour zones (>0.5 pixel value) appear in the range of 43-127 and 210-300 pixels (corresponds with the location of the cells). While for TPF even a single image without averaging resulted in a high contrast image. It was decided to use 3 averages for all further imaging.

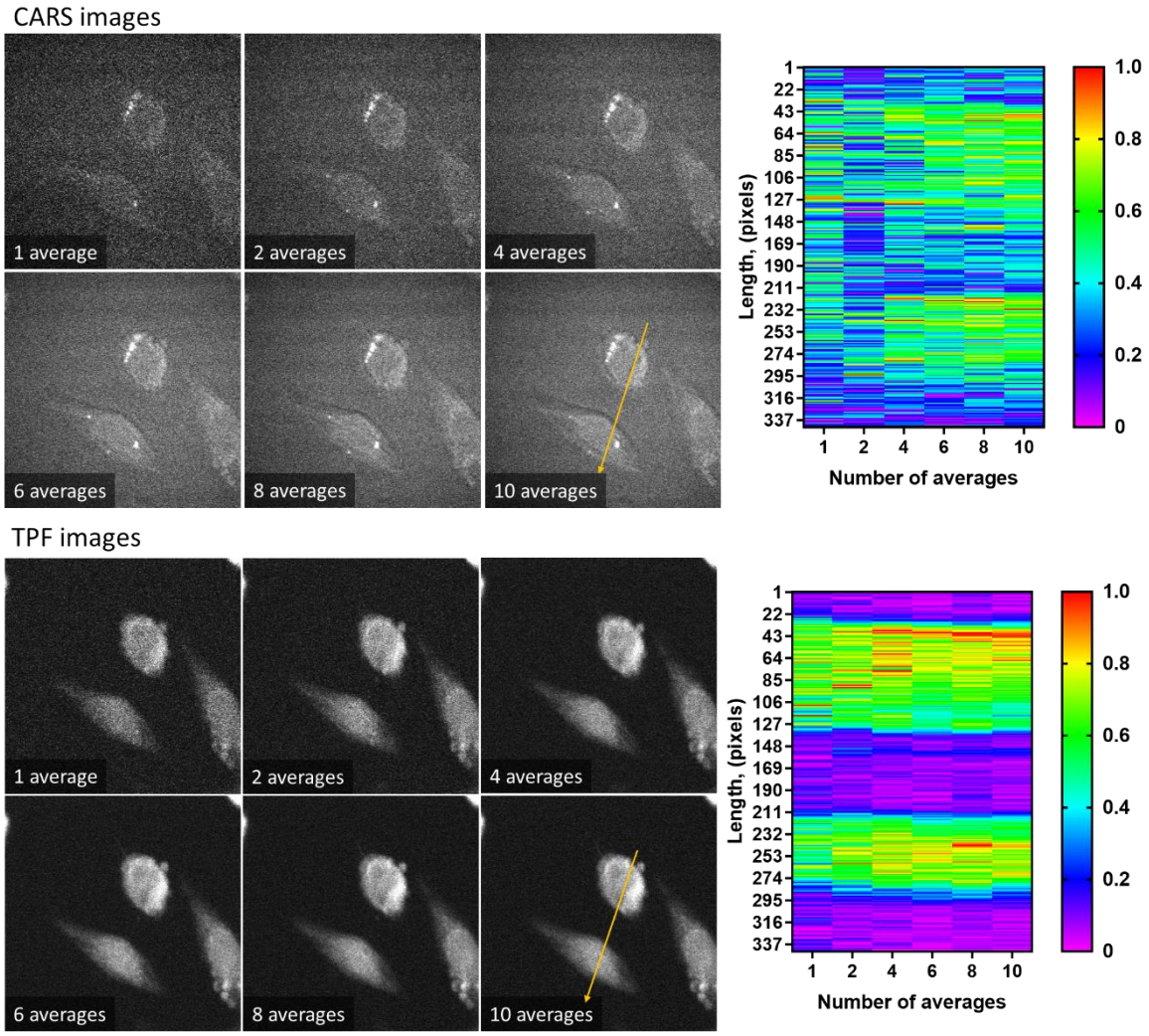

Figure 3.6. Dependence of image quality based on the number of averages. The images were acquired at 8 µs PDT and 40:20 mW pump:Stokes. The heat-map shows normalised pixel intensity values of each image. The yellow arrow shows the sampling area and the direction.

The photobleaching was assessed to ensure continuous exposure did not influence the signal output and thus the image and data quality. After acquiring the images required for the experiments, a few random images were assessed by reducing the zoom by one value (from 6x to 5x) and scanning a new larger area. In CARS the area from previous imaging had no differences in

grey values compared to the previously unexposed area outside of the yellow square (**Figure 3.7**). However, the signal in the TPF channel dropped by nearly 50% (**Figure 3.7F**).

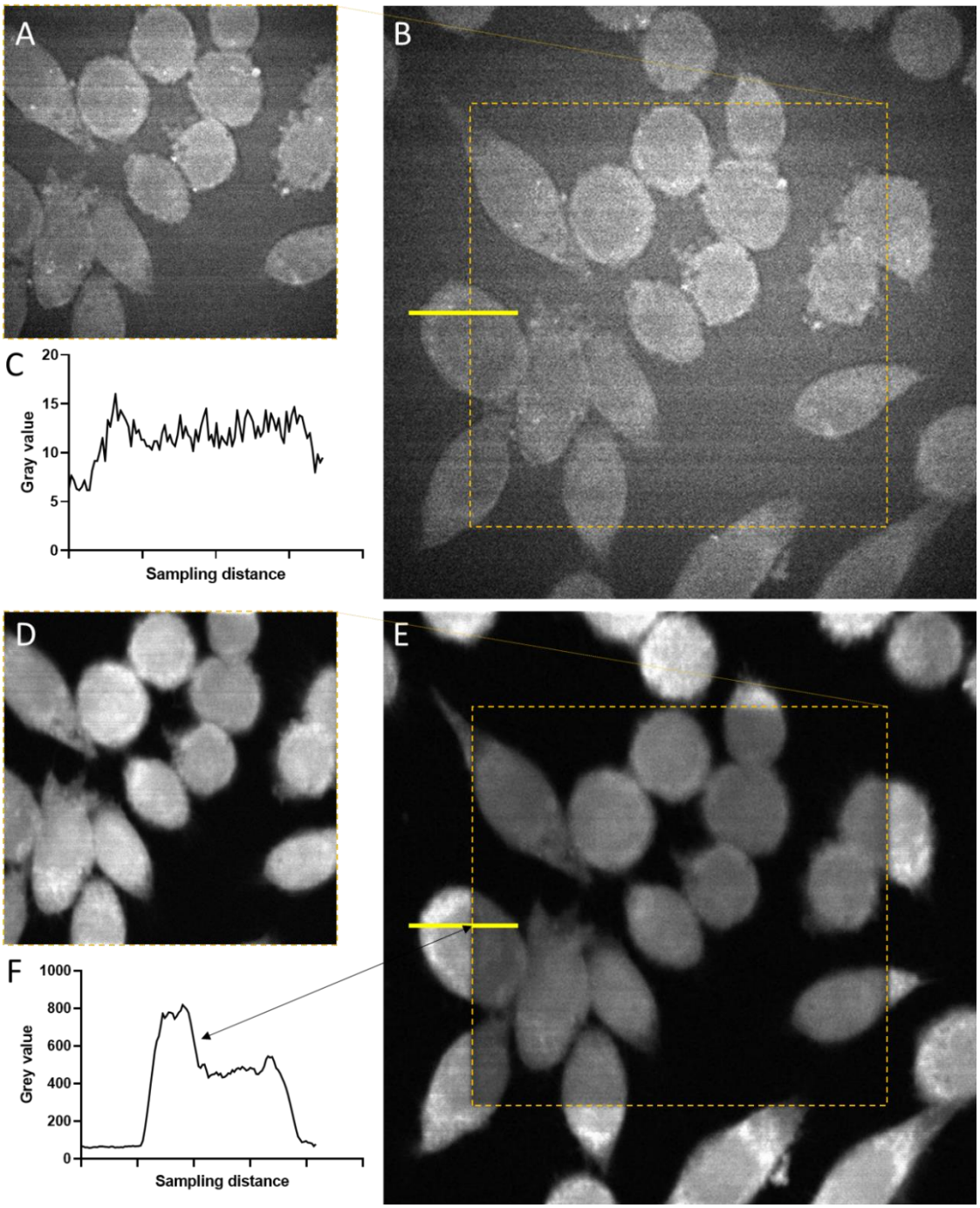

Figure 3.7. Photobleaching of RAW264.7 cells. A – an area of interest imaged with CARS at 6x zoom, **B** – the same area at 5x zoom an image later, **C** – pixel intensity graph corresponding to the sampling area (yellow line); **D** – an area of interest imaged with TPF at 6x zoom, **E** – the same area at 5x zoom an image later, **F** – pixel intensity graph corresponding to the sampling area. The arrowheads point to where the pixel intensity drops.

3.4.2 Imaging of AuNPs in cells and tissue

Multimodal imaging was then used to see whether it is possible to visualise 20 nm AuNPs taken up by RAW264.7 cells. After a few trial experiments with standard conditions (see **Section 2.6**), severe photodamage was noticed which led to the destruction of the cells (**Figure 3.8**). Thus, for the imaging of all cells treated with AuNPs the total laser power was reduced by 50% and PDT was set at 8 µs.

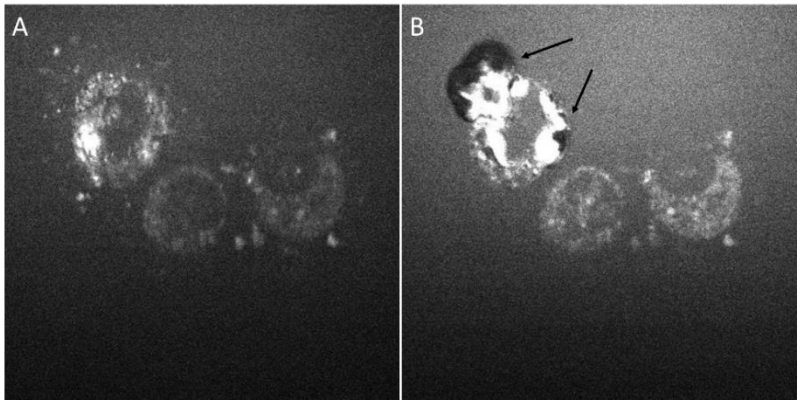

Figure 3.8. A representative image of RAW264.7 cell photodamage. A – intact cells, no photodamage; **B** – photodamaged cell, black arrows indicate burning (bubbling) sites.

There were no AuNPs observed in CARS channels, while there was a strong signal in SHG and TPF channels (**Figure 3.9**). There was no interference for any endogenous cell molecules in SHG channel and AuNPs were resolved without any interference and background signal, while in the TPF channel they were overlapping with cell's autofluorescence.

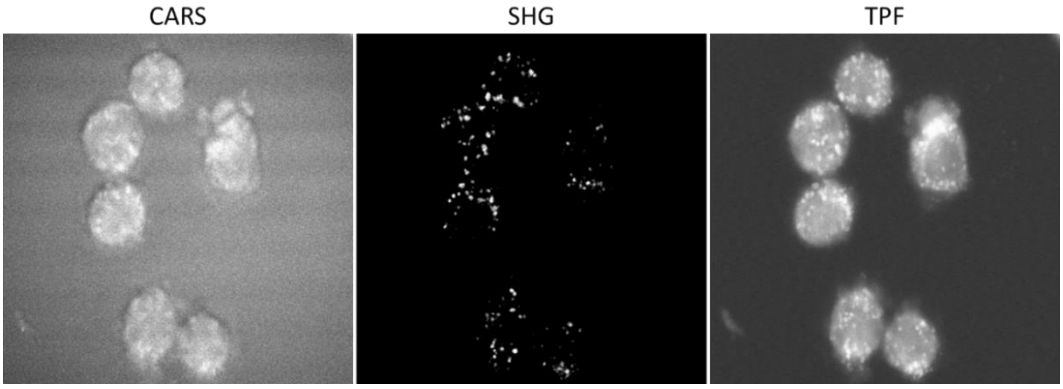

Figure 3.9. Multimodal images of RAW264.7 cells exposed to 20 nm AuNPs. The data is recorded in the form of 3 individual images corresponding to CARS, SHG and TPF imaging channels. The images are presented as a Z-stack of 15 images. Bright spots within the cells in the SHG and TPF images correspond to 20 nm AuNPs aggregates. Animated versions available via supplementary data.

As there were no cell borders seen in the SHG channel, the images were combined with CARS, TPF or both channels (**Figure 3.10**). Merging CARS and SHG channels proved enough to see the boundaries of the cells, while TPF + SHG resulted in much better contrast and image details. The combination of all three channels did not have any extra benefit and CARS images were not used.

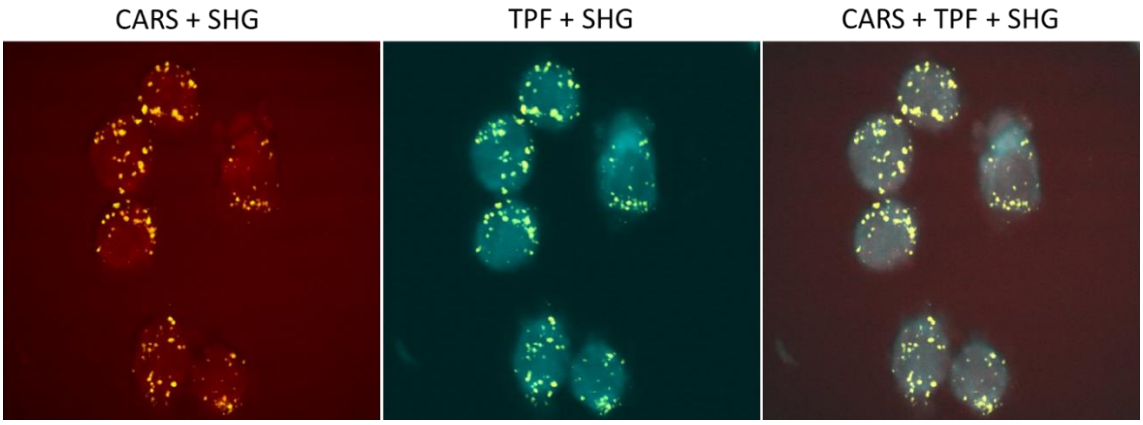

Figure 3.10. Composite images of RAW264.7 containing 20 nm AuNPs acquired with the multimodal imaging system. False coloured. Red – CARS, yellow – SHG, cyan – TPF. Animated versions available via supplementary data.

The cells, exposed to the same amount of AuNPs under the same conditions, were analysed with TEM to assess the morphology and distribution of AuNPs aggregates within the cell (**Figure 3.11A**). The majority of particles clustered into circular aggregates, ranging from several particles per aggregate to several hundred (visible per cell slice). 3View images were acquired to see the distribution across the whole cells (**Figure 3.12**). Due to lower magnification, it was not possible to resolve individual particles, however, it allowed for the assessment of the distribution of larger aggregates within cell. The images suggest that there was no translocation into the nucleus and particles were contained within the cytoplasm. Additionally, **Figure 3.12B** allows the visualisation of the size distribution of all aggregates.

The multimodal imaging was applied for lung tissue imaging. Due to practical limitations, it was not possible to obtain mouse lung tissue with the guaranteed presence of AuNPs. Thus, AuNPs were artificially deposited onto the lung slices (wild type mouse) by dipping the tissue into an AuNPs suspension (7×10^{10} particles/ml) for 1 min and blotting or washing the excess with water. However, no particles were observed in samples washed with water (**Figure 3.13**), either due to their absence or interference with the tissue's autofluorescence. The samples which were only blotted were not suitable for imaging as the tissue burned instantly. Despite numerous attempts, it was not possible find the balance between the concentration of AuNPs and/or incubation times, as all tested combinations resulted either in an indistinguishable signal or severe burns.

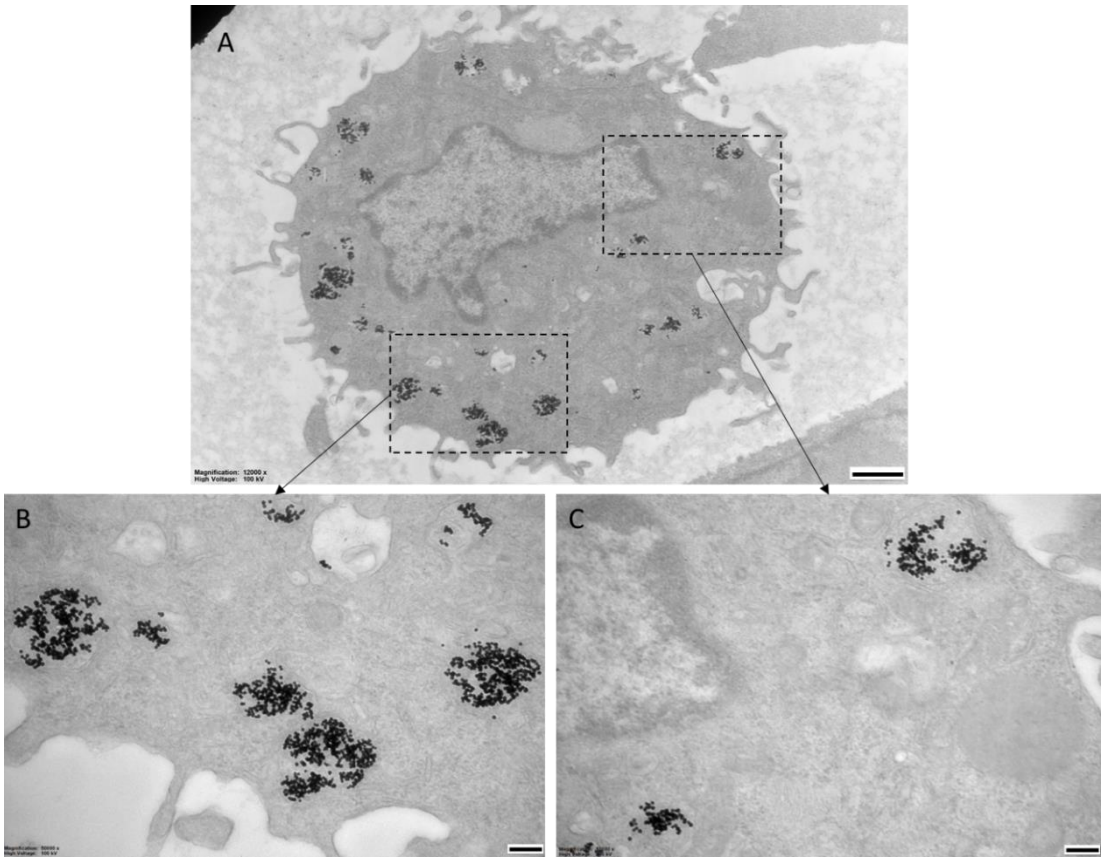

Figure 3.11. Transmission electron microscopy image of RAW264.7 cell incubated with 20 nm AuNPs. **A** – a representative image of a cell with AuNPs aggregates within the cytoplasm at 12.000 times magnification, scale bar – 1 µm; **B** and **C** – 50.000 times magnified areas showing the morphology of AuNPs aggregates, scale bar 200 nm.

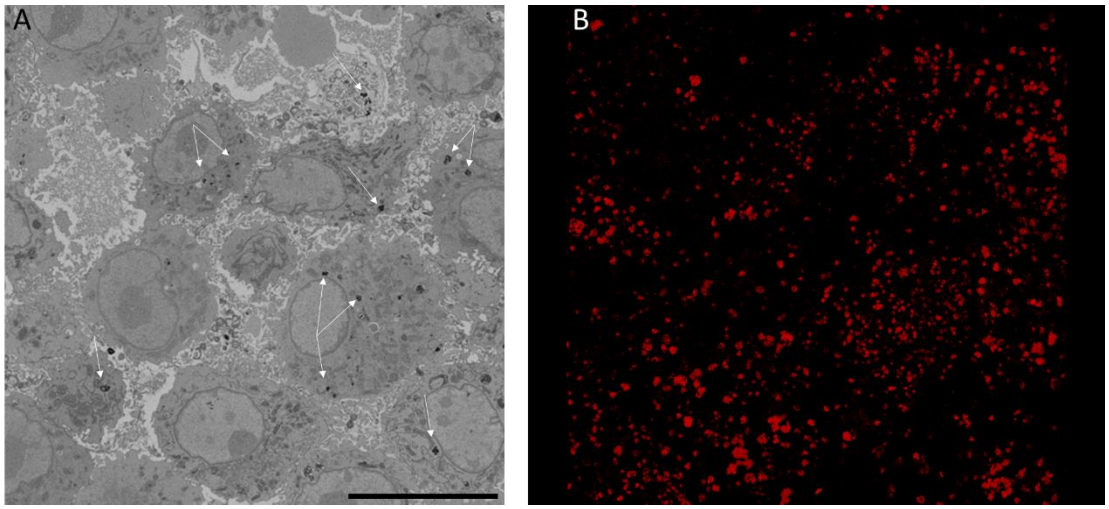

Figure 3.12. 3View images of RAW264.7 cells incubated with 20 nm AuNPs. **A** – a representative 3View image (1 of 500). Arrows point at selected AuNPs aggregates. **B** – Z-stack projection of all 20 nm AuNPs isolated from 3View image. Animated versions available via supplementary data.

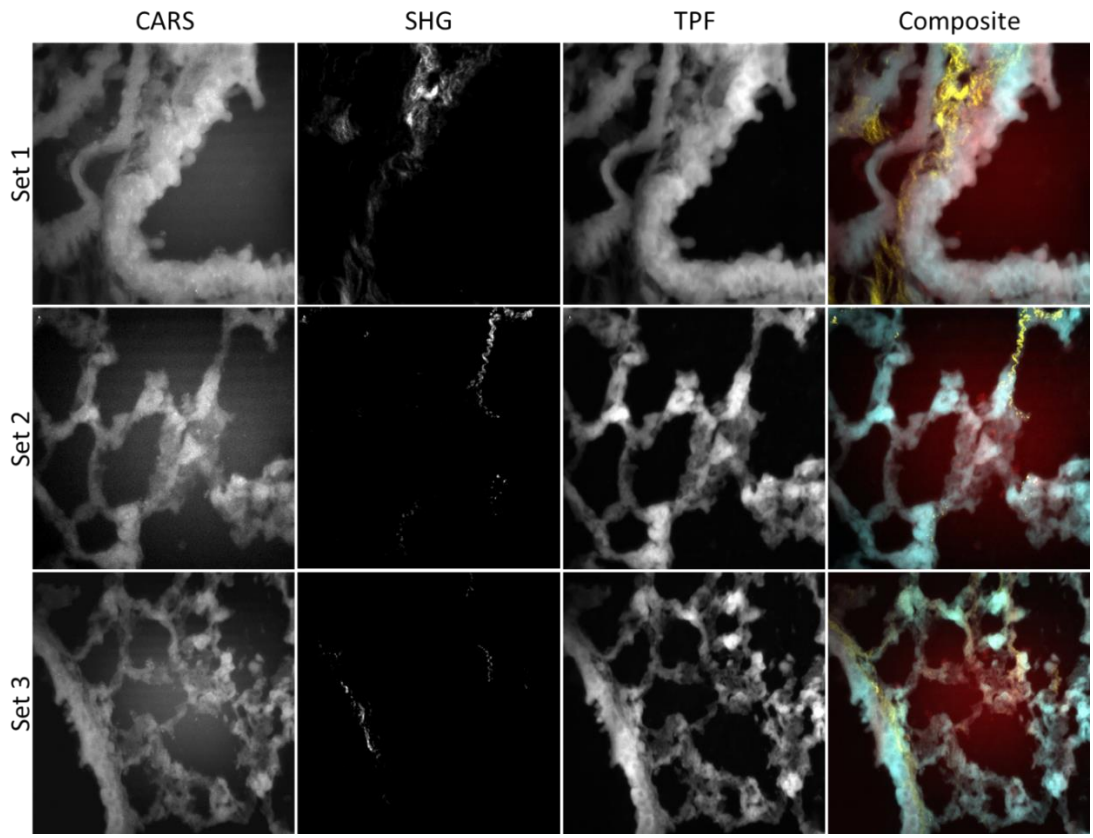

Figure 3.13. Representative images of mouse lung tissue incubated with 20 nm AuNPs. Mouse lung tissue imaged using CARS, SHG and TPF channels. Composite false coloured images are presented as CARS in red, SHG in yellow and TPF in cyan. Images were taken using 40x objective and x4 digital zoom.

3.5 Summary of the results

Within this chapter, non-destructive and label-free CARS, SHG, and TPF techniques were applied in the form of synchronous multimodal microscopy for the imaging of the biological samples. The system was utilised for 2D and 3D imaging to localise and characterise 20 nm AuNPs within the single cells and tissue, thus addressing Aim 1 (**Section 1.5**):

1. Develop multimodal imaging methods, based on CARS, SHG and TPF for label-free imaging of gold nanoparticles (AuNPs) inside the cells.

The main results and achievements reported in this chapter are:

- The synchronous multimodal imaging system was successfully optimised for label-free single cells and tissue imaging with no or minimal photodamage (**Table 3.1**). It is the first time when such a setup was used for AuNPs imaging within single cells.
- CARS imaging of single cells demonstrated a low signal-to-noise ratio and low contrast imaging AuNPs, hence the power was enough to see the cell's outline (membrane) only.
- SHG allowed semi-selective imaging of AuNPs within single cells.
- TPF was the most suitable for the imaging of single cells. It provided the best signal-to-noise ratio when imaging the cells and internalised AuNPs.
- TPF and SHG composite images were found to be the best combination for the visualisation of AuNPs within single cells.
- CARS, SHG and TPF provided high signal-to-noise ratio imaging lung tissue samples. However, no combination allowed selective imaging of AuNPs within the tissue.
- The size and morphology of AuNPs aggregates visible on multimodal microscopy images was characterised and correlated with those visible on TEM micrographs.
- The reliability of 3D multimodal microscopy images for localisation of AuNPs within the cell was supported by 3View micrographs. It is the first time when reconstructed images from multimodal microscopy were directly compared with 3View images.

Table 3.1. Primary settings for multimodal microscopy imaging for different samples.

	Pump laser	Stokes laser	Pixel dwell time	Number of averages
For the cells without AuNPs	40 mW	20 mW	32 µs	3
For the cells with AuNPs	20 mW	10 mW	8 µs	3
Lung tissue	10-80 mw	10-80 mW	8-32 µs	1-3

3.6 Discussion

3.6.1 Optimisation of imaging parameters

The abundance of lipids in biological systems combined with their strong CH_2 stretching vibration signal makes them a preferred target for qualitative and quantitative CARS imaging.[240] While there is a considerable number of articles available on CARS studying lipids, different researchers use different imaging parameters, such as laser power or pixel dwell time, which is often difficult to replicate since most CARS imaging systems are built in-house and perform differently. Thus, 40 µm polystyrene beads were always used before each experiment as a reference sample to calibrate the system and verify the origin of the signal, as polystyrene is a polymer rich in aliphatic bonds which ensures a strong CH_2-related signal. They were also used to test CARS in 3D imaging mode. Since all particles were approximately the same size (40 µm), 40-50 images with 1 µm step were required to reconstruct a full image, as is shown in **Figure 3.2**, demonstrating that the system can both penetrate the sample and produce 3D images.

As the main goal was to apply CARS in imaging of the cells and tissue, further optimisation steps were performed with the RAW264.7 cell line. While all the imaging was performed in multimodal mode (simultaneous acquisition of CARS, SHG and TPF signals), the SHG signal was not shown, as there were no SHG active molecules detected. Most of these molecules are either not produced by RAW264.7 cells or below the detection limit. As can be seen in **Figure 3.3** and **Figure 3.4**, there was no CARS signal when the pump or Stokes lasers were off, as expected. CARS occurs when a target molecule is irradiated using two laser beams, a pump beam (ω_P) and a Stokes beam (ω_S). When these beams interact with the sample and the difference between ω_P and ω_S equals the vibrational frequency, CARS signal is generated at a frequency $\omega_{CARS} = 2\omega_P - \omega_S$.[241] The images were grainy (high noise) at 15:45, 20:40 and 25:35 mW of pump:Stokes, while the quality significantly increased after 30:30 mW. The best quality was at about 2:1 ratio, which also could be predicted by the ω_{CARS} equation above.

The image quality of TPF did not have much of a difference when the ratios were changed, as TPF emission relies on a single laser. In essence, a fluorophore with an excitation wavelength of λ_{max} is excited with two photons with double the wavelength of $2\lambda_{max}$, which is often used in flavin adenine dinucleotide (FAD) and nicotinamide adenine dinucleotide (NADH) imaging in metabolism studies[217,242] or label-free imaging studies[243]. Specifically, to excite FAD with TPF at λ_{max} 450 nm, the sample has to be irradiated with two 900 nm photons resulting in emission at about 550 nm (**Figure 3.14**). The signal from the TPF channel was collected using 520/20 nm bandpass filters

(allows the passage of waves between 510 and 530 nm), which allows for the collection of FAD emission signal. Since the imaging system is set at 797.2 nm (pump) and 1031 nm (Stokes), the pump and Stokes excite the molecules with λ_{max} at 398.6 nm and 515.5 nm, respectively. This corresponds to FAD for the pump, but the Stokes is out of range and excites neither FAD nor NADH. However, when both lasers are on, their spatiotemporal overlap provides an additional excitation route for two-colour two-photon excited fluorescence, which is equivalent to having a third virtual laser – λ_v – providing the two-photon excitation at $\lambda_v = \frac{1}{2}(\lambda_1 + \lambda_2) = 914.1$ nm,[240] which is a wavelength required for TPF excitation of FAD at 457 nm. Hence, the simultaneous excitation with pump and Stokes lasers targets the maximum excitation absorbance and yields a stronger signal. It is possible to further increase the emission signal by changing the filter from 520/20 nm to a 550/20 (or broader) bandpass filter, altering the laser wavelengths, and even differentiating FAD and NADH, which has been done by other researchers[240,242], but this is beyond the scope of this study and the achieved results were sufficient to move forward.

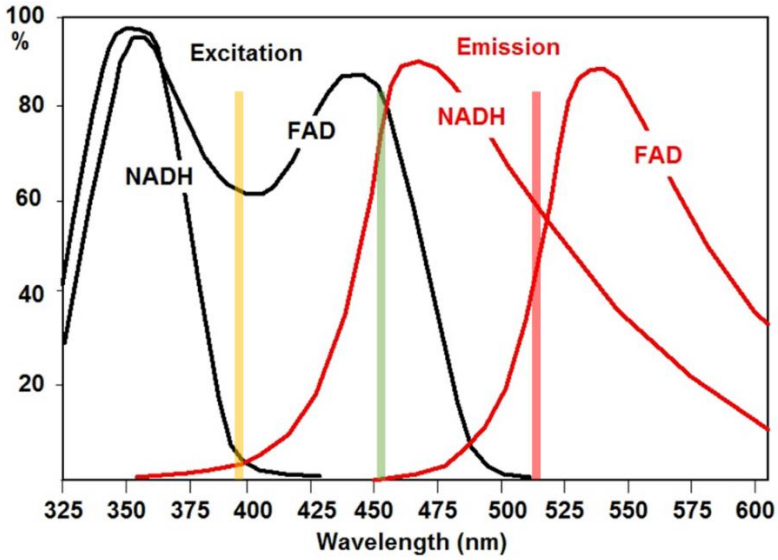

Figure 3.14 Excitation and emission spectra of NADH and FAD. Vertical lines correspond to excitation wavelengths induced by the multimodal imaging setup lasers. Yellow – excitation wavelength for pump, red – excitation wavelength for Stokes, green – excitation wavelength for virtual third laser. Reprinted and adapted with permission from Becker & Hickl GmbH[244].

The pixel dwell time was analysed as a part of imaging optimisation and results are shown in **Figure 3.5**. This is an important parameter as it affects the speed of image acquisition and the quality of the image, which is directly related to any possible photodamage due to prolonged sample illumination. Pixel dwell time is a parameter that describes the duration of the laser beam

when focused on a single pixel. The higher the PDT, the more photons can be collected from the actual sample, but the slower the scan speed. Samples with a low concentration of molecules of interest produce noisy images, however, a longer photon collection time overcomes this. As can be seen, there was a significant improvement in the quality for CARS at 32 µs PDT, but no significant difference for TPF. At higher PDT imaging artefacts appeared, which were most likely associated with computer's processing power. While for a single image high PDT values might be acceptable, they become impractical for Z-scans or high throughput imaging. For example, it takes about 8.4 sec to scan an image at 512×512 pixels resolution and 32 PDT. Doubling the PDT also doubles the scan time and increases the risk of photodamage (an example of photodamage can be seen in **Figure 3.7**). Additionally, the time will be greater multiplied by the equivalent number of image averages and Z-stacks taken, if any.

Image averaging is a processing technique used to increased signal to noise ratio for images corrupted by random noise. The process works by calculating an average for the pixel intensity in the set of images. Each image has a stable signal (i.e. cells, cellular structures, NPs) and random noise. The image signal has a stronger influence over the noise's average, and since the noise is random it is cancelled out during the averaging process. Such image processing results in an enhanced signal, while the noise tends to be reduced by a factor approximately equal to the square root of the number of images averaged.[245] While it was expected that the more averages taken, the better quality will be, the main goal of **Figure 3.6** was to determine the least number of averages required to balance the quality and acquisition time. While even at a single image cell outlines could be distinguished, the heat map shows that the least number of averages for CARS was 4 in order to see a clear numerical difference between the cells and background. There was little difference for the TPF, however in the case of ≥2 averages the signal was more consistent, compared to a single image.

As it was discussed in **Section 1.4.3**, during TPF imaging a part of the energy is absorbed by a sample, which in turn might lead to photodamage. To test this, RAW264.7 cells were exposed to standard imaging conditions during the routine imaging process. After acquiring an image at 6x digital zoom, the subsequent image was acquired at the identical area and settings, but 5x zoom instead. The results shown in **Figure 3.7** indicate that no photobleaching occurred in CARS, as expected, which is in agreement with previously published studies[190]. However, the overall difference between the noise and signal is relatively low and might be not noticed in the case of minor signal degradation. At the same time, TPF resulted in an almost 50% pixel intensity reduction between the first and the second images. While it might appear as a significant

reduction, this is still at least an order of magnitude higher than the background and has little effect on the signal to noise ratio during qualitative analysis. While TPF is known to cause photobleaching, it is less severe compared to confocal microscopy. Moreover, TPF provides optical sectioning for 3D imaging, but in contrast to confocal microscopy there is no photobleaching and phototoxicity above and below the plane of focus.[246]

One of the significant achievements and improvements of imaging process optimisation is that the system was upgraded and optimised to work in a synchronous mode, where the images from multiple channels were recorded simultaneously and overlaid in real time. In the previous studies in order to acquire images from two different channels the system parameters had to be changed between two image acquisitions, leading to increased photodamage risk and more complicated image analysis.[8]

3.6.2 Imaging of AuNPs in cells and tissue

During the initial imaging of RAW264.7 treated with AuNPs, most cells suffered severe photodamage under standard imaging conditions (**Figure 3.8**). This was associated with localised surface plasmon resonance (LSPR), which has a high light-to-heat conversion efficiency. When metal NPs are exposed to the electromagnetic field, they undergo charge separation due to the collective oscillation of free surface electrons, induced by incident light of a specific wavelength. This collective motion of surface electrons generates heat.[247,248] Such photothermal properties are used in photothermal therapy (PTT) for the treatment of tumours. Gold NPs are delivered inside to the tumour tissue and irradiated with a near-infrared laser, increasing the surrounding temperature to 50-70 °C which leads to the death of tumour cells.[249,250] However, these photothermal effects are undesirable during the imaging. The sample can be irreversibly destroyed by instantaneous heating, which affects both the surrounding media and particles. The former is observed as the melting, evaporation, or fragmentation of the particle. Additionally, rapid heating of the particle vaporises a thin layer of the surrounding fluid, producing a microscopic version of an underwater explosion and cavitation bubble formation.[251] All these effects may alter the results. To minimise the photodamage, the laser power was reduced two-fold where necessary. While this minimised the photodamage, it also reduced the signal output from the cells, resulting in little contrast and strong noise. Thus, in all subsequent experiments, the laser power was varied based on the tolerance of the cells and tissue, but did not exceed those stated in **Section 2.6**.

It is known that AuNPs exhibit unique optical properties (mainly due to LSPR), and some imaging-related applications of those are summarised in **Section 1.4.** Further steps were taken to discover the ways to image AuNPs within the cells and tissue and, if possible, to find whether it is possible to image AuNPs selectively, thus eliminating interference from any endogenous molecules. All images were acquired in three channels: CARS, SGH and TPF, and representative images are shown in **Figure 3.9**. As expected, the particles were visible in all three channels due to their photoluminescence. However, AuNPs were almost undistinguishable in the CARS channel due to weak signal, except for large aggregates. In the SHG channel, it was possible to image AuNPs only. While it allows for simplified visual assessment and quantification, the overall signal was relatively weak. On the other hand, TPF acted as a combination of SHG and CARS, with a strong signal from FAD (providing a clear outline of the cells) and AuNPs. Depending on the size of AuNPs aggregates the peak signal was 2-10 times stronger than FAD signal. Such a difference allows for differentiating the AuNPs signal from FAD by simple thresholding. To further enhance the visualisation of AuNPs within the cells, the channels were combined, creating composite images (**Figure 3.10**). The SHG channel was used as a primary signal source for AuNPs, as no extra image manipulations were required to extract the signal of interest. The combination of CARS and TPF did not provide any extra benefit, as the CARS signal was weak and only introduced unnecessary background. The combination of the SHG and TPF channels provided the easiest to interpret results that required minimal manipulation. Overall, TPF showed to be more versatile for the imaging of AuNPs within the cells.

The main limitation in the imaging of NPs is the resolution. The “gold standard” for the imaging of NPs is transmission electron microscopy (TEM), as it provides the best resolution possible. Instead of using photons (which are used in conventional microscopy), the beam employs electrons, allowing for a resolution exceeding 0.2 nm, compared to 400 nm in light microscopy.[252] As a result, all particles and aggregates will not be resolved due to the Abbe diffraction limit. Because the system operates in epi-detection (back-scattered signal collection), AuNPs will appear larger than they are, as remitted and scattered light propagates in all directions. An extra complication is that the size of the aggregates also alters the signal intensity in a non-linear manner. To understand the link between the size of the particles and the images, as well as to understand where they are localised within the cells, electron microscopy was used. There were no particles observed in the nucleus on TEM images (**Figure 3.11**), which is in agreement with multimodal imaging, where reconstructed 3D images do not have any signal in the corresponding area. Most particles formed aggregates of various sizes and accumulated in membrane-bound vesicles, as evident by a layer of membrane surrounding the aggregates. Since TEM is limited to the imaging

of single ultra-thin sections (less than 100 nm), 3View was used as a complementary method to gather more information (**Figure 3.12**). Since the technique is relatively new, the primary goal was to explore its application for future work, rather than to solely focus on its analytical capabilities. It was confirmed that 20 nm AuNPs were distributed within the cytoplasm and did not accumulate in the nucleus. It was also possible to selectively isolate AuNPs aggregates in the image to build their distribution map. This data also allows for the quantification and measuring of the size and the morphology of the aggregates, however, due to significant computational power requirements to perform these calculations, the data was not analysed further at this stage. The main benefit of 3View over TEM was the possibility to see through the whole-cell, and eliminating the chance of missing particles within the single cell, which can easily happen with ultra-thin sections, as well as reconstructing the 3D morphology of aggregates, which is impossible otherwise. On the other hand, the setup inherited SEM limitations, such as reduced resolution, preventing the visualisation of aggregates at finer details. Also, the sample preparation is more laborious than conventional SEM and image acquisition requires hours (depends on the number of slices).

One of the main aims was to perform the imaging of AuNPs in tissue. Due to practical reasons, the lung tissue slices were directly exposed to colloidal 20 nm AuNPs to increase the chances of finding the particles in a large and thick tissue slice. However, the main complications were the inability to selectively image AuNPs and severe burning. If the concentration of particles was too high, the tissue burned, leave a large burned-out zone, as if a chain reaction was triggered, which was not visible with cells, where only a small area was damaged. If the concentration was too low, then particles were either not found at all, or found below the detection limit. As can be seen in **Figure 3.13**, opposite to the imaging of the cells the tissue generates a very strong signal in all three channels. AuNPs could no longer be selectively detected in the SHG channel due to the interference from collagen, which is abundant in tissue. While TPF images had unusually bright areas, which can be interpreted as AuNPs, these areas did not always correlate with the SHG channel. Thus, if there was a bright area on TPF but nothing on SHG, this was most likely a false positive, while if there was a signal in both channels, it was not possible to differentiate whether the signal was from collagen or from AuNPs.

3.7 Conclusions

Multimodal imaging was optimised to collect high-contrast information-rich images with chemical selectivity to lipids, collagen, and FAD in cells and tissue. The system was successfully applied for

imaging single cells treated with 20 nm AuNPs, where AuNPs were semi-selectively imaged in the SHG channel. However, due to the intrinsic properties of AuNPs, the laser power was reduced by at least 50%, which notably reduced the image quality. The imaging channels, based on their relative importance in the imaging of AuNPs within the cells, were ranked as follows: TPF>SHG>CARS. The distribution of AuNPs aggregates within the cells visible in composite images was in agreement with electron microscopy data. The imaging of AuNPs in mouse lung tissue was unsuccessful, as it was not possible to differentiate AuNP signals from native tissue structures.

Chapter 4 *In vitro*. Interaction of AuNPs with proteins and the role of SP-A and SP-D in nanotoxicology.

4.1 Introduction

Surfactant proteins A and D are well studied as innate immunity proteins. They bind to microorganisms and allergens of biological origin, which is important in clearance, immunological and toxicological responses. It was proposed, by Kendall et al[253], that the same might be true for particles of non-biological origin, such as those originating from air pollution or engineered particles. While almost two decades have passed since the hypothesis was raised, there is still limited understanding of how these proteins interact with nanoparticles. This is mainly due to a nearly infinite number of different nanoparticles, as every size, shape and chemistry exhibit unique properties and hence require an individual approach.

While the selection of model nanoparticles for nanotoxicological studies has to resemble environment-relevant particles, it is not always possible. The environmental particles are a cocktail of various morphologies, compositions and adsorbed impurities. Such particles will introduce too many variables into the experiments making it difficult to interpret the results. Hence, 20 nm spherical AuNPs were chosen as a model. This shape was chosen as the most environmental relevant. As mentioned in **Chapter 1**, smaller particles have the highest chances of reaching alveoli, hence 20 nm were chosen as particles of a similar size have the highest health concerns. Finally, AuNPs are stable in biological medium (do not dissolve or undergo other biotransformation) and are generally considered to be inert and non-toxic.

This chapter presents the *in vitro* work, which combines “test tube” and cell culture experiments. The work builds a basic understanding of the behaviour of AuNPs in physiological-like buffers and the importance of stabilising molecules, and explores whether SP-A and SP-D can selectively bind to AuNPs and induce their aggregation. Cell culture experiments explore whether the surfactant proteins impact the viability of the cells and/or increase the phagocytosis. Multimodal imaging was used for the first time to semi-quantify the impact of SP-A and SP-D on the uptake of AuNPs.

4.2 Aims and objectives

This chapter addresses the aims and objectives summarised in clauses 2 and 3 of **Section 1.5,** which are**:**

2. Characterise the interaction of AuNPs with SP-A and SP-D

2.1. Determine the behaviours of gold nanoparticles in physiological-like fluids.

2.2. Characterise and quantify the interaction of AuNPs with SP-A and SP-D, applying dynamic light scattering, static light scattering, transmission electron microscopy (TEM), serial block-face three-dimensional electron microscopy, sodium dodecyl sulphate polyacrylamide gel electrophoresis (SDS-PAGE) and Bradford assay.

3. Characterise the possible *in vitro* nanotoxicity of gold NPs on cell culture models in the presence of SP-A and SP-D.

3.1. Determine the role of SP-A and SP-D in potential toxicity of NPs by 3-(4,5-dimethylthiazol-2-yl)-2,5 diphenyl tetrazolium bromide (MTT) and lactate dehydrogenase (LDH) assays.

3.2. Detect and quantify the number of internalised AuNPs by multimodal microscopy (established in aim 1) and confirm these findings by electron microscopy.

3.3. Establish the link between AuNPs uptake by the cells and the presence of SP-A and SP-D.

4.3 Methods

All methods used in this chapter are detailed in **Chapter 2**.

4.4 Results

4.4.1 Characterisation and stability of AuNPs under physiologically relevant conditions

Mixing AuNPs with TBS, a physiological-like buffer, at room temperature led to a colour shift, which was observed by the naked eye (**Figure 4.1**). Suspension of 20 nm AuNPs (7×10^{10} particles/ml) in TBS^{Ca}, TBS^{EDTA} led to a colour shift from red to blue/purple. Water, 10 mM EDTA and 20 mM Tris did not affect the colour. Because calcium is an important co-factor for the SP-A and SP-D lectin binding activity, three different concentrations were additionally tested to find the

lowest non-aggregating concentration (**Figure 4.1B**). All tested concentrations induced colour change indication particle aggregation.

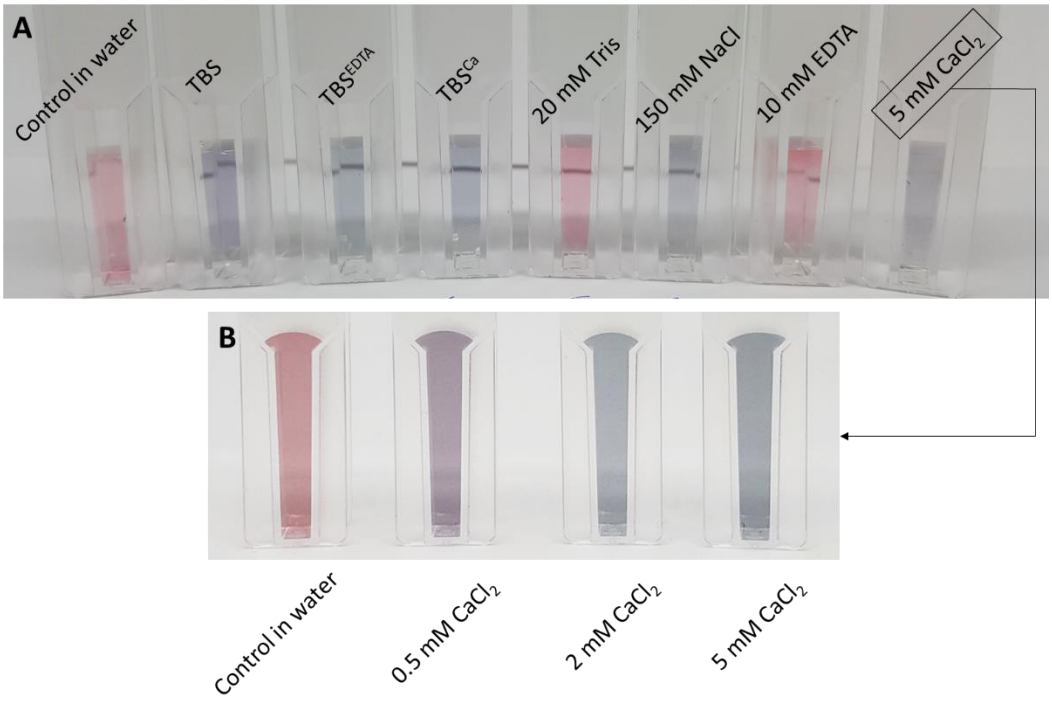

Figure 4.1. Influence of solvent on the colour of 20 nm AuNPs. 20 nm AuNPs colloidal gold in red-coloured suspension. A blue-coloured shift indicates aggregation. **A** – colour shifts in corresponding TBS^{Ca} or TBS^{EDFA} individual components. **B** – colour shift in different $CaCl_2$ concentrations. Concentration of AuNPs – 7×10^{10} particles/ml.

The hydrodynamic diameter (Z-average ± SD) of AuNPs in pure water measured by DLS was 25.53 ± 0.56 nm, which is within the expected range. After the addition of 150 mM NaCl or 5 mM $CaCl_2$, the size of AuNPs was increasing throughout the measurement process (15 min), resulting in an average size of 211.51 ± 56.21 nm in the presence of NaCl and 191 ± 47.94 nm in the presence of $CaCl_2$ (**Figure 4.2**). The data for blank water is not depicted on the chart as the corresponding Z-average was equal to zero.

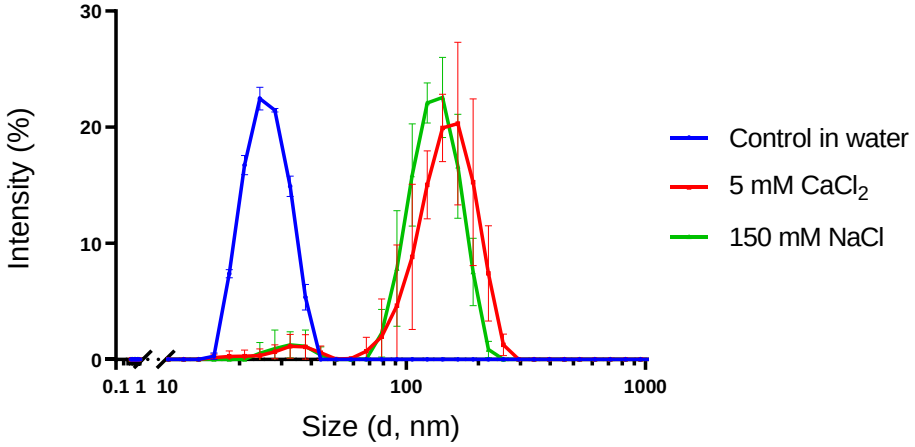

Figure 4.2. DLS-measured aggregation of 20 nm AuNPs in the presence of 5 mM $CaCl_2$ and 150 mM NaCl. Mean size ± SD. Data represent averages of three individual experiments measured in triplicates. Concentration of AuNPs – 7×10^{10} particles/ml.

A more complex and biologically relevant medium used for the next DLS measurement steps was RPMI 1640 cell culture medium (phenol red-free). The medium had an uneven size distribution between replicates and varied greatly (**Figure 4.3**). Addition of 1% HI FCS into the RPMI medium showed a wide size distribution ranging from several nanometres to about 10 µm (**Figure 4.4**). Once particles were mixed with HI FCS supplemented media, they increased in size to 65.83 ± 4.68 nm (x2.5 times, compared to AuNPs in water). However, in the serum-free medium, the size was increasing with each subsequent measurement throughout the analysis, with a final Z-average of 286.4 ± 41.65 nm after 15 min. The dynamics of the size increase can be seen in **Figure 4.5**, where each subsequent peak corresponds to the increased intensity and size. The static light scattering was used as an additional verification method (**Figure 4.6**). The scattering peak for 20 nm AuNPs in water was at about 550 nm wavelength and reached 100 intensity units. The same particles in a serum-free medium and in TBS had a higher intensity and a red-shifted profile, with about 500 intensity units and peaks at 700 and 660 nm, respectively. The particles with RPMI and 1% HI FCS had a similar profile to the control in water, but the graph was wider. The medium with 1% serum had two minor peaks at about 20 intensity units, observed at 525 nm and 625 nm.

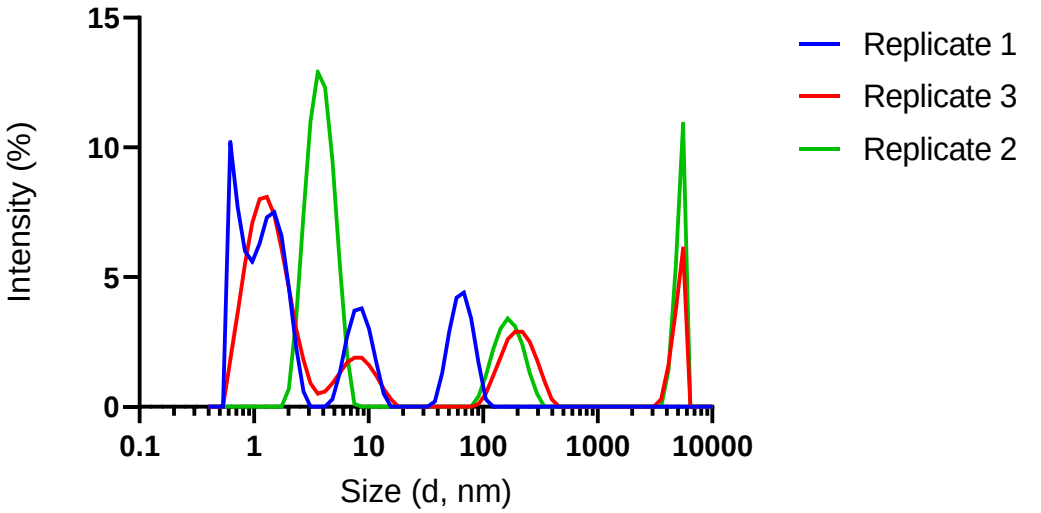

Figure 4.3. DLS data of phenol red-free RPMI 1640 medium demonstrating the size distribution of macromolecules. The intensity peaks were randomly distributed across three replicates. The data represent a triplicate of a single experiment. Each replicate is individually represented.

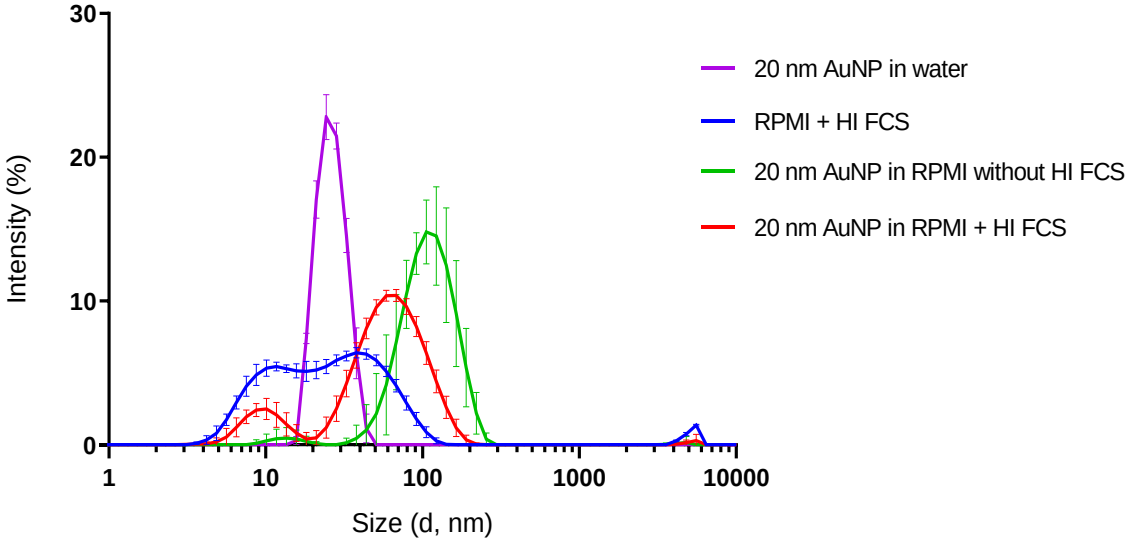

Figure 4.4. DLS-measured aggregation of 20 nm AuNPs in RPMI 1640 medium in the presence or absence of HI FCS. AuNPs aggregation is induced upon suspension in serum-free medium (green). The presence of serum resulted in smaller average sized particles (red) compared to no serum present (green). Concentrations: AuNPs – 7×10^{10} particles/ml; HI FCS – 1%. Mean size ± SD. Data represent the averages of six data points within a single experiment recorded with 2 min intervals.

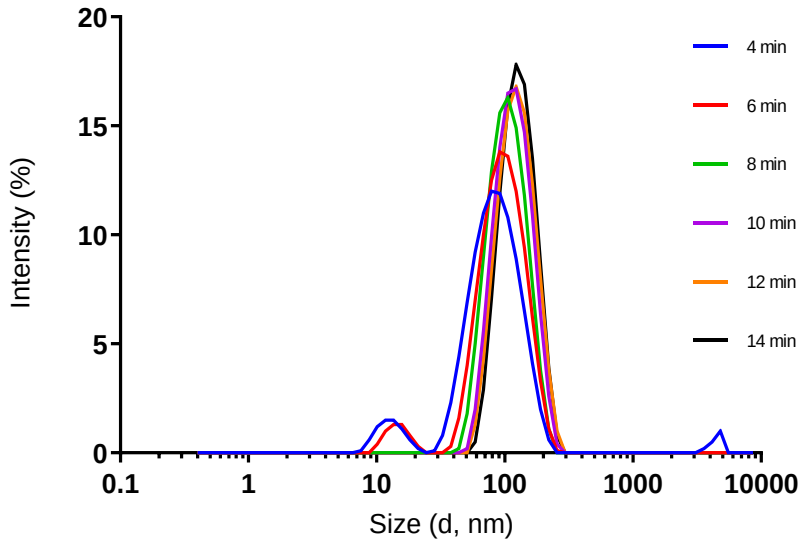

Figure 4.5. The dynamics of 20 nm AuNPs size increase over 14 min in serum-free RPMI 1640 media. The first 2-4 min are required to prepare the sample and heat it to 37 °C, hence the first data point starts at 4 min. Each consecutive measurement results in a higher intensity and larger size peaks. Concentration of AuNPs – 7×10^{10} particles/ml.

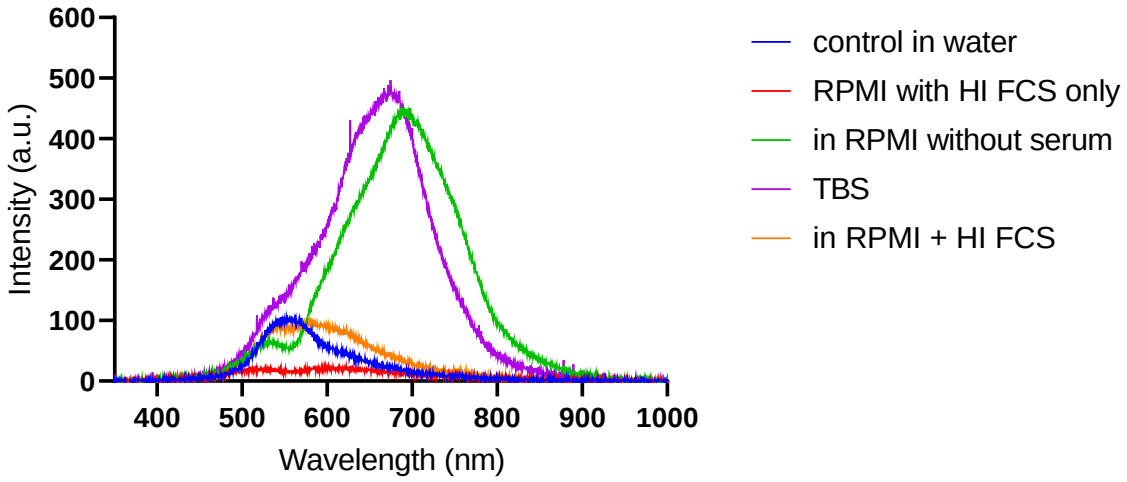

Figure 4.6. Static light scattering-measured aggregation of AuNPs in physiologically relevant buffers. An increase in size resulted in intensity and wavelength increase. Particles with 1% HI FCS only had a slight shift in wavelength. Concentrations: AuNPs – 7×10^{10} particles/ml. Data represents the mean of two independent experiments.

The protein corona's role on the prevention of AuNP aggregation was measured by resuspending HI FCS coated 20 nm AuNPs in a serum-free medium (**Figure 4.7**). Particles which were washed once had a larger surface charge -23 ± 1.47 mV and a smaller particle size of 157 ± 4.74 nm,

compared to those washed twice with a -28.8 ± 3.27 mV surface charge and a 179.7 ± 7.77 nm diameter. *NB: it was not possible to measure the size of the particles immediately after the wash due to the equipment's location.*

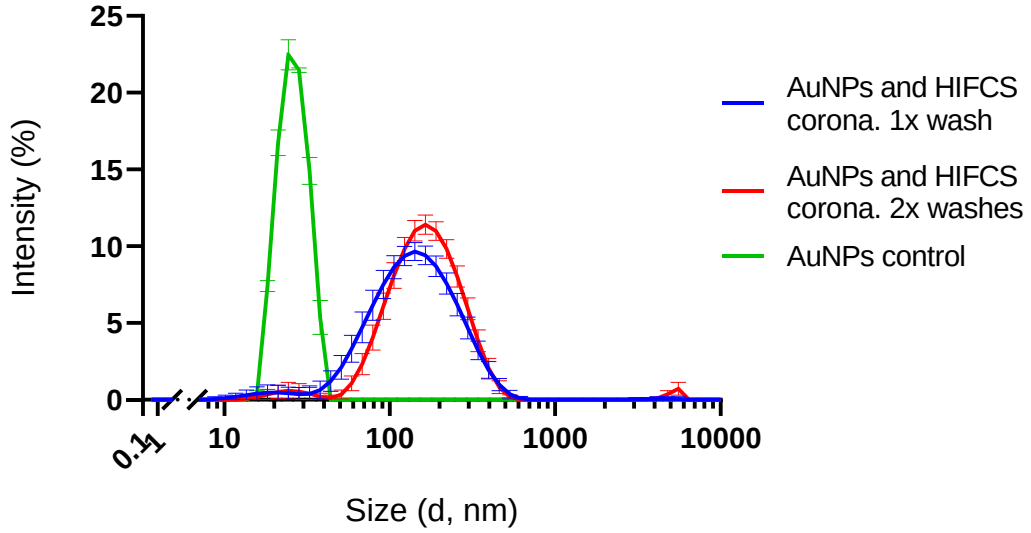

	AuNPs	AuNPs + HI FCS. 1x wash	AuNPs + HI FCS. 2x wash
Zeta potential	-29 ± 1.69 mV	-23 ± 1.47 mV	-28.8 ± 3.27 mV
Z-average	25.53 ± 0.56 nm	157 ± 4.74 nm	179.7 ± 7.77 nm

Figure 4.7. DLS-measured stability of serum-coated 20 nm AuNPs in serum-free RPMI medium. The particles were incubated in RPMI 1640 supplemented with 1% HI FCS for 30 min to form protein corona. The particles were washed once or twice and resuspended in RPMI media. The data was recorded 2 hours after the washing. Concentrations: AuNPs – 7×10^{10} particles/ml; HI FCS – 1%. Mean size ± SD. Data represent averages of three parallel experiments measured in triplicate.

Transmission electron microscopy images (**Figure 4.8**) were used to support DLS and SLS findings on particle stability in the presence of serum. Particles resuspended in water were uniform in size and shape, as expected and reported by the manufacturer. The particles in the serum-free medium were predominantly aggregated, forming clumps and chains ranging from several hundred nanometres to tens of micrometres. There were no individual particles found. In the presence of 1% HI FCS, there were multiple individual particles detected and no aggregates larger than 1 µm in diameter were found.

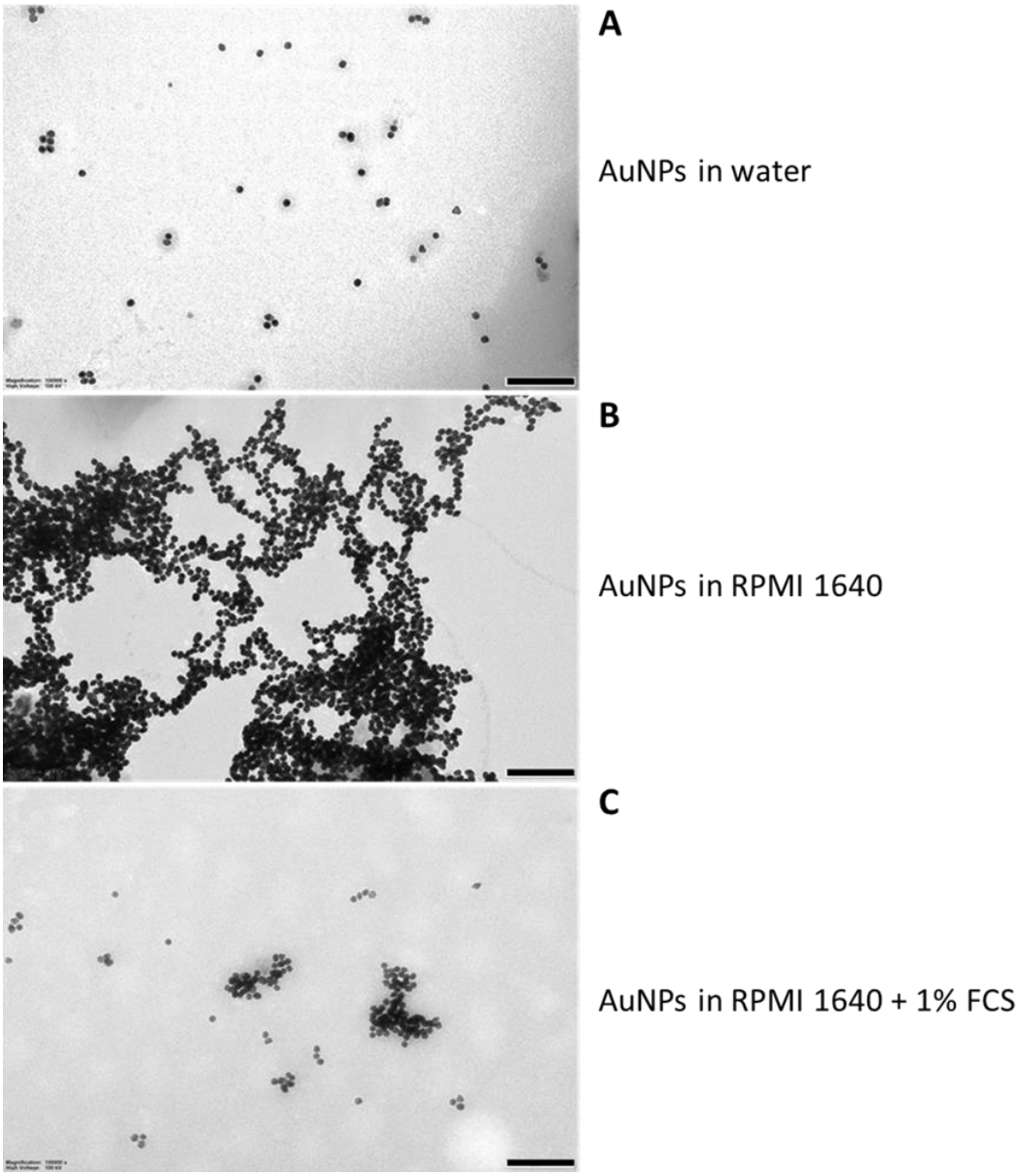

Figure 4.8 Representative TEM micrographs of 20 nm AuNPs. A – in water; **B** – in serum-free RPMI 1640, particles formed both clump and chain-like aggregates; **C** – in RPMI 1640 + 10% HI FCS. In the presence of 1% HI FCS the average size of aggregates was significantly smaller than in serum-free media. Scale bars are 200 nm. 200k magnification.

4.4.2 Adsorption of SP-A and SP-D to AuNPs

The adsorption of SP-A and SP-D and their role in the aggregation of 20 nm AuNP was analysed in RPMI 1640 medium by DLS. Firstly, SP-A and SP-D were measured alone to determine their hydrodynamic diameter. SP-A showed two peaks, where the first peak was 39.63 ± 0.56 nm and the second 163.5 ± 20.22 nm. SP-D was uniform in size with a peak at 532 ± 50.68 nm. Bovine

serum albumin was used as a non-specific protein control, as it binds to nanoparticles in a non-specific fashion via electrostatic interactions.[254,255] The protein size was uniform with Z-average 8.91 ± 0.49 nm. The interaction of AuNPs with SP-A increased the Z-average of the particles to 85.73 ± 16.69 nm (**Figure 4.9**). The Zeta potential increased to -19 ± 3.5 mV (compared to -29 ± 1.69 mV for control AuNPs). When AuNPs were mixed with SP-D, the size was similar to SP-D alone – 439.6 ± 37.6 nm (**Figure 4.10**). The Zeta potential increased to -17.7 ± 2.31 mV (compared to -29 ± 1.69 mV for control AuNPs). The interaction of AuNPs with BSA resulted in the more stable and predictable size of nanoparticles with a Z-average of 47.92 ± 6.63 nm, with a shoulder between 200 and 400 nm (**Figure 4.11**). The Zeta-potential was not measured for AuNPs with BSA.

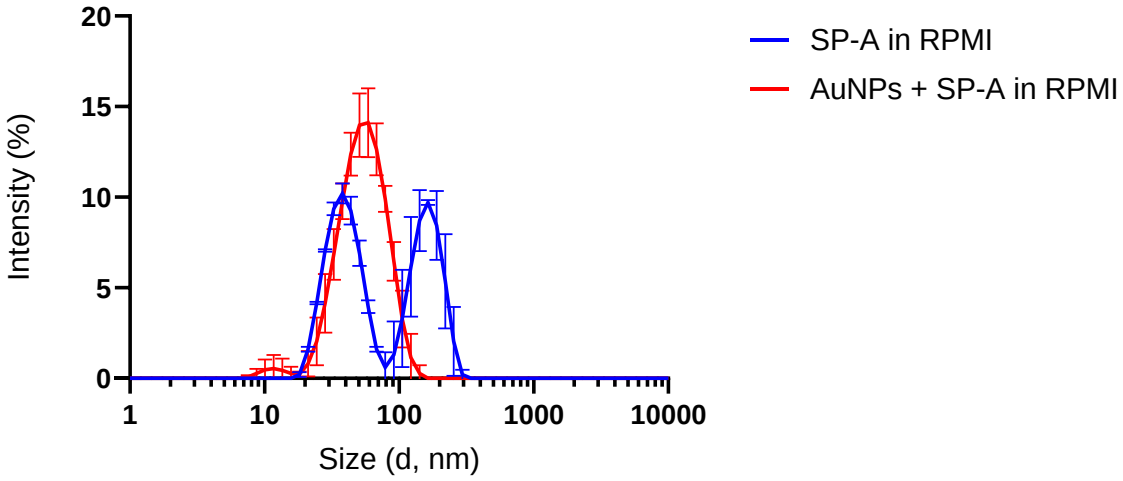

Figure 4.9. Dynamic light scattering measured interaction of 20 nm AuNPs and 20 µg/ml SP-A in RPMI media. Mean size ± SD. Data represent the averages of six data points within a single experiment recorded with 2 min intervals. Concentrations: AuNPs – 7×10^{10} particles/ml.

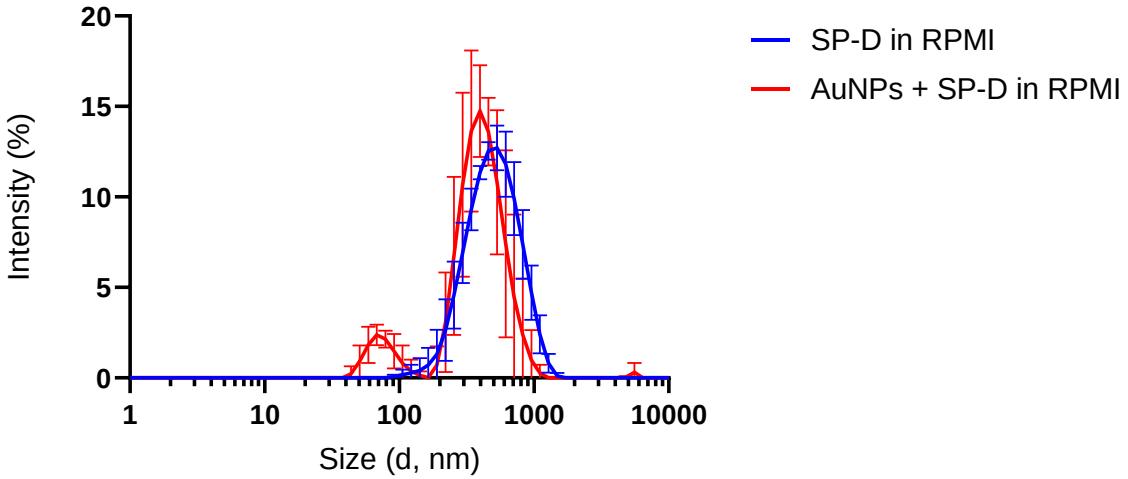

Figure 4.10. Dynamic light scattering measured interaction of 20 nm AuNPs and 20 µg/ml SP-D in RPMI media. Mean size ± SD. Concentrations: AuNPs – 7×10^{10} particles/ml. Data represent the averages of six data points within a single experiment recorded with 2 min intervals.

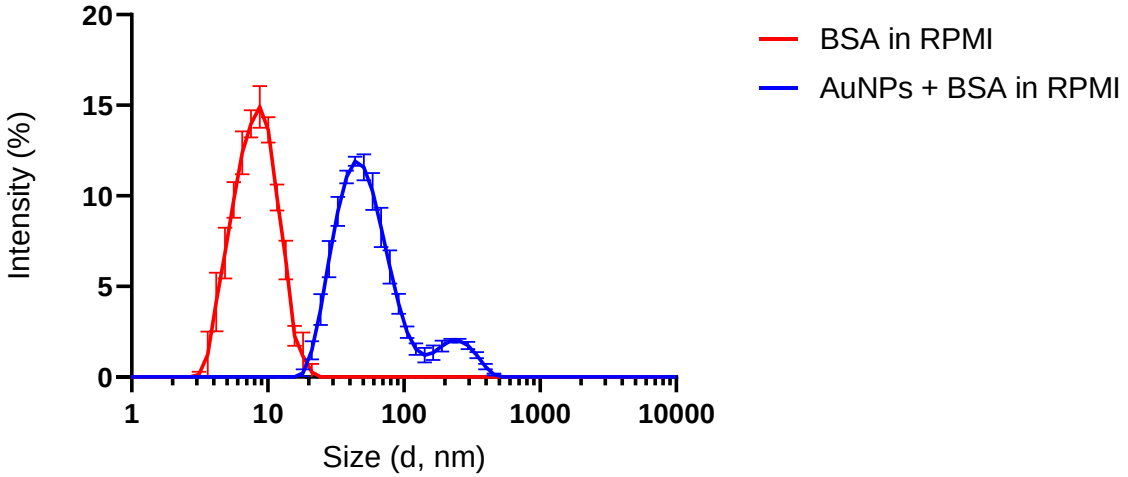

Figure 4.11. Dynamic light scattering measured interaction of 20 nm AuNPs and 20 µg/ml BSA in RPMI media. Mean size ± SD. Concentrations: AuNPs – 7×10^{10} particles/ml. Data represent the averages of six data points within a single experiment recorded with 2 min intervals.

It was attempted to quantify the amount of proteins adsorbed to AuNPs. Firstly, 500 µl of 20 µg/ml of SP-A, SP-D and BSA were incubated in low protein binding (LoBind) tubes with TBS^{Ca} and TBS^{EDTA} for 30 min at 37 °C to evaluate the adsorption of proteins onto the tube walls, as binding to the tube will reduce the concentration in the solution and lead to inaccurate results.

After washing the tubes with reducing buffer (to strip any proteins from the tube walls), the buffer was analysed with SDS-PAGE and stained with SimplyBlue and silver staining. There were no proteins detected on the stained gels other than positive controls, indicating no adsorption. Hence, LoBind tubes were used for all experiments. However, staining the tubes with Bradford assay reagent showed significant protein adsorption to LoBind tubes in the corresponding order – SP-A>SP-D>BSA – where SP-A showed the strongest adsorption and BSA the least (**Figure 4.12**). The tubes washed with Bradford reagent only were not stained and remained clear. It is important to note that colour intensity of the proteins stained with Bradford reagent depends on their structure and thus different proteins of the same concentration develop different colour intensities (**Figure 4.13**).

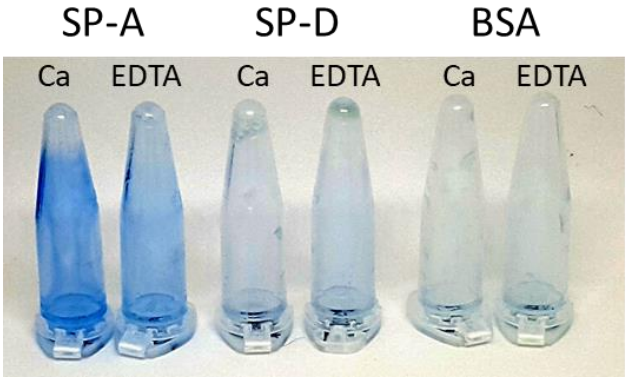

Figure 4.12. Visualisation of protein adsorption to LoBind tubes using Bradford reagent. The colour intensity indicating the amount of protein was the following SP-A>SP-D>BSA. The presence of calcium or EDTA in TBS had no or minimal effect. Representative images selected from two independent experiments. The tubes were incubated with 500 µl of 20 µg/ml SP-A, SP-D and BSA in TBS^{Ca} or TBS^{EDTA}.

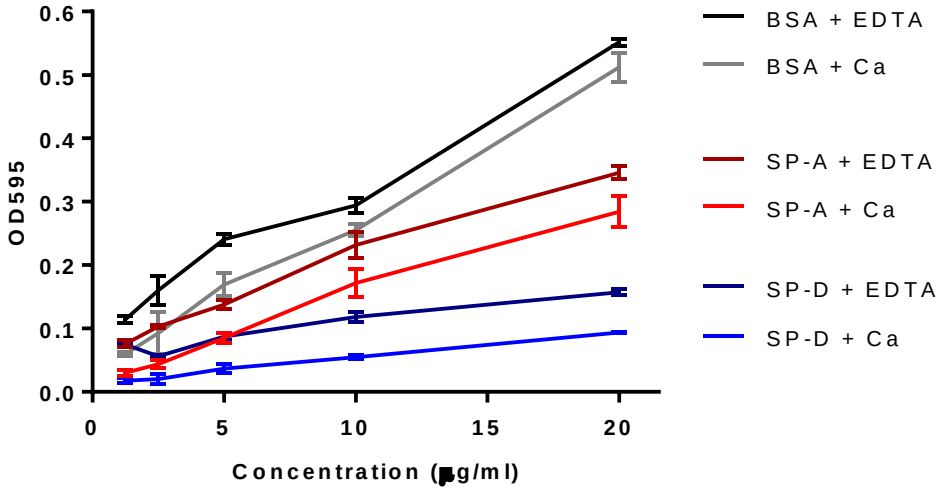

Figure 4.13. Bradford assay standard curves for SP-A, SP-D and BSA. The data represents the mean of three independent experiments conducted in triplicate ±SD. Samples prepared via two-fold serial dilutions.

Surfactant proteins and BSA were incubated with 20 nm AuNPs in TBS^{Ca} and TBS^{EDTA}. The particles were centrifuged to separate the supernatant and particles, the latter were further washed to remove any unbound proteins. The samples were split and analysed with Bradford assay (supernatant only) and SDS-PAGE (supernatant and sediments). SDS-PAGE of the sediments indicated that all three proteins adsorbed to AuNPs (**Figure 4.14)**. The intensity of the SP-A band with calcium was higher compared to the corresponding control. SP-D showed an uncharacteristic high-intensity band at about 65 kDa which was not present in the control. The opposite of surfactant proteins, BSA had a lower intensity band corresponding to adsorbed proteins compared to the control. The same gel was analysed by western blot (**Figure 4.15**). SP-A and SP-D appeared at a significantly higher intensity than controls. Insignificant SP-A contamination was detected in SP-D samples. The intensity of the BSA control was higher than in the samples. Analysis of the supernatants showed a significant reduction in the concentration of SP-A and SP-D. BSA corresponding bands were of similar intensity in control and samples (**Figure 4.16**).

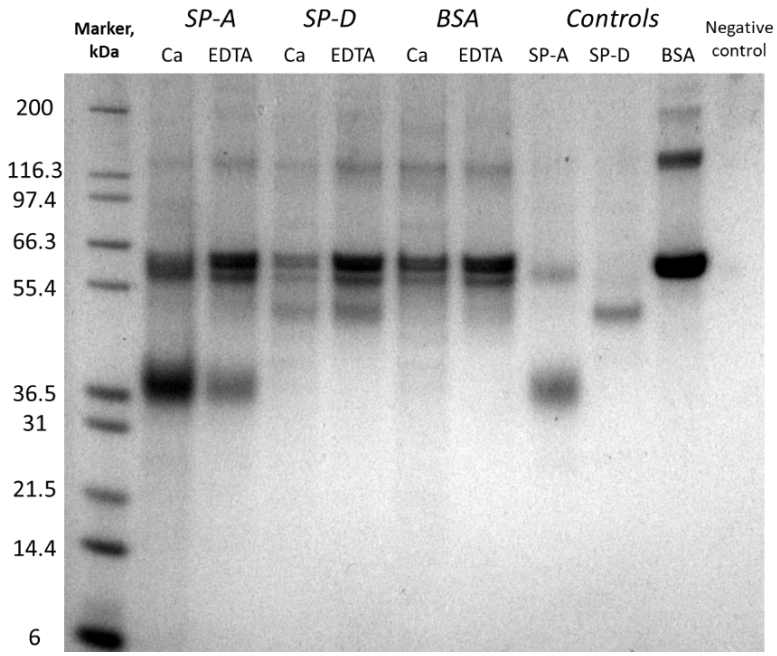

Figure 4.14. SDS-PAGE SimplyBlue staining of 20 nm AuNPs incubated with SP-A, SP-D and BSA. Adsorption of 20 µg/ml SP-A, SP-D and BSA to 7×10^{10} AuNPs in the presence of calcium and EDTA. The samples were reduced before SDS-PAGE. Controls correspond to the equal volume of centrifuged 20 µg/ml protein sample (about 0.2 µg of protein in 10 µl). Representative image of three independent experiments.

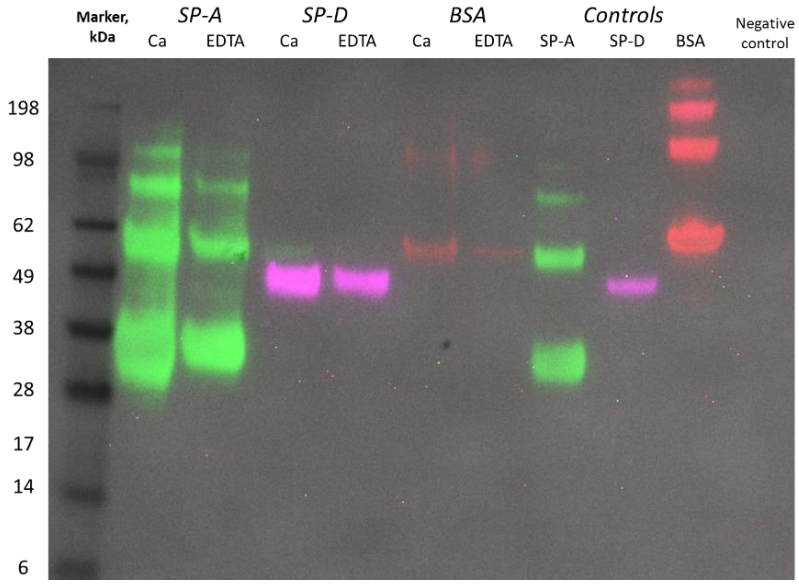

Figure 4.15. SDS-PAGE western blot of protein adsorption to 20 nm AuNPs. Adsorption of 20 µg/ml SP-A, SP-D and BSA to 7×10^{10} AuNPs in the presence of calcium and EDTA. Controls correspond to the equivalent volume of the sample without AuNPs (about 5 µg of protein). Colour coded composite image. Green – SP-A, magenta – SP-D, red – BSA. Representative image of two individual experiments.

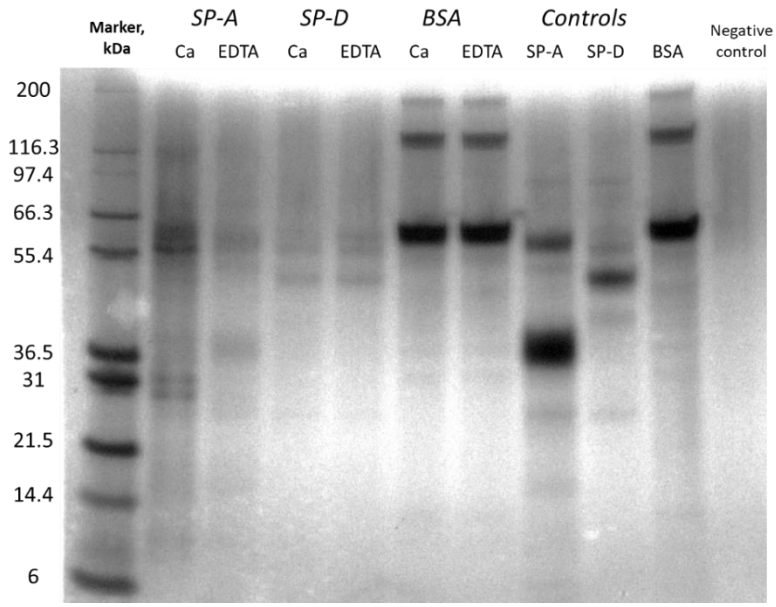

Figure 4.16. SDS-PAGE silver staining of supernatant collected from 20 nm AuNPs incubated with SP-A, SP-D and BSA. Adsorption of 20 µg/ml SP-A, SP-D and BSA to 7×10^{10} AuNPs in the presence of calcium and EDTA. The samples were reduced before the analysis. Controls correspond to the equal volume of centrifuged 20 µg/ml protein sample (about 0.2 µg of protein in 10 µl). Representative image of three independent experiments.

For the next step, proteins were mixed in a 1:1:1 ratio yielding a total concentration of 30 µg/ml. Particles were incubated in this mixture following the same process as above. According to the SimplyBlue staining results (**Figure 4.17**), BSA was absent or below the detection limit, since no corresponding bands were observed. SP-A was identified as expected at 38 and 65 kDa. The band for SP-D was detected at 49 kDa, but was unclear and appeared as a cluster of multiple bands. Two out of 3 proteins were found to bind to AuNPs. Western blot was used to confirm the results and identify each band (**Figure 4.18**). The results were the same as with SimplyBlue. There was no BSA detected, suggesting its absence. SP-A and SP-D were resolved and detected at the expected regions in the level with controls. The intensity of the corresponding bands was reduced in the presence of EDTA.

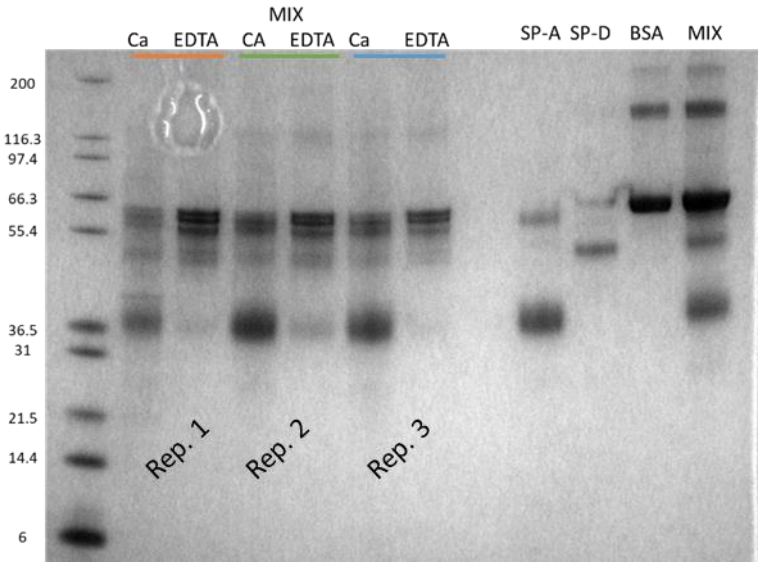

Figure 4.17. SDS-PAGE SimplyBlue staining of SP-A, SP-D and BSA protein mix adsorption to 20 nm AuNPs. Adsorption of 30 µg of proteins mixed in a ratio of 1:1:1 to 7×10^{10} AuNPs in the presence of calcium and EDTA. Controls denote to 4 µg of SP-A, SP-D, BSA and 9 µg of the mix without AuNPs. Three replicates (Rep.1, 2 and 3) were analysed on the presented gel.

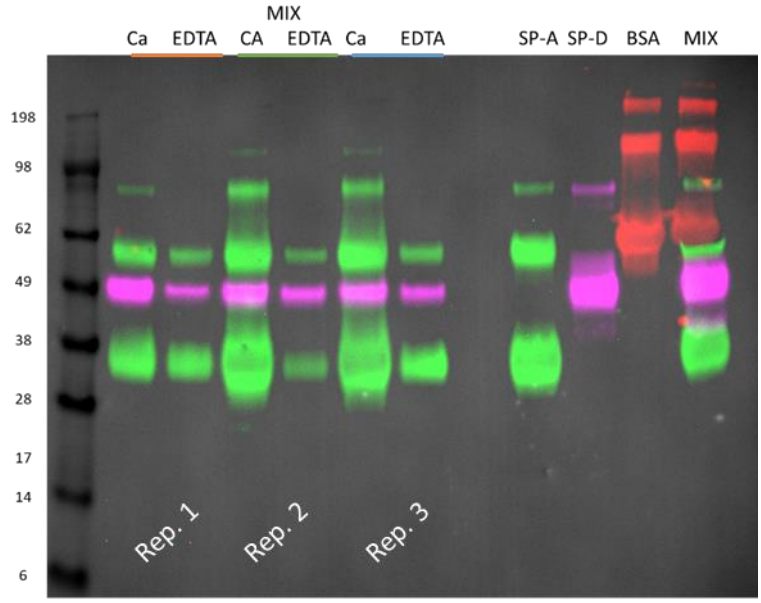

Figure 4.18. SDS-PAGE western blot of SP-A, SP-D and BSA protein mix adsorption to 20 nm AuNPs. Adsorption of 30 µg of proteins mixed in a ratio of 1:1:1 to 7×10^{10} AuNPs in the presence of calcium and EDTA. Controls denote to 4 µg of SP-A, SP-D, BSA and 9 µg of the mix without AuNPs. Three replicates (Rep.1, 2 and 3) were analysed on the presented gel. Green – SP-A, magenta – SP-D, red – BSA.

Bradford assay was conducted as a second verification method and to quantitatively measure the adsorbance of the proteins. At first, the role of centrifugal forces was tested on the sedimentation of the proteins in TBS^{Ca} and TBS^{EDTA} (**Figure 4.19**). The results showed a significant 5-fold and 2-fold decrease in SP-A and SP-D concentration in the supernatant, respectively. The concentration of BSA after the centrifuging was approximately the same as before. In the presence of calcium, the amount of sedimented protein was slightly higher than in the presence of EDTA. The proteins were then analysed with 20 nm AuNPs under identical conditions (**Figure 4.20**). Total protein concentration reduced in SP-A and SP-D, both in the presence of calcium and EDTA. Statistically significant differences were observed in SP-A in TBS^{Ca} and SP-D in TBS^{EDTA}, with 45% (p=0.016) and 30% (p=0.041) protein concentration reduction, respectively. BSA remained unchanged.

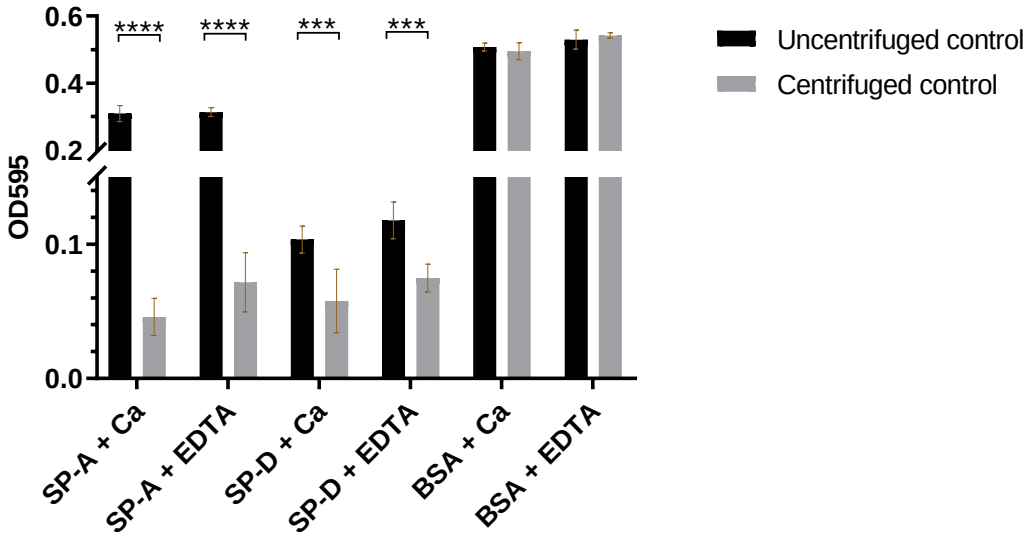

Figure 4.19. The differences in supernatant SP-A, SP-D and BSA quantity before and after centrifuging at 4,000 × g measured by Bradford assay. Protein quantity is expressed in optical density units. Each protein was at 10 µg/ml and 7×10^{11} particles/ml. Data represent the mean of four independent experiments conducted in triplicate. Mean size ± SD. *** - p<0.001, **** - p<0.0001, t-test.

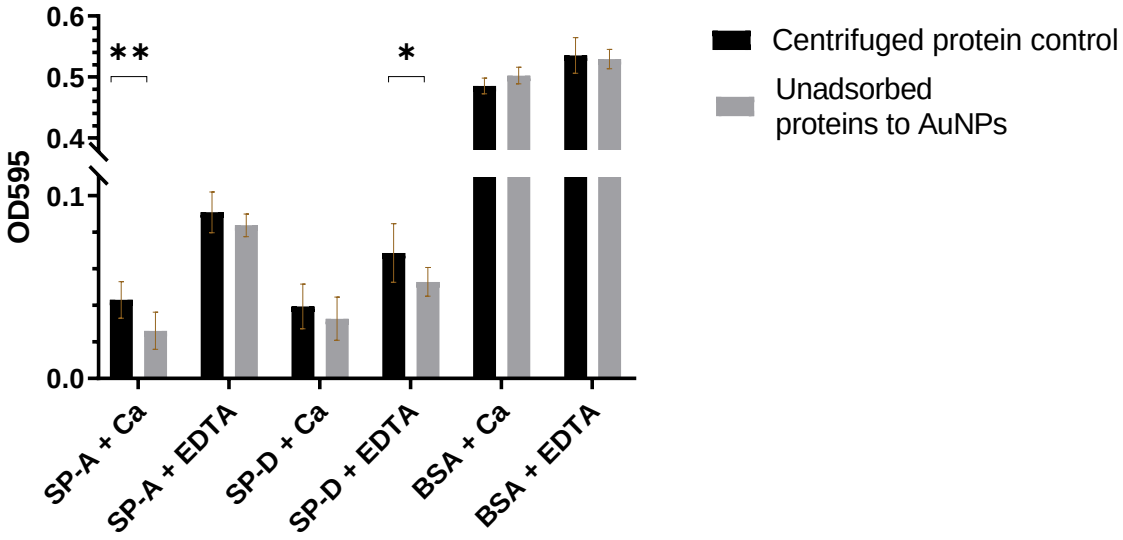

Figure 4.20. The differences in supernatant SP-A, SP-D and BSA quantity after incubation with AuNPs and centrifuging at 4,000 × g measured by Bradford assay. Protein quantity is expressed in optical density units. Each protein was at 10 µg/ml and 7×10^{11} particles/ml. Data represent the mean of three independent experiments conducted in triplicates. Mean size ± SD. * - $p<0.05$, ** - $p<0.01$, t-test.

4.4.3 Cell culture experiments

A concentration-dependent standard curve was created to determine LD_{50} (a concentration required to kills 50% of the population) for 20 nm AuNPs and the influence of 1% and 10% HI FCS in cell culture medium (**Figure 4.21**). There was no significant difference in viability between 1% and 10% HI FCS. The LD_{50} for both 1% and 10% HI FCS was about 16 times dilution factor (or 4.375×10^{10} particles/ml).

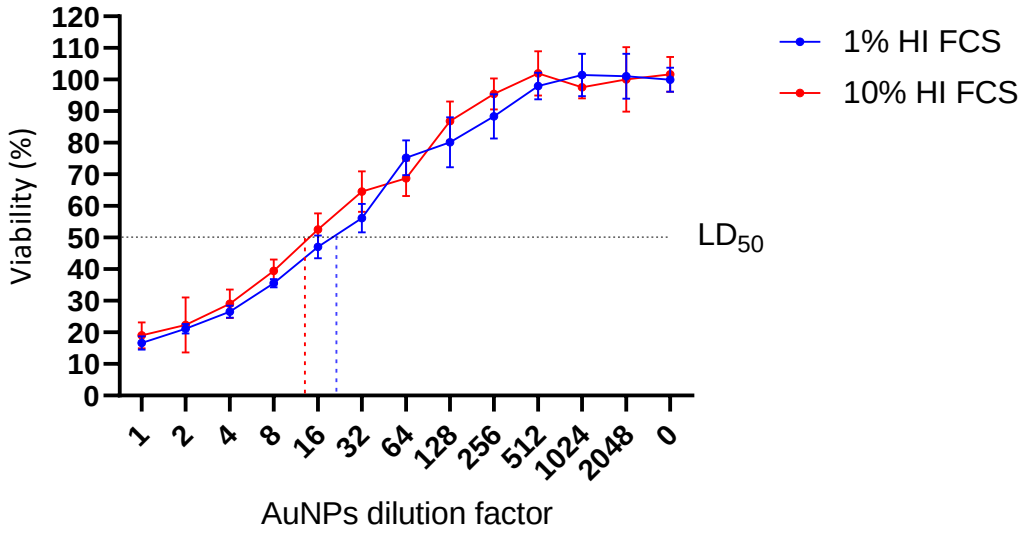

Figure 4.21. Concentration-dependent toxicity of 20 nm AuNPs on RAW264.7 measured by MTT assay. The cells were exposed for 24 h. The dilutions were performed as two-fold serial dilutions. The 1x dilution factor equals 7×10^{11} particles/ml. Data was collected in the presence of 10% and 1% HI FCS. Mean of two individual experiments in quadruplicate. Normalised data. Mean size ± SD.

Light microscopy images were taken for cell cultures incubated with AuNPs with serum-free and 1% HI FCS supplemented media (Figure 4.22). The data showed similar results to those seen in Section 4.4.1. Absence of HI FCS resulted in the aggregation of the particles and subsequent sedimentation on the bottom of the plate in the form of black precipitates. The area around the cells had a reduced number of these precipitates, which is visible as a clear area. The cells also had black-coloured incorporations. The medium with 1% HI FCS prevented the particles from precipitation and the cells had red-coloured incorporations. It was noticed that the stabilisation of the particles depended on the concentration of HI FCS. In the presence of 1% HI FCS and 7×10^{11} particles/ml – the particles precipitated, which was not observed with 7×10^{10} particles/ml.

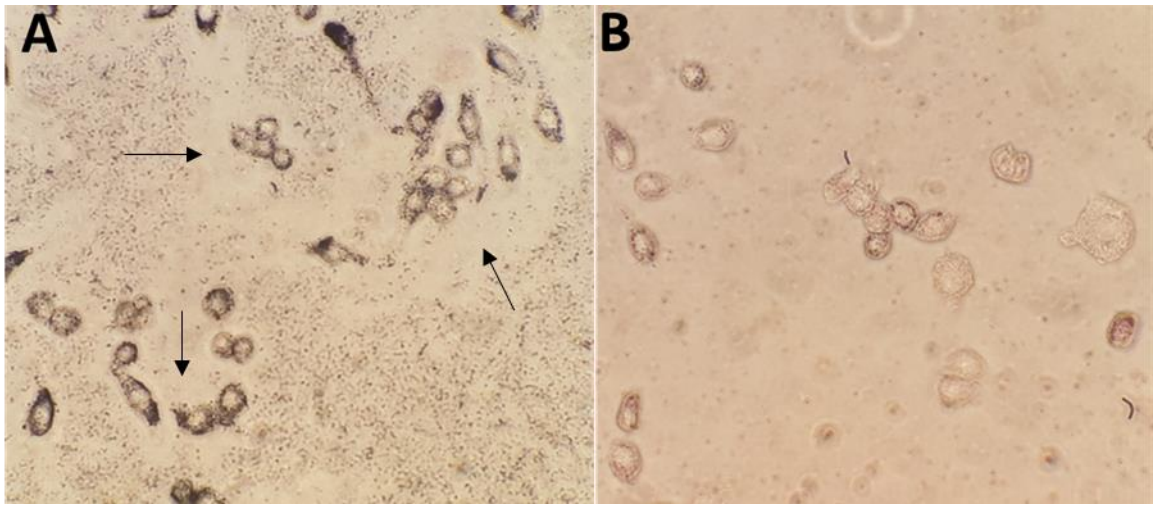

Figure 4.22 Light microscopy images of RAW264.7 cells exposed to AuNPs. The cells were exposed to 7×10^{10} particles/ml for 24 h; arrows point at selected areas with a reduced amount of precipitates. **A** – Serum-free RPMI; **B** – RPMI with 1% FCS. 400 times magnification.

The role of BSA (**Figure 4.23**), SP-A (**Figure 4.24**) and SP-D (**Figure 4.25**) on the toxicity of AuNPs was assessed using MTT assay. All three proteins showed similar effects which were not statistically significant comparing to each other. The viability of the cells incubated with AuNPs was around the expected 40%. After the addition of 10, 5 or 1 µg/ml of either protein the survival rate increased by about 50% ($p<0.0001$, t-test) in all three cases. It was noticed that with the addition of the proteins the survival rate also increased in a concentration-dependent manner. There was a 10-20% viability reduction in protein only controls for SP-A and SP-D at 10 and 5 µg/ml. LDH assay was used as an additional method. The results did not show any differences between the controls and experimental samples (**Figure 4.26**, **Figure 4.27** and **Figure 4.28**).

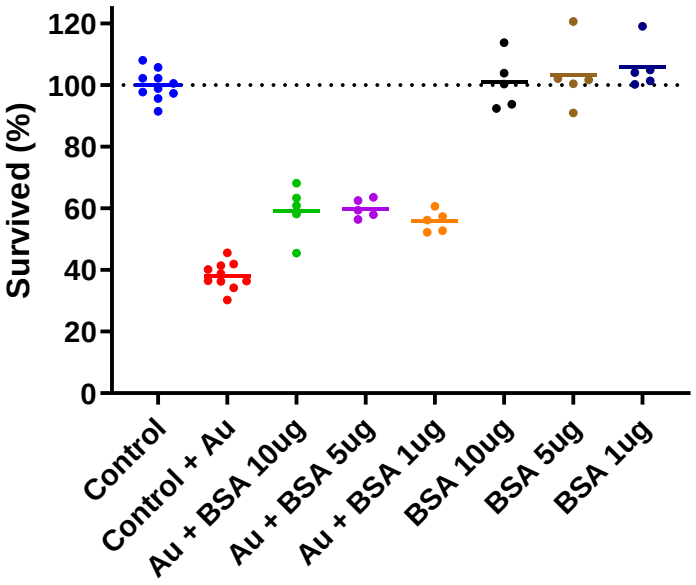

Figure 4.23. MTT assay. Dependence of 20 nm AuNPs toxicity on RAW264.7 in the presence of BSA. All experiments were performed in 1% HI FCS supplemented RPMI medium and 7×10^{10} particles/ml for 24 h. Each data point is an average of triplicates from at least 5 individual experiments.

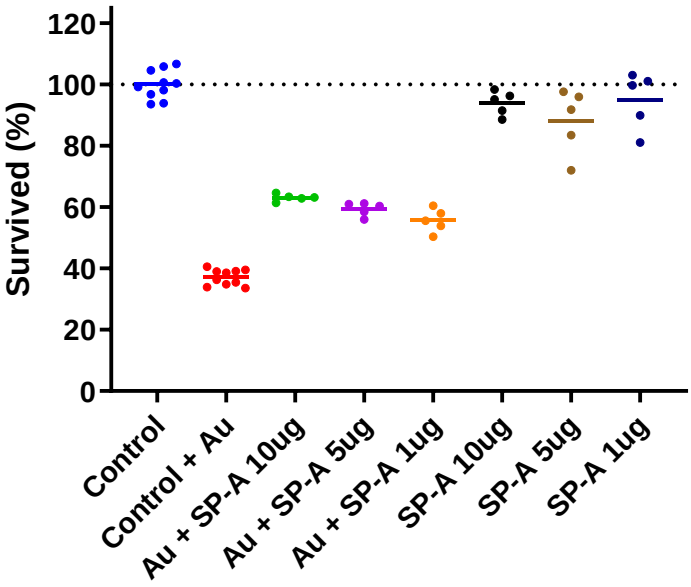

Figure 4.24. MTT assay. Dependence of 20 nm AuNPs toxicity on RAW264.7 in the presence of SP-A. All experiments were performed in 1% HI FCS supplemented RPMI medium and 7×10^{10} particles/ml for 24 h. Each data point is an average of triplicates from at least 5 individual experiments.

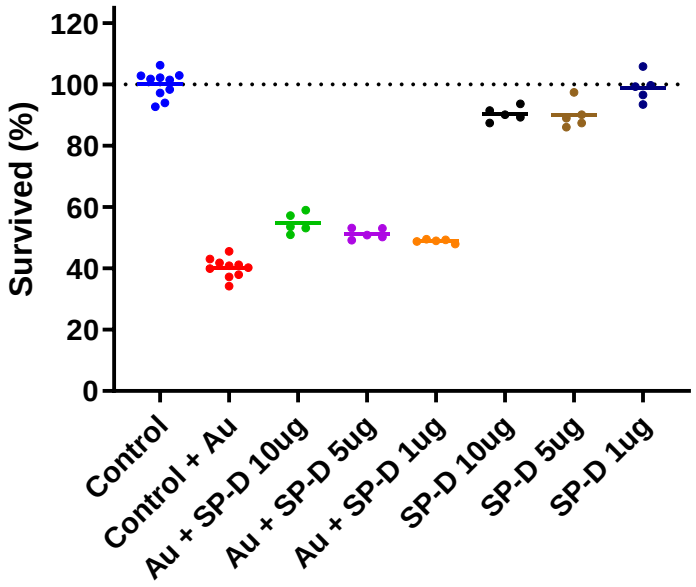

Figure 4.25. MTT assay. Dependence of 20 nm AuNPs toxicity on RAW264.7 in the presence of SP-D. All experiments were performed in 1% HI FCS supplemented RPMI medium and 7×10^{10} particles/ml for 24 h. Averages of triplicates from at least 5 individual experiments.

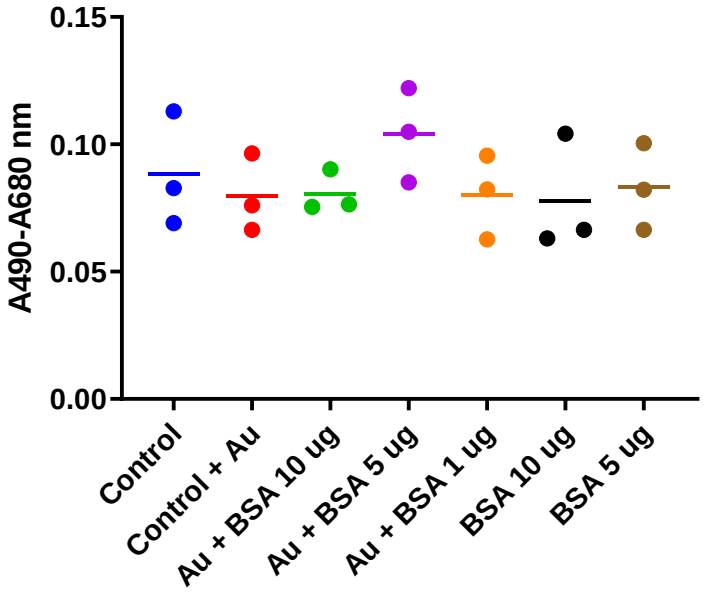

Figure 4.26. LDH assay. Dependence of 20 nm AuNPs toxicity on RAW264.7 in the presence of BSA. All experiments were performed in 1% HI FCS supplemented RPMI medium and 7×10^{10} particles/ml for 24 h. Triplicates of the single individual experiment.

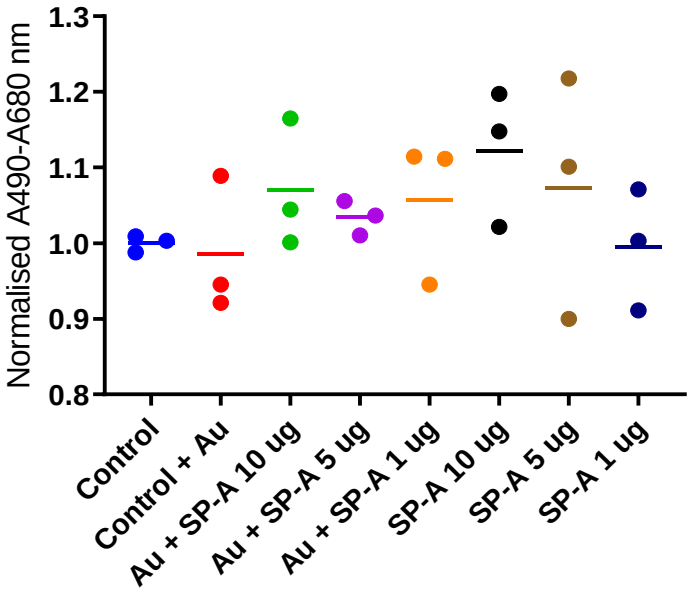

Figure 4.27. LDH assay. Dependence of 20 nm AuNPs toxicity on RAW264.7 in the presence of SP-A. All experiments were performed in 1% HI FCS supplemented RPMI medium, and 7×10^{10} particles/ml for 24 h. Triplicates of the single individual experiment.

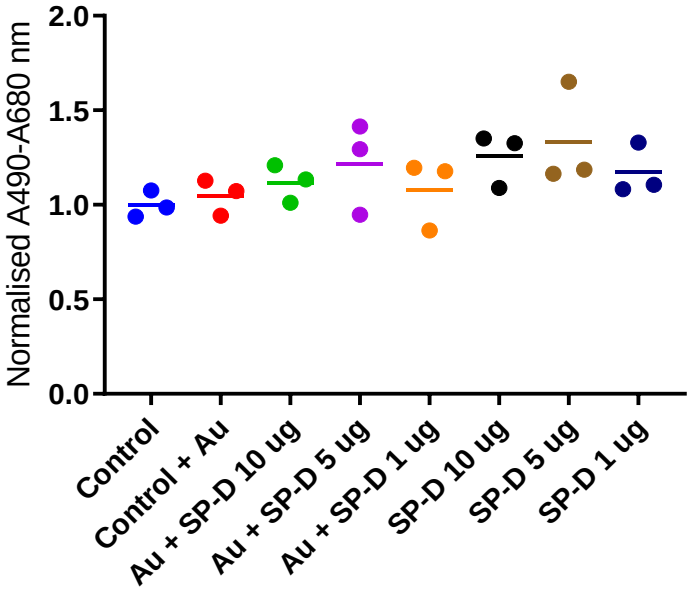

Figure 4.28. LDH assay. Dependence of 20 nm AuNPs toxicity on RAW264.7 in the presence of SP-D. All experiments were performed in 1% HI FCS supplemented RPMI medium and 7×10^{10} particles/ml for 24 h. Triplicates of the single individual experiment.

Whole-cell SDS-PAGE and western blot were done to determine whether nanoparticles facilitate the cellular uptake of SP-A and SP-D. Cells were incubated with 1% HI FCS medium in the presence

of SP-A, SP-D and BSA, as well as the same proteins with AuNPs. SDS-PAGE revealed multiple unidentifiable protein bands ranging from more than 198 kDa to 10 kDa (**Figure 4.29)**. There was no visible difference between experimental groups, neither in a band profile nor intensity. Whole-cell immunoblotting **(Figure 4.30**) showed the presence of BSA in all experimental samples. The SP-A bands were identified in each row where it was added. SP-D was not identified in any rows except controls. There was BSA interference noticed in SP-A and SP-D control, which, however, was not seen in SDS-PAGE. Also, SP-D was observed as two bands in the mix control and appeared at lower weight, 38 and 45 kDa.

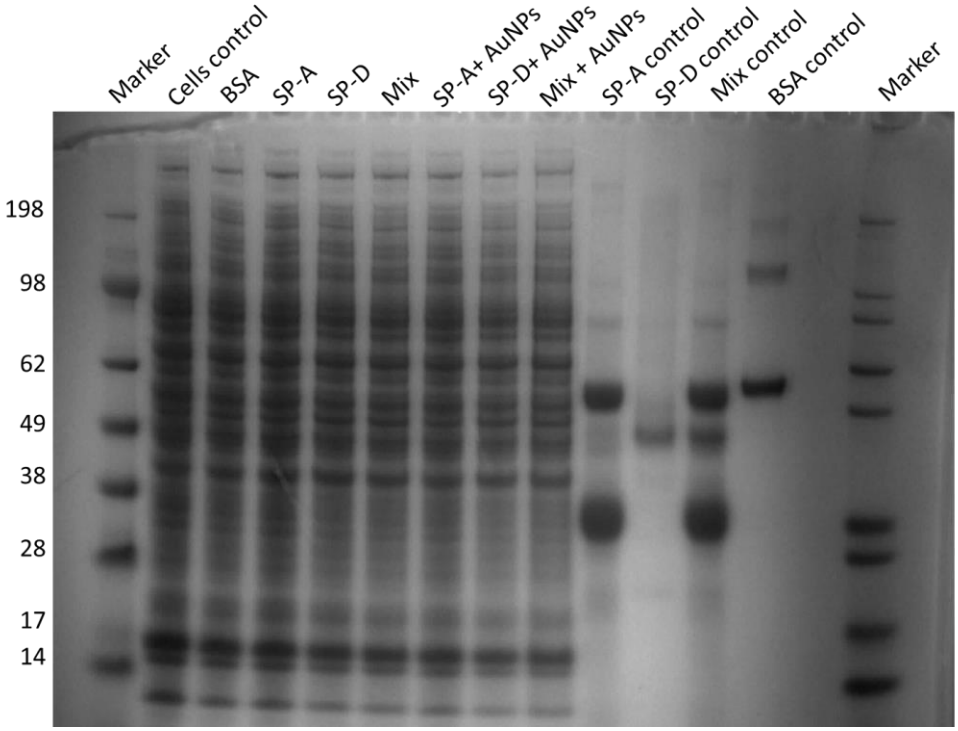

Figure 4.29. Whole-cell SDS-PAGE in the presence of SP-A, SP-D and nanoparticles after 4 hours. 10 µl of approximately 1×10^6 cells lysate were used for each row. **Cells control** – RAW264-7 cells grown with 0.5% HI FCS supplemented medium. **BSA, SP-A, SP-D** – the cells were grown as in control with the addition of 10 µg/ml of the corresponding protein. **Protein + AuNPs** – corresponding proteins with 7×10^{10} particles/ml. Protein controls – 10 µg of protein control. **Mix** – 30 µg of SP-A:SP-D:BSA mix at 1:1:1 ratio.

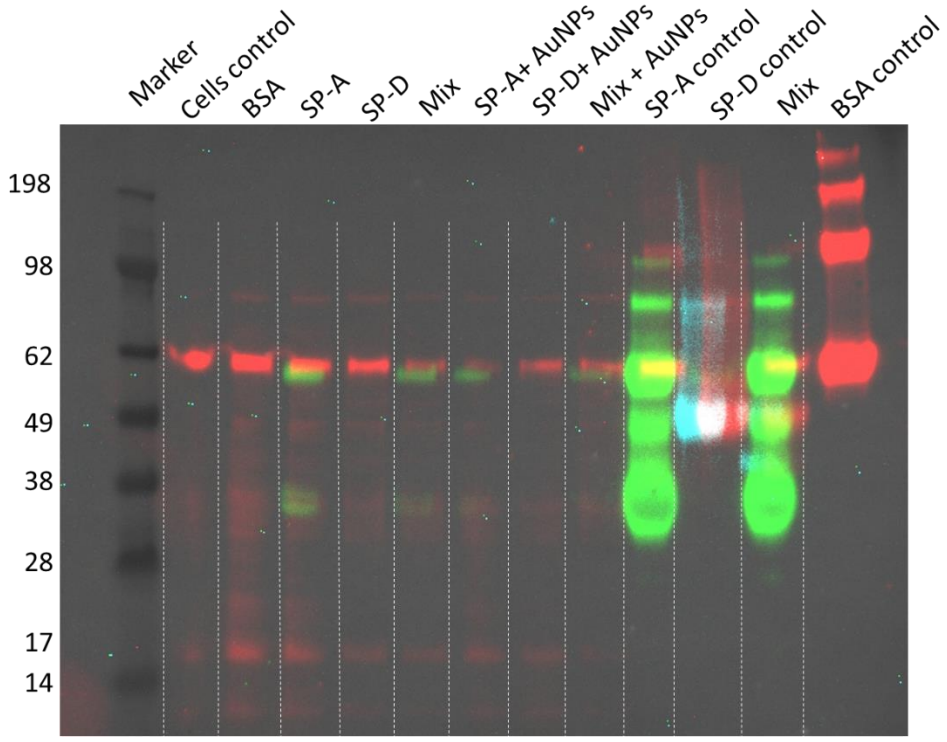

Figure 4.30 Whole-cell immunoblotting in the presence of SP-A, SP-D and nanoparticles after 4 hours. 10 µl of approximately 1 × 10^6 cells lysate was used for each row. **Cells control** – RAW264-7 cells grown with 0.5% HI FCS supplemented medium. **BSA, SP-A, SP-D** – the cells were grown as in control with the addition of 10 µg/ml of the corresponding protein. **Protein + AuNPs** – corresponding proteins with 7 × 10^{10} particles/ml. Protein controls – 10 µg of protein control. **Mix** – 30 µg of SP-A:SP-D:BSA mix at 1:1:1 ratio. Green – SP-A, magenta – SP-D, red – BSA.

Multimodal imaging was employed to semi-quantify the amount of AuNPs internalised by cells in the presence of surfactant proteins (**Figure 4.32**). The media supplemented with 0.5% HI FCS was used. There was no difference between control (AuNPs in cell culture medium) and BSA (AuNPs + BSA in cell culture medium). There was reduced uptake in SP-A and SP-A:SP-D but it was not statistically significant. The uptake of AuNPs in the presence of SP-D was significantly suppressed by about 60%. There were no bright pixels found in negative control cells treated with cell culture medium only.

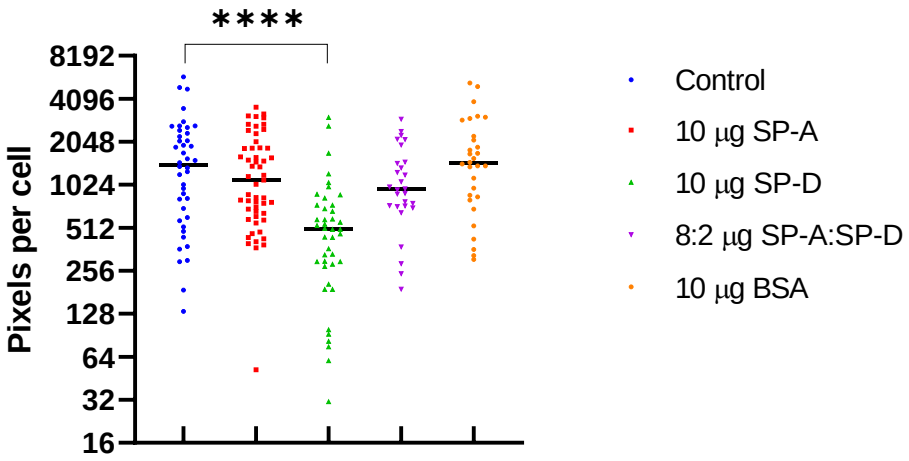

Figure 4.31. Uptake of 20 nm AuNPs by RAW264.7 cell line semi-quantified using multimodal imaging. Pixels per cell were quantified as a sum of all bright areas in the SHG channel across the whole Z-stack of a cell using ImageJ. Data represent three individual experiments with at least 20 replicates each. The control was cells with AuNPs and no protein. Negative control – 10 images of AuNPs untreated cells (no bright pixels were found, equals 0). Black horizontal lines – median. **** - $p<0.0001$ (Mann-Whitney, t-test). Log_2 scale.

4.5 Summary of the results

Within this chapter, the stability of AuNPs in multiple physiological-like conditions was explored and the ability of SP-A and SP-D to selectively adsorb or aggregate AuNPs was investigated. Additionally, the role of SP-A and SP-D was analysed on possible AuNPs toxicity and/or uptake alterations using the macrophage-like cell line, thus addressing Aims 2 and 3 (**Section 1.5**):

2. Characterise the interaction of AuNPs with SP-A and SP-D

3. Characterise the possible *in vitro* nanotoxicity of gold NPs on cell culture models in the presence of SP-A and SP-D.

The main results and achievements reported in this chapter are:

- AuNPs showed to be highly susceptible to salt buffers, which induced their aggregation at as low as 0.5 mM $CaCl_2$ concentrations and led to precipitation.
- Addition of proteins (i.e. BSA or serum) stabilised AuNPs in high salt buffers for at least 24 hours (*in vitro*) in a concentration-dependent manner.
- It was not possible to determine the role of SP-A and SP-D in the aggregation of AuNPs in a calcium-dependent manner using spectroscopy-based techniques, due to both protein and particles self-aggregation.
- For the first time it was shown that both SP-A and SP-D self-agglomerate and precipitate even at low concentrations (e.g. 20 µg/ml) and centrifugal forces (4000 × g).
- For the first time the affinity of SP-A and SP-D to plastic tube walls (and other plastic surfaces) was visually demonstrated compared to BSA, using Bradford reagent.
- There was evidence of higher SP-A (with Ca^{2+} - $p=0.001$, without Ca^{2+} - $p=0.065$) and SP-D (with Ca^{2+} - $p=0.237$, without Ca^{2+} - $p=0.065$) affinity to AuNPs compared to BSA ($p>0.6$).
- LD_{50} for 20 nm AuNPs was around 7×10^{11} particles/ml and did not change a lot in the presence of 1% or 10% of HI FCS.
- There was no evidence of SP-A or SP-D aided AuNPs toxicity reduction in the macrophage-like cell line, compared to BSA. The viability was insignificantly improved irrespective of the protein type (SP-A, SP-D, or BSA) compared to no added protein.
- Semi-quantification using the multimodal imaging showed that SP-A suppressed the uptake of AuNPs in RAW264.7 cell line by about 25% ($p=0.445$), while SP-D by almost 65% ($p<0.001$). The 4:1 SP-A:SP-D mixture reduced the uptake by 35% ($p=0.199$). BSA had no impact on the uptake. This is the first time the technique was applied for such a study.

4.6 Discussion

After the addition of AuNP into high salt buffers, the changes in colour were immediately observed, indicating that particles were destabilised and aggregating. It is well known that the colour of AuNPs depends on their size and shape. For the spherical particles, the larger they are, the higher the red-shifted absorption maximum is (**Figure 4.32**). The observed colour shift is explained by how AuNPs interact with light. An oscillating electric field of the light interacts with free electrons on the surface on AuNPs, causing a collective oscillation of electron charge that is in resonance with the frequency of visible light.[256] This collective oscillation of electrons on the surface of AuNPs is known as surface plasmon resonance (SPR). As the size of AuNPs increases and/or as the distance between particles decreases due to aggregation, a shift to a longer wavelength and peak broadening of the SPR is observed.[257] In the case of 20 nm AuNPs, used in the experiments, the SPR caused absorption of light (λ_{max}) at about 520 nm (green colour), yielding a characteristic red colour. As the size increased, the opposite process was observed, where λ_{max} shifted to a red region and particles appeared blue/purple, which is in agreement with observed results in **Figure 4.1** and **Figure 4.6**.

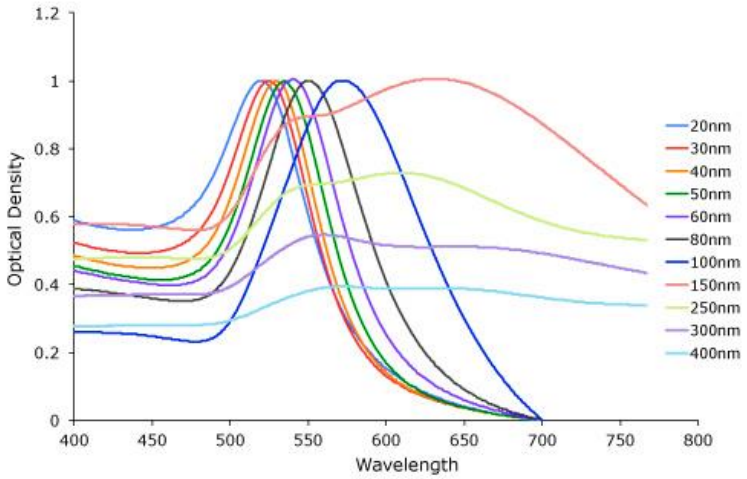

Figure 4.32. Gold nanoparticle size dependant surface plasmon resonance. Note the shift in the absorption maximum to the red region as AuNPs increases in size. Reprinted from [258], distributed under CC BY 4.0 license.

The colour shift induced by TBS^{Ca} and TBS^{EDTA}, as observed in **Figure 4.1**, was associated with salts present in the buffers. After the addition of NPs to individual components of the buffer system, it was concluded, that 150 mM NaCl and 5 mM $CaCl_2$ caused the aggregation. This was also confirmed with DLS (**Figure 4.2**), where the size increased significantly and after the first

measurement (3 minutes post mixing) the size was at least 4 times larger than initial. 20 mM Tris and 10 mM EDTA did not affect aggregation, which was confirmed by no shift in colour. There are surprisingly few papers in the nanotoxicology focused literature where this effect is highlighted, explained how it was avoided, overcame or what impact it had on the results where a physiological-like medium has been used. This effect has to be addressed as it can potentially influence the *in vitro* and *in vivo* collected data due to actual particle size change. Since 150 mM of NaCl is considered to be a physiological concentration, it cannot be removed or replaced to prevent aggregation, as it will alter the osmolarity and cause cells to rupture. SP-A and SP-D are calcium-dependent proteins which require at least 2 mM of calcium ions[8] (some sources cite 0.6 mM as the minimum concentration[259], while some indicate calcium-mediated difference at 0.15 mM[107]), meaning calcium is also an essential variable in these experiments, but even at 0.5 mM $CaCl_2$, the aggregation was induced. Moreover, it has been shown that divalent cations have a stronger aggregation effect on NPs than monovalent ions at the same concentration.[260] Nanoparticles do not aggregate due to repulsive forces where particles repel each other because of the same surface charge (either positive or negative). However, once salts are added, counter-ions diffuse around the nanoparticles and screen the surface charge, allowing particles to come close to each other and stick together.[261]

Next, the experiments were transferred into a more biologically relevant buffer model. For that purpose, RPMI 1640 medium was chosen, as it is essential for all *in vitro* cell culture experiments. Since both 20 nm AuNPs and the cell culture medium are red coloured and share similar absorbance spectra[262], the colourless (phenol red-free) medium was used in all spectrophotometric experiments to avoid any interference. While there were multiple peaks observed in the unsupplemented medium, they were randomly scattered across the whole size range (**Figure 4.3**). It was decided that these peaks would have no or minimal influence on any results, as counts per second did not pass the software quality check. Mixing 20 nm AuNP with non-supplemented RPMI 1640 showed very similar results to TBS both seen with DLS and SLS (**Figure 4.4** and **Figure 4.6**). The size kept increasing for a least 15 minutes, with an increase observed after each measurement (**Figure 4.5**). There were small peaks observed between 10 and 20 nm. Considering the particles were at least 20 nm, those peaks most likely had a different source of origin than the particles themselves. This was explained using multiple scattering effect.[263] The DLS measurements are based on measuring the time scale of light fluctuations at the detector caused by Brownian motion of dispersed particles. Small particles diffuse rapidly and result in rapid intensity fluctuations at the detector; large particles diffuse slower with longer scattered light fluctuations at the detector. In ideal measurements, the particles have to be dilute

enough so that the light scattered from a single particle reaches the detector without interference from other particles. Multiple scattering is the process when the light is scattered from a diffusing particle and is then rescattered by one or more particles before reaching the detector. The rescattering changes the time of the light fluctuations at the detector and thus results do not represent the true particle size. Hence, it is important to adjust the concentration (number of particles) for each specific size (refer to **Figure 4.33**). All experiments were optimised for 20 nm AuNPs, their aggregation led to the increase in size and hence rescattering. The intensity of each subsequent peak also increased with size, as the amount of light scattered from a particle is strongly dependent on its size. According to Rayleigh scatting, the scattered light intensity is proportional to the sixth power of the diameter of the particle.[264] Hence, larger particles at the same concentration will scatter the light stronger than smaller, which explains the increased scattering intensity for larger particles (applicable both for DLS and SLS). The effect might be multiplied by the presence of non-homogenous size distribution in a high salt buffer.

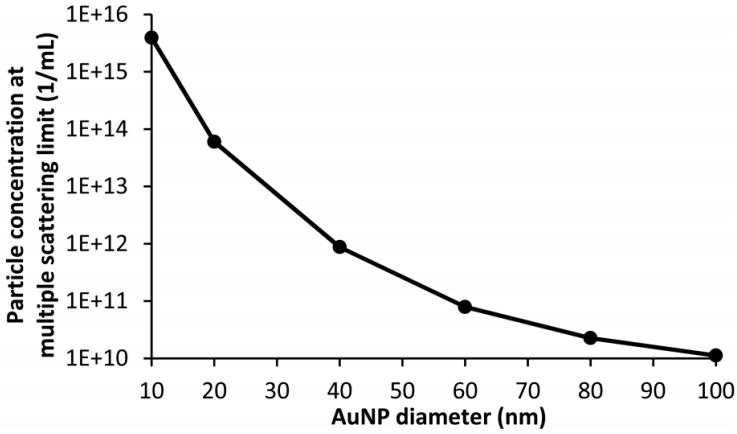

Figure 4.33. Predicted DLS concentration limit beyond which multiple scattering occurs. Reprinted with permission from Zheng et al[263]. Copyright (2016) American Chemical Society.

The addition of AuNPs to RPMI medium supplemented with 1% HI FCS prevented aggregation of NPs. According to the DLS results, 20 nm AuNPs increased in size up to about 70-80 nm. However, the size remained stable from the first to the last measurement (about 15 min). This can be explained by the formation of a protein corona on the surface of NPs. Nanoparticles are usually stabilised by repulsive forces, originating from the surface charge, or via the creation of a repulsive barrier (such as citrate or other detergents) that prevents their aggregation upon collision. In the presence of strong electrolytes, these barriers may be destroyed. Proteins can adsorb to the NPs, creating a physical barrier (i.e. steric stabilisation), preventing or reducing the aggregation by physically not allowing particles to collide.[265] The DLS data was fully supported by

the SLS results, where differences in light scattering intensity were not observed, suggesting that the size did not change or changed insignificantly. Even when there were no free proteins in the high-salt buffer, the particles with pre-formed protein corona remained stable (**Figure 4.7**). When the particles were pre-incubated in 1% HI FCS supplemented medium and then washed once or twice, they were relatively stable upon resuspension in serum-free medium. The hydrodynamic diameter increased from 25 nm for bare particles to 157 nm (1x wash) and 180 nm (2x washes) for pre-incubated. It was not possible to establish the actual aggregation degree for the particles as it is not possible to measure the thickness of protein corona by DLS. Since the protein corona is dynamic and can form soft and hard layers, the thickness may vary significantly depending on the incubation time. The zeta-potential difference between 1x and 2x washed particles was relatively small and it is difficult to conclude whether any charge difference came from the protein corona. The Zeta potential was measured in 0.1x PBS, as conventional buffers (i.e. RPMI medium) are not suitable due to high salt concentration, which leads to the corrosion of the electrodes during the analysis. Pure water was not used either, as a certain concentration of electrolytes is required to conduct the electric charge.

As the last verification step of the behaviour of AuNPs in high salt buffers and the impact of proteins on their stability, the morphology of AuNPs and their aggregates were analysed with TEM (**Figure 4.8**). The images revealed that AuNPs in water were of uniform spherical shape and did not form aggregates, as predominantly single particles were observed on the grid with occasional clusters of less than 10 particles. After incubation in RPMI, the particles formed large aggregates of various sizes, ranging from several hundred nanometres to several microns. However, AuNPs incubated in RPMI medium with 1% HI FCS did not form any large aggregates and were more similar to those seen in the water.

Previously, using DLS, it has been shown that SP-A and SP-D can bind to polystyrene beads with different surface modifications and induce aggregation.[10] The major difference between gold and polystyrene particles is that the latter are stable in high ionic strength solvents, while gold aggregates immediately. Use of the regular TBS buffer with the addition of calcium or EDTA induced the immediate aggregation, which was inconsistent between the experiments and it was unclear whether the aggregation protein or salt-induced. Thus, since such a buffer model was not applicable for this model anyway, the experiments were transferred into the RPMI 1640 medium. The cell culture medium allows significantly less control due to a large number of additives (see **Appendix C**) but provides a more realistic model which can be translated into cell culture experiments. The main issue is that no calcium can be added due to the presence of phosphates,

which lead to the formation of insoluble calcium phosphate salts. On the other hand, the medium already has about 0.425 mM Ca^{2+}, which is just below the reported minimum for SP-A/SP-D activation. Nonetheless, the DLS experiments were performed in RPMI medium (**Figure 4.9** to **Figure 4.11**). The higher protein concentrations, 20 µg/ml, were used to allow for better protein corona formation. There was no protein-induced aggregation detected. The primary issue was due to the introduction of two components of very different sizes, such as 20 nm AuNPs, self-aggregating 20 nm SP-A and 100 nm SP-D, and about 8 nm BSA (nominal sizes). As it was discussed before, larger particles scatter the light much more strongly than smaller particles, thus invalidating SP-D results (100 nm >> 20 nm), where most of the signal might come from the protein alone. SP-A and AuNPs were approximately the same size, however, both the AuNPs and SP-D self-aggregated, also invalidating the results. Finally, BSA stabilised AuNPs as expected from previous results. The BSA was not expected to self-aggregate, as previous results showed it was stable in the buffers. The average size of AuNPs + BSA was about 48 nm. Considering the diameter of BSA and corona formation, the size fell within an expected range.

None of the spectrometric techniques allowed for the establishment of whether SP-A/SP-D can selectively and in a calcium-dependent manner bind to AuNPs and induce their aggregation. Hence, due to intrinsic AuNP properties, any technique that requires the particles to remain stable in a buffer could not be applied. Another approach employed SDS-PAGE based techniques, which was adapted from Schulze et al[108]. It is already established that proteins adsorb to AuNPs forming protein corona. Thus, if particles are incubated in a protein-containing solution and then washed, to remove any excess and unbound proteins, the hard corona can be removed under reducing conditions and analysed with SDS-PAGE, while the supernatant can also be analysed quantitively as the protein concentration will reduce because of the corona formation. Firstly, to avoid any false-positive results SP-A, SP-D and BSA adsorption to the tubes were tested. It was hypothesised that if any proteins adsorb to the tube walls, they can be reduced and removed, allowing for their collection and further analysis with SDS-PAGE. The tubes were washed with 50 µl of reducing buffer (the same used for SDS-PAGE) at 90 °C for 10 min with end-to-end mixing every 1 min. However, silver staining did not show any traces of the proteins in the reducing buffer collected from the tubes, suggesting no protein adsorption.

In a different experiment, the same process was followed, but instead of applying reducing buffer, 200 µl of Bradford assay reagent was added in each tube with end-to-end mixing for 10 min. After the wash, all adsorbed proteins were stained blue (**Figure 4.12**). The tube with SP-A was the most colour-intense. There was also a slight difference between the calcium and EDTA tubes, with

calcium being more colour-intense, but it was not possible to measure this quantitatively. SP-D was also stained but to a much lesser extent than SP-A. BSA was stained only slightly, suggesting it has very low affinity for LoBind tubes. This numbers can be further normalised to staining susceptibility of these proteins by the Bradford assay (**Figure 4.13**), where BSA is 5 times more sensitive than SP-D, and 2 times more than SP-A. According to the manufacturer, LoBind protein tubes provide 80% higher sample recovery compared to vessels made from standard materials.[266] There are several possible explanations for the observed result. Firstly, it is explained by Van der Waals forces, but these forces are very weak, and all proteins had to be washed off under reducing conditions. Secondly, the tubes are made of polypropylene which has no functional groups that can be charged and facilitate electrostatic interaction. Next, the manufacturer points out that tubes are designed to repel the hydrophobic protein core. Since SP-A and SP-D are hydrophilic they could adsorb to the walls due to hydrophilic and hydrophobic forces. Finally, surfactant proteins have a high affinity to sugar moieties (i.e. LPS) and the tube's surface may share some structural similarities resulting in strong binding. However, it does not explain the resistance to reducing conditions.

The particles incubated with the proteins were spun down, washed, reduced and loaded onto an SDS-PAGE gel (**Figure 4.14**). All particles had characteristic bands indicating the formation of the protein corona. Moreover, the bands were much brighter than corresponding controls with the same concentration, suggesting that particles led to up-concertation of proteins on the surface. As expected, the intensity of the SP-A band in the presence of calcium was higher, compared to EDTA. However, there was no difference between SP-D and BSA with or without calcium. These two proteins could bind to the surface in a non-specific fashion via electrostatic interaction. Moreover, unexplained bands with a molecular weight different from the SP-A, SP-D and BSA proteins were observed at 118 kDa across all samples, which were never seen in controls even at high protein concentrations. SP-D also had an uncharacteristic band at 60 kDa, which was similar to SP-A dimer. It was hypothesised that these bands were because of a protein structure/conformation change after interaction with AuNPs, which might have resulted in an altered migration speed in the electric field. Studies indicated that nanoparticle-protein interactions result in conformation changes.[267] For example, AuNPs were shown to induce conformational changes in BSA in a concentration dependent manner.[268] The Western blot analysis showed similar results (**Figure 4.15**). No unexplained bands were seen in SimplyBlue staining. Unidentified bands could be further analysed using other analytical techniques, such as mass spectroscopy, but this was beyond the scope of the study. Slight SP-A contamination was noticed in SP-D samples, which was also expected and associated with the SP-D purification

process. While it could be due to cross-contamination or overflowing of the wells, these bands have already been seen previously. The supernatants were collected and analysed with silver staining (**Figure 4.16**). Silver staining showed that both SP-A and SP-D were at significantly lower concentrations, compared to control samples, indicating that most of the proteins were bound to nanoparticles. BSA remained at approximately the same intensity as control. The same experiments were performed with a 1:1:1 SP-A:SP-D:BSA mixture. It is estimated that the SP-A:SP-D ratio in the human body is about 10:1, but for initial experiments, the equivalent masses were used for simplicity. SDS-PAGE showed (**Figure 4.17**) distinct SP-A bands at 35 kDa which were more saturated in the presence of calcium than EDTA. SP-A was visible at 45 kDa but with a larger band at about 60 kDa. BSA could not be resolved due to overlap with SP-A. Western blot (**Figure 4.18**) showed that no BSA was adsorbed to AuNP, which was unexpected. There were several explanations. One, is that SP-A and SP-D have a significantly higher affinity to AuNPs than BSA and hence "outcompeted" it. However, BSA was detected in previous results and its presence was expected. That led to the second explanation. It was noticed that at very high SP-A and SP-D concentrations (around 3 mg/ml) proteins self-agglomerated and precipitated over some time. It was hypothesised that SP-A and SP-D formed sub-micron agglomerates at lower concentrations which were spun down. As a result, SP-A and SP-D precipitate, forming high concentration protein pellets, and were picked up during AuNP collection (as the particles were spun down too) and analysed as false-positive results. Yet, it is unclear why SP-A and SP-D controls were still visible at such high intensity (**Figure 4.16**). It is possible AuNPs could facilitate the precipitation.

The supernatants of the centrifuged and non-centrifuged proteins were quantitatively analysed by the Bradford assay to understand the behaviour of surfactant proteins in the buffers. Centrifuging SP-A and SP-D led to a significant decrease in concentration (**Figure 4.19**), SP-A in TBS^{Ca} reduced by 85% and 75% in TBS^{EDTA}. The concentration of SP-D in TBS^{Ca} reduced by 45% and 35% in TBS^{EDTA}. The concentration of BSA did not change. In subsequent experiments when SP-A and SP-D were dissolved in Milli-Q water and their supernatants were analysed by Bradford assay, the SP-A concentration remained at a similar level as before centrifuging, though SP-D still reduced by the same amount. Considering DLS data, SDS-PAGE and Bradford assay it can be concluded that SP-A self-agglomeration is strongly influenced by salts. For the SP-D the results are not as straightforward, but salts might have an equally important impact as in SP-A. The confirmation for this hypothesis, at least for SP-A, was found in a study by Ruano at el[269] who showed that salts, such as NaCl and $CaCl_2$, pH and temperature lead to the self-aggregation of SP-A. A similar explanation could be applied for SP-D, as it belongs to the same family of collectins. Such behaviour was unforeseen, as SP-A and SP-D are water-soluble (hydrophilic)

proteins, meaning 4,000 × g at 37 °C and physiological-like buffer should not be enough to spin them down, as most hydrophilic proteins require ultracentrifuges to do so.[270,271] For example, BSA dissolved in PBS requires more than 450,000 × g and two hours to precipitate.[272] There is limited literature on the topic, what makes comparing the results complicated, as in some cases authors do not mention how the control samples were prepared and what influence centrifugation had[8,273], in other cases authors described the control preparation, but used very different buffer system with different salt concentrations[108], which could have a direct effect on the protein properties. Nonetheless, considering this limitation and using centrifuged controls in parallel, the results showed that both SP-A and SP-D bind to AuNPs (**Figure 4.20**). There was about a 50% (p=0.001) SP-A reduction in the supernatant in TBS^{Ca} and a 10% (p=0.065) reduction in TBS^{EDTA}. SP-D also showed an 18% (p=0.237) reduction in the supernatant in TBS^{Ca} and a 22% (p=0.019) reduction in TBS^{EDTA}. There were no changes in BSA observed (less than 3% reduction).

Considering the explanations above, the SDS-PAGE data (**Figure 4.14**-**Figure 4.18**) has to be re-evaluated and also interpreted with caution. As it has been shown that the proteins precipitate when centrifuged. It is now clear that their concentration in the supernatant will reduce significantly as they accumulate in a form of a pellet on the bottom, as illustrated in **Figure 4.34**. Hence, when SDS-PAGE is used to analyse the supernatant the drop in concentration (visible as a less intense band or its absence) is not related to protein corona formation on AuNPs; instead the proteins self-aggregate and then precipitate due to centrifuging. At the same time, when the supernatant is removed, a combination of all unbound proteins and AuNPs with protein corona is on the bottom. Since SDS-PAGE requires the collection of the particles and their transfer on the gel, all aggregated unbound proteins are collected too, leading to high-intensity bands and false-positive results. In addition to the inability to apply any AuNPs size-dependent techniques, no centrifuge-based methods can be used too, as unbound proteins cannot be safely removed from the system without influencing the results.

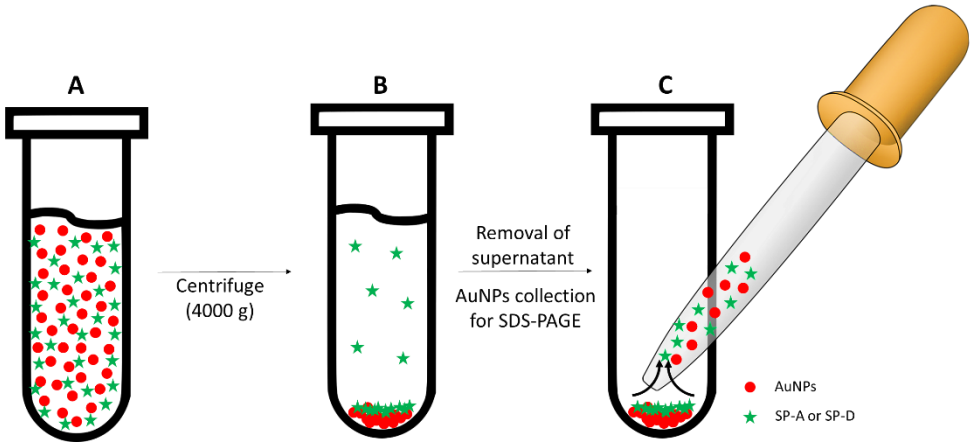

Figure 4.34. An illustration explaining the limitations of centrifuge-based methods for SP-A and SP-D analyses. A – the initial sample containing SP-A/SP-D and AuNPs is expected to be evenly dispersed. **B** – the centrifugal forces pull both AuNPs and the proteins to the bottom, removing particles from the supernatant and reducing protein concentration. **C** – collection AuNPs inevitably drags in the undesired unbound proteins.

The final steps in studying the *in vitro* properties of SP-A and SP-D and their role in nanotoxicity were performed in mouse leukemic monocyte/macrophage-like cell line (RAW264.7). The cell line has been described as an appropriate macrophage model and is widely used studying a broad range of bio-nano interactions where a macrophage model is required.[274–276] Unlike the human-derived THP-1 cell line, they do not require differentiation, thus reduce the culturing time and variability. As mentioned before, HI FCS is required in the medium to stabilise AuNPs and maintain their original size. Moreover, the presence of serum is required to mimic physiological-like conditions, as once particles contact any biological fluid, they immediately form a protein corona. The uptake of NPs also depends on their surface and, specifically, protein corona. Finally, the serum contains hormones and growth factors which maintain the cell culture in a stress-free state over prolonged periods of incubation. These were the main reasons why experiments were performed in a serum-supplemented medium. To minimise the interference from HI FCS proteins during SP-A/SP-D studies, the concentration was reduced to 1% in RPMI medium. The cells were serum-starved overnight to synchronise their growth cycles.

To begin with, the LD_{50} was established for AuNPs in both 1% and 10% HI FCS (**Figure 4.21**). Both for 1% and 10% HI FCS the LD_{50} was close to 4.375×10^{10} particles/ml. At 1.367×10^{9} particles/ml the viability returned to 100%. To keep the consistency across all the *in vitro* experiments it was decided to use 7×10^{10} particles/ml, as it also allowed easier and more accurate sample preparation, hence minimising variability. To illustrate the importance of serum (or any other

additive) on stabilisation of AuNPs, the cells were exposed to AuNPs in the absence and presence of 1% HI FCS (**Figure 4.22**). Serum-free media, as expected, induced the aggregation of the particles, which precipitate on the bottom of the flask. While serum-free media allows greater control over the molecular composition of the media and reduced interference with proteins of interest (SP-A and SP-D), the results from this approach cannot be extrapolated to 20 nm AuNPs, since the size is the key parameter in nanotoxicology studies. As AuNPs precipitated on the bottom, their concentration in suspension dropped and aggregates become more accessible to the cells because: 1 – larger particles are phagocytosed easier; 2 – all particles are now on the bottom, hence there are more available particles around a cell. If 1% of HI FCS is added, then AuNPs maintain their size and stay suspended. As can be seen from **Figure 4.22B** even particles inside the cells were still red, suggesting they were within their original size.

When the SP-A, SP-D and BSA were tested in combination with AuNPs there was no difference in viability found (**Figure 4.23**-**Figure 4.25**). Compared to AuNPs only, the addition of one of the three proteins equally increased the viability of the cells (from 40% to 60%) and there was no difference found. It was hypothesised that no difference was observed due to mannan-binding lectin, conglutinin and collectin-43 (later two found in Bovidae only) – collectin-family proteins found in serum which have similar roles to SP-A and SP-D.[277] While the exact concentration of serum-present collectins is not known, however, they could compete with SP-A and SP-D and mask their impact. But it is still interesting that the addition of only 1-10 μg/ml of the protein led to such an increase in viability. For the reference, 1% supplemented medium contains about 400 μg/ml of proteins. In SP-A and SP-D protein controls, there was a minor reduction in viability, most likely associated with LPS in these proteins, which is present in BALF purified proteins. The exact impact of the proteins on the viability of the cells can be seen in **Figure 4.35.** Similar to MTT, there was no significant difference found across the samples analysed with LDH assay (**Figure 4.26** to **Figure 4.28**). The collected data largely support the inert and non-toxic properties of AuNPs published in literature.[183,278–280] It was not possible to establish the nanotoxicological role of SP-A and SP-D in the RAW264.7 cell line.

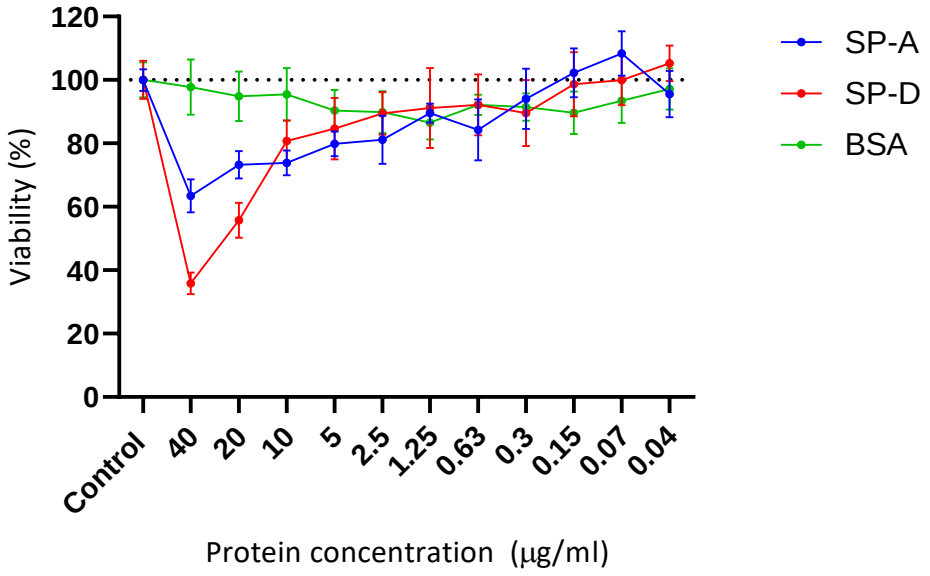

Figure 4.35. Concentration-dependent impact of SP-A, SP-D and BSA on the viability of RAW264.7 cells. The proteins of interest may reduce the viability of the cells. Data represent averages of three independent experiments performed in duplicated. Mean ± SD.

Whole-cell SDS-PAGE SimplyBlue staining and western blot analyses were used to determine whether the concentration of proteins, specifically SP-A and SP-D, increases inside the cells in the presence of AuNPs (**Figure 4.29**, **Figure 4.30**). It was hypothesised that due to protein corona formation the amount of internalised proteins will be higher compared to the cells which were not exposed to AuNPs. To avoid protein destruction, which might happen in lysosomes, the incubation time was reduced to 4 h. However, the hypothesis did not find any support, as no increase of internalised SP-A or SP-D in the presence of AuNPs was observed. Moreover, no SP-D bands were detected in any experiments.

Multimodal imaging was used to semi-quantify the number of AuNPs taken by cells (**Figure 4.31**). Since, at the current stage, the technique allows only relative quantification – no mass or particle number could be measured, all values were expressed as pixels per cell. There was no difference observed between the cells treated with AuNPs only and AuNPs with BSA, media values were 1465 and 1430 pixels per cells, respectively. The results met expectations, as BSA was already present in HI FCS and its addition was not expected to impact the results. The SP-A reduced the uptake of AuNPs by about 25% ($p=0.445$), while SP-D by almost 65% ($p<0.001$). The 4:1 SP-A:SP-D mixture reduced the uptake by 35% ($p=0.199$). Such ratio was chosen to represent higher SP-A abundance in the BALF.[62] The results were opposite to expectations. It was hypostatised that

surfactant proteins will aggregate AuNPs, making them easier to phagocytose or facilitate their uptake, where SP-A/SP-D act as signalling molecules. However, in all cases, there was a reduction of internalised particles. There are two important points to consider. First, there was significant cell-to-cell variability with up to two orders of magnitude difference. Second, the selection of the cells for imaging is still a manual process and might be a subject for subconscious bias during the selection process.

While the applied methods were semi-quantitative it did not allow to express the concentration in mass or number particles per cell. Instead, it allowed comparing the results between the different group. However, there are recent studies showing that two-photon microscopy can be used for quantification[221], as the values extracted from the images can be correlated to the data collected by ICP-MS. Such a correlation was not performed within this study as it required extensive method development and can be performed in future. On the other hand, synchronous multimodal imaging developed in this study may allow more accurate correlation with ICP-MS data, as localisation of particles can be performed in a more precise fashion.

4.7 Conclusions

It was established that AuNPs are sensitive to high-salt buffers and the presence of proteins is required to stabilise them and prevent from gravity precipitation. The spectrophotometric methods were found largely inapplicable for studying the ability of SP-A and SP-D to agglutinate AuNPs, thus it is not understood whether the aggregation of AuNPs is induced by the proteins or salts. Surfactant proteins showed to be highly adsorptive in “test-tube” experiments in the SP-A>SP-D order, both to the AuNPs and plastic tubes. There was tentative evidence of higher SP-A and SP-D affinity to AuNPs compared to BSA. The proteins did not influence the toxicity of AuNPs in cell culture but are likely to inhibit the uptake of AuNPs.

The *in vitro* methods used in this study had multiple limitations and reproducibility issues associated with the intrinsic properties of AuNPs. More research employing additional techniques is required to support the findings and build a better understanding of the surfactant proteins and AuNP interactions.

Chapter 5 Clearance and translocation of AuNPs from the respiratory system in wild type and knockout mice

5.1 Introduction

The respiratory system is an attractive route for drug delivery due to its large surface area available in alveoli and high vascularisation, which makes the lungs an appropriate site for drug absorption. Nanomedicine is an emerging research field, as it allows for the incorporation of drugs inside the particles or on their surface, while the particles themselves can be modified to target specific cells and organs. However, the respiratory system has evolved defence mechanisms to inactivate and clear any foreign bodies once deposited. This includes both microorganisms, as well as environmental and engineered nanoparticles. As already discussed in this work, SP-A and SP-D are two innate immunity proteins that help to keep the lungs in a non-infectious and non-inflamed state. However, the proteins cannot differentiate "good" nanomedicine from "bad" nanopollution, while the uptake of nanoparticles also depends on the health of the organism. Hence it is important to understand the *in vivo* role of surfactant proteins.

Gold nanoparticles have gained a lot of attention, as they allow simple surface modification to attach drugs, biomarkers or alter the charge while being biocompatible and non-toxic in *in vivo* models.[281–283] However, biocompatibility depends on the size and surface modification. In general, the toxicity is inversely proportional to the size.[284] While there are many *in vitro* studies, the number of *in vivo* studies investigating the role of surfactant proteins on the uptake and translocation of nanoparticles is very limited[109,110].

Experimental research is the vital route to collect the information. If the study aims to understand a concept which will be applicable for humans, then the most reliable data and information will be obtained from volunteers (i.e. human studies). However, in reality this is not always possible due to ethical or technical issues. Hence, the majority of experiments are performed *in vitro*, using cells cultures and test tubes. While such experiments provide important data often in a short time, they might not resemble the complexity of the whole organism. Hence, *in vivo* experiments are required to fill the gaps. Traditionally, rodents (i.e. mice or rats) have been the most often used model for biomedical research, as they share anatomical and genetic similarities[285,286]; humanised models bridge the gaps between humans and animals[287]. Yet, it is important to understand the differences and limitations of each model for a particular study.

The study was designed to evaluate the *in vivo* clearance and translocation to the secondary organs of 20 nm AuNPs from the respiratory system following short term nose-only exposure. This is the first known study that used SP-A and SP-D genetic knockout mice to research the role of the surfactant proteins. While knockout mice are the best currently available model, there are some differences compared to humans, which are summarised in **Table 5.1**. Potentially the most significant ones are airway branching type and tree generations. Reduced branching number and its different structure in mice may potentially lead to larger number of particles reaching alveoli, while gas-exchange units at the end of short paths will be exposed to higher concentrations of inhaled particles. Almost 20 times larger minute volumes mean there is a greater air volume per mass unit circulated and hence higher chance of deposition. Finally, humans have an increased number of ciliated cells, meaning the clearance speed might differ from mice.

Table 5.1. Anatomical differences between mice and human respiratory systems.

Feature	Mouse	Human
Lung lobes	Four right, one left	Three right, two left
Cartilaginous airways	Trachea and primary bronchi	Trachea through small intersegmental bronchi in the lung
Respiratory bronchiole	Absent to rare	Present
Airway branching pattern	Monopodial	Dichotomous
Respiratory tree generations	13	23
Airways to lung ratio	11%	5.7% in rats (not found for humans)
Trachea	Nonciliated > ciliated > basal	Ciliated > basal > nonciliated and mucous
Primary bronchi	Nonciliated ≥ ciliated > basal	Ciliated > nonciliated > mucous > basal
Terminal bronchioles	Nonciliated > ciliated	Ciliated > nonciliated
Alveoli	Relative cell numbers are not well defined in mice	Type II cells > type I cells; type I cells are very thin but have a much greater cell volume than type II cells
Alveoli size (mean linear intercept)	80 µm	210 µm
Blood-gas barrier thickness	0.32 µm	0.62 µm
Total lung capacity	1 ml	6000 ml
Breath rate	255 per min	12 per minute
Tidal volume	0.15 ml	500 ml
Minute volume	1500 ml/min/kg	85 ml/min/kg
SP-A form	Homomeric SP-A	SP-A1 and/or SP-A2

5.2 Aims and objectives

This chapter addresses the aims and objectives summarised in clause 4 of **Section 1.5, which are:**

4. Characterise the potential *in vivo* translocation and toxic effects of NPs using mice deficient for SP-A, deficient for SP-D and wild-type mice.

4.1. Expose deficient and wild-type mice to 20 nm AuNP in the established inhalation model.

4.2. Quantify the concentration of AuNPs in the lungs, liver, spleen, and kidneys via multimodal imaging, inductively coupled plasma mass spectrometry (ICP-MS), single particle ICP-MS, laser ablation ICP-MS and TEM.

5.3 Methods

All methods used in this chapter are detailed in **Chapter 2**.

5.4 Results

The mice were exposed to AuNPs on 4 consecutive days. One AKO mouse died (in a 7-days group) after the exposure. The cause of death was unknown but unlikely to be associated with the exposure to AuNPs.

Aerosols from each day were analysed. **Table 5.2** summarised the aerosol characteristics. On average mice were exposed to 2.68×10^6 particles/cm^3 with a geometric mean diameter of 70.3 nm (by number) or 187.4 nm (by mass), which corresponds to 3687 µg/m^3 of AuNPs or 472 µg/m^3 of elemental gold. Filters used for aerosolised AuNPs collection and analysis are presented in **Figure 5.1**. The filters appear pale-violet coloured due to collected AuNPs on the surface. **Figure 5.2** graphically represents the size distribution of AuNPs, which is summarised in the table below. According to the presented data, the aerosol characteristics were consistent on different experimental days.

Table 5.2. Aerosol characteristics and parameters. AuNPs aerosol characterisation of the first single 3 h exposure *in vivo* experiments**. Filter number** – filters from each experiment. **Geometric mean diameter** – the size of AuNPs as the most abundant *number* and *mass*. **Gravimetric AuNPs mass concentration** – calculated from passed air through the filter and weighed AuNPs on it. **Mass of Au** – the mass of pure gold per m^3 of air determined by ICP-MS.

Filter number	Number of AuNPs	Geometric mean diameter (number)	Geometric mean diameter (mass)	Gravimetric AuNPs mass concentration	Mass of Au
#	#/cm^3	nm	nm	µg/m^3	µg/m^3
1	2.63×10^6	69.2	189.8	3493	423.8
2	2.79×10^6	71	194.3	3946	506.5
3	2.65×10^6	70.6	180.8	3486	442.8
4	2.64×10^6	70.4	184.5	3822	515.8
Average	*2.68×10^6*	*70.3*	*187.4*	*3687*	*472.2*
SD	*7×10^4*	*0.8*	*5.9*	*233*	*45.8*

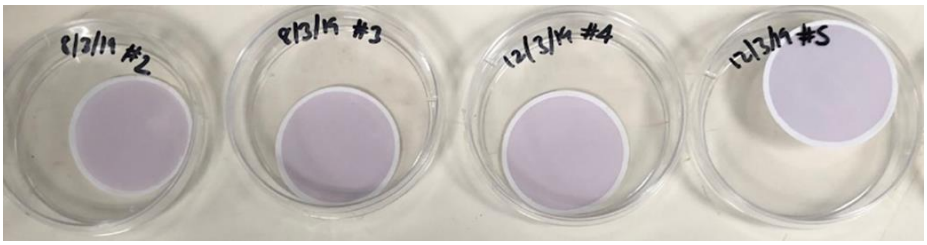

Figure 5.1. Filters with deposited AuNPs after each exposure experiment. Each filter corresponds to an individual exposure experiment on a separate day.

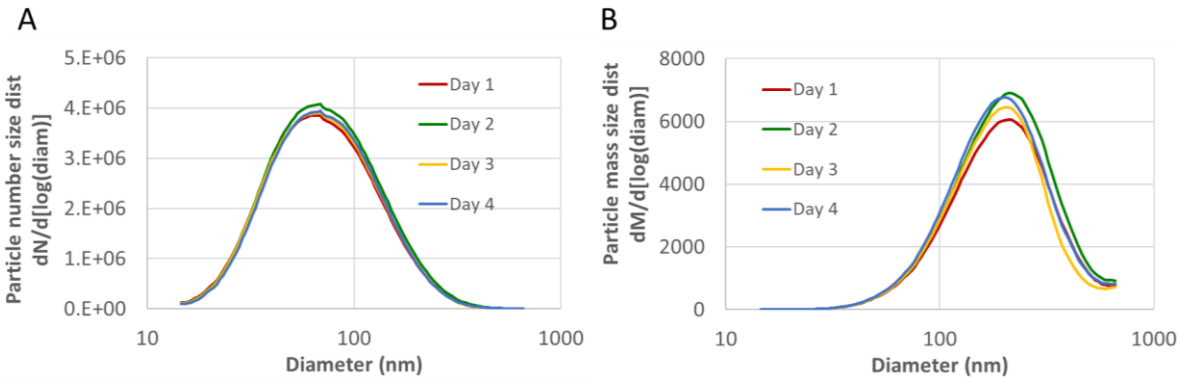

Figure 5.2. Aerosolised particle size distribution by number and mass. Graphical comparison of normalised AuNPs size distribution on each experimental day. **A** - Geometric mean diameter (number), **B** - Geometric mean diameter (mass).

The particles were also collected on a TEM grid for further microscopy analysis. Transmission electron microscopy showed (**Figure 5.3**) that AuNPs mostly appeared as small aggregates of 50-100 nm on diameter. Almost no individual particles were noticed. Some large aggregates (500-2000 nm) were noticed, yet they were rare. As it can be seen in **Figure 5.3D,** the particles clustered around an unknown spherical structure. SEM was used to further analyse the morphology of unknown structures (**Figure 5.4**). There were no large salt crystals detected. The particles were still seen around spherical structures, but the image depth was not sufficient to determine their morphology.

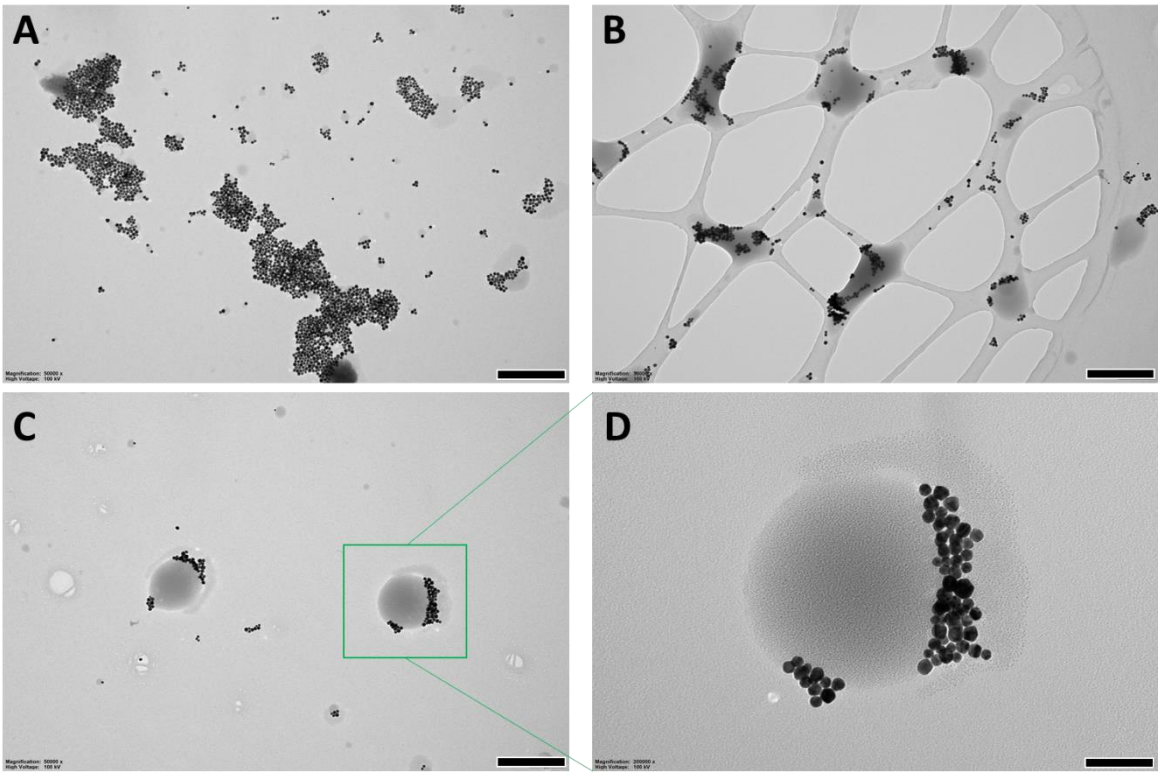

Figure 5.3. Representative TEM images of collected aerosolised 20 nm AuNPs. **A**, **B, C** – general view of AuNPs size distribution and degree of aggregation. 50.000x magnification, 400 nm scale bar. **D** – close look on AuNPs around an unidentified sphere. 200.000x magnification, 100 nm scale bar. Representative images from 2 TEM grids from the individual exposure days.

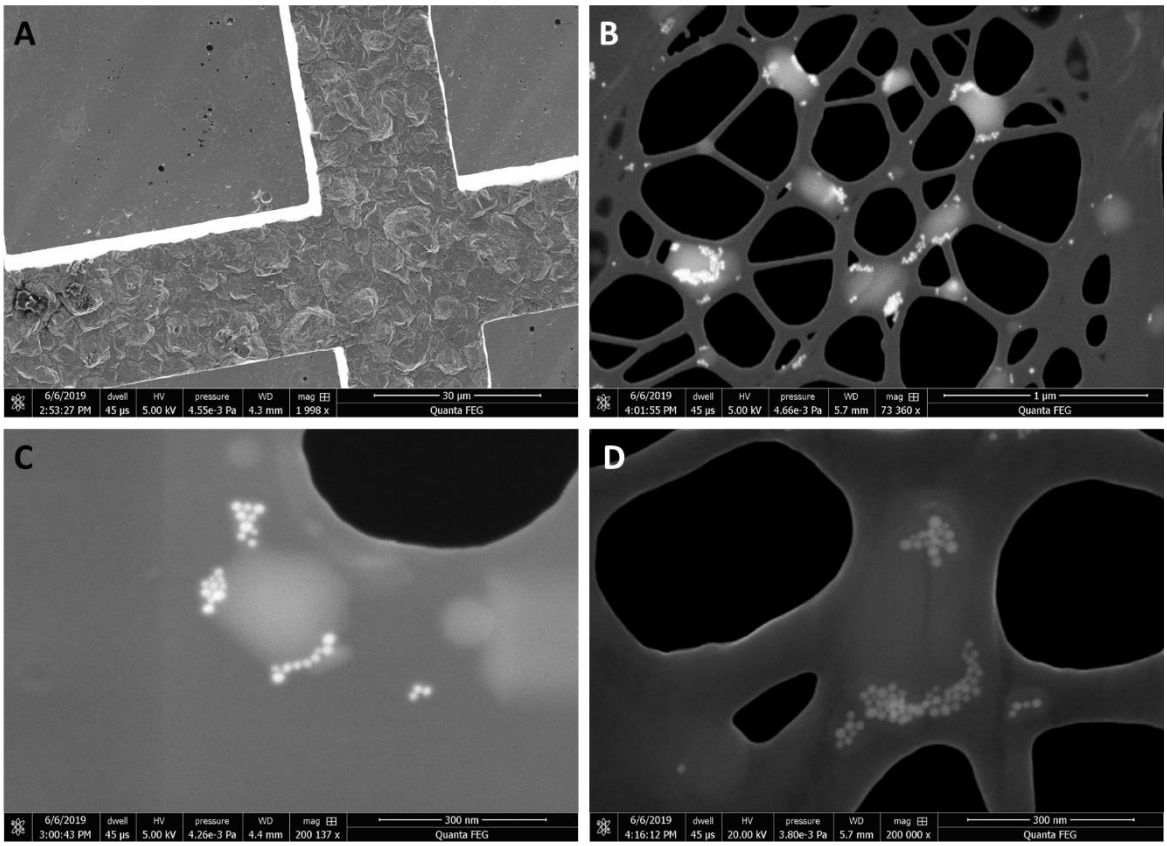

Figure 5.4. Representative SEM images of collected aerosolised 20 nm AuNPs. **A** – general view on a TEM grid at 2000x magnification to visualise any salts. **B** – general view on a TEM grid at 73500x magnification to visualise AuNPs. **C** and **D** – close look on AuNPs around unidentified spheres at 200.000x magnification. Representative images from a single TEM grid.

Inductively coupled plasma mass spectrometry was used to quantify total mass and number of AuNPs in lungs, liver, kidneys, and spleen, as well as to measure the clearance rate within 28 days. No particles were found (or below the detection limit) in the liver, kidneys, and spleen, hence the data is not shown. Right after the exposure (0 days) the mean mass concentration of AuNPs was 3.75 µg/g (micrograms of AuNPs per gram of lung tissue, **Figure 5.5**) and the number was 3×10^6 particles/mg (**Figure 5.6**). The concentration consistently decreased with time and on day 28 comprised 25% compared to day 0. There was no statistical significance in differences between genotypes. The approximate biological half-life for AuNP mass concentrations was: WT – 17 days, AKO – 23 days, DKO – 11 days; number concentration was: WT – 7 days, AKO – 3 days, DKO – 16 days (**Figure 5.7**). Single-particle ICP-MS also showed that the average size of the remaining particles in the lungs increased with time. The change was as follows: WT – 34→40 nm, AKO – 34→41 nm, DKO – 35→38 nm (**Figure 5.8**). Multimodal imaging was used to semi-quantify AuNPs collected from the lungs and to compare the results between genotypes (**Figure 5.9**). The

maximum concentration of AuNPs in macrophages peaked after day 7 with almost four-fold increase for WT and two-fold for AKO and DKO. Overall the uptake in SP-A and SP-D knockout mice was lower compared to WT, but statistically significant differences were observed at day 7, where the two-fold reduction was observed for DKO (p=0.0063) and AKO (p=0.0795).

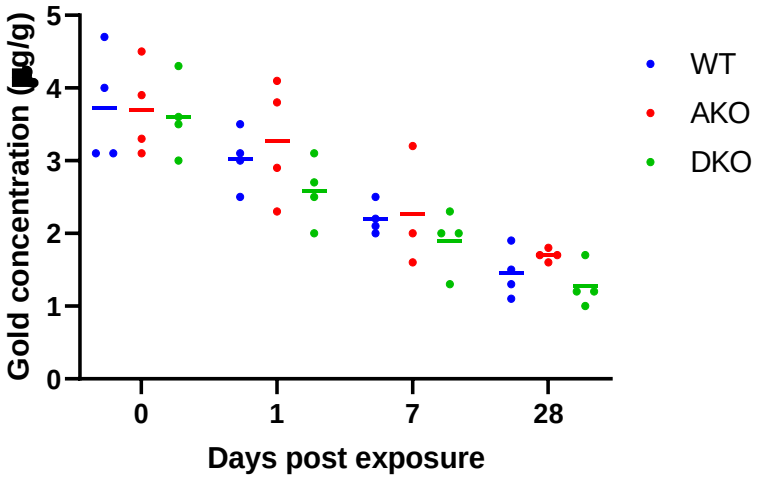

Figure 5.5. Clearance of inhaled AuNPs from mice lungs after a single 3 h exposure. The graph shows a time-dependent **mass** reduction of inhaled AuNPs in each mouse genotype. Samples were analysed with ICP-MS. Each point corresponds to an individual mouse. Blue – wild type mice, red – SP-A knockout, green – SP-D knockout.

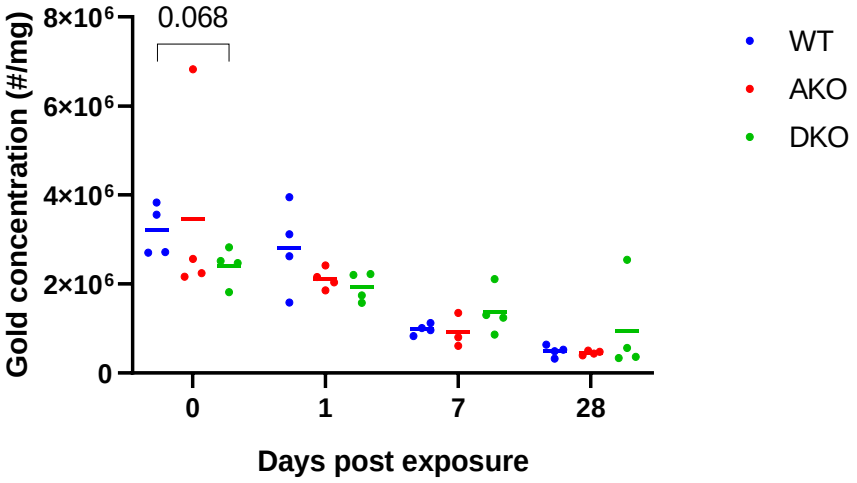

Figure 5.6. Clearance of inhaled AuNPs from mice lungs after a single 3 h exposure. The graph shows a time-dependent **number** reduction of inhaled AuNPs in each mouse genotype. Samples were analysed with ICP-MS. Each point corresponds to an individual mouse. Blue – wild type mice, red – SP-A knockout, green – SP-D knockout. The data was collected by Dr Adam Laycock.

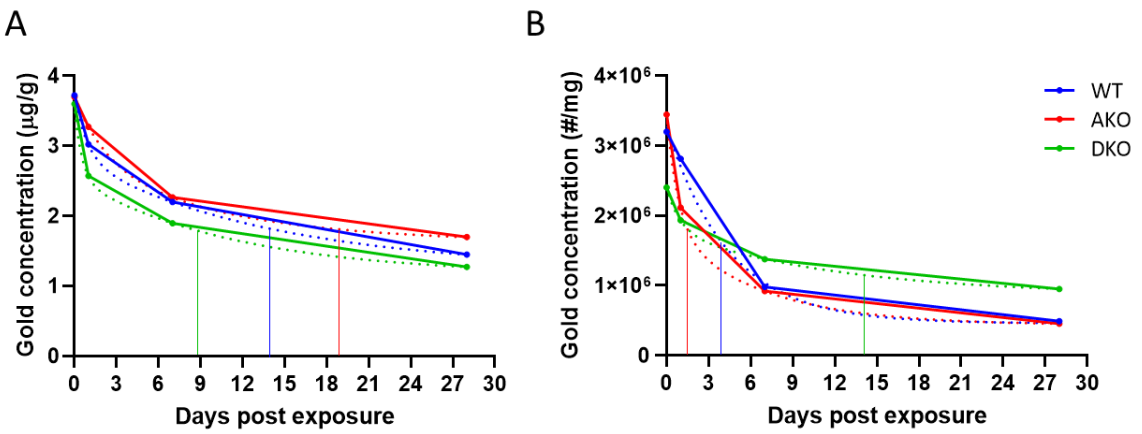

Figure 5.7. The approximate biological half-life of inhaled AuNPs in mice lungs. A – mass concentration. **B** – number concentration. Vertical lines show the time required for AuNPs concentration to decrease in half compared to the maximum concentration for each sample. Non-linear fit (two-phase decay). Data points show the mean only. Blue – wild type mice, red – SP-A knockout, green – SP-D knockout. The data was collected by Dr Adam Laycock.

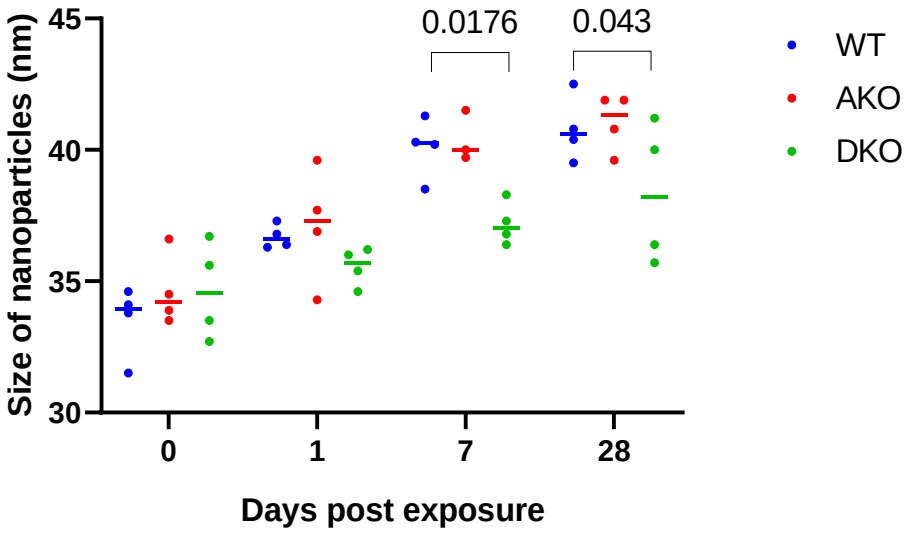

Figure 5.8. Time-dependent size change of inhaled AuNPs detected in mice lungs. Mice were exposed nose-only for a single 3 h dose. The graph shows a dynamic change of AuNPs size increase in mice lungs. Samples were analysed with SP-ICP-MS. Blue – wild type mice, red – SP-A knockout, green – SP-D knockout.

From day 0 to day 7 there was an inversely proportional relationship between the number concentration of AuNPs in the lungs and macrophages. While the number of AuNPs dropped consistently in the lungs, an increase in macrophages was observed to day 7, and then reduced

significantly on day 28 (**Figure 5.10**). SP-A mice macrophages showed a different pattern with a plateau from day 1 to day 7.

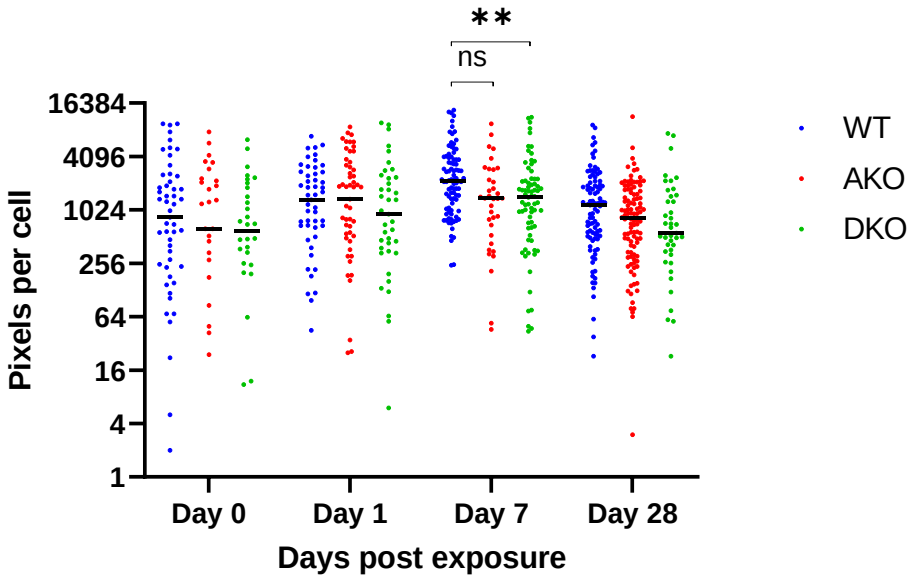

Figure 5.9. Uptake of inhaled 20 nm AuNPs by mice macrophages semi-quantified using multimodal imaging. Pixels per cells were quantified as a sum of all bright areas in SHG channel across the whole Z-stack of a cell using ImageJ. Statistical values: ns – 0.0795; ** - 0.0063, Kruskal-Wallis test. Blue – wild type mice, red – SP-A knockout, green – SP-D knockout. At least 10 different macrophages per each mouse were analysed.

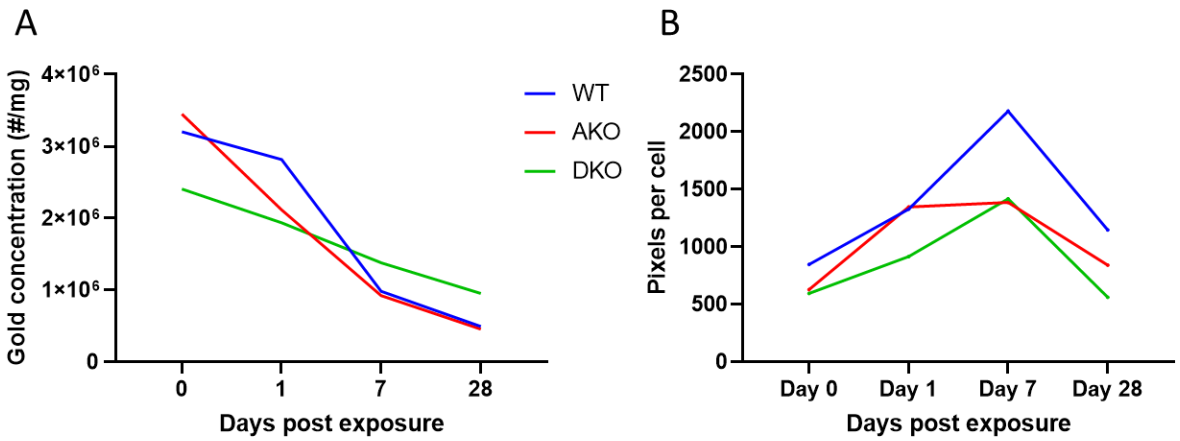

Figure 5.10. Comparison of AuNPs concentration changes in mice lungs and macrophages. A – number concentration in mice lungs measured with SP-ICP-MS; mean values, taken from Figure 5.6. **B** – pixels per cell concentration in mice macrophages measured with multimodal microscopy; median values, taken from **Figure 5.9**. Blue – wild type mice, red – SP-A knockout, green – SP-D knockout.

Multimodal imaging was used for rapid AuNP visualisation and to determine its applicability on tissue (**Figure 5.11**). Only CARS and SHG channels were used. No differences were detected between the unexposed control and AKO or DKO exposed. Laser ablation ICP-MS was used to visualise the distribution of AuNPs within the lungs. Firstly, an unexposed control lung of wild type mouse was analysed (**Figure 5.12**). As expected, very little gold was detected. Then, the experimental mice 7 days post-exposure were imaged (**Figure 5.13**). The data showed that all three genotypes had an even distribution of AuNPs from the centre to the peripheral of the lungs. Transmission electron microscopy was applied to characterise the particles in the cells (**Figure 5.14**). Detected particles appeared as relatively small aggregates comprised of tens to hundreds of particles.

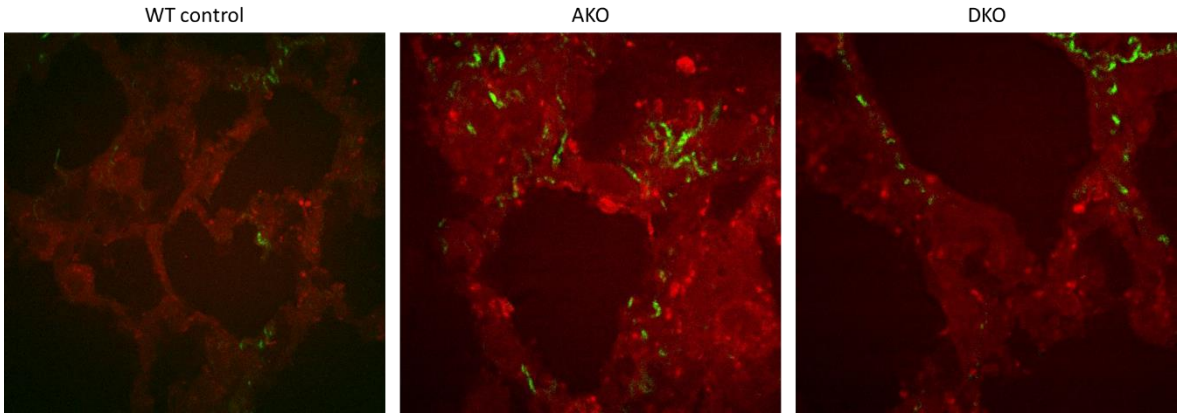

Figure 5.11. Multimodal microscopy imaging of mice lung tissue 7 days post-exposure. Composite images of CARS and SHG channels aimed to visualise AuNPs. 40x objective and additional 3x optical zoom, 512x512 resolution. Red – CARS, green – SHG.

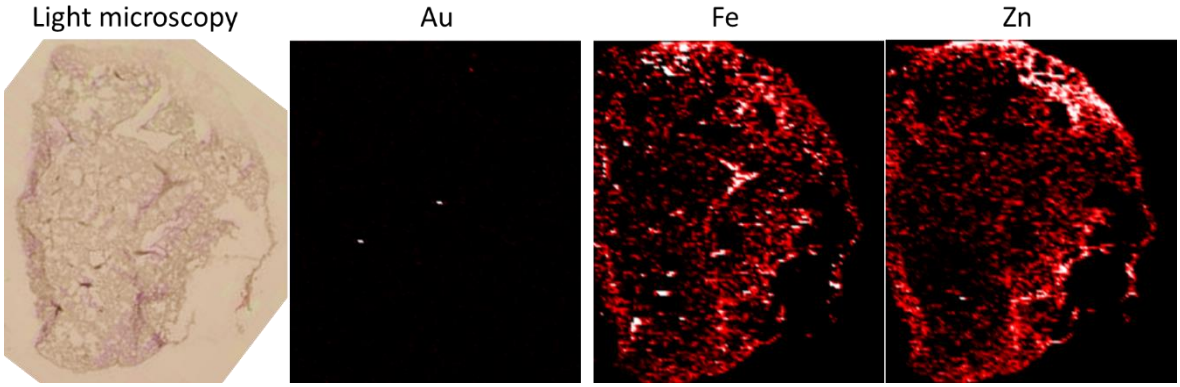

Figure 5.12. LA-ICP-MS of a control mouse lung unexposed to AuNPs. Light microscopy displays an analysed sample. Au, Fe and Zn – metals analysed by LA-ICP-MS. Lung tissue of a wild type mouse.

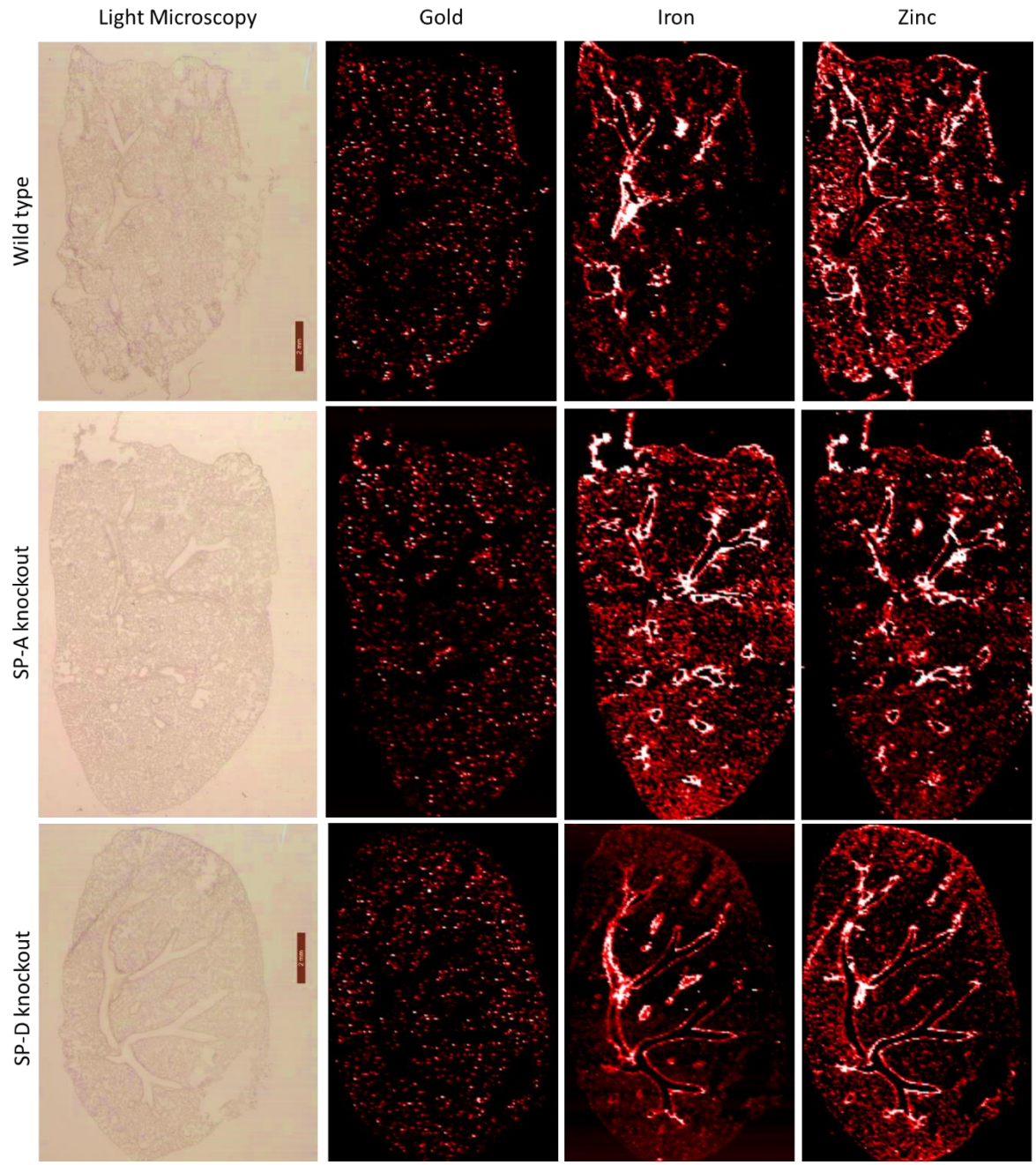

Figure 5.13 LA-ICP-MS of mice lungs exposed to AuNPs. **Light microscopy** displays analysed samples. **Gold**, **iron,** and **zinc** – metals analysed by LA-ICP-MS. Lung tissue of a wild type mouse. Samples correspond to randomly selected WT, AKO, and DKO mice 7 days post-exposure. Scale bar – 2 mm.

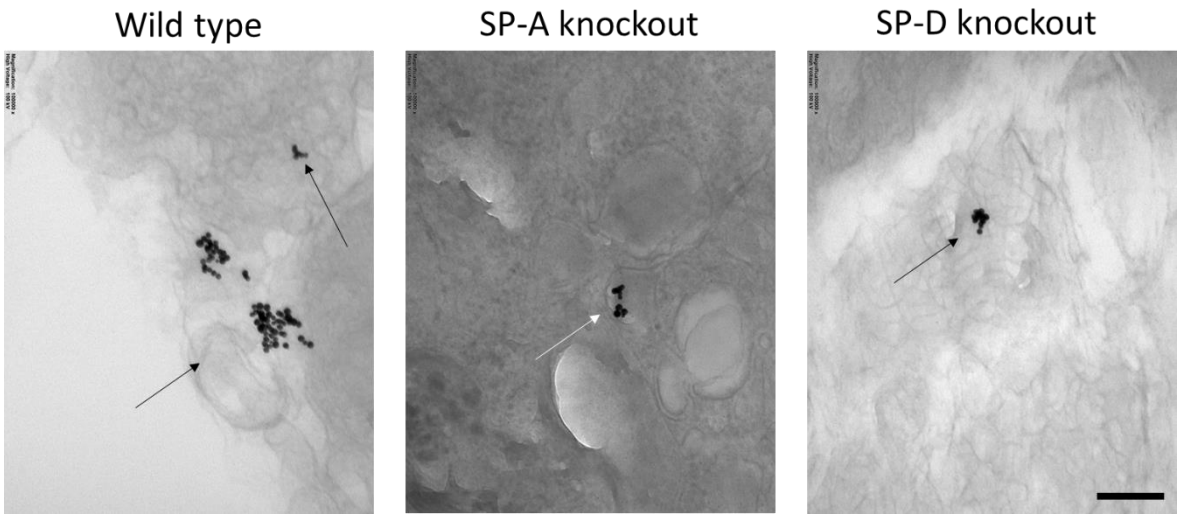

Figure 5.14. TEM micrographs of mice lungs exposed to AuNPs. 7 days post-exposure mice lungs were used. Images collected at 100.000x magnification, scale bar 200 nm.

A follow-up experiment was performed but increasing a single 3 h exposure to five 3 h exposures (one 3 h exposure repeated every day 5 times). **Table 5.3** summarises aerosol characteristics. The mass of pure Au was not quantified yet due to time restrictions. The mass of AuNPs was higher and less consistent compared to the first experiment. The size of the aerosolised AuNPs was relatively consistent with slight day-to-day variations (**Figure 5.15**).

Table 5.3. Aerosol characteristics and parameters. AuNPs aerosol characterisation of the first single 3 h exposure *in vivo* experiments**. Filter number** – filters from each experiment. **Geometric mean diameter** – the size of AuNPs as the most abundant *number* and *mass*. **Gravimetric AuNPs mass concentration** – calculated from passed air through the filter and weighed AuNPs on it. **Mass of Au** – the mass of pure gold per m^3 of air determined by ICP-MS (quantification pending).

Filter number	Number of AuNPs	Geometric mean diameter (number)	Geometric mean diameter (mass)	Gravimetric AuNPs mass concentration	Mass of Au
#	#/cm^3	nm	nm	µg/m^3	µg/m^3
1	4.07×10^6	64.6	151.6	1176	-
2	3.52×10^6	58.6	131.7	5241	-
3	4.05×10^6	59.5	133.3	7189	-
4	4.16×10^6	60.2	136.5	6718	-
5	4.04×10^6	60.1	135.5	18579	-
Average	*3.97×10^6*	*60.6*	*137.7*	*3687*	-
SD	*0.25×10^6*	*2.3*	*8.0*	*233*	-

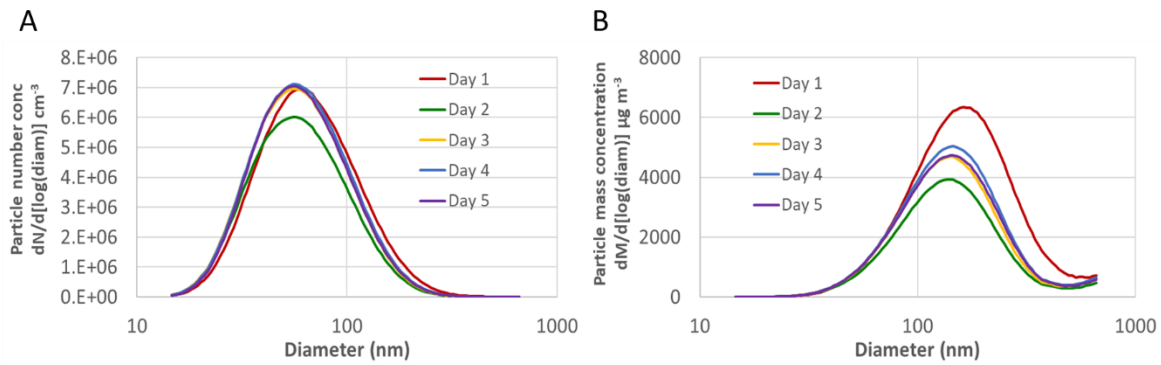

Figure 5.15. Aerosolised particles size distribution by number and mass. Graphical comparison of normalised AuNPs size distribution on each experimental day. **A** - Geometric mean diameter (number), **B** - Geometric mean diameter (mass).

Both mass and number concentrations increased three to four-fold (**Figure 5.16** and **Figure 5.17**), compared to the same time points for a single 3 h exposure described **above**. Biological half-life was not estimated due to the insufficient number of time points. The mean AuNPs diameter was 38-40 nm for WT and AKO, and 33-34 nm for DKO (**Figure 5.18**).

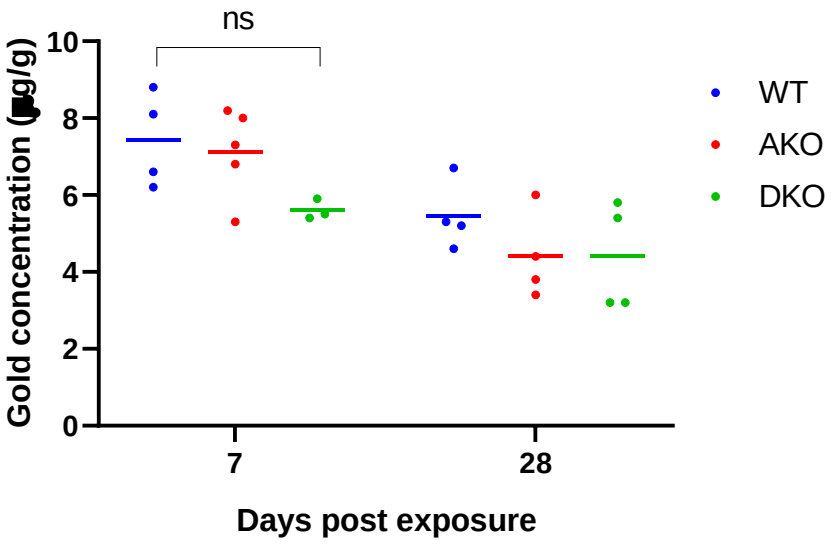

Figure 5.16. Clearance of inhaled AuNPs from mice lungs after extended exposure. Mice were exposed to nose-only 3 h/day for 5 consecutive days. The graph shows a time-dependent **mass** reduction of inhaled AuNPs in each mouse genotype. Samples were analysed with ICP-MS. Each point corresponds to an individual mouse. Blue – wild type mice, red – SP-A knockout, green – SP-D knockout. Ns – p=0.0563.

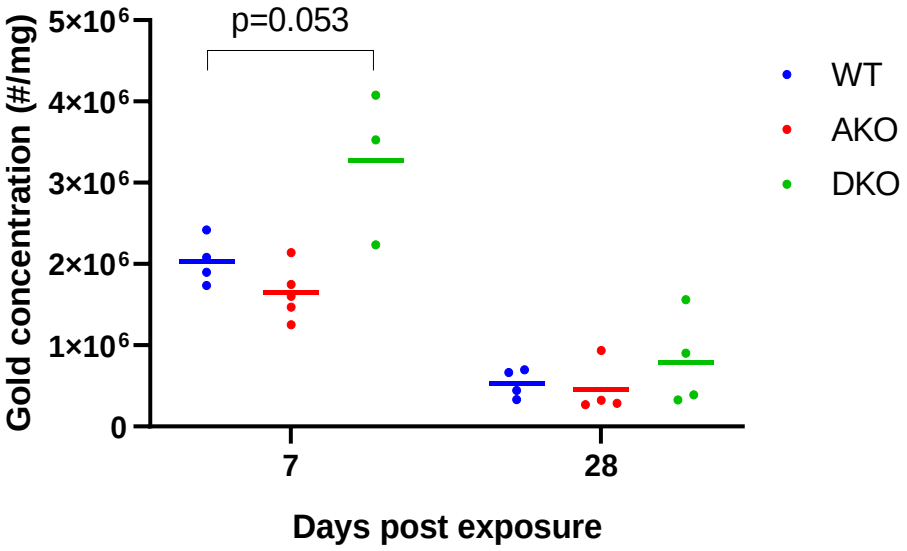

Figure 5.17. Clearance of inhaled AuNPs from mice lungs after extended exposure. Mice were exposed to nose-only 3 h/day for 5 consecutive days. The graph shows a time-dependent **number** reduction of inhaled AuNPs in each mouse genotype. Samples were analysed with ICP-MS. Each point corresponds to an individual mouse. Blue – wild type mice, red – SP-A knockout, green – SP-D knockout.

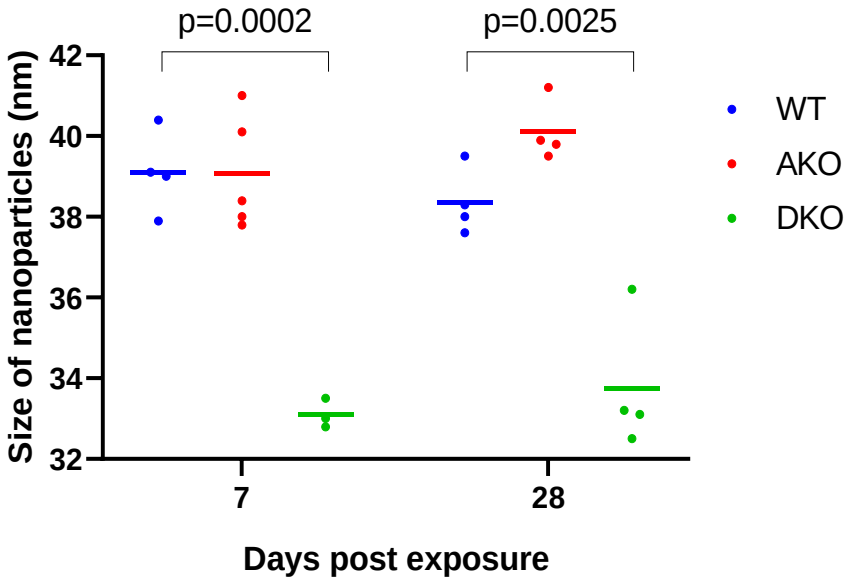

Figure 5.18. Time-dependent size change of inhaled AuNPs detected in mice lungs. Mice were exposed to nose-only 3 h/day for 5 consecutive days. The graph shows a dynamic change of AuNPs size increase in mice lungs. Samples were analysed with SP-ICP-MS. Blue – wild type mice, red – SP-A knockout, green – SP-D knockout.

5.5 Summary of the results

Within this chapter, the *in vivo* clearance and translocation to the secondary organs of 20 nm AuNPs from the respiratory system following nose-only exposure in SP-A$^{-/-}$, SP-D$^{-/-}$ and WT mice investigated, thus addressing Aim 4 (**Section 1.5**):

4. Characterise the potential *in vivo* translocation and toxic effects of NPs using mice deficient for SP-A, deficient for SP-D and wild-type mice.

The main results and achievements reported in this chapter are:

- This was the first time when genetically SP-A and SP-D knockout mice models were used to study the role of surfactant proteins in the clearance and uptake of AuNPs, exposed via nose-only inhalation.
- There was no statistically significant difference in the clearance rate of 20 nm AuNPs from the lungs between genotypes within the time points. However, insignificant differences were observed in SP-D$^{-/-}$ mice, where the mass of AuNPs reduced quicker and number of particles slower.
- The average diameter of AuNPs aggregates after 7 and 28 days post-exposure was smaller in SP-D$^{-/-}$ mice compared to WT and SP-A$^{-/-}$ by about 10% ($p=0.0176$) and 8% ($p=0.043$), respectively.
- No translocation to secondary organs was detected via ICP-MS.
- Semi-quantification of internalised AuNPs within mice macrophages by multimodal microscopy showed increased uptake by WT mice macrophages, compared to knockouts. The biggest difference was observed 7 days post-exposure where SP-A$^{-/-}$ and SP-D$^{-/-}$ mice macrophages had about 50% less ($p=0.0795$ and $p=0.0063$, respectively) internalised AuNPs than WT.
- The uptake of AuNPs by macrophages was reverse proportional to the clearance of AuNPs from the lungs until day 7.
- Laser ablation ICP-MS confirmed homogenous distribution of AuNPs within the lung tissue. However, no AuNPs were detected or distinguished using multimodal microscopy.

5.6 Discussion

The present study investigated the *in vivo* role of SP-A and SP-D on the clearance of 20 nm AuNPs. While there were already *in vivo* studies investigating the role of surfactant proteins on nanoparticle clearance, this is the first study using both genetic knockout mice and nose only AuNP aerosol inhalation, hence providing the most realistic and accurate model available to date.

According to **Table 5.2**, the actual particle diameter was larger than the nominal size. Such difference was expected, as when AuNP colloidal solution (in 0.1 mM PBS, citrate capped) is nebulised and liquid is evaporated, the distance between particles decreases forcing them to stick to each other, as the distance of the repulsive barrier is not enough to keep them apart (**Figure 5.19**). Moreover, as the volume decreases, the concentration of salts increases, potentially facilitating the aggregation. Electron microscopy images confirmed aggregation of nanoparticles. Most particles appeared in aggregates of at least 3 particles. The mean or the median number of particles per aggregate was not counted though, as the data collected by Scanning Mobility Particle Sizer was deemed sufficient.

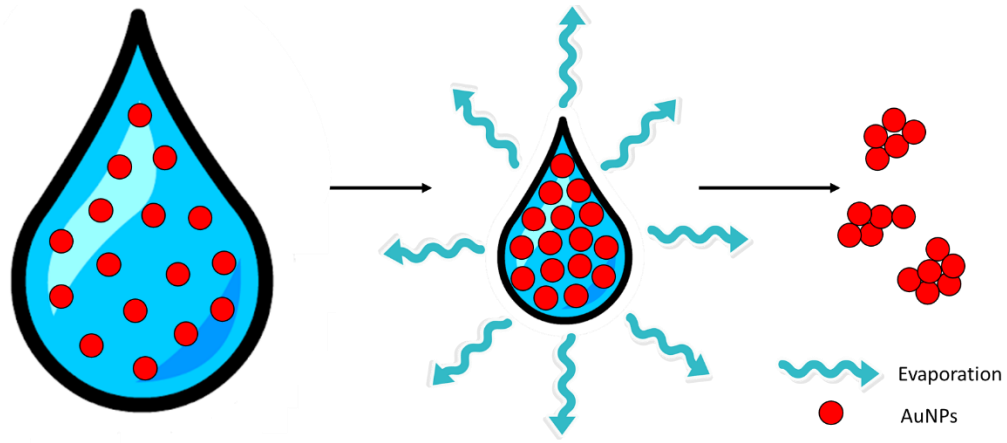

Figure 5.19. A schematic explanation of AuNPs aggregation due to liquid evaporation. In the initial droplet, the particles are evenly distanced and repulsive forces are sufficient to keep them apart. When the liquid evaporates, the volumes reduces while the number of particles remains the same, hence the distance between particles also reduces. Particles form aggregates due to collision and clumping.

An unusual effect was observed in **Figure 5.3C,** where particles clustered around a spherical object. This was not an uncommon effect and was seen for aggregates of ~150 nm. First, it was thought to be a TEM grid defect which made particles to stick around it during the deposition, yet

no such individual (without particles) defects were found. Since AuNPs are citrate capped and resuspended in 0.1 mM PBS, the most obvious explanation is that the spheres are salt crystals. While the manufacturer said the particles were “reactant-free, 99% purity”, there was still a chance of residual chemical presence which could form crystals. The main concern was that crystals do not form spherical shapes. No explanation or at least similar precedent was found in the literature. The same grids were analysed under SEM, as this technique provides more depth of field and allows better morphology characterisation. If the spheres were salt crystals indeed, it was expected to see more of those and at lower magnification, as per **Figure 5.3A**, but nothing unusual was found. Then, the spheres with AuNPs were imaged directly, but it was still not possible to understand their origin or at least physical properties. The only conclusion from electron microscopy images was made that, considering the diameter of the spheres and that electrons could pass through it easily, the structures were not electron-dense. The spheres may be dust particles caught during the aerosol generation.

Mass spectrometry was used to quantify the clearance and translocation of AuNPs from the lungs to secondary organs. There was no translocation detected (or the translocation was below the detection limit) to the kidneys, liver, or spleen at either time points. The lungs, as expected, had the highest concentration of AuNPs. However, there was no statistical significance between genotypes, which was unexpected. DKO mice had slightly less mass concentration (yet, not statistically significant). However, DKO is the only of three genotypes which have a different phenotype, characterised by chronic inflammation, emphysema, and fibrosis in the lungs.[288] Inflammation and impaired pulmonary surfactant recycling could lead to constricted airways, reducing the airflow and AuNP deposition aerodynamics (refer to **Section 1.3.1**), while the reduced surface area of the lung directly reduces AuNP deposition sites.

Figure 5.7 side by side compares mass and number concentrations of AuNPs in the lungs. It can be noticed that DKO mice had overall smaller mass concentration and larger number concentration compared to WT and AKO. Surfactant protein D deficiency is known to cause so called “leaky lungs”, where the molecules from the lungs can leak into the bloodstream due to the loss of air–blood barrier integrity.[289] It can be hypothesised that the total mass of AuNPs in DKO mice decreases as the particles penetrate the lungs easier due to the differences in the phenotype, compared to WT and AKO mice, which have no structural abnormalities. On the other hand, the number of the particles in DKO mice is larger as the average size is smaller, compared to WT and AKO. This is supported by **Figure 5.8**, which shows that the average size of AuNPs was smaller in DKO mice than in WT or AKO. It is easier to understand the concept from **Figure 5.20**, which

explains the results observed in **Figure 5.7** and **Figure 5.8**. Hence, the difference in average size, mass and number concentrations might be due to quicker and easier penetration of air-blood barrier by AuNPs in DKO mice, compared to WT and AKO. However, the hypothesis was not confirmed as no particles in secondary organs were found.

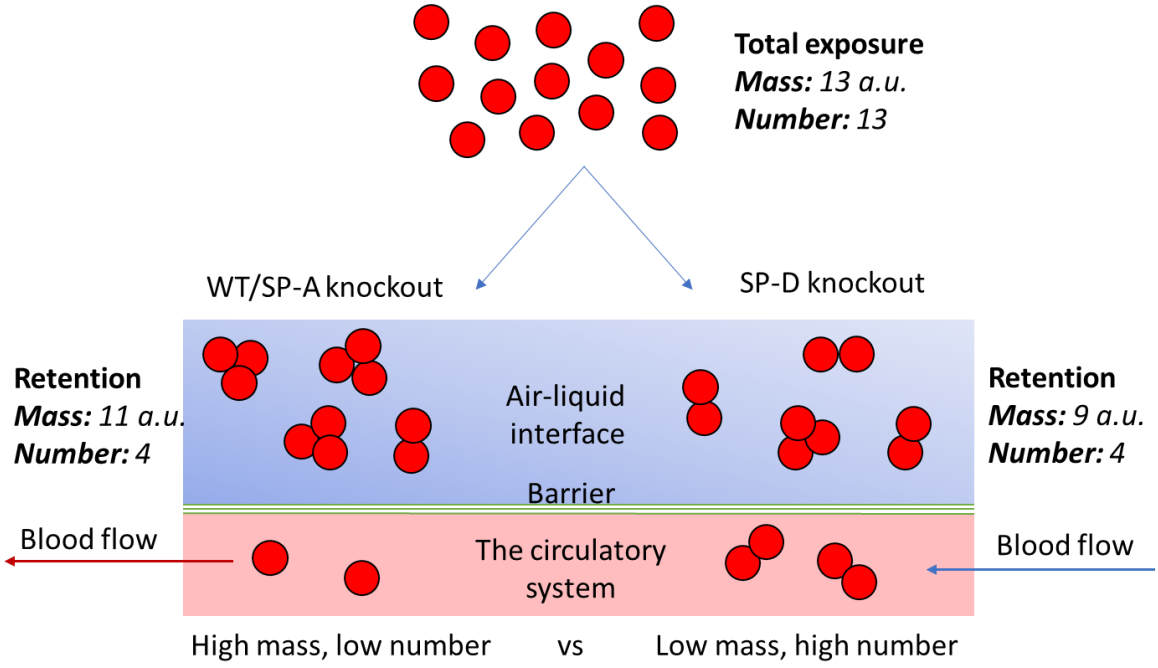

Figure 5.20. Illustration of AuNPs mass and total number distribution in WT/AKO and DKO mice. In this example, all mice are exposed to an equal number (13) of AuNPs. Once they are deposited into the lung, they are likely to further aggregate. Wild type and AKO have healthy lung phenotype and particles cannot penetrate air–blood barrier easily, while DKO mice have leaky lungs and larger particles escape easier. Particles smaller in diameter will represent larger fraction by number, compared to larger particles of the same total mass. Particles which crossed the barrier are removed via the circulatory system and are not quantified. Animated version available via supplementary data.

It was also noticed that DKO had about 25% fewer number particles at day 0 than WT and AKO, but the same mass concentration. It is possible that single-particle analysis was not accurate enough, as the machine operated at its size detection limit, hence the variation and contradicting data. **Figure 5.21** shows the mass spectrometer calibration data, where the signal from 20 nm AuNPs is just above the background noise and the signal threshold might lead to the loss of some recorded events. While just slightly larger, 30 nm AuNPs, can be quantified with much less background interference.

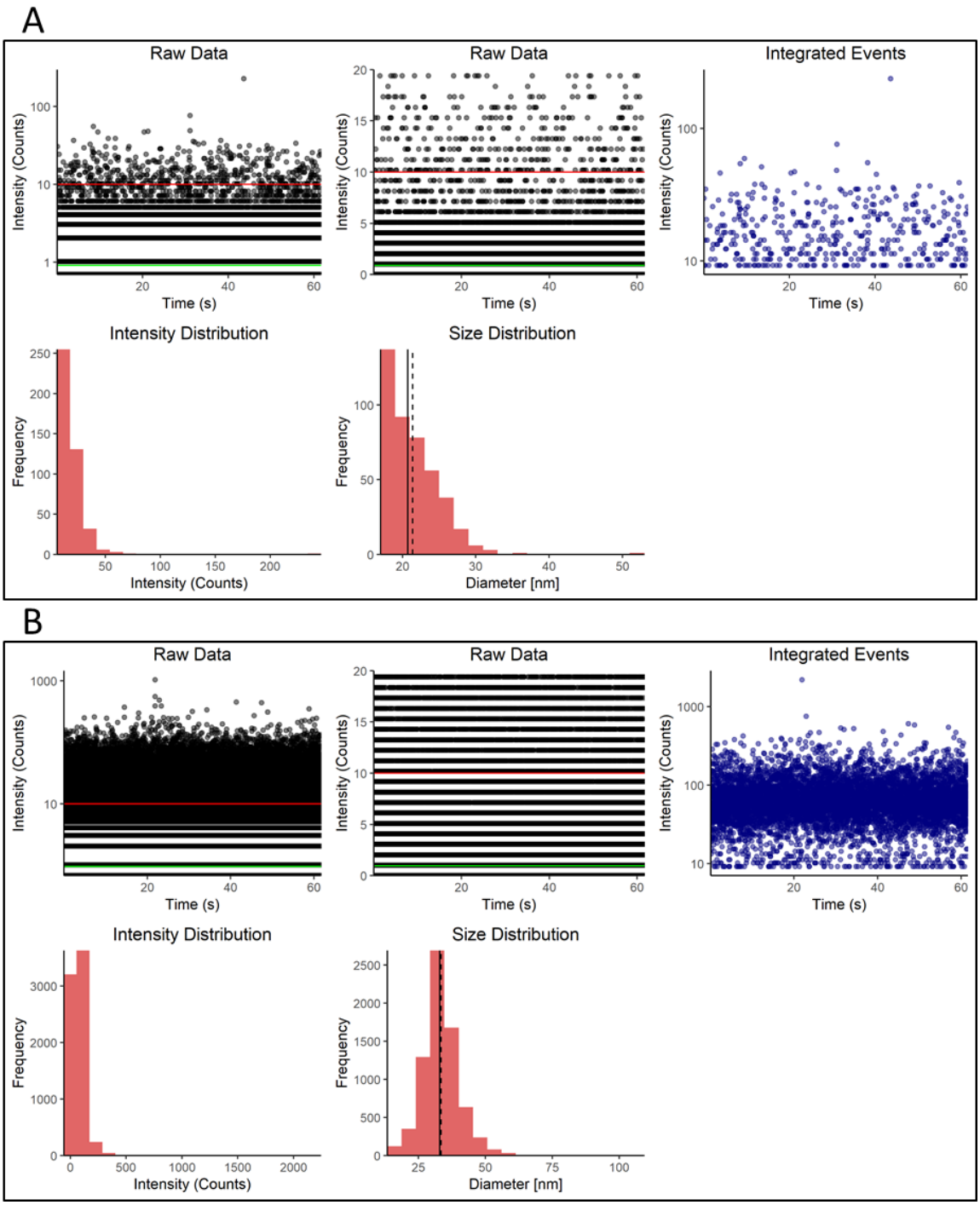

Figure 5.21. Single-particle ICP-MS calibration data. **A** – data for 20 nm AuNPs. **B** – data for 30 nm AuNPs. The data shows that 20 nm AuNPs were at the limit of the detection, while 30 nm were resolved well.

Multimodal imaging was used to semi-quantify the concentration of AuNPs from BALF collected macrophages (**Figure 5.9**). The data showed a reduced uptake of AuNPs by macrophages in both SP-A and SP-D knockout mice, with a significant difference at day 7, where a peak in the uptake was noticed for all mice. Interestingly, this data is in contradiction of the *in vitro* data from

Chapter 4. *In vivo* data showed the suppression in uptake in the absence of SP-A and SP-D compared to WT, while *in vitro* data showed suppression in the presence of the proteins. The exact reason for such a difference is not known and requires in-depth analysis and application of complementary quantification techniques (such as mass spectrometry). It can be speculated that *in vivo* is a more complex model with an increased number of variables and hence should be treated as more biologically accurate and relevant, compared to *in vitro* experiments. Also, the cell line-derived macrophages do not share the same genotype/phenotype as knockout mice macrophages and might show different results.

An interesting AuNP concentration relationship was observed when comparing lung and macrophage data (**Figure 5.10**). While the concentration in the lungs dropped at each time point, AuNP concentration in macrophages increased until day 7 and only then dropped. This suggests that macrophages are important in clearing the nanoparticles from the respiratory system, as discussed in **Section 1.3.2**. It is also interesting to see that even at day 0 (which is about 2-5 hours post-exposure) macrophages were taking up the particles, indicating that macrophage clearance is rapid and starts as soon as 2 hours post-exposure. Considering the mice were exposed for 3 hours and harvested with a delay, the uptake might start much earlier. Also, the increase in AuNP concentration in the macrophages until day 7 allows hypothesising that a single macrophage resides within the lungs for at least a week, before it is removed via the mucociliary escalator. It is probable that their half-life is even longer, as at day 28 the concentration of phagocytosed AuNPs is still relatively high.

While there was no success in applying multimodal imaging for AuNP visualisation in the lung tissue in **Chapter 3**, this time the presence of AuNPs in the lungs was confirmed by ICP-MS and the method was applied again (**Figure 5.11**). However, there was no difference observed between the unexposed control and 7 days post-exposure lungs. Hence, it was concluded that multimodal imaging requires further development for AuNP imaging inside the tissue. Laser ablation ICP-MS (**Figure 5.13**), however, confirmed that AuNPs were present and evenly distributed in the lung tissue, both deep inside (near bronchi) and on the periphery. There was no clear difference in distribution between WT or knockout mice to draw any conclusion. As a last verification step, TEM was used to confirm the presence of AuNPs inside the lung cells (ATI or ATII) rather than on the surface of alveoli (**Figure 5.14**). Indeed, the particles were located within the cells, but the method itself was highly difficult in application. The issue is that particles are 20 nm in diameter, while the aggregates usually do not exceed 150 nm. This means at least 20,000x magnification is required to

spot the particles across a single 80 nm thick slice. Hence, the method cannot be used to generate representative images, as it requires time-consuming and manual scanning of individual slices.

A follow-up study was performed with an increased number of exposures. Mice were exposed for 5 consecutive days for 3 h under the same conditions. The idea was to introduce more particles into the lung and hence circulatory system to increase the chances of finding the particles in secondary organs. It is also important to note that due to limited literature availability and novelty of the exposure system, the exposure times and concentrations are determined by a trial-and-error approach, which can be optimised in future work. Hence, the number of time points was also reduced, where the highest translocation was expected. Unfortunately, at the time of writing, there was no ICP-MS data available on secondary organs (all but lungs). The lung ICP-MS results showed the same pattern as in the first experiment. The main difference was a three to four-fold increase in mass concentration and the same increase in number concentration compared to the first experiment. Thus the 7 days post-exposure values in experiment two were equivalent to 1-day post-exposure values in experiment one. Such an increase might be a promising factor to detect any translocation to secondary organs and possibly see a bigger difference between genotypes.

It was noted that DKO mice had a reverse correlation between mass concentration and number concentration in both experiments. In the first one-time exposure experiment, this could be attributed to a systematic error or a sample processing induced artefact, but it is unlikely to be an artefact in two independent experiments. The difference in both cases showed to be statistically significant. First of all, it is evident that the mass concentration in both experiments in DKO mice is lower, than in other genotypes. This suggests that the particles from DKO mice lungs are removed quicker. However, it is not known whether the particles pass directly though the epithelial cells into circulation, are taken up by macrophages, or are removed via the mucociliary escalator. Then, it is consistent that the number of particles in DKO is greater, starting with day 7 post-exposure. This data has to be interpreted with mean particle size measured by SP-ICP-MS, where AuNPs in DKO mice are smaller. Increased AuNP size suggests the particles are aggregated more strongly in AKO and DKO mice. Hence, multiple particles form larger aggregates, reducing the total number of AuNPs that can be detected. On the other hand, DKO mice had smaller AuNPs, meaning the larger number of freely available particles can be detected.

While it is difficult to interpret such data without additional investigation, it can be hypothesised that DKO mice have reduced AuNP opsonisation ability, hence the particles form smaller aggregates. Due to reduced opsonisation, smaller particles are cleared from the lungs quicker,

presumably by penetration of the air−blood barrier directly into the circulatory system. The WT and AKO mice have greater AuNP opsonisation, hence the particles are larger, which facilitates uptake by macrophages and reduces membrane penetration, resulting in the particles staying longer in the lungs.

Multiple *in vivo*[290] and *in silico*[291] studies have shown that translocation is inversely proportional to the diameter of the particle, while the uptake by macrophages increases with the size of the particles[292]. Some studies indicate that particles smaller than 38 nm have greater translocation properties from the lungs to lymph nodes, while particles as small as 5 nm could already be detected in urine 30 min post-administration.[293] Studies using 20 nm TiO_2 indicate that mucociliary clearance dominates the translocation to lymph nodes, as the greater proportion of particles was found in faeces.[294] Overall, considering the study results, it can be concluded that SP-D might alter the clearance rate and mechanism of inhaled AuNPs.

The last time *in vivo* role of SP-A and SP-D in the clearance of NPs was analysed in 2013 by Schleh et al[110] and included wild type mice only and focused on intranasal administration of SP-D only. This study offers a major upgrade to what has been published before. Choosing knockout mice allowed to investigate the clearance when one of the surfactant proteins is missing, as additional administration of the protein to wild type mice is not an ideal method, as the proteins are already present in healthy lungs. Nose-only AuNPs aerosol exposure ensured that particles were distributed as evenly as possible within the lung, which cannot be achieved via nose/intratracheal instillation. Yet, future work should include a wider range of analyses, such as measurement of inflammatory markers, differential cell count and histology (e.g. eosin and haematoxylin staining).

5.7 Conclusions

The data showed there is tentative evidence that SP-D might be important in mediating the clearance rate and mechanism of inhaled 20 nm AuNPs. The study did not establish whether the difference was dependent exclusively due to protein or was phenotype-driven. The conclusion was partially supported by a reduced number of internalised AuNPs by lung macrophages, quantified by multimodal microscopy. No translocation to secondary organs was found. More research is required to establish a clearance mechanism.

Chapter 6 Characterisation of environmental nanoparticles

6.1 Introduction

From smog hanging over cities to smoke inside the home, air pollution is a major environmental health hazard. According to the World Health Organisation (WHO), around 8 million people died in 2016 because of air pollution, where a total of 3.8 million deaths were linked to indoor and 4.2 million to outdoor air pollution, associated with particles smaller than 2.5 µm ($PM_{2.5}$). It is estimated that 80% of people living in urban areas are exposed to an increased concentration of particulate matter, which does not satisfy WHO guidelines. Yet, no threshold has been identified below which no health damage is observed. The main sources and adverse health effects were reviewed in **Section 1.3.**

Table 6.1 Breakdown of deaths attributed to air pollution.[295,296]

Outdoor air pollution-caused deaths	Indoor air pollution-caused deaths
58% – ischaemic heart disease and strokes	46% - ischaemic heart disease and strokes
18% – acute lower respiratory infections	28% - pneumonia
18% – chronic obstructive pulmonary disease	20% - chronic obstructive pulmonary disease
6% – lung cancer	8% - lung cancer

The aim of this chapter is to characterise environmental nanoparticles (PM_{10}, $PM_{2.5}$ and $PM_{0.1}$) collected in Southampton's harbour by analysing their elemental composition, size, and morphology. In addition, preliminary cell culture viability tests were conducted to determine the impact of SP-A and SP-D.

6.2 Aims and objectives

This chapter addresses the aims and objectives summarised in clause 5 of **Section 1.5,** which are:

5. Characterise environmental nanoparticles collected from Southampton's harbour and investigate their toxicity.

5.1. Determine elemental composition, size, and morphology of environmental nanoparticles.

5.2. Expose the cell line to environmental particles and determine their toxicity via MTT assay.

6.3 Methods

All methods used in this chapter are detailed in **Chapter 2**.

6.4 Results

The particles were purified into glass tubes and appeared as black or dark brown suspension (**Figure 6.1**)which precipitated over time. **Figure 6.2** represents selected SEM and TEM micrographs of collected environmental PM_{10}, $PM_{2.5}$ and $PM_{0.1}$. SEM images demonstrate morphological variations within each fraction. The variability in morphology decreased with each fraction, as in $PM_{0.1}$ only uniform spherical particles were seen. TEM micrographs provide higher magnification images to see individual particles and the complexity of particle aggregates. While the individual particles from PM_{10} were mostly a single piece of material, smaller fraction particles were composed of multiple sub-particles. Particles with a well-defined morphology were attributed to biological particles, such as pollen. The size of pollen grains varies between 15 µm and 200 µm and was expected to be seen in this fraction.[297]

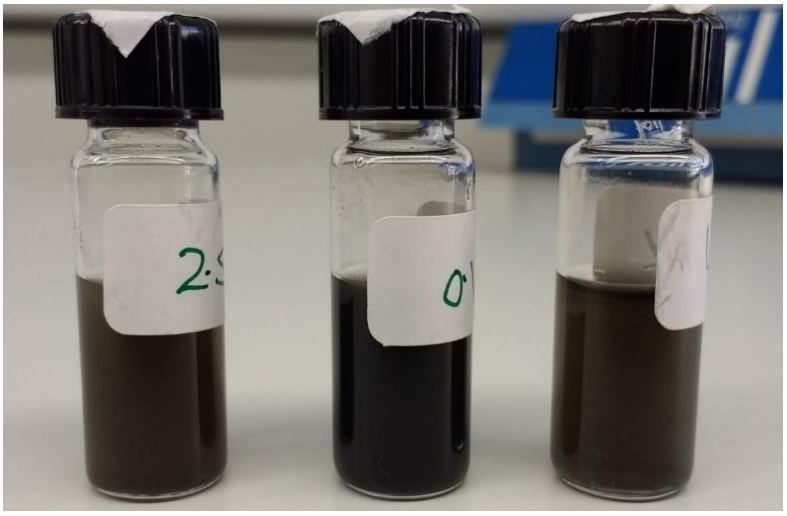

Figure 6.1. Environmental particles resuspended in water. Left to right – PM_{10}, $PM_{2.5}$ and $PM_{0.1}$. Resuspended at 5 mg/ml. Photo by Dr Matt Loxham.

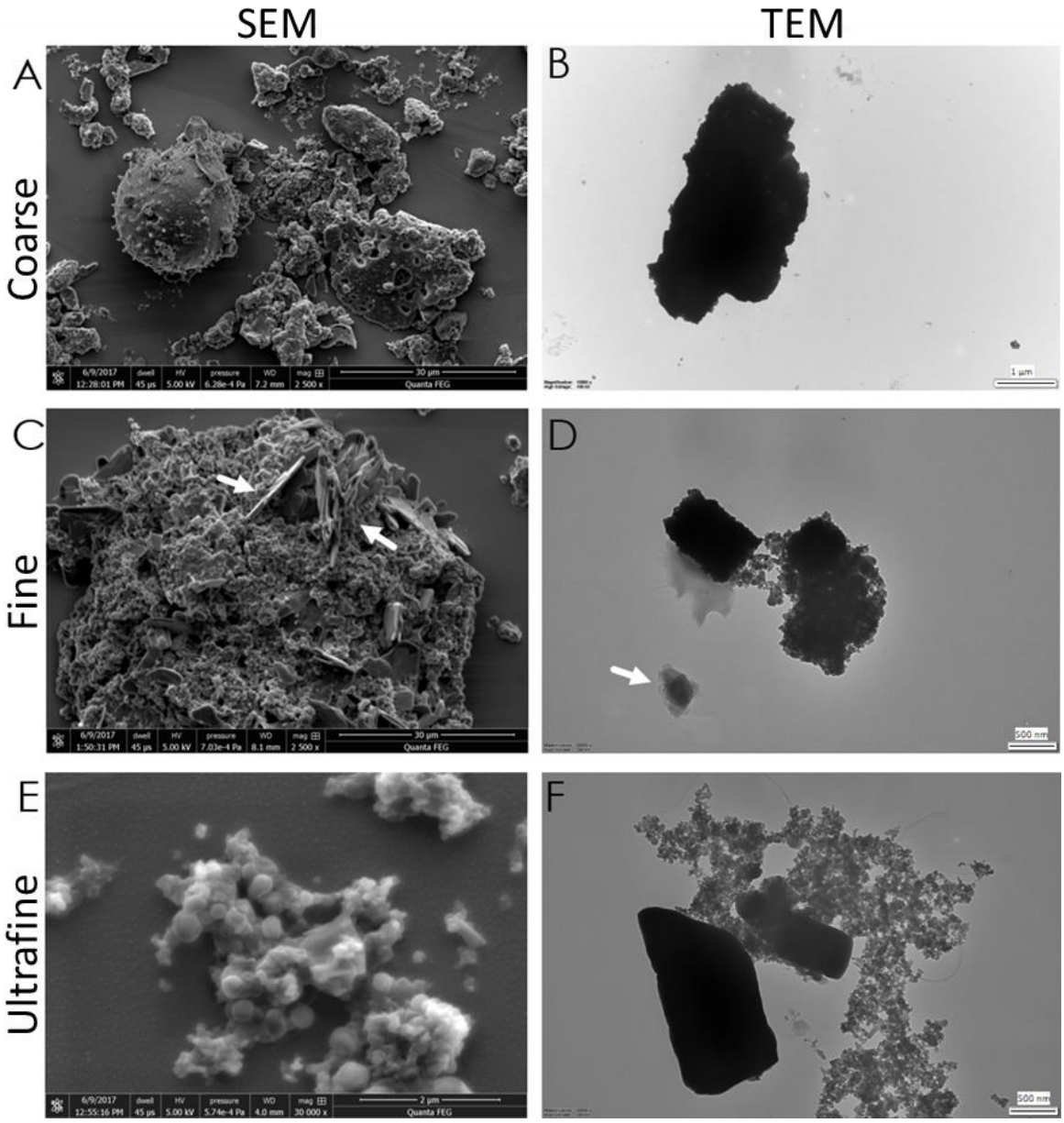

Figure 6.2. Selected electron microscopy micrographs of environmental particles. Scale bars: **A** and **C** – 30 µm; **E** – 2 µm; **B** – 1 µm; D, F – 500 nm. Arrows at **C** and **D** point at similar plate-like structures. Original images are available via supplementary data.

Energy dispersive x-ray spectroscopy was used as a rapid and straightforward analytical methodology for qualitative elemental analysis of environmental particles (the graphs are not shown). Coarse particles showed to have the largest number of different elements. C, O, S and Si were the most abundant. Less abundant, but still detectable were Al, Mg, Ti, Fe, Na, K and Ca, as well as Cu, Cr, Pb, Sn, Sc, Co, Mo and As. Fine particles had less variability and were mostly made of C, O, S, Si, Na, K, Cl, Fe, Mg and Al. Ultrafine particles showed to have a limited number of elements, such as C, O, Na, Si, S and sometimes Fe with Al. *Note: as particles were imaged on a carbon tape – carbon as the most detected signal most likely originated from it.* Mass spectrometry was used to determine the elemental composition of environmental particles. The

most abundant detected elements were Na, Ca, Mg, K, Al, Fe and Zn (above 1000 µg/g). Other elements were at significantly lower concentrations or beyond the detection limit (**Figure 6.4**).

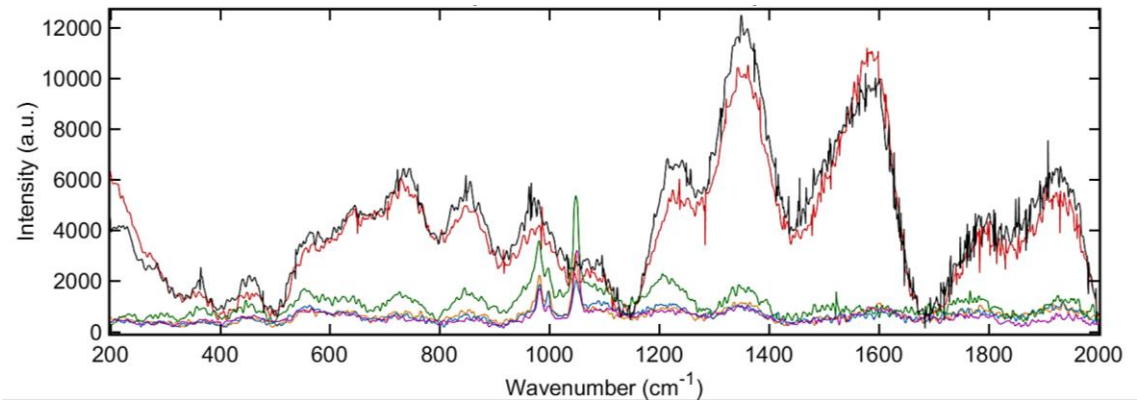

Figure 6.3. Raman spectroscopy of environmental particles. The smallest $PM_{0.1}$ fraction was analysed. The peaks at 1350 and 1550 cm^{-1} correspond to carbon. Data represent six individually plotted sampling areas within the same sample. The data collected by Adam Lister.

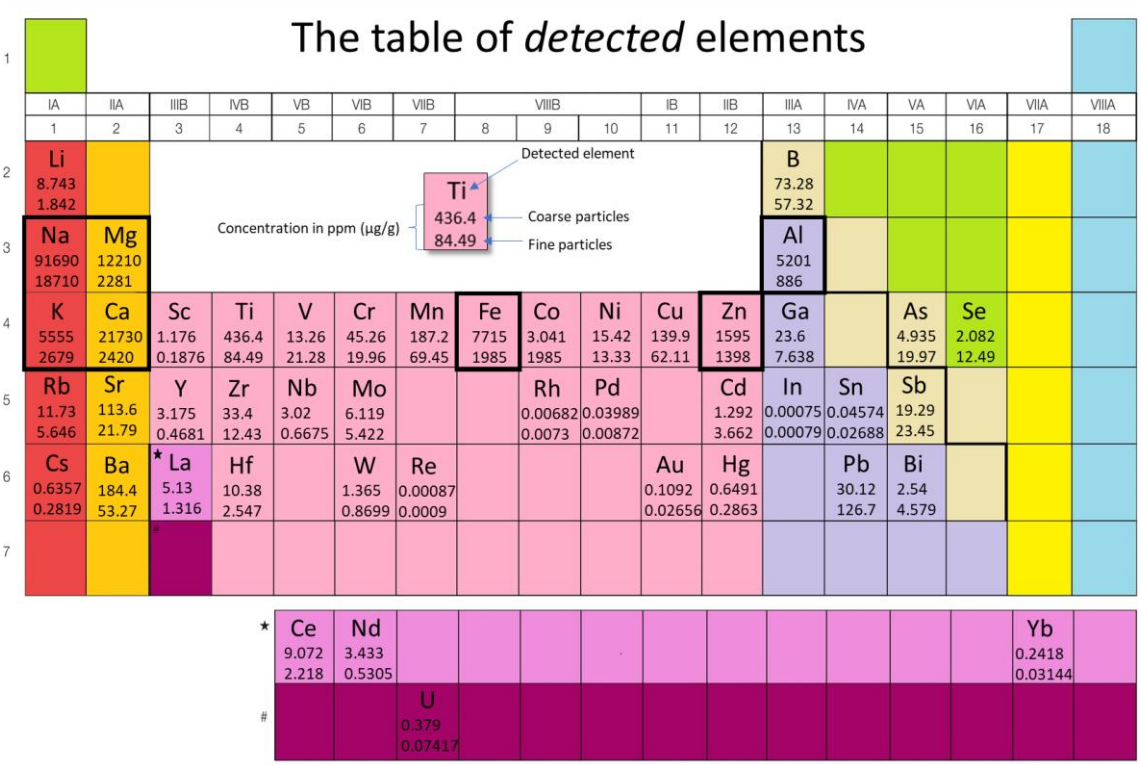

Figure 6.4. A periodic table of detected elements in environmental nanoparticles by ICP-MS. The top number in each cell corresponds to the concentration of PM_{10} and the bottom to $PM_{2.5}$ in ppm (µg/g). Concentrations were measured using ICP-MS. The $PM_{0.1}$ fraction was not analysed by the time of writing. Black frames highlight the most abundant elements.

A concentration-dependent standard curve was created to determine LD_{50} for PM_{10} and $PM_{2.5}$ and compared to AuNPs. The $PM_{0.1}$ were not used due to very limited sample availability. The LD_{50} for $PM_{2.5}$ and AuNPs after 4 h incubation was not found, while for PM_{10} it was unclear in the range from 50 µg/ml to 12.5 µg/ml (**Figure 6.5**). For 24 h incubation, the LD_{50} for $PM_{2.5}$ was 12.5 µg/ml and 3.125 µg/ml for PM_{10} (**Figure 6.6**). Based on the LD_{50} concentrations the impact of PM_{10}, $PM_{2.5}$ and $PM_{0.1}$ were assessed on the viability of RAW264.7 cells in the presence of SP-A and SP-D (**Figure 6.7-Figure 6.9**). Similar to results seen in Chapter 4 there was a slight increase in viability in the presence of SP-A and SP-D.

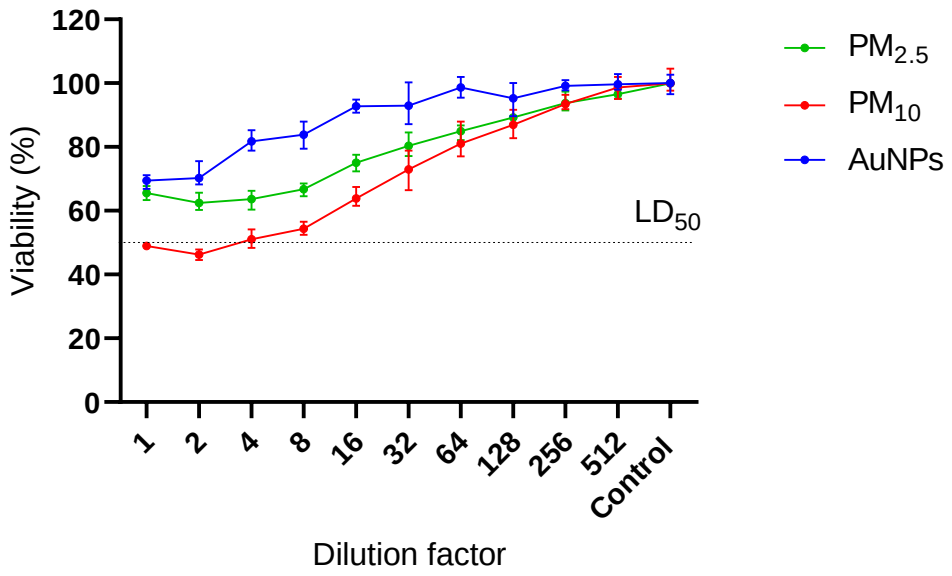

Figure 6.5. Concentration-dependent toxicity of PM_{10} and $PM_{2.5}$ on RAW264.7 measured by MTT assay. The cells were exposed for 4 h. Two-fold serial dilutions. The 1x dilution factor equals 50 µg/ml. Data was collected in the presence of 1% HI FCS. Data represent triplicates of a single experiment. Normalised data. Mean size ± SD.

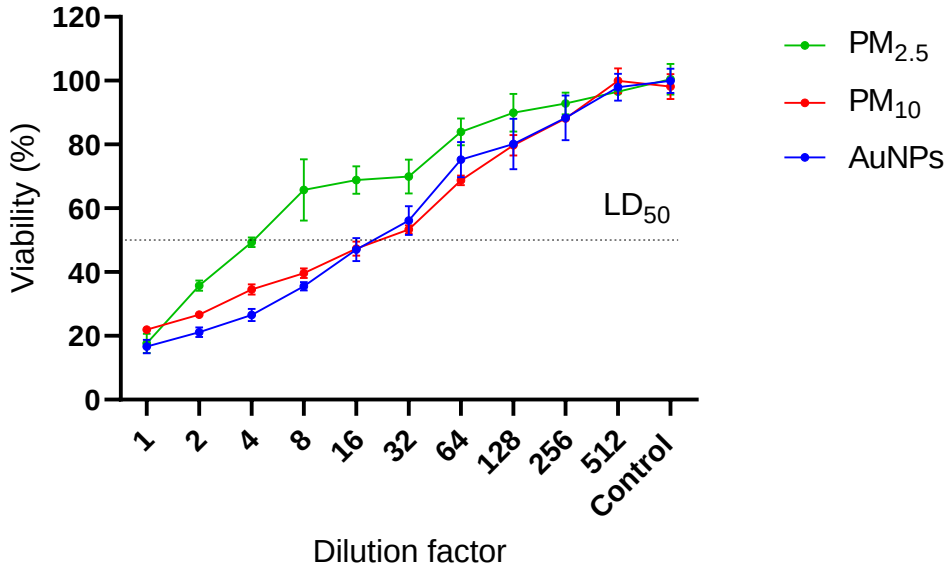

Figure 6.6. Concentration-dependent toxicity of PM_{10} and $PM_{2.5}$ on RAW264.7 measured by MTT assay. The cells were exposed for 24 h. Two-fold serial dilutions. The 1x dilution factor equals 50 µg/ml. Data was collected in the presence of 1% HI FCS. Data represent triplicates of a single experiment. Normalised data. Mean size ± SD.

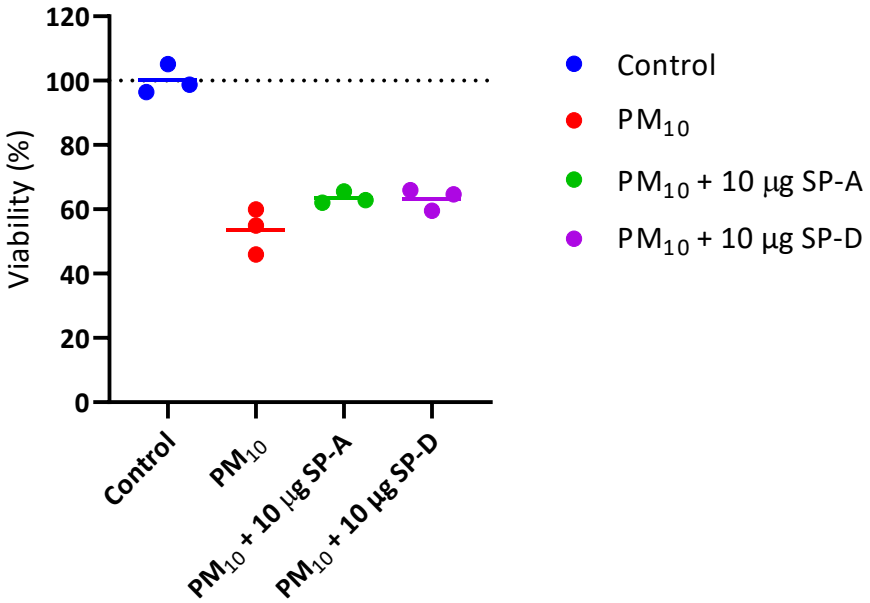

Figure 6.7. MTT assay. Dependence of PM_{10} toxicity on RAW264.7 in the presence of SP-A and SP-D. All experiments were performed in 1% HI FCS supplemented RPMI medium and 25 µg/ml of PM_{10} for 24 h. Averages of triplicate from 3 individual experiments.

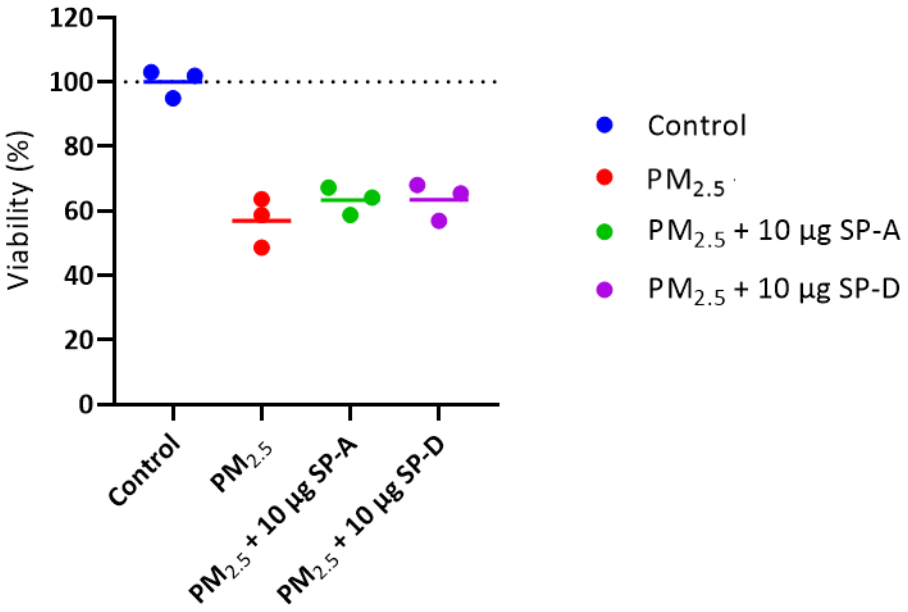

Figure 6.8. MTT assay. Dependence of $PM_{2.5}$ toxicity on RAW264.7 in the presence of SP-A and SP-D. All experiments were performed in 1% HI FCS supplemented RPMI medium and 3.125 µg/ml of $PM_{0.1}$ for 24 h. Averages of triplicate from 3 individual experiments.

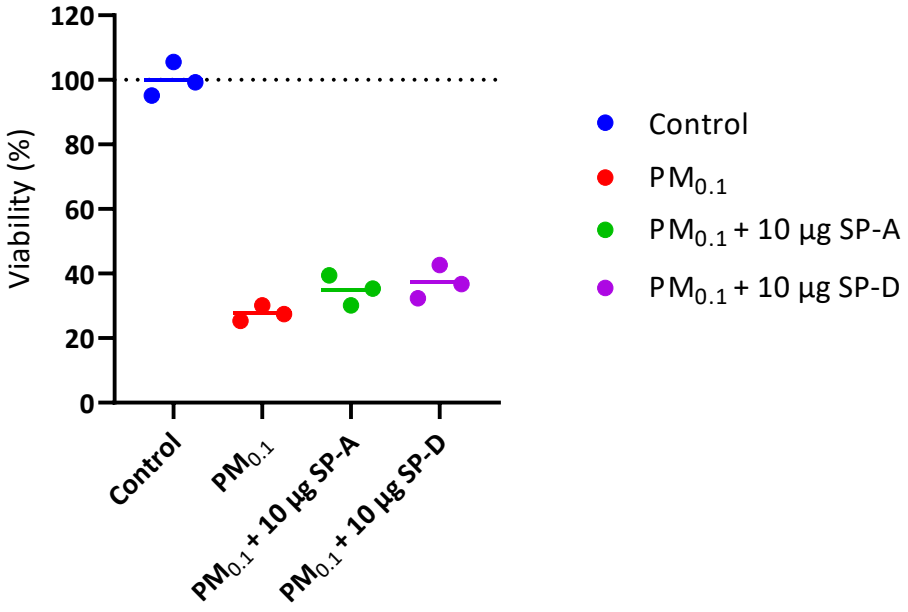

Figure 6.9. MTT assay. Dependence of $PM_{0.1}$ toxicity on RAW264.7 in the presence of SP-A and SP-D. All experiments were performed in 1% HI FCS supplemented RPMI medium and 2.5 µg/ml of $PM_{0.1}$ for 24 h. Averages of triplicate from 3 individual experiments.

6.5 Summary of the results

Within this chapter, environmental nanoparticles collected at Southampton's harbour were characterised based on their morphology and chemical composition. Additionally, preliminary experiments were performed to evaluate their toxicity on the macrophage-like cell line and the role of SP-A and SP-D, thus addressing Aim 5 (**Section 1.5**):

5. Characterise environmental nanoparticles collected from Southampton's harbour and investigate their toxicity.

The main results and achievements reported in this chapter are:

- The morphology of environmental particles depends on their size faction (PM_{10}, $PM_{2.5}$, $PM_{0.1}$). The complexity of the particles reduced with size. PM_{10} were made of heterogeneous large and smaller particles clustered into aggregated and particles of biological origin (e.g. pollen). $PM_{2.5}$ were unique to have plate-like structures. $PM_{0.1}$ were composed of relatively uniform spherical nanoparticle.
- The chemical composition of environmental particles depends on their size faction. The smaller the fraction, the less metallic composition. The most abundant chemical elements, measured by ICP-MS, were Na, Ca, Mg, K, Al, Fe and Zn.
- The toxicity of environmental particles was tested on RAW264.7 cell, where LD_{50} for $PM_{2.5}$ was 12.5 µg/ml and 3.125 µg/ml for PM_{10}. Neither SP-A nor SP-D improved the viability of the cells.

6.6 Discussion

Imaging with both SEM and TEM provided the information on morphology and size distribution of collected environmental particles. Traditional DLS could not be used as particles were unstable and heterogeneous. In general, on SEM micrographs particles were larger than on TEM. A possible explanation is because of the differences in specimen preparation. For SEM imaging, particles were left to dry, while for TEM imaging the suspension was blotted after 30 sec, resulting in more available particles for SEM imaging compared to TEM. Additionally, SEM specimens were coated with a 5 nm platinum layer. However, this is unlikely to be an issue for the observed differences in size between the two methods, because in TEM images the smallest detected particles were about 10-15 nm, while in SEM the smallest was about 80 nm. The resolution differences between two imaging techniques were likely the cause leading to "cherry-picking" and hence different results.

Images of PM_{10} showed this fraction had the largest variability in size and morphology (**Figure 6.2, A** and **B)**. A significant size variability was observed, ranging from 80 nm to 20 µm; shapes varied between spherical, elongated, fibrous and spiky (pollen), suggesting various sources of origin. PM_{10} were mostly made of a single piece of material, particles were too large and too dense to see through them. Particles as small as 20-25 nm were detected occasionally. Imaging the $PM_{2.5}$ fraction with SEM (**Figure 6.2, C** and **D**) revealed interesting aggregates containing flat, plate-like structures. These structures are thought to be friction derived particles, which is supported by data from literature[37]. These plate-like structures were exclusively seen in the $PM_{2.5}$ fraction. A significant number of particles formed 20-40 µm agglomerates, suggesting they were composed of a large number of smaller particles, as the majority of >10 µm had to be blocked by the filter. TEM micrographs showed large (1-5 µm) particles with a dense core and multiple smaller (10-80 nm) particles around it. Plate-like structures, seen in SEM, were also detected. The $PM_{0.1}$ fraction, compared to the other two, was very homogenous in its composition (**Figure 6.2, E** and **F**). It was significantly easier to resolve individual particles, as they were not forming large and high-density aggregates. Yet, large 500-1000 nm structures were still observed. The majority of NP were spherical with a size range of 10 to 80 nm, which is consistent with the literature.[37,298]

The EDX was used as a rapid technique to qualitatively determine elemental composition. All fractions shared sulphur, oxygen, and silicon. Potassium, sodium, calcium and magnesium where the most abundant metals detected. In general, the particles showed a less metallic profile in the order of PM_{10}>$PM_{2.5}$>$PM_{0.1}$. Carbon was detected in all samples. However, this signal could potentially be a background signal from the carbon tape, as all particles were dried and analysed

on it. The EDX data were supported with ICP-MS, with more elements detected and quantified (**Figure 6.4**). Only coarse and fine particles were analysed using ICP-MS. It was noted that high amounts of K, Na, Ca, and Mg were found in these particles. High potassium concentration has been previously linked to biomass burning.[299] Considering the particles were collected in the harbour, high sodium and magnesium contents possibly originated from sea spray. These two elements may account for up to 80% of PM_{10} in coastal regions.[300] Most of the other metals are associated with mechanical abrasion processes, construction or fuel additives.[301] Since carbon is of high interest as an air pollutant but was not successfully identified with EDX or ICP-MS, Raman spectroscopy was applied (**Figure 6.3**). Only the smallest fraction, $PM_{0.1}$, was used, as it has the greatest health concerns. The Raman spectroscopy data confirmed the presence of carbon, though no quantification was possible.

The toxicity data for environmental particles was assessed by determining LD_{50} first. Since the particles were heterogeneous and no experiments could be designed using the number of particles or surface area as concentration, the mass was used instead. For the standard curve, the same mass of PM_{10} and $PM_{2.5}$ was used as was for 20 nm AuNPs (refer to **Chapter 4**). $PM_{0.1}$ was not used due to a limited sample availability. After 4 hours the toxicity was as follows: AuNPs>$PM_{2.5}$>PM_{10} (least to most toxic, **Figure 6.5**), and $PM_{2.5}$> PM_{10}≥AuNPs (least to most toxic, **Figure 6.6**) after 24 h. Overall the toxicity of environmental and AuNPs was quite similar, which would not normally be expected. Possibly, the toxicity of environmental particles was reduced as they tend to aggregate quickly, hence increasing in size (it is known that larger particles are less toxic), while AuNPs did not change in size. Similar to the results seen with AuNPs in **Chapter 4**, SP-A and SP-D did not increase the viability of the cells in the presence of all three particulate matter fractions. The BSA was not used due to limited sample availability and there was no reason to expect a different result from before.

6.7 Conclusions

The findings suggest that spherical NPs in the size range of 10 to 80 nm were the most abundant (by number) in the atmosphere, while larger NPs were in fact aggregates of smaller particles. Thus, spherical particles are suggested for *in vivo* and *in vitro* experiments. The most abundant detected elements were Na, Ca, Mg, K, Al, Fe and Zn, with a large number of other metals of lower and trace concentrations. SP-A and SP-D did not show to significantly improve the viability of the cells; more research applying alternative analyses is required.

In-depth analysis of environmental nanoparticles was beyond the scope of this study, however, the data collected by this preliminary work can be used for future work and directions to better understand the role of SP-A and SP-D in environment-relevant models.

Chapter 7 Summary and future work

The research hypothesis of this PhD project was that lung surfactant proteins A and D bind to and opsonise inhaled engineered gold nanoparticles reducing *in vivo* translocation to the secondary organs. To confirm the hypothesis, the study was divided into several research sub-projects to address the hypothesis and build the layer of evidence using multiple verification techniques and approaches.

The development of multimodal microscopy methods for non-invasive, non-destructive, and label-free imaging of AuNPs in biological samples was the first step in the study and is covered in **Chapter 3**. The experiments showed that TPF was the optimal option if general cell imaging was required, as the signal from FAD was strong and provided good contrast against the non-resonant background. The signal from CARS was very weak and provided little contrast, and thus was not desirable for imaging, unless selective lipid imaging is required. SHG was used for AuNPs imaging, as they were visualised in a semi-selective fashion (as there was no interference from cellular components) and required minimal image processing. The same information could be extracted from TPF images, though more processing steps were needed. For the imaging of the cells treated with AuNPs, a combination of SHG and TPF showed to be preferential. However, the multimodal imaging was not applicable for tissue treated with AuNPs, as the interference from the tissue biological components interfered and could not be separated. Overall, the system showed promising results for application with single cells.

The imaging methods were significantly improved by the introduction of the third dimension (Z-scale) overall semi-automation, compared to the previous work. For the future, the methods have to be optimised to reduce the photodamage due to intrinsic photothermal properties of AuNPs. A combination of light microscopy with lower power SHG/TPF, as well as different light filter combinations can be explored. While it is known the system can visualise AuNPs in the cells, it was not possible to do so in tissue within this experiment. Tissue imaging has significant biomedical relevance, and hence future work should focus on method optimisation. Finally, 3View imaging was used for an exploratory purpose. While sample preparation is labour intensive, imaging is long, and data analysis is computation heavy, the results can be both qualitative (visual, particle distribution and morphology at high resolution) and quantitative (numerical value of internalised particles or aggregates), hence the technique has to be used as an additional verification method.

In vitro experiments are the foundation of biomedical research. This study was no exception, and the work is covered in **Chapter 4**. The main objective was to determine whether SP-A and SP-D

can selectively (or non-selectively) bind to AuNPs and induce their aggregation, as it is seen with bacteria or polymer particles. The study applied a range of biophysical methods, however, most had limitations. The results from DLS were interfered with by salts-induced aggregation of AuNPs and the proteins themselves. Protein analyses methods (SDS-PAGE, Bradford assay) had a high chance of false-positives or negative findings due to protein precipitation due to centrifuging. However, there is tentative evidence that SP-A and SP-D do have a higher affinity to AuNPs, compared to BSA. These results have to be interpreted with caution, and other techniques have been applied to confirm the findings.

Cell culture experiments did not show any changes in AuNP treated cell viability in the presence of surfactant proteins, compared to BSA. Yet, the addition of extra protein showed to reduce the toxicity. Semi-quantitative multimodal imaging showed that SP-A and SP-D suppressed AuNP uptake, compared to the control. The results have to be verified by an established technique. It remains unknown whether the results were influenced by the presence of HI FCS or not.

Unmodified AuNPs are very sensitive to the surrounding environment and hence very difficult to work with. The analyses techniques should account for that, and any methods that might be sensitive to destabilised particles have to be avoided. One of the alternative methods – surface-enhanced Raman spectroscopy (SERS), a technique that is based on a significant enhancement of inelastic scattering of molecules adsorbed on gold or silver nanostructures and allows for the detection and quantification of low-abundance molecules.[302] The technique is not sensitive to AuNP aggregation, while allows for accurate analysis of adsorbed proteins, and hence should be explored in future. The quartz-crystal microbalance (QCM) method was used in this study to overcome the aggregation of AuNPs and proteins. There was little time available with the machine, as the work was performed at the Facility for Environmental Nanoscience Analysis and Characterisation (FENAC; University of Birmingham), and the majority of the time was spent on calibration and optimisation. However, trial results confirmed the method could be further developed and applied to measure the affinity of SP-A and SP-D to Au surfaces. **Figure 7.1** shows an example of SP-A binding to the Au surface in the presence of calcium. A difference of 40 Hz was observed once SP-A was injected, which was 60% more compared to BSA and calcium. However, the experiment was not finished, and the data is not complete.

Cell culture experiments focused on one cell type only – RAW264.7. More cells lines should be used in future to mimic the surface of the lungs, such as A549 (alveolar type I-like cell line) and TT1 (alveolar type II-like cell line). This will help to understand not only the impact on macrophages but whether the surfactant proteins reduce the toxicity in pneumocytes. Additional tests have to be applied as well, such as a reactive oxygen species (ROS) assay. This study

attempted to quantify ROS by applying a CellRox kit, though the assay was unsuccessful several times and the assay was not replicated due to high cost.

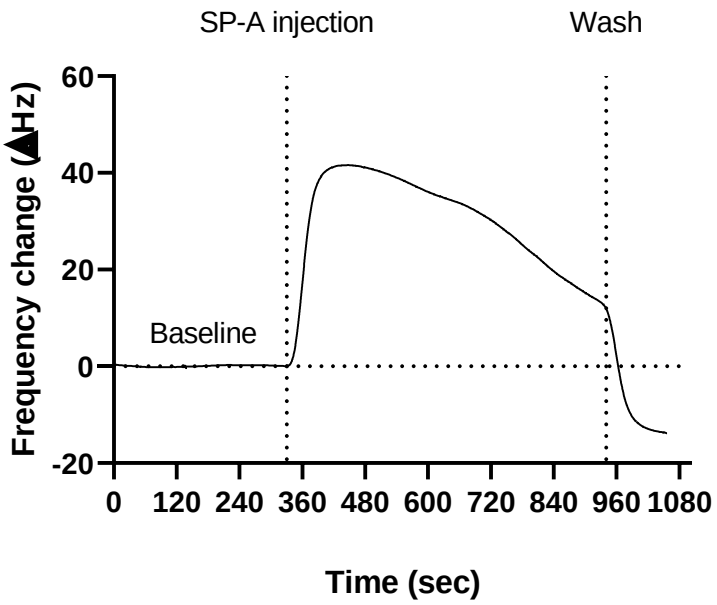

Figure 7.1. An example of the QCM trial experiment results. The chart shows SP-A binding to the gold surface. Baseline – a background signal variation. SP-A injections – indicates the moment when SP-A was introduced into the system. Wash – end of the experiment.

Arguably the most important part of this study was *in vivo* experiments, covered in **Chapter 5**, as they were the final and logical step to test all previously collected knowledge and hypotheses. The study used genetic knockout mice for the first time to study the role of SP-A and SP-D. While there was no statistically significant evidence of any difference between genotypes, there is tentative evidence in favour of SP-D knockout mice. Wild type and AKO showed very similar clearance rates and the average size of AuNPs aggregates. However, DKO showed to be more efficient in reduction by mass and struggled with clearance by particle number. Also, the average size of the aggregates was smaller, compared to AKO and WT. Multimodal imaging indicated that at day 7 DKO and AKO macrophages internalised significantly fewer AuNPs. There was no translocation to secondary organs detected in either genotype.

This was the first study, and the experimental conditions had to be adapted based on information available in the literature, as well as trial and error. Yet, this provides valuable information for a future experiment. First of all, the duration of the exposure (or their number) will have to be increased to maximise the chances of translocation detection. Use of the same gender only mice might be considered to reduce variability. Next, the quantity of AuNPs was quantified by ICP-MS, which is a laborious method. Future experiments should consider the application of radioactive nanoparticles to allow for rapid quantification in the whole organism without lengthy sample

processing. This study explored the use of X-ray microtomography (µCT) for a rapid AuNP quantification in the entire organ (**Figure 7.2**). However, the resolution was not sufficient to resolve even larger aggregates within the lung tissue. Since it was a one-time trial experiment, it is unclear whether the technique should be applied again.

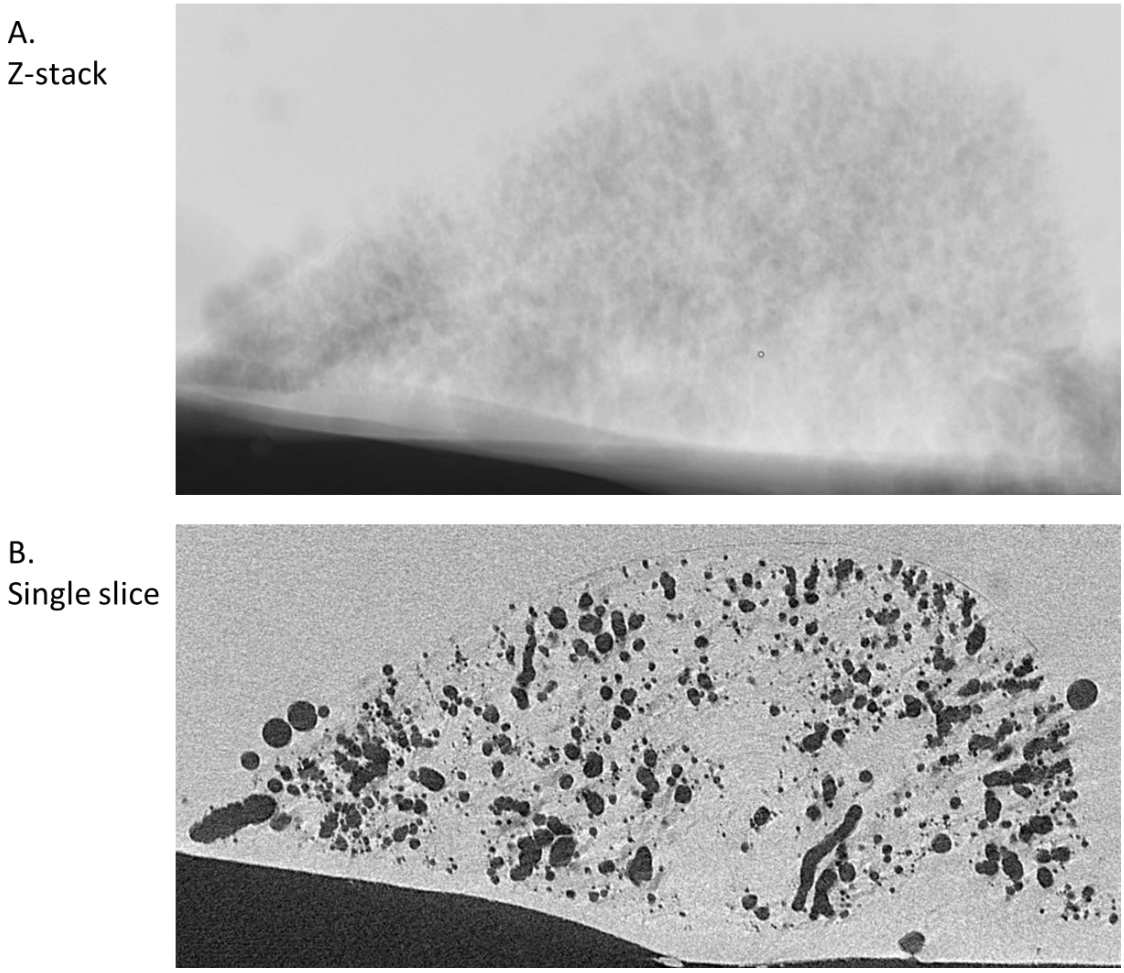

Figure 7.2. µCT images of wild type mouse lungs 1-day post AuNPs exposure. The left lung lobe was frozen in OCT. **A** – Z-stack projection of 1500 images. **B** – a single image from the middle of the stack. Black areas – air cavities not filled with OCT.

One of the reasons to use AuNPs for the experiments was that it is not naturally present in the organism, making it possible to quantify with ICP-MS without interference. While AuNPs have biomedical relevance, polymeric particles, such as polystyrene, have higher relevance mimicking environmental pollution and are known to have adverse effects, yet cannot be easily quantified with ICP-MS. This can be solved by employing polystyrene nanoparticles with a gold core, hence the surface will function as a polystyrene particle, while the core will be exploited for ICP-MS. This would allow for the *in vivo* experiments with SP-A and SP-D to validate the findings from the previously published *in vitro* based studies with surface modified PS particles[8,10].

Finally, **Chapter 6** was a side project to establish a better understanding of the relevance of AuNPs as a model used within this research and to determine future steps and project directions. The data showed the size distribution and morphology of the particles. The smallest fraction, $PM_{0.1}$, was of the most interest due to known health hazards. The particles were spherical and formed larger aggregates. ICP-MS data showed the heterogenous elemental composition with more than 30 elements detected. Basic understanding of SP-A and SP-D interaction between environmental particles has to be established using test-tube experiments (to assess agglutination) and cell culture experiments (measure uptake, inflammatory response). A field flow fractionator can be used to separate heterogeneous environmental particles into more homogenous (by size) fractions, allowing a higher degree of control and data reproducibility. Such a system is available at the FENAC, University of Birmingham. It was planned to use the technique, but not possible due to time restrictions and a very limited sample. Described methods and experiments will require large quantities of particles, which have to be collected in advance. It is also important to note that the composition (and hence the toxicological profile) will be subject to batch-to-batch variation, affected by the season and weather conditions. Nevertheless, such experiments will be highly relevant from the environmental health perspective and will shed light on the SP-A and SP-D role.

For future work, most of the methods applied in **Chapter 4** can be applied for environmental particles while addressing the mentioned limitations, as a logical continuation of the work performed with AuNPs. Multimodal imaging can be used to establish whether it is possible to imagine such a diverse mixture without using any labels and avoiding photodamage.

Appendix A List of materials and reagents

Consumable	Full name	Order code	Supplier
96-Well Microplates	Thermo Scientific™ Nunc™ MicroWell™ 96-Well Microplates	10212811	Fisher Sci
Bradford Assay Reagent, Detergent Compatible	Thermo Scientific™ Pierce™ Detergent Compatible Bradford Assay Reagent	15308096	Fisher Sci
Bradford Protein Assay	Thermo Scientific™ Pierce™ Coomassie Plus™ (Bradford) Protein Assay	10495315	Fisher Sci
BSA Polyclonal Antibody	BSA Polyclonal Antibody, Invitrogen™	10092782	Fisher Sci
Butanol	1-Butanol, 99%, extra pure, ACROS Organics™, 2.5 L	10376070	Fisher Sci
Calcium Chloride	Calcium Chloride, Extra Pure, SLR, Fused, Granular, Fisher Chemical	10478590	Fisher Sci
Cell Culture Flasks	Thermo Scientific™ Nunc™ EasYFlask™ Cell Culture Flasks	10364131	Fisher Sci
Cell Scrapers	Fisherbrand™ Cell Scrapers	11597692	Fisher Sci
CellROX™ Deep Red Reagent	Invitrogen™ Molecular Probes™ CellROX™ Deep Red Reagent	12013765	Fisher Sci
Coverslips	Thermo Scientific™ Nunc™ Thermanox™ Coverslips	10252961	Fisher Sci
Disposable Pipette Basins	Fisherbrand™ Disposable Pipette Basins	11978485	Fisher Sci
Divinyl sulfone	Alfa Aesar™ Divinyl sulfone, 97%, stab. with 0.05% hydroquinone	11393386	Fisher Sci
DMSO	Dimethyl Sulfoxide, Certified AR for Analysis, Fisher Chemical	10206581	Fisher Sci
Dounce tissue grinder set, 15 mL complete	Dounce tissue grinder set, 15 mL complete	D9938-1SET	Sigma-Aldrich
Fetal Bovine Serum	Gibco™ Fetal Bovine Serum, qualified, heat inactivated, E.U.-approved, South America Origin	11550356	Fisher Sci
Folded Capillary Zeta Cell (box of 10)	Folded Capillary Zeta Cell (box of 10)	DTS1070	Malvern
Gel Loading Buffer, 10X	Invitrogen™ BlueJuice™ Gel Loading Buffer, 10X	10666143	Fisher Sci
Glutaraldehyde	Alfa Aesar™ Glutaraldehyde, 25% aq. soln., 100 mL	11433107	Fisher Sci
Gold nanoparticles, 20nm	Alfa Aesar™ Gold nanoparticles, 20nm, supplied in 0.1mM PBS, reactant-free, 99%, OD1, 524nm absorption	15494605	Fisher Sci
Haemocytometer	Brand™ Blaubrand™ Neubauer Rhodium Coated Counting Chamber	10350141	Fisher Sci
High Capacity Endotoxin Removal Resin	Thermo Scientific™ Pierce™ High Capacity Endotoxin Removal Resin	12351973	Fisher Sci
Hydrochloric Acid, 32%	Hydrochloric Acid, 32%, Certified AR for Analysis, d=1.16, Fisher Chemical	10458980	Fisher Sci
Invitrogen™ 1 Kb Plus DNA Ladder	Invitrogen™ 1 Kb Plus DNA Ladder	11578636	Fisher Sci

Isopropanol	*Isopropanol, Certified AR for Analysis, Fisher Chemical*	*10315720*	*Fisher Sci*
Isopropanol, Extra Pure	*Isopropanol, Extra Pure, SLR, Fisher Chemical*	*10588630*	*Fisher Sci*
LAL Chromogenic Endotoxin Quantitation Kit	*Thermo Scientific™ Pierce™ LAL Chromogenic Endotoxin Quantitation Kit*	*12117850*	*Fisher Sci*
LDH assay kit	*Invitrogen™ CyQUANT™ LDH Cytotoxicity Assay*	*16270972*	*Fisher Sci*
LoBind Microcentrifuge Tube	*Eppendorf™ Polypropylene Protein LoBind Microcentrifuge Tube*	*10708704*	*Fisher Sci*
Mark12™ Standard, Unstained	*Invitrogen™ Novex™ Mark12™ Standard, Unstained*	*10154962*	*Fisher Sci*
Methanol	*GiMethanol, Certified AR for Analysis, Fisher Chemical*	*10284580*	*Fisher Sci*
Microscopic Slides with Ground Edges	*Fisherbrand™ Microscopic Slides with Ground Edges*	*11562203*	*Fisher Sci*
Mowiol® 4-88	*Mowiol® 4-88*	*81381-50G*	*Sigma-Aldrich*
MTT (Thiazolyl Blue tetrazolium bromide)	*Alfa Aesar™ Thiazolyl Blue tetrazolium bromide, 98%*	*11312727*	*Fisher Sci*
N-Acetyl-D-mannosamine monohydrate, 99%,	*N-Acetyl-D-mannosamine monohydrate, 99%, Alfa Aesar™*	*11367606*	*Fisher Sci*
Non-treated Flasks	*Thermo Scientific™ Nunc™ Non-treated Flasks*	*10076901*	*Fisher Sci*
Novex™ NuPAGE™ 4-12% Bis-Tris Protein Gels, 1.0mm, 12 well	*Invitrogen™ Novex™ NuPAGE™ 4-12% Bis-Tris Protein Gels, 1.0mm, 12 well*	*10247002*	*Fisher Sci*
Novex™ NuPAGE™ 4-12% Bis-Tris Protein Gels, 1.0mm, 17 well	*Invitrogen™ Novex™ NuPAGE™ 4-12% Bis-Tris Protein Gels, 1.0mm, 17 well*	*10780345*	*Fisher Sci*
NuPAGE™ 4-12% Bis-Tris Protein Gels, 1.0mm, 10 well	*Invitrogen™ Novex™ NuPAGE™ 4-12% Bis-Tris Protein Gels, 1.0mm, 10 well*	*15714312*	*Fisher Sci*
OCT Embedding Matrix	*Cellpath™ OCT Embedding Matrix*	*15212776*	*Fisher Sci*
OGP	*1-O-n-Octyl-β-D-glucopyranoside, 98%, ACROS Organics*	*10541794*	*Fisher Sci*
OGP	*n-Octyl-β-D-glucopyranoside (White Crystalline Powder), Fisher BioReagents*	*10326843*	*Fisher Sci*
Paraformaldehyde, powder, 95%, 500g	*Paraformaldehyde, powder, 95%, 500g*	*158127*	*Sigma-Aldrich*
PBS (sterile)	*Gibco™ PBS, pH 7.4 (sterile)*	*11593377*	*Fisher Sci*
PBS, 10X Powder	*PBS, Phosphate Buffered Saline, 10X Powder, pH 7.4, Fisher BioReagents*	*10051163*	*Fisher Sci*
Phire™ Animal Tissue Direct PCR Kit	*Thermo Scientific™ Phire™ Animal Tissue Direct PCR Kit*	*15183133*	*Fisher Sci*
PIPES	*Alfa Aesar™ PIPES, 98%, 25g*	*11448900*	*Fisher Sci*
PVDF Transfer Stack	*Invitrogen™ Novex™ iBlot™ PVDF Transfer Stack*	*11524906*	*Fisher Sci*
Round Coverslip dia. 13mm #1.5	*Thermo Scientific Menzel X1000 Round Coverslip dia. 13mm #1.5 (0.16-0.19mm)*	*11588492*	*Fisher Sci*

RPMI 1640 Medium, no phenol red	*Gibco™ RPMI 1640 Medium, no phenol red*	*11530406*	*Fisher Sci*
RPMI 1640 Medium	*Gibco™ RPMI 1640 Medium*	*11530586*	*Fisher Sci*
Sample Reducing Agent (10X)	*Invitrogen™ NuPAGE™ Sample Reducing Agent (10X)*	*11569166*	*Fisher Sci*
SeeBlue™ Plus2 Pre-stained Protein Standard	*Invitrogen™ Novex™ SeeBlue™ Plus2 Pre-stained Protein Standard*	*10174502*	*Fisher Sci*
Silver Staining Kit	*Invitrogen™ Novex™ SilverXpress™ Silver Staining Kit*	*10052662*	*Fisher Sci*
SimplyBlue™ SafeStain	*Invitrogen™ Novex™ SimplyBlue™SafeStain*	*10533053*	*Fisher Sci*
Sterile PES Syringe Filter – 1	*Fisherbrand™ Sterile PES Syringe Filter – 1*	*15206869*	*Fisher Sci*
Sterile PES Syringe Filter – 2	*Fisherbrand™ Sterile PES Syringe Filter – 2*	*15216869*	*Fisher Sci*
Sterile Polystyrene Disposable Serological Pipets	*Fisherbrand™ Sterile Polystyrene Disposable Serological Pipets with Magnifier Stripe*	*11809660*	*Fisher Sci*
SYBR™ Safe™ DNA Gel Stain	*Invitrogen™ SYBR™ Safe™ DNA Gel Stain*	*10328162*	*Fisher Sci*
Syringe Filter Unit, 0.22 µm, PVDF, 33 mm, gamma sterilized	*Millex-GV Syringe Filter Unit, 0.22 µm, PVDF, 33 mm, gamma sterilized*	*SLGV033RS*	*Merck Millipore*
Syringe Filter Unit, 0.45 µm, PVDF, 33 mm, gamma sterilized	*Millex-HV Syringe Filter Unit, 0.45 µm, PVDF, 33 mm, gamma sterilized*	*SLHV033RS*	*Merck Millipore*
tert-Butyl hydroperoxide, 70%	*tert-Butyl hydroperoxide, 70% Solution in water, ACROS Organics™*	*10266090*	*Fisher Sci*
TRIS-buffered saline (TBS, 20X)	*Alfa Aesar™ TRIS-buffered saline (TBS, 20X) pH 7.4, 1L*	*15413579*	*Fisher Sci*
UVette	*Eppendorf™ UVette™*	*10412121*	*Fisher Sci*
Virkon	*Day Impex™ Virkon™ Disinfectant Virucidal Drum*	*12358667*	*Fisher Sci*
Western Blot Stripping Buffer	*Thermo Scientific™ Restore™ Western Blot Stripping Buffer*	*10057103*	*Fisher Sci*

Appendix B Fiji scripts

These are Fiji (ImageJ) scripts for image analysis. The scripts are ready to be used as they are by copying and pasting into the software.

B.1 Split and save three-channel images

```
macro split_color{
 dir1 = getDirectory("Choose source directory");
 list = getFileList(dir1);
 dir2 = dir1+"CARS"+File.separator;
 File.makeDirectory(dir2);
 dir3 = dir1+"SHG"+File.separator;
 File.makeDirectory(dir3);
 dir4 = dir1+"TPF"+File.separator;
 File.makeDirectory(dir4);
setBatchMode(true);
 for (i=0; i<list.length; i++) {
 open(dir1+list[i]);
 title1=File.nameWithoutExtension;
 for (j=1; j<=3; j++){
  run("Make Substack...", " slices="+j);
  if (j==1)
       {
        c = "CARS";
        a = dir2;
        saveAs("tif", a+title1+"-"+c+".tif");
       }
  else if(j==2)
       {
        c = "SHG";
        a = dir3;
        saveAs("tif", a+title1+"-"+c+".tif");
       }
  else if (j==3)
       {
        c = "TPF";
        a = dir4;
        saveAs("tif", a+title1+"-"+c+".tif");
       }
  wait(100);
  close();
 }
 close();
 }
 showMessage("Macro is finished");
}
```

B.2 Counting pixels in image stacks

```
run("Clear Results");
```

```
setOption("ShowRowNumbers", false);
for (slice=1; slice<=nSlices; slice++) {
 setSlice(slice);
 getRawStatistics(n, mean, min, max, std, hist);
 for (i=0; i<hist.length; i++) {
  setResult("Value", i, i);
  setResult("Count"+slice, i, hist[i]);
 }
}
resultRows = nResults;
for (k=0; k< resultRows; k++) {
 tot = 0;
 for (l=1; l <= nSlices; l++) {
  ntot = parseInt(getResult("Count"+l, k));
  tot = tot + ntot;
 }
 print("Value " + k + " = " + tot);
}
```

B.3 Plot and save the profile on the image stack

```
macro "Stack profile Data" {
   if (!(selectionType()==0 || selectionType==5 || selectionType==6))
    exit("Line or Rectangle Selection Required");
   setBatchMode(true);
   run("Plot Profile");
   Plot.getValues(x, y);
   run("Clear Results");
   for (i=0; i<x.length; i++)
     setResult("x", i, x[i]);
   close();
   n = nSlices;
   for (slice=1; slice<=n; slice++) {
     showProgress(slice, n);
     setSlice(slice);
     profile = getProfile();
     sliceLabel = toString(slice);
     sliceData = split(getMetadata("Label"),"\n");
     if (sliceData.length>0) {
       line0 = sliceData[0];
       if (lengthOf(sliceLabel) > 0)
         sliceLabel = sliceLabel+ " ("+ line0 + ")";
     }
     for (i=0; i<profile.length; i++)
       setResult(sliceLabel, i, profile[i]);
   }
   setBatchMode(false);
   updateResults;
}
```

B.4 Create 3D projection out of 2 channel images

```
macro split_color{
```

```
dir1 = getDirectory("Choose source directory");
list = getFileList(dir1);
dir2 = getDirectory("Choose CARS directory")
dir3 = getDirectory("Choose SHG directory")
setBatchMode(true);
for (i=0; i<list.length; i++) {
open(dir1+list[i]);
title1=File.nameWithoutExtension;
for (j=1; j<=2; j++){
 run("Properties...", "channels=2 slices=1 frames=1 unit=micron pixel_width=352
pixel_height=352 voxel_depth=0.25"); // set image properties here eg: scale etc
 run("Make Substack...", " slices="+j);
 if (j==1)
 {
  c = "CARS";
  a = dir2;
  saveAs("tif", a+title1+"-"+c+".tif");
  tag1 = getInfo("image.filename");
 }
 else if(j==2)
 {
  c = "SHG";
  a = dir3;
  saveAs("tif", a+title1+"-"+c+".tif");
  tag2 = getInfo("image.filename");
 }
 wait(100);
 close();
}
close();
}
setBatchMode(false);
CARSseq = dir2 + "/" + tag1;
run("Image Sequence...", "open=[CARSseq] sort");
rename("CARS")
SHGseq = dir3 + "/" + tag2;
run("Image Sequence...", "open=[SHGseq] sort");
rename("SHG")
run("Merge Channels...", "c6=CARS c7=SHG create ignore");
saveAs("tif", dir1+"composite-Stack")
run("3D Project...", "projection=[Brightest Point] axis=Y-Axis slice=352.86 initial=0 total=360
rotation=10 lower=1 upper=255 opacity=0 surface=100 interior=50"); // set the parameters of the
3D //project here
saveAs("tif", dir1+"composite-3D")
```

Appendix C Composition of SF RPMI 1640 medium

Components	Concentration (mg/L)
Inorganic salts	
Calcium nitrate	100.00
Potassium chloride	400.00
Magnesium sulphate	48.84
Sodium chloride	6000.00
Sodium bicarbonate	2000.00
Sodium Phosphate	800.85
Other components	
Glucose	2000.00
Glutathione Reduced	1.00
Phenol red	5.00
Amino acids	
L-Arginine	200.00
L-Asparagine monohydrate	56.80
L-Aspartic Acid	20.00
L-Cystine	50.00
L-Glutamic Acid	20.00
L-Glutamine	300.00
Glycine	10.00
L-Histidine	15.00
L-Hydroxyproline	20.00
L-Isoleucine	50.00
L-Leucine	50.00
L-Lysine hydrochloride	40.00
L-Methionine	15.00
L-Phenylalanine	15.00
L-Proline	20.00
L-Serine	30.00
L-Threonine	20.00
L-Tryptophan	5.00
L-Tyrosine	20.00
L-Valine	20.00
Vitamins	
Biotin	0.20
Calcium D-pantothenate	0.25
Choline Chloride	3.00
Folic Acid	1.00
i-Inositol	35.00
Niacinamide	1.00
para-Aminobenzoic Acid (PABA)	1.00
Pyridoxine hydrochloride	1.00
Riboflavin	0.20
Thiamine hydrochloride	1.00
Vitamin B12	0.005

List of References

1. Chen, S., Arsenault, C., Gingras, Y. & Larivière, V. Exploring the interdisciplinary evolution of a discipline: the case of Biochemistry and Molecular Biology. *Scientometrics* **102**, 1307–1323 (2014).

2. Van Noorden, R. Interdisciplinary research by the numbers. *Nature* vol. 525 306–307 (2015).

3. Donaldson, K., Stone, V. & Tran, C. L. doi: 10.1136/oem.2004.013243. *Occup. Environ. Med.* **61**, 727–728 (2004).

4. Suh, W. H., Suslick, K. S., Stucky, G. D. & Suh, Y. H. Nanotechnology, nanotoxicology, and neuroscience. *Progress in Neurobiology* vol. 87 133–170 (2009).

5. STATNANO. Nanotechnology Products Database. https://product.statnano.com/ (2019).

6. Kagan, V. E., Bayir, H. & Shvedova, A. A. Nanomedicine and nanotoxicology: two sides of the same coin. *Nanomedicine Nanotechnology, Biol. Med.* **1**, 313–316 (2005).

7. Ostrowski, A. *et al.* Overview about the localization of nanoparticles in tissue and cellular context by different imaging techniques. *Beilstein J. Nanotechnol.* **6**, 263–280 (2015).

8. McKenzie, Z. *et al.* Surfactant protein A (SP-A) inhibits agglomeration and macrophage uptake of toxic amine modified nanoparticles. *Nanotoxicology* **5390**, 1–11 (2015).

9. Kendall, M. *et al.* Surfactant protein D (SP-D) alters cellular uptake of particles and nanoparticles. *Nanotoxicology* **7**, 963–73 (2013).

10. McKenzie, Z. *et al.* Nanoparticles modulate surfactant protein A and D mediated protection against influenza A infection in vitro. *Philos. Trans. R. Soc. B Biol. Sci.* **370**, 20140049–20140049 (2014).

11. Whitwell, H. *et al.* Nanoparticles in the lung and their protein corona: the few proteins that count. *Nanotoxicology* **10**, 1385–1394 (2016).

12. The European Committee. Commission recommendation of 18 October 2011 on the definition of nanomaterial (2011/696/EU). *Off. J. Eur. Union* **L275**, 38–40 (2011).

13. Barlow, S. *et al. The Potential Risks Arising from Nanoscience and Nanotechnologies on Food and Feed Safety*. *The EFSA Journal* vol. 958 (2009).

14. ISO. ISO/TS 80004-2:2015 - Nano-objects. *Nanotechnologies Vocab.* (2015).

15. Cho, K., Wang, X., Nie, S., Chen, Z. & Shin, D. M. Therapeutic nanoparticles for drug delivery in cancer. *Clin. Cancer Res.* **14**, 1310–1316 (2008).

16. Kulkarni, S. A. & Feng, S.-S. Effects of Particle Size and Surface Modification on Cellular Uptake and Biodistribution of Polymeric Nanoparticles for Drug Delivery. *Pharm. Res.* **30**, 2512–2522 (2013).

17. Kreyling, W. G., Semmler-Behnke, M. & Chaudhry, Q. A complementary definition of nanomaterial. *Nano Today* **5**, 165–168 (2010).

18. Auffan, M. *et al.* Towards a definition of inorganic nanoparticles from an environmental, health and safety perspective. *Nat. Nanotechnol.* **4**, 634–641 (2009).

19. Yokoyama, T. *et al.* Basic Properties and Measuring Methods of Nanoparticles. in *Nanoparticle Technology Handbook* 3–47 (Elsevier, 2018). doi:10.1016/B978-0-444-64110-6.00001-9.

20. Lai, S. L., Guo, J. Y., Petrova, V., Ramanath, G. & Allen, L. H. Size-dependent melting properties of small tin particles: Nanocalorimetric measurements. *Phys. Rev. Lett.* **77**, 99–102 (1996).

21. Bastus, N. ., Casals, E., Ojea, I., Varon, M. & Puntes, V. The Reactivity of Colloidal Inorganic Nanoparticles. in *The Delivery of Nanoparticles* 377–400 (2012). doi:10.5772/35238.

22. Blakemore, R. Magnetotactic bacteria. *Science (80-.).* **190**, (1975).

23. Buzea, C., Pacheco, I. I. & Robbie, K. Nanomaterials and nanoparticles: Sources and toxicity. *Biointerphases* **2**, MR17–MR71 (2007).

24. Taylor, D. A. & Kulmala, M. Dust in the wind. *Environ. Health Perspect.* **110**, 80–87 (2002).

25. Shi, Z., Shao, L., Jones, T. P. & Lu, S. Microscopy and mineralogy of airborne particles collected during severe dust storm episodes in Beijing, China. *J. Geophys. Res. D Atmos.* **110**, 1–10 (2005).

26. Husar, R. B. *et al.* Asian dust events of April 1998. *J. Geophys. Res. Atmos.* **106**, 18317–18330 (2001).

27. Fedotov, P. S. S. on the E. C. of E. N. S. in a R. C. C. H. H. M. B. U. D. and V. A. & Ermolin, M. S. Study on the Elemental Composition of Environmental Nanoparticles Separated in a

Rotating Coiled Column: How Hazardous May Be Urban Dust and Volcanic Ash. *Nano Hybrids Compos.* **13**, 288–293 (2017).

28. Maruf Hossain, A. M. M., Park, S., Kim, J. S. & Park, K. Volatility and mixing states of ultrafine particles from biomass burning. *J. Hazard. Mater.* **205**–**206**, 189–197 (2012).

29. Kumar, P. *et al.* Ultrafine particles in cities. *Environ. Int.* **66**, 1–10 (2014).

30. Dall'Osto, M. *et al.* Remarkable dynamics of nanoparticles in the urban atmosphere. *Atmos. Chem. Phys.* **11**, 6623–6637 (2011).

31. Kittelson, D. B. Recent Measurements of Nanoparticle Emissions from Engines Current Research on Diesel Exhaust Particles. *Curr. Res. Diesel Exhaust Part.* **9**, 451–457 (2001).

32. Pandey, A. K., Nandgaonkar, M., Pandey, U., Suresh, S. & Varghese, A. The Effect of Cerium Oxide Nano Particles Fuel Additive on Performance and Emission of Karanja Biodiesel Fueled Compression Ignition Military 585kW Heavy Duty Diesel Engine. in *SAE Technical Papers* vols 2018-Septe (SAE International, 2018).

33. Gan, Y. & Qiao, L. Combustion characteristics of fuel droplets with addition of nano and micron-sized aluminum particles. *Combust. Flame* **158**, 354–368 (2011).

34. Wang, J. & Pui, D. Y. H. Dispersion and filtration of carbon nanotubes (CNTs) and measurement of nanoparticle agglomerates in diesel exhaust. *Chem. Eng. Sci.* **85**, 69–76 (2013).

35. Kumar, P., Robins, A., Vardoulakis, S. & Britter, R. A review of the characteristics of nanoparticles in the urban atmosphere and the prospects for developing regulatory controls. *Atmos. Environ.* **44**, 5035–5052 (2010).

36. Kittelson, D. B. Engines and nanoparticles: A review. *J. Aerosol Sci.* **29**, 575–588 (1998).

37. Loxham, M. *et al.* Physicochemical characterization of airborne particulate matter at a mainline underground railway station. *Environ. Sci. Technol.* **47**, 3614–3622 (2013).

38. Kukutschová, J. *et al.* On airborne nano/micro-sized wear particles released from low-metallic automotive brakes. *Environ. Pollut.* **159**, 998–1006 (2011).

39. Slezakova, K., Morais, S. & Carmo Pereir, M. do. Atmospheric Nanoparticles and Their Impacts on Public Health. *Current Topics in Public Health* (2013). doi:10.5772/54775.

40. Sanderson, P., Delgado-Saborit, J. M. & Harrison, R. M. A review of chemical and physical

characterisation of atmospheric metallic nanoparticles. *Atmos. Environ.* **94**, 353–365 (2014).

41. Bahadar, H., Maqbool, F., Niaz, K. & Abdollahi, M. Toxicity of nanoparticles and an overview of current experimental models. *Iran. Biomed. J.* **20**, 1–11 (2016).

42. Huefner, A. *et al.* Gold nanoparticles explore cells: Cellular uptake and their use as intracellular probes. *Methods* **68**, 354–363 (2014).

43. Cassano, D. *et al.* Photothermal effect by NIR-responsive excretable ultrasmall-in-nano architectures. *Mater. Horizons* **6**, 531–537 (2019).

44. Whitehead, K. A. *et al.* Degradable lipid nanoparticles with predictable in vivo siRNA delivery activity. *Nat. Commun.* **5**, (2014).

45. Cho, H.-J. *et al.* Polyethylene glycol-conjugated hyaluronic acid-ceramide self-assembled nanoparticles for targeted delivery of doxorubicin. *Biomaterials* **33**, 1190–1200 (2012).

46. Haaj, S. B., Magnin, A., Pétrier, C. & Boufi, S. Author's personal copy Starch nanoparticles formation via high power ultrasonication. *Carbohydr. Polym.* **92**, 1625–1632 (2013).

47. Crapo, J. D., Barry, B. E., Gehr, P., Bachofen, M. & Weibel, E. R. Cell number and cell characteristics of the normal human lung. *Am. Rev. Respir. Dis.* **126**, 332–337 (1982).

48. Gonzalez, R. F., Allen, L. & Dobbs, L. G. Rat alveolar type I cells proliferate, express OCT-4, and exhibit phenotypic plasticity in vitro. *Am. J. Physiol. - Lung Cell. Mol. Physiol.* **297**, (2009).

49. Dobbs, L., Johnson, M., Vanderbilt, J., Allen, L. & Gonzalez, R. The great big alveolar TI cell: Evolving concepts and paradigms. *Cellular Physiology and Biochemistry* vol. 25 55–62 (2010).

50. Maynard, R. L. & Downes, N. *Anatomy and Histology of the Laboratory Rat in Toxicology and Biomedical Research*. *Anatomy and Histology of the Laboratory Rat in Toxicology and Biomedical Research* (2019). doi:10.1016/c2016-0-02030-2.

51. Alcorn, J. L. *Lung Epithelial Biology in the Pathogenesis of Pulmonary Disease*. *Lung Epithelial Biology in the Pathogenesis of Pulmonary Disease* (Elsevier, 2017). doi:10.1016/B978-0-12-803809-3.00004-X.

52. Hussell, T. & Bell, T. J. Alveolar macrophages: Plasticity in a tissue-specific context. *Nature Reviews Immunology* vol. 14 81–93 (2014).

53. Misharin, A. V., Budinger, G. R. S. & Perlman, H. The lung macrophage: A jack of all trades. *American Journal of Respiratory and Critical Care Medicine* vol. 184 497–498 (2011).

54. Maus, U. A. *et al.* Resident alveolar macrophages are replaced by recruited monocytes in response to endotoxin-induced lung inflammation. *Am. J. Respir. Cell Mol. Biol.* **35**, 227–235 (2006).

55. Mlika, M., Basit, H. & Kaul, P. *Alveolar Proteinosis*. *StatPearls* (StatPearls Publishing, 2019).

56. Serrano, A. G. & Pérez-Gil, J. Protein-lipid interactions and surface activity in the pulmonary surfactant system. *Chemistry and Physics of Lipids* vol. 141 105–118 (2006).

57. Parra, E. *et al.* A combined action of pulmonary surfactant proteins SP-B and SP-C modulates permeability and dynamics of phospholipid membranes. *Biochem. J.* **438**, 555–564 (2011).

58. Goerke, J. Pulmonary surfactant: functions and molecular composition. *Biochim. Biophys. Acta - Mol. Basis Dis.* **1408**, 79–89 (1998).

59. De La Serna, J. B., Perez-Gil, J., Simonsen, A. C. & Bagatolli, L. A. Cholesterol rules: Direct observation of the coexistence of two fluid phases in native pulmonary surfactant membranes at physiological temperatures. *J. Biol. Chem.* **279**, 40715–40722 (2004).

60. Chakraborty, M. & Kotecha, S. Pulmonary surfactant in newborn infants and children. *Breathe* vol. 9 476–488 (2013).

61. Kishore, U. *et al.* Surfactant proteins SP-A and SP-D in human health and disease. *Arch. Immunol. Ther. Exp. (Warsz).* **53**, 399–417 (2005).

62. Greene, K. E. *et al.* Serial changes in surfactant-associated proteins in lung and serum before and after onset of ARDS. *Am. J. Respir. Crit. Care Med.* **160**, 1843–1850 (1999).

63. McGuire, J. F. Surfactant in the middle ear and eustachian tube: A review. *International Journal of Pediatric Otorhinolaryngology* vol. 66 1–15 (2002).

64. Whitsett, J. A., Nogee, L. M., Weaver, T. E. & Horowitz, A. D. Human surfactant protein B: Structure, function, regulation, and genetic disease. *Physiol. Rev.* **75**, 749–757 (1995).

65. Melton, K. R. *et al.* SP-B deficiency causes respiratory failure in adult mice. *Am J Physiol Lung Cell Mol Physiol* **285**, 543–549 (2003).

66. Guttentag, S. H. *et al.* Surfactant protein B processing in human fetal lung. *Am. J. Physiol.*

275, L559-66 (1998).

67. McCormack, F. X. Structure and properties of surfactant protein C. *Biochim. Biophys. Acta* **1408**, 161–172 (1998).

68. Hime, N. J. *et al.* Childhood interstitial lung disease due to surfactant protein C deficiency: Frequent use and costs of hospital services for a single case in Australia. *Orphanet J. Rare Dis.* **9**, 36 (2014).

69. Walther, F. J. *et al.* Surfactant protein C peptides with salt-bridges ('ion-locks') promote high surfactant activities by mimicking the α-helix and membrane topography of the native protein. *PeerJ* **2014**, (2014).

70. Kishore, U. *et al.* Surfactant proteins SP-A and SP-D: Structure, function and receptors. *Mol. Immunol.* **43**, 1293–1315 (2006).

71. Pandit, H., Madhukaran, S. P., Nayak, A. & Madan, T. SP-A and SP-D in host defense against fungal infections and allergies. *Front. Biosci. (Elite Ed).* **4**, 651–661 (2012).

72. Hillaire, M. L. B., Haagsman, H. P., Osterhaus, A. D. M. E., Rimmelzwaan, G. F. & Van Eijk, M. Pulmonary surfactant protein D in first-line innate defence against influenza A virus infections. *J. Innate Immun.* **5**, 197–208 (2013).

73. Palaniyar, N. *et al.* Structural changes of surfactant protein A induced by cations reorient the protein on lipid bilayers. *J. Struct. Biol.* **122**, 297–310 (1998).

74. Crouch, E., Persson, A., Chang, D. & Heuser, J. Molecular structure of pulmonary surfactant protein D (SP-D). *J. Biol. Chem.* **269**, 17311–9 (1994).

75. Silveyra, P. & Floros, J. Genetic complexity of the human surfactant-associated proteins SP-A1 and SP-A2. *Gene* **531**, 126–132 (2013).

76. DiAngelo, S. *et al.* Novel, non-radioactive, simple and multiplex PCR-cRFLP methods for genotyping human SP-A and SP-D marker alleles. *Dis. Markers* **15**, 269–81 (1999).

77. Oberley, R. E. & Snyder, J. M. Recombinant human SP-A1 and SP-A2 proteins have different carbohydrate-binding characteristics.

78. Mikerov, A. N. *et al.* SP-A1 and SP-A2 variants differentially enhance association of Pseudomonas aeruginosa with rat alveolar macrophages. *Am J Physiol Lung Cell Mol Physiol* **288**, L150-8 (2005).

79. Huang, W., Wang, G., Phelps, D. S., Al-Mondhiry, H. & Floros, J. Human SP-A genetic variants and bleomycin-induced cytokine production by THP-1 cells: effect of ozone-induced SP-A oxidation. *Am J Physiol Lung Cell Mol Physiol* **286**, L546-53 (2004).

80. Anchez-Barbero, F., Rivas, G., Steinhilber, W. & Casals, C. Structural and functional differences among human surfactant proteins SP-A1, SP-A2 and co-expressed SP-A1/SP-A2: role of supratrimeric oligomerization. *Biochem. J* **406**, 479–489 (2007).

81. Thorenoor, N., Umstead, T. M., Zhang, X., Phelps, D. S. & Floros, J. Survival of surfactant protein-A1 and SP-A2 transgenic mice after Klebsiella pneumoniae infection, exhibits sex-, gene-, and variant specific differences; Treatment with surfactant protein improves survival. *Front. Immunol.* **9**, (2018).

82. Crouch, E. C. Surfactant protein-D and pulmonary host defense. *Respiratory Research* vol. 1 93–108 (2000).

83. Jakel, A. Ligands and receptors of lung surfactant proteins SP-A and SP-D. *Front. Biosci.* **18**, 1129–1140 (2013).

84. Sorensen, G. L. Surfactant protein D in respiratory and non-respiratory diseases. *Frontiers in Medicine* vol. 5 1 (2018).

85. Mo, Y. K. *et al.* Surfactant protein expression in human skin: Evidence and implications. *J. Invest. Dermatol.* **127**, 381–386 (2007).

86. Miyamura, K. *et al.* Surfactant proteins A (SP-A) and D (SP-D): Levels in human amniotic fluid and localization in the fetal membranes. *Biochim. Biophys. Acta (BBA)/Lipids Lipid Metab.* **1210**, 303–307 (1994).

87. Bräuer, L. *et al.* Detection of surfactant proteins A and D in human tear fluid and the human lacrimal system. *Investig. Ophthalmol. Vis. Sci.* **48**, 3945–3953 (2007).

88. Madsen, J. *et al.* Expression and Localization of Lung Surfactant Protein A in Human Tissues. *Am. J. Respir. Cell Mol. Biol.* **29**, 591–597 (2003).

89. Madsen, J. *et al.* Localization of Lung Surfactant Protein D on Mucosal Surfaces in Human Tissues. *J. Immunol.* **164**, 5866–5870 (2000).

90. Fisher, J. H. & Mason, R. Expression of pulmonary surfactant protein D in rat gastric mucosa. *Am. J. Respir. Cell Mol. Biol.* **12**, 13–18 (1995).

91. Herías, M. V. *et al.* Expression sites of the collectin SP-D suggest its importance in first line

host defence: Power of combining in situ hybridisation, RT-PCR and immunohistochemistry. *Mol. Immunol.* **44**, 3324–3332 (2007).

92. Pastva, A. M., Wright, J. R. J. R. & Williams, K. L. Immunomodulatory Roles of Surfactant Proteins A and D: Implications in Lung Disease. *Proc. Am. Thorac. Soc.* **4**, 252–257 (2007).

93. Ariki, S., Nishitani, C. & Kuroki, Y. Diverse functions of pulmonary collectins in host defense of the lung. *Journal of Biomedicine and Biotechnology* vol. 2012 (2012).

94. Nayak, A., Dodagatta-Marri, E., Tsolaki, A. G. & Kishore, U. An insight into the diverse roles of surfactant proteins, SP-A and SP-D in innate and adaptive immunity. *Front. Immunol.* **3**, 1–21 (2012).

95. Ariki, S. *et al.* Pulmonary collectins play distinct roles in host defense against Mycobacterium avium. *J. Immunol.* **187**, 2586–2594 (2011).

96. LeVine, A. M. & Whitsett, J. A. Pulmonary collectins and innate host defense of the lung. *Microbes Infect.* **3**, 161–166 (2001).

97. Wu, H. *et al.* Surfactant proteins A and D inhibit the growth of Gram-negative bacteria by increasing membrane permeability. *J. Clin. Invest.* **111**, 1589–1602 (2003).

98. Bufler, P. *et al.* Surfactant protein A and D differently regulate the immune response to nonmucoid Pseudomonas aeruginosa and its lipopolysaccharide. *Am. J. Respir. Cell Mol. Biol.* **28**, 249–256 (2003).

99. Giannoni, E., Sawa, T., Allen, L., Wiener-Kronish, J. & Hawgood, S. Surfactant proteins A and D enhance pulmonary clearance of Pseudomonas aeruginosa. *Am. J. Respir. Cell Mol. Biol.* **34**, 704–710 (2006).

100. Lemos, M. P., McKinney, J. & Rhee, K. Y. Dispensability of surfactant proteins A and D in immune control of Mycobacterium tuberculosis infection following aerosol challenge of mice. *Infect. Immun.* **79**, 1077–1085 (2011).

101. Sato, A., Whitsett, J. A., Scheule, R. K. & Ikegami, M. Surfactant protein-D inhibits lung inflammation caused by ventilation in premature newborn lambs. *Am. J. Respir. Crit. Care Med.* **181**, 1098–1105 (2010).

102. Bersani, I., Speer, C. P. & Kunzmann, S. Surfactant proteins A and D in pulmonary diseases of preterm infants. *Expert Review of Anti-Infective Therapy* vol. 10 573–584 (2012).

103. George, C. L. S., Goss, K. L., Meyerholz, D. K., Lamb, F. S. & Snyder, J. M. Surfactant-

associated protein A provides critical immunoprotection in neonatal mice. *Infect. Immun.* **76**, 380–390 (2008).

104. Noah, T. L. *et al.* Bronchoalveolar lavage fluid surfactant protein-A and surfactant protein-D are inversely related to inflammation in early cystic fibrosis. *Am. J. Respir. Crit. Care Med.* **168**, 685–691 (2003).

105. Sato, A., Whitsett, J. A., Scheule, R. K. & Ikegami, M. Surfactant protein-D inhibits lung inflammation caused by ventilation in premature newborn lambs. *Am. J. Respir. Crit. Care Med.* **181**, 1098–1105 (2010).

106. Watson, A. *et al.* Generation of novel trimeric fragments of human SP-A and SP-D after recombinant soluble expression in E. coli. *Immunobiology* **225**, 151953 (2020).

107. Salvador-Morales, C. *et al.* Binding of pulmonary surfactant proteins to carbon nanotubes; potential for damage to lung immune defense mechanisms. *Carbon N. Y.* **45**, 607–617 (2007).

108. Schulze, C., Schaefer, U. F., Ruge, C. A., Wohlleben, W. & Lehr, C. M. Interaction of metal oxide nanoparticles with lung surfactant protein A. *Eur. J. Pharm. Biopharm.* **77**, 376–383 (2011).

109. Ruge, C. A. *et al.* Pulmonary Surfactant Protein A-Mediated Enrichment of Surface-Decorated Polymeric Nanoparticles in Alveolar Macrophages. *Mol. Pharm.* **13**, 4168–4178 (2016).

110. Schleh, C. *et al.* Biodistribution of inhaled gold nanoparticles in mice and the influence of surfactant protein D. *J. Aerosol Med. Pulm. Drug Deliv.* **26**, 24–30 (2013).

111. Ikegami, M. *et al.* Characteristics of surfactant from SP-A-deficient mice. *Am. J. Physiol. - Lung Cell. Mol. Physiol.* **275**, L247-54 (1998).

112. Korfhagen, T. R., Levine, A. M. & Whitsett, J. A. Surfactant protein A (SP-A) gene targeted mice. *Biochimica et Biophysica Acta - Molecular Basis of Disease* vol. 1408 296–302 (1998).

113. Hawgood, S. & Poulain, F. R. The pulmonary collectins and surfactant metabolism. *Annu. Rev. Physiol.* **63**, 495–519 (2001).

114. Bates, S. R., Dodia, C., Tao, J.-Q. & Fisher, A. B. Surfactant protein-A plays an important role in lung surfactant clearance: evidence using the surfactant protein-A gene-targeted mouse. *Am. J. Physiol. Lung Cell. Mol. Physiol.* **294**, L325-33 (2008).

115. Harrod, K. S., Trapnell, B. C., Otake, K., Korfhagen, T. R. & Whitsett, J. A. SP-A enhances viral clearance and inhibits inflammation after pulmonary adenoviral infection. *Am. J. Physiol.* **277**, L580–L588 (1999).

116. Botas, C. *et al.* Altered surfactant homeostasis and alveolar type II cell morphology in mice lacking surfactant protein D. *Proc. Natl. Acad. Sci. U. S. A.* **95**, 11869–74 (1998).

117. Madan, T. *et al.* Susceptibility of mice genetically deficient in SP-A or SP-D gene to Invasive Pulmonary Aspergillosis. *Mol. Immunol.* **47**, 1923–1930 (2010).

118. Montalbano, A. P., Hawgood, S. & Mendelson, C. R. Mice deficient in surfactant protein A (SP-A) and SP-D or in TLR2 manifest delayed parturition and decreased expression of inflammatory and contractile genes. *Endocrinology* **154**, 483–498 (2013).

119. Yoshida, M. & Whitsett, J. A. Alveolar macrophages and emphysema in surfactant protein-D-deficient mice. *Respirology* **11**, 37–40 (2006).

120. Knudsen, L. *et al.* Truncated recombinant human SP-D attenuates emphysema and type II cell changes in SP-D deficient mice. *Respir. Res.* **8**, 70 (2007).

121. Hawgood, S. *et al.* Sequential targeted deficiency of SP-A and -D leads to progressive alveolar lipoproteinosis and emphysema. *Am. J. Physiol. Lung Cell. Mol. Physiol.* **283**, L1002-10 (2002).

122. Lourenço, R. V. & Cotromanes, E. Clinical Aerosols. *Arch. Intern. Med.* **142**, 2163–2172 (1982).

123. Yhee, J., Im, J. & Nho, R. Advanced Therapeutic Strategies for Chronic Lung Disease Using Nanoparticle-Based Drug Delivery. *J. Clin. Med.* **5**, 82 (2016).

124. Zeng, X. M., Martin, G. P. & Marriott, C. *Particulate Interactions in Dry Powder Formulations for Inhalation*. *Journal of Chemical Information and Modeling* vol. 53 (2001).

125. Williams, R. O., Carvalho, T. C. & Peters, J. I. Influence of particle size on regional lung deposition - What evidence is there? *International Journal of Pharmaceutics* vol. 406 1–10 (2011).

126. Heyder, J. Deposition of Inhaled Particles in the Human Respiratory Tract and Consequences for Regional Targeting in Respiratory Drug Delivery. *Proc. Am. Thorac. Soc.* **1**, 315–320 (2004).

127. Sturm, R. Spatial visualization of theoretical nanoparticle deposition in the human

respiratory tract. *Ann. Transl. Med.* **3**, (2015).

128. Vieira, F., Kung, J. W. & Bhatti, F. Structure, genetics and function of the pulmonary associated surfactant proteins A and D: The extra-pulmonary role of these C type lectins. *Ann. Anat.* **211**, 184–201 (2017).

129. Garcia, G. J. M., Schroeter, J. D. & Kimbell, J. S. Olfactory deposition of inhaled nanoparticles in humans. *Inhal. Toxicol.* **27**, 394–403 (2015).

130. Mühlfeld, C., Gehr, P. & Rothen-Rutishauser, B. Translocation and cellular entering mechanisms of nanoparticles in the respiratory tract. *Swiss Med. Wkly.* **138**, 387–391 (2008).

131. Andujar, P., Lanone, S., Brochard, P. & Boczkowski, J. Respiratory effects of manufactured nanoparticles. *Rev. Mal. Respir.* **28**, e66–e75 (2011).

132. Bakand, S. & Hayes, A. Toxicological considerations, toxicity assessment, and risk management of inhaled nanoparticles. *Int. J. Mol. Sci.* **17**, 1–17 (2016).

133. Geiser, M. *et al.* Ultrafine particles cross cellular membranes by nonphagocytic mechanisms in lungs and in cultured cells. *Environ. Health Perspect.* **113**, 1555–1560 (2005).

134. Liu, Q., Guan, J., Qin, L., Zhang, X. & Mao, S. Physicochemical properties affecting the fate of nanoparticles in pulmonary drug delivery. *Drug Discovery Today* vol. 25 150–159 (2020).

135. Kreyling, W. G., Semmler-Behnke, M., Takenaka, S. & Möller, W. Differences in the biokinetics of inhaled nano-versus micrometer-sized particles. *Acc. Chem. Res.* **46**, 714–722 (2013).

136. Bhattacharya, J. & Westphalen, K. Macrophage-epithelial interactions in pulmonary alveoli. *Seminars in Immunopathology* vol. 38 461–469 (2016).

137. Qiao, H., Liu, W., Gu, H., Wang, D. & Wang, Y. The transport and deposition of nanoparticles in respiratory system by inhalation. *J. Nanomater.* **2015**, (2015).

138. Geiser, M. *et al.* The role of macrophages in the clearance of inhaled ultrafine titanium dioxide particles. *Am. J. Respir. Cell Mol. Biol.* **38**, 371–376 (2008).

139. Madl, A. K. & Pinkerton, K. E. Health effects of inhaled engineered and incidental nanoparticles. *Crit. Rev. Toxicol.* **39**, 629–658 (2009).

140. Zhang, J., Wu, L., Chan, H.-K. & Watanabe, W. Formation, characterization, and fate of inhaled drug nanoparticles ☆. *Adv. Drug Deliv. Rev.* **63**, 441–455 (2011).

141. Semmler-Behnke, M. *et al.* Biodistribution of 1.4- and 18-nm gold particles in rats. *Small* **4**, 2108–2111 (2008).

142. Miller, M. R. *et al.* Inhaled Nanoparticles Accumulate at Sites of Vascular Disease. *ACS Nano* **11**, 4542–4552 (2017).

143. Chen, J. *et al.* Inhaled Nanoparticles Accumulate at Sites of Vascular Disease. *Toxicology* **222**, 195–201 (2006).

144. Elsaesser, A. & Howard, C. V. Toxicology of nanoparticles. *Adv. Drug Deliv. Rev.* **64**, 129–137 (2012).

145. Wang, S. H., Lee, C. W., Chiou, A. & Wei, P. K. Size-dependent endocytosis of gold nanoparticles studied by three-dimensional mapping of plasmonic scattering images. *J. Nanobiotechnology* **8**, (2010).

146. Sakai, N., Matsui, Y., Nakayama, A., Tsuda, A. & Yoneda, M. Functional-dependent and size-dependent uptake of nanoparticles in PC12. in *Journal of Physics: Conference Series* vol. 304 012049 (IOP Publishing, 2011).

147. Shang, L., Nienhaus, K. & Nienhaus, G. U. Engineered nanoparticles interacting with cells: Size matters. *Journal of Nanobiotechnology* vol. 12 (2014).

148. Li, K., Zhao, X., Hammer, B. K., Du, S. & Chen, Y. Nanoparticles Inhibit DNA Replication by Binding to DNA: Modeling and Experimental Validation. **7**, 9664–9674 (2013).

149. Jang, H., Ryoo, S. R., Kostarelos, K., Han, S. W. & Min, D. H. The effective nuclear delivery of doxorubicin from dextran-coated gold nanoparticles larger than nuclear pores. *Biomaterials* **34**, 3503–3510 (2013).

150. Lebedová, J., Hedberg, Y. S., Odnevall Wallinder, I. & Karlsson, H. L. Size-dependent genotoxicity of silver, gold and platinum nanoparticles studied using the mini-gel comet assay and micronucleus scoring with flow cytometry. *Mutagenesis* **33**, 77–85 (2018).

151. Wagner, S. C. *et al.* Nanoparticle-induced folding and fibril formation of coiled-coil-based model peptides. *Small* **6**, 1321–1328 (2010).

152. Wu, W. hui *et al.* TiO2 nanoparticles promote β-amyloid fibrillation in vitro. *Biochem. Biophys. Res. Commun.* **373**, 315–318 (2008).

153. Bucciantini, M. *et al.* Inherent toxicity of aggregates implies a common mechanism for protein misfolding diseases. *Nature* **416**, 507–511 (2002).

154. Wang, F., Salvati, A. & Boya, P. Lysosome-dependent cell death and deregulated autophagy induced by amine-modified polystyrene nanoparticles. *Open Biol.* **4**, (2018).

155. Xia, T., Kovochich, M., Liong, M., Zink, J. I. & Nel, A. E. Cationic polystyrene nanosphere toxicity depends on cell-specific endocytic and mitochondrial injury pathways. *ACS Nano* **2**, 85–96 (2008).

156. Maejima, I. *et al.* Autophagy sequesters damaged lysosomes to control lysosomal biogenesis and kidney injury. *EMBO J.* **32**, 2336–47 (2013).

157. Miyayama, T. & Matsuoka, M. Involvement of lysosomal dysfunction in silver nanoparticle-induced cellular damage in A549 human lung alveolar epithelial cells. *J. Occup. Med. Toxicol.* **11**, 1 (2016).

158. Kroemer, G. & Jäättelä, M. Lysosomes and autophagy in cell death control. *Nature Reviews Cancer* vol. 5 886–897 (2005).

159. Lee, J. H. *et al.* Biopersistence of silver nanoparticles in tissues from Sprague-Dawley rats. *Part. Fibre Toxicol.* **10**, 36 (2013).

160. Brunner, T. J. *et al.* In vitro cytotoxicity of oxide nanoparticles: Comparison to asbestos, silica, and the effect of particle solubility. *Environ. Sci. Technol.* **40**, 4374–4381 (2006).

161. Boyles, M. S. P. *et al.* Multi-walled carbon nanotube induced frustrated phagocytosis, cytotoxicity and pro-inflammatory conditions in macrophages are length dependent and greater than that of asbestos. *Toxicol. Vitr.* **29**, 1513–1528 (2015).

162. Jaurand, M.-C. F., Renier, A. & Daubriac, J. Mesothelioma: Do asbestos and carbon nanotubes pose the same health risk? *Part. Fibre Toxicol.* **6**, 16 (2009).

163. Gratton, S. E. A. *et al.* The effect of particle design on cellular internalization pathways. *Proc. Natl. Acad. Sci.* **105**, 11613–11618 (2008).

164. Qiu, Y. *et al.* Surface chemistry and aspect ratio mediated cellular uptake of Au nanorods. *Biomaterials* **31**, 7606–7619 (2010).

165. Dayem, A. A. *et al.* The role of reactive oxygen species (ROS) in the biological activities of metallic nanoparticles. *Int. J. Mol. Sci.* **18**, (2017).

166. Zhu, X., Hondroulis, E., Liu, W. & Li, C. Z. Biosensing approaches for rapid genotoxicity and cytotoxicity assays upon nanomaterial exposure. *Small* **9**, 1821–1830 (2013).

167. Wang, Y. *et al.* A study of the mechanism of in vitro cytotoxicity of metal oxide nanoparticles using catfish primary hepatocytes and human HepG2 cells. *Sci. Total Environ.* **409**, 4753–4762 (2011).

168. Choudhury, S. R. *et al.* Zinc oxide nanoparticles-induced reactive oxygen species promotes multimodal cyto- and epigenetic toxicity. *Toxicol. Sci.* **156**, 261–274 (2017).

169. Maiolo, D., Del Pino, P., Metrangolo, P., Parak, W. J. & Baldelli Bombelli, F. Nanomedicine delivery: does protein corona route to the target or off road? *Nanomedicine (Lond).* **10**, 3231–47 (2015).

170. Lundqvist, M. *et al.* The nanoparticle protein corona formed in human blood or human blood fractions. *PLoS One* **12**, 1–15 (2017).

171. Lynch, I. *et al.* The nanoparticle-protein complex as a biological entity; a complex fluids and surface science challenge for the 21st century. *Adv. Colloid Interface Sci.* **134**–**135**, 167–174 (2007).

172. Rahman, M., Laurent, S., Tawil, N., Yahia, L. & Mahmoudi, M. Protein-Nanoparticle Interactions. **15**, 21–45 (2013).

173. Tenzer, S. *et al.* Rapid formation of plasma protein corona critically affects nanoparticle pathophysiology. *Nat. Nanotechnol.* **8**, 772–781 (2013).

174. Gorshkov, V., Bubis, J. A., Solovyeva, E. M., Gorshkov, M. V. & Kjeldsen, F. Protein corona formed on silver nanoparticles in blood plasma is highly selective and resistant to physicochemical changes of the solution. *Environ. Sci. Nano* **6**, 1089–1098 (2019).

175. Kendall, M. & Holgate, S. Health impact and toxicological effects of nanomaterials in the lung. *Respirology* **17**, 743–758 (2012).

176. Pino, P. Del *et al.* Protein corona formation around nanoparticles - from the past to the future. *Mater. Horizons* **1**, 301–313 (2014).

177. Kendall, M. Fine airborne urban particles (PM2.5) sequester lung surfactant and amino acids from human lung lavage. *Am. J. Physiol. - Lung Cell. Mol. Physiol.* **293**, 1053–1058 (2007).

178. Sohaebuddin, S. K., Thevenot, P. T., Baker, D., Eaton, J. W. & Tang, L. Nanomaterial

cytotoxicity is composition, size, and cell type dependent. *Part. Fibre Toxicol.* **7**, (2010).

179. Smith, P. J. *et al.* Cellular entry of nanoparticles via serum sensitive clathrin-mediated endocytosis, and plasma membrane permeabilization. *Int. J. Nanomedicine* **7**, 2045–2055 (2012).

180. García-Álvarez, R., Hadjidemetriou, M., Sánchez-Iglesias, A., Liz-Marzán, L. M. & Kostarelos, K. In vivo formation of protein corona on gold nanoparticles. The effect of their size and shape. *Nanoscale* **10**, 1256–1264 (2018).

181. Hu, Q., Bai, X., Hu, G. & Zuo, Y. Y. Unveiling the Molecular Structure of Pulmonary Surfactant Corona on Nanoparticles. *ACS Nano* **11**, 6832–6842 (2017).

182. Coradeghini, R. *et al.* Size-dependent toxicity and cell interaction mechanisms of gold nanoparticles on mouse fibroblasts. *Toxicol. Lett.* **217**, 205–216 (2013).

183. Pan, Y. *et al.* Size-dependent cytotoxicity of gold nanoparticles. *Small* **3**, 1941–1949 (2007).

184. Wittmaack, K. In search of the most relevant parameter for quantifying lung inflammatory response to nanoparticle exposure: Particle number, surface area, or what? *Environ. Health Perspect.* **115**, 187–194 (2007).

185. Oberdörster, G., Oberdörster, E. & Oberdörster, J. Concepts of Nanoparticle Dose Metric and Response Metric. *Environ. Health Perspect.* **115**, A290 (2007).

186. Mottier, A. *et al.* Surface Area of Carbon Nanoparticles: A Dose Metric for a More Realistic Ecotoxicological Assessment. *Nano Lett.* **16**, 3514–3518 (2016).

187. Delmaar, C. J. E. *et al.* A practical approach to determine dose metrics for nanomaterials. *Environ. Toxicol. Chem.* **34**, 1015–1022 (2015).

188. Schmid, O. & Stoeger, T. Surface area is the biologically most effective dose metric for acute nanoparticle toxicity in the lung. *J. Aerosol Sci.* **99**, 133–143 (2016).

189. Sager, T. M. & Castranova, V. Surface area of particle administered versus mass in determining the pulmonary toxicity of ultrafine and fine carbon black: Comparison to ultrafine titanium dioxide. *Part. Fibre Toxicol.* **6**, 1–12 (2009).

190. Moura, C. C., Bourdakos, K. N., Tare, R. S., Oreffo, R. O. C. & Mahajan, S. Live-imaging of Bioengineered Cartilage Tissue using Multimodal Non-linear Molecular Imaging. *Sci. Rep.* **9**, (2019).

191. Camp Jr, C. H. & Cicerone, M. T. Chemically sensitive bioimaging with coherent Raman scattering. *Nat. Photonics* **9**, 295–305 (2015).

192. Patel, I. I., Steuwe, C., Reichelt, S. & Mahajan, S. Coherent anti-Stokes Raman scattering for label-free biomedical imaging. *J. Opt. (United Kingdom)* **15**, 94006–94023 (2013).

193. Freudiger, C. W. *et al.* Multicolored stain-free histopathology with coherent Raman imaging. *Lab. Investig.* **92**, 1492–1502 (2012).

194. Potcoava, M. C., Futia, G. L., Aughenbaugh, J., Schlaepfer, I. R. & Gibson, E. A. Raman and coherent anti-Stokes Raman scattering microscopy studies of changes in lipid content and composition in hormone-treated breast and prostate cancer cells. *J. Biomed. Opt.* **19**, 111605 (2014).

195. Guerenne-Del Ben, T. *et al.* Multiplex coherent anti-Stokes Raman scattering highlights state of chromatin condensation in CH region. *Sci. Rep.* **9**, (2019).

196. Arzumanyan, G. M. *et al.* Highly Sensitive Coherent Anti-Stokes Raman Scattering Imaging of Protein Crystals. *J. Am. Chem. Soc.* **138**, 13457–13460 (2016).

197. Cheng, J.-X., Volkmer, A. & Xie, X. S. Theoretical and experimental characterization of coherent anti-Stokes Raman scattering microscopy. *J. Opt. Soc. Am. B* **19**, 1363 (2002).

198. Tong, L., Lu, Y., Lee, R. J. & Cheng, J. X. Imaging receptor-mediated endocytosis with a polymeric nanoparticle-based coherent anti-stokes Raman scattering probe. *J. Phys. Chem. B* **111**, 9980–9985 (2007).

199. Rago, G. *et al.* CARS microscopy for the visualization of micrometer-sized iron oxide MRI contrast agents in living cells. *Biomed. Opt. Express* **2**, 2470 (2011).

200. Scown, T. M. *et al.* Assessment of cultured fish hepatocytes for studying cellular uptake and (eco)toxicity of nanoparticles. *Environ. Chem.* **7**, 36–49 (2010).

201. Johnston, H. J., Mouras, R., Brown, D. M., Elfick, A. & Stone, V. Exploring the cellular and tissue uptake of nanomaterials in a range of biological samples using multimodal nonlinear optical microscopy. *Nanotechnology* **26**, (2015).

202. Huang, X., Jain, P. K., El-Sayed, I. H. & El-Sayed, M. A. Plasmonic photothermal therapy (PPTT) using gold nanoparticles. *Lasers in Medical Science* vol. 23 217–228 (2008).

203. Eguchi, A., Lu, P., Kim, Y. & Milster, T. D. Characterization of emission from aggregated gold nanoparticles excited nonlinearly by 1560-nm femtosecond laser. *J. Nanophotonics* **11**, 1

(2017).

204. Williams, R. M., Zipfel, W. R. & Webb, W. W. Interpreting second-harmonic generation images of collagen I fibrils. *Biophys. J.* **88**, 1377–1386 (2005).

205. Campagnola, P. Second harmonic generation imaging microscopy: Applications to diseases diagnostics. *Anal. Chem.* **83**, 3224–3231 (2011).

206. Mohler, W., Millard, A. C. & Campagnola, P. J. Second harmonic generation imaging of endogenous structural proteins. *Methods* **29**, 97–109 (2003).

207. Mostaço-Guidolin, L., Rosin, N. L. & Hackett, T. L. Imaging collagen in scar tissue: Developments in second harmonic generation microscopy for biomedical applications. *International Journal of Molecular Sciences* vol. 18 (2017).

208. Yuan, C. *et al.* Changes in the crystallographic structures of cardiac myosin filaments detected by polarization-dependent second harmonic generation microscopy. *Biomed. Opt. Express* **10**, 3183 (2019).

209. Van Steenbergen, V. *et al.* Molecular understanding of label-free second harmonic imaging of microtubules. *Nat. Commun.* **10**, (2019).

210. Zhuo, Z. Y. *et al.* Second harmonic generation imaging - A new method for unraveling molecular information of starch. *J. Struct. Biol.* **171**, 88–94 (2010).

211. Cox, G. C. & Feijo, J. Second harmonic imaging of plant polysaccharides. in *Multiphoton Microscopy in the Biomedical Sciences IV* vol. 5323 335 (2004).

212. Moreaux, L., Sandre, O., Blanchard-Desce, M. & Mertz, J. Membrane imaging by simultaneous second-harmonic generation and two-photon microscopy. *Opt. Lett.* **25**, 320 (2000).

213. Breunig, H. G., Weinigel, M. & König, K. In Vivo Imaging of ZnO Nanoparticles from Sunscreen on Human Skin with a Mobile Multiphoton Tomograph. *Bionanoscience* **5**, 42–47 (2014).

214. Grange, R., Lanvin, T., Hsieh, C.-L., Pu, Y. & Psaltis, D. Imaging with second-harmonic radiation probes in living tissue. *Biomed. Opt. Express* **2**, 2532 (2011).

215. Pantazis, P., Maloney, J., Wu, D. & Fraser, S. E. Second harmonic generating (SHG) nanoprobes for in vivo imaging. *Proc. Natl. Acad. Sci. U. S. A.* **107**, 14535–14540 (2010).

216. Denk, W., Strickler, J. H. & Webb, W. W. Two-photon laser scanning fluorescence microscopy. *Science (80-.).* **248**, 73–76 (1990).

217. Stringari, C. *et al.* Multicolor two-photon imaging of endogenous fluorophores in living tissues by wavelength mixing. *Sci. Rep.* **7**, (2017).

218. Dolmans, D. E. J. G. J., Fukumura, D. & Jain, R. K. Photodynamic therapy for cancer. *Nature Reviews Cancer* vol. 3 380–387 (2003).

219. Alifu, N. *et al.* Aggregation-induced emission nanoparticles as photosensitizer for two-photon photodynamic therapy. *Mater. Chem. Front.* **1**, 1746–1753 (2017).

220. Shen, Y., Shuhendler, A. J., Ye, D., Xu, J. J. & Chen, H. Y. Two-photon excitation nanoparticles for photodynamic therapy. *Chemical Society Reviews* vol. 45 6725–6741 (2016).

221. Morales-Dalmau, J. *et al.* Quantification of gold nanoparticle accumulation in tissue by two-photon luminescence microscopy. *Nanoscale* **11**, 11331–11339 (2019).

222. Wright, J. R., Wager, R. E., Hawgood, S., Dobbs, L. & Clements, J. A. Surfactant Apoprotein Mr = 26,000-36,000 Enhances Uptake of Liposomes by Type II Cells. **262**, 2888–2894 (1987).

223. Strong, P. *et al.* A novel method of purifying lung surfactant proteins A and D from the lung lavage of alveolar proteinosis patients and from pooled amniotic fluid. *J. Immunol. Methods* **220**, 139–149 (1998).

224. Gill, S. C. & von Hippel, P. H. Calculation of protein extinction coefficients from amino acid sequence data. *Anal. Biochem.* **182**, 319–26 (1989).

225. Raschke, W. C., Baird, S., Ralph, P., Nakoinz, I. & Coon, H. Functional macrophage cell lines transformed by abelson leukemia virus. *Cell* **15**, 261–267 (1978).

226. Jena, P., Mohanty, S., Mallick, R., Jacob, B. & Sonawane, A. Toxicity and antibacterial assessment of chitosancoated silver nanoparticles on human pathogens and macrophage cells. *Int. J. Nanomedicine* **7**, 1805–1818 (2012).

227. PAGE, A. M., LAGNADO, J. R., FORD, T. W. & PLACE, G. Calcium alginate encapsulation of small specimens for transmission electron microscopy. *J. Microsc.* **175**, 166–170 (1994).

228. Korfhagen, T. R. *et al.* Altered surfactant function and structure in SP-A gene targeted mice. *Proc. Natl. Acad. Sci. U. S. A.* **93**, 9594–9599 (1996).

229. Portal, C. *et al.* In vivo imaging of the Muc5b gel-forming mucin. *Sci. Rep.* **7**, 44591 (2017).

230. Loeschner, K. *et al.* Detection and characterization of silver nanoparticles in chicken meat by asymmetric flow field flow fractionation with detection by conventional or single particle ICP-MS. *Anal. Bioanal. Chem.* **405**, 8185–8195 (2013).

231. Rueden, C. T. *et al.* ImageJ2: ImageJ for the next generation of scientific image data. *BMC Bioinformatics* **18**, 529 (2017).

232. Teipel, S. *et al.* Multimodal imaging in Alzheimer's disease: Validity and usefulness for early detection. *The Lancet Neurology* vol. 14 1037–1053 (2015).

233. Yarbakht, M. *et al.* Nonlinear Multimodal Imaging Characteristics of Early Septic Liver Injury in a Mouse Model of Peritonitis. *Anal. Chem.* **91**, 11116–11121 (2019).

234. Marcu, L., Fishbein, M. C., Maarek, J. M. I. & Grundfest, W. S. Discrimination of human coronary artery atherosclerotic lipid-rich lesions by time-resolved laser-induced fluorescence spectroscopy. *Arterioscler. Thromb. Vasc. Biol.* **21**, 1244–1250 (2001).

235. Motz, J. T. *et al.* In vivo Raman spectral pathology of human atherosclerosis and vulnerable plaque. *J. Biomed. Opt.* **11**, 021003 (2006).

236. Pande, A. N., Kohler, R. H., Aikawa, E., Weissleder, R. & Jaffer, F. A. Detection of macrophage activity in atherosclerosis in vivo using multichannel, high-resolution laser scanning fluorescence microscopy. *J. Biomed. Opt.* **11**, 021009 (2006).

237. Le, T. T., Langohr, I. M., Locker, M. J., Sturek, M. & Cheng, J.-X. Label-free molecular imaging of atherosclerotic lesions using multimodal nonlinear optical microscopy. *J. Biomed. Opt.* **12**, 054007 (2007).

238. Bocklitz, T. W. *et al.* Pseudo-HE images derived from CARS/TPEF/SHG multimodal imaging in combination with Raman-spectroscopy as a pathological screening tool. *BMC Cancer* **16**, 1–11 (2016).

239. Ali, N. *et al.* Automatic label-free detection of breast cancer using nonlinear multimodal imaging and the convolutional neural network ResNet50. *Transl. Biophotonics* **1**, (2019).

240. Jaeger, D. *et al.* Label-free in vivo analysis of intracellular lipid droplets in the oleaginous microalga Monoraphidium neglectum by coherent Raman scattering microscopy. *Sci. Rep.* **6**, 2–10 (2016).

241. Tolles, W. M., Nibler, J. W., McDonald, J. R. & Harvey, A. B. Review of the Theory and

Application of Coherent Anti-Stokes Raman Spectroscopy (Cars). *Appl. Spectrosc.* **31**, 253–272 (1977).

242. Cao, R., Wallrabe, H. K. & Periasamy, A. Multiphoton FLIM imaging of NAD(P)H and FAD with one excitation wavelength. *J. Biomed. Opt.* **25**, 1 (2020).

243. Costa Moura, C. *et al.* Quantitative temporal interrogation in 3D of bioengineered human cartilage using multimodal label-free imaging. *Integr. Biol. (United Kingdom)* **10**, 635–645 (2018).

244. Metabolic Imaging - Becker & Hickl GmbH. https://www.becker-hickl.com/applications/metabolic-imaging/.

245. Olympus Life Sciences. Image Averaging and Noise Removal - Java Tutorial | Olympus Life Science. https://www.olympus-lifescience.com/en/microscope-resource/primer/java/digitalimaging/processing/imageaveraging/.

246. Benninger, R. K. P. & Piston, D. W. Two-photon excitation microscopy for unit 4.11 the study of living cells and tissues. *Curr. Protoc. Cell Biol.* **Chapter 4**, (2013).

247. Amendola, V., Pilot, R., Frasconi, M., Maragò, O. M. & Iatì, M. A. Surface plasmon resonance in gold nanoparticles: A review. *J. Phys. Condens. Matter* **29**, (2017).

248. Jana, J., Ganguly, M. & Pal, T. Enlightening surface plasmon resonance effect of metal nanoparticles for practical spectroscopic application. *RSC Adv.* **6**, 86174–86211 (2016).

249. Zhang, Y. *et al.* Temperature-dependent cell death patterns induced by functionalized gold nanoparticle photothermal therapy in melanoma cells. *Sci. Rep.* **8**, (2018).

250. MacKey, M. A., Ali, M. R. K., Austin, L. A., Near, R. D. & El-Sayed, M. A. The most effective gold nanorod size for plasmonic photothermal therapy: Theory and in vitro experiments. *J. Phys. Chem. B* **118**, 1319–1326 (2014).

251. Lin, C. P. & Kelly, M. W. Cavitation and acoustic emission around laser-heated microparticles. *Appl. Phys. Lett.* **72**, 2800–2802 (1998).

252. Wang, Z. L. & Lee, J. L. Electron Microscopy Techniques for Imaging and Analysis of Nanoparticles. in *Developments in Surface Contamination and Cleaning: Second Edition* vol. 1 395–443 (Elsevier Inc., 2008).

253. Kendall, M., Brown, L. & Trought, K. Molecular adsorption at particle surfaces: A PM toxicity mediation mechanism. *Inhal. Toxicol.* **16**, 99–105 (2004).

254. Brewer, S. H., Glomm, W. R., Johnson, M. C., Knag, M. K. & Franzen, S. Probing BSA binding to citrate-coated gold nanoparticles and surfaces. *Langmuir* **21**, 9303–9307 (2005).

255. Dominguez-Medina, S., McDonough, S., Swanglap, P., Landes, C. F. & Link, S. In situ measurement of bovine serum albumin interaction with gold nanospheres. *Langmuir* **28**, 9131–9 (2012).

256. Sigma-Aldrich Co. Gold Nanoparticles: Properties and Applications | Sigma-Aldrich. https://www.sigmaaldrich.com/technical-documents/articles/materials-science/nanomaterials/gold-nanoparticles.html.

257. Mühlig, S. *et al.* Optical properties of a fabricated self-assembled bottom-up bulk metamaterial. *Opt. Express* **19**, 9607 (2011).

258. Gold Nanoparticle Properties Background. http://www.cytodiagnostics.com/store/pc/Gold-Nanoparticle-Properties-d2.htm.

259. Haagsman, H. P. *et al.* The major lung surfactant protein, SP 28-36, is a calcium-dependent, carbohydrate-binding protein. *J. Biol. Chem.* **262**, 13877–13880 (1987).

260. Wang, H. *et al.* Effects of monovalent and divalent metal cations on the aggregation and suspension of Fe3O4magnetic nanoparticles in aqueous solution. *Sci. Total Environ.* **586**, 817–826 (2017).

261. Pamies, R. *et al.* Aggregation behaviour of gold nanoparticles in saline aqueous media. *J. Nanoparticle Res.* **16**, (2014).

262. Wang, D. *et al.* 808 nm driven Nd3+-sensitized upconversion nanostructures for photodynamic therapy and simultaneous fluorescence imaging. *Nanoscale* **7**, 190–197 (2015).

263. Zheng, T., Bott, S. & Huo, Q. Techniques for Accurate Sizing of Gold Nanoparticles Using Dynamic Light Scattering with Particular Application to Chemical and Biological Sensing Based on Aggregate Formation. *ACS Appl. Mater. Interfaces* **8**, 21585–21594 (2016).

264. Fukui, T., Baba, T., Katamoto, T., Suda, A. & Nogi, K. Evaluation Methods for Properties of Nanostructured Body. in *Nanoparticle Technology Handbook* 301–363 (2018). doi:10.1016/B978-0-444-64110-6.00006-8.

265. Gebauer, J. S. *et al.* Impact of the Nanoparticle − Protein Corona on Colloidal Stability and Protein Structure. *Langmuir* **28**, 9673–9679 (2012).

266. Weiß, N., Wente, W. & Müller, P. *Eppendorf LoBind®: Evaluation of protein recovery in Eppendorf Protein LoBind Tubes and Plates*. (2010).

267. De Paoli Lacerda, S. H. *et al.* Interaction of gold nanoparticles with common human blood proteins. *ACS Nano* **4**, 365–379 (2010).

268. Wangoo, N., Suri, C. R. & Shekhawat, G. Interaction of gold nanoparticles with protein: A spectroscopic study to monitor protein conformational changes. *Appl. Phys. Lett.* **92**, 133104 (2008).

269. Ruano, M. L. F., García-Verdugo, I., Miguel, E., Pérez-Gil, J. & Casals, C. Self-aggregation of surfactant protein A. *Biochemistry* **39**, 6529–6537 (2000).

270. GE Healthcare. Purifying Challenging Proteins. *Gen. Electr. Co.* **28**-**9095**–**31**, 1–107 (2007).

271. Sattayasai, N. Protein Purification. in *Chemical Biology* (2012). doi:10.5772/35425.

272. Chien, M. L. & Coulter, B. *Prediction of Bovine Serum Albumin Pelleting Using the ESP Pelleting Run Simulation from the Optima EXPert Software*. https://www.beckmancoulter.com/wsrportal/bibliography?docname=A-1938B.pdf.

273. Gasser, M. *et al.* The adsorption of biomolecules to multi-walled carbon nanotubes is influenced by both pulmonary surfactant lipids and surface chemistry. *J. Nanobiotechnology* **8**, 31 (2010).

274. Marquardt, C., Fritsch-Decker, S., Al-Rawi, M., Diabaté, S. & Weiss, C. Autophagy induced by silica nanoparticles protects RAW264.7 macrophages from cell death. *Toxicology* **379**, 40–47 (2017).

275. Zhang, W. *et al.* Suppressing the cytotoxicity of CuO nanoparticles by uptake of curcumin/BSA particles. *Nanoscale* **8**, 9572–9582 (2016).

276. Pang, L. *et al.* Exploiting macrophages as targeted carrier to guide nanoparticles into glioma. *Oncotarget* **7**, 37081–37091 (2016).

277. Holmskov, U. L. *Collectins and collectin receptors in innate immunity*. *APMIS, Supplement* vol. 108 (2000).

278. Vetten, M. A. *et al.* Label-free in vitro toxicity and uptake assessment of citrate stabilised gold nanoparticles in three cell lines. *Part. Fibre Toxicol.* **10**, (2013).

279. Taratummarat, S. *et al.* Gold nanoparticles attenuates bacterial sepsis in cecal ligation and

puncture mouse model through the induction of M2 macrophage polarization. *BMC Microbiol.* **18**, (2018).

280. Orlando, A. *et al.* Evaluation of gold nanoparticles biocompatibility: a multiparametric study on cultured endothelial cells and macrophages. *J. Nanoparticle Res.* **18**, 1–12 (2016).

281. Chen, Y. *et al.* Gold nanoparticles coated with polysarcosine brushes to enhance their colloidal stability and circulation time in vivo. *J. Colloid Interface Sci.* **483**, 201–210 (2016).

282. Xu, J. *et al.* Dose Dependencies and Biocompatibility of Renal Clearable Gold Nanoparticles: From Mice to Non-human Primates. *Angew. Chemie* **130**, 272–277 (2018).

283. Cheng, Y. H., Riviere, J. E., Monteiro-Riviere, N. A. & Lin, Z. Probabilistic risk assessment of gold nanoparticles after intravenous administration by integrating in vitro and in vivo toxicity with physiologically based pharmacokinetic modeling. *Nanotoxicology* **12**, 453–469 (2018).

284. Chen, Y. S., Hung, Y. C., Liau, I. & Huang, G. S. Assessment of the in vivo toxicity of gold nanoparticles. *Nanoscale Res. Lett.* **4**, 858–864 (2009).

285. Beck, A. P. & Meyerholz, D. K. Evolving challenges to model human diseases for translational research. *Cell and Tissue Research* 1–7 (2020) doi:10.1007/s00441-019-03134-3.

286. Rosenthal, N. & Brown, S. The mouse ascending: Perspectives for human-disease models. *Nature Cell Biology* vol. 9 993–999 (2007).

287. Justice, M. J. & Dhillon, P. Using the mouse to model human disease: Increasing validity and reproducibility. *DMM Disease Models and Mechanisms* vol. 9 101–103 (2016).

288. Wert, S. E. *et al.* Increased metalloproteinase activity, oxidant production, and emphysema in surfactant protein D gene-inactivated mice. *Proc. Natl. Acad. Sci. U. S. A.* **97**, 5972–5977 (2000).

289. Kuroki, Y., Takahashi, H., Chiba, H. & Akino, T. Surfactant proteins A and D: Disease markers. *Biochimica et Biophysica Acta - Molecular Basis of Disease* vol. 1408 334–345 (1998).

290. Kreyling, W. G. *et al.* Air-blood barrier translocation of tracheally instilled gold nanoparticles inversely depends on particle size. *ACS Nano* **8**, 222–233 (2014).

291. Bachler, G. *et al.* Translocation of gold nanoparticles across the lung epithelial tissue

barrier: Combining in vitro and in silico methods to substitute in vivo experiments. *Part. Fibre Toxicol.* **12**, 18 (2015).

292. Chono, S., Tanino, T., Seki, T. & Morimoto, K. Influence of particle size on drug delivery to rat alveolar macrophages following pulmonary administration of ciprofloxacin incorporated into liposomes. *J. Drug Target.* **14**, 557–566 (2006).

293. Choi, H. S. *et al.* Rapid translocation of nanoparticles from the lung airspaces to the body. *Nat. Biotechnol.* **28**, 1300–1303 (2010).

294. Pujalté, I., Dieme, D., Haddad, S., Serventi, A. M. & Bouchard, M. Toxicokinetics of titanium dioxide (TiO2) nanoparticles after inhalation in rats. *Toxicol. Lett.* **265**, 77–85 (2017).

295. World Health Organization. Ambient (outdoor) air pollution. *WHO* https://www.who.int/news-room/fact-sheets/detail/ambient-(outdoor)-air-quality-and-health (2018).

296. World Health Organization. Household air pollution and health. *WHO media centre* 1–6 https://www.who.int/news-room/fact-sheets/detail/household-air-pollution-and-health (2016).

297. Pacini, E. Pollination. in *Encyclopedia of Ecology, Five-Volume Set* 2857–2861 (Elsevier Inc., 2008). doi:10.1016/B978-008045405-4.00859-4.

298. Mohan, D. Toxicity of exhaust nanoparticles. *African J. Pharm. Pharmacol.* **7**, 318–331 (2013).

299. Watson, J. G., Chow, J. C. & Houck, J. E. PM2.5 chemical source profiles for vehicle exhaust, vegetative burning, geological material, and coal burning in Northwestern Colorado during 1995. *Chemosphere* **43**, 1141–1151 (2001).

300. European Environment Agency. *Particulate matter from natural sources and related reporting under the EU Air Quality Directive in 2008 and 2009*. (2012).

301. Air Quality Expert Group. *Particulate Matter in the UK: Summary*. www.defra.gov.uk (2005) doi:10.1093/bmb/ldg028.

302. Banaei, N., Foley, A., Houghton, J. M., Sun, Y. & Kim, B. Multiplex detection of pancreatic cancer biomarkers using a SERS-based immunoassay. *Nanotechnology* **28**, 455101 (2017).